UNIVERSITÀ DEGLI STUDI DI PADOVA
Dipartimento di Fisica e Astronomia “Galileo Galilei”

CORSO DI DOTTORATO DI RICERCA IN ASTRONOMIA
CICLO XXXII

Intermediate Luminosity Optical Transients

Direttore della scuola: Ch.mo Prof. Giampaolo Piotto
Supervisore: Dr. Andrea Pastorello

Dottorando: Yongzhi Cai

Sommario

Oltre alle supernove (SNe), pochissime esplosioni cosmiche sono in grado di rilasciare una quantità di energia cinetica dell'ordine di 10^{51} erg (1 foe). Negli anni passati, moderne "all-sky surveys" hanno permesso di scoprire numerosi transienti peculiari che rilasciavano energie molto più modeste. Con il nome di *transienti ottici di luminosità intermedia* o *transienti nel "gap"*, ci riferiamo ad oggetti che sono più deboli delle tipiche SNe ma più luminosi delle classiche novae (cioè hanno magnitudine nell'intervallo -10< M_V < -15 mag). In questo intervallo di luminosità scarsamente popolato (il "gap"), troviamo diversi tipi di transienti stellari, tra cui supernove deboli, eruzioni giganti di stelle massicce incluse le Variabili Luminose Blu (LBV), i transienti rossi di luminosità intermedia (ILRTs) e le novae rosse luminose (LRNe). Questi transienti di "gap" possono essere prodotti da diversi meccanismi fisici, e talvolta la loro classificazione è un compito arduo. Uno degli obiettivi principali di questo studio è caratterizzare le proprietà osservative e correlare i parametri fisici dei transienti di "gap", svelandone la natura. In questo lavoro di tesi, ho studiato in dettaglio un recente evento transiente debole e rosso, AT 2017be, classificato come ILRT, e ho mostrato come una supernova prodotta da cattura elettronica (EC SN) sia lo scenario più probabile per spiegare l'evento eruttivo osservato. Un'analisi approfondita su un grande campione di ILRTs favorisce lo stesso meccanismo di esplosione per tutti questi transienti. Infine, ho studiato un oggetto senza precedenti, AT 2018hso, che rivela proprietà osservative intermedie tra quelle degli ILRT e le LRNe, e che rendono una sua precisa classificazione incerta. Tuttavia, le osservazioni di follow-up supportano la tesi che sia un LRN, quindi probabilmente un transiente prodotto da un evento di coalescenza stellare.

Abstract

Beyond supernovae (SNe), very few cosmic explosions can release an amount of kinetic energy of the order of 10^{51} erg (1 foe). In past years, modern all-sky surveys discovered numerous peculiar transients releasing much lower energies. With the label of *Intermediate Luminosity Optical Transients* or *Gap Transients*, we refer to objects fainter than typical SNe but brighter than classical novae (i.e., they lay in the magnitude range -10< M_V < -15 mag). In this poorly populated luminosity range (the "gap"), we find several types of stellar transients, including faint supernovae, giant eruptions of massive stars including luminous blue variables (LBVs), intermediate-luminosity red transients (ILRTs), and luminous red novae (LRNe). These gap transients may originate from various physical mechanisms, and sometimes the classification is a tricky task. A major goal of this research work is characterising the observational properties and correlating the physical parameters of gap transients, shedding light on their nature. In this thesis project, I studied in detail a recent faint and red transient, AT 2017be, classified as an ILRT, and show that an electron-capture supernova (EC SN) is the most likely scenario to explain the observed outburst. In-depth analysis on a large ILRT sample favours the same explosion mechanism for all of them. Finally, I studied an unprecedented object, AT 2018hso, that reveals transitional observational properties between ILRTs and LRNe, making its precise classification dubious. However, follow-up observations support it to be a LRN, hence most likely a transient produced by a stellar merging event.

List of Papers

The five papers are included in this PhD thesis, which are referred to as **Paper I**, **Paper II**, **Paper III**, **Paper IV**, **Paper V**.

Paper I, Cai et al. (2018); Y-Z. Cai, A. Pastorello, M. Fraser, M. T. Botticella, C. Gall, I. Arcavi, S. Benetti, E. Cappellaro, N. Elias-Rosa, J. Harmanen, G. Hosseinzadeh, D. A. Howell, J. Isern, T. Kangas, E. Kankare, H. Kuncarayakti, P. Lundqvist, S. Mattila, C. McCully, T. M. Reynolds, A. Somero, M. D. Stritzinger, and G. Terreran. (2018). *AT 2017be – a new member of the class of intermediate-luminosity red transients.* MNRAS, 480, 3424.

Paper II, Cai et al. (2019a); Y-Z. Cai, A. Pastorello, M. Fraser, S. J. Prentice, T. M. Reynolds, E. Cappellaro, S. Benetti, A. Morales-Garoffolo, A. Reguitti, N. Elias-Rosa, S. Brennan, E. Callis, G. Cannizzaro, A. Fiore, M. Gromadzki, F. J. Galindo-Guil, C. Gall, T. Heikkilä, E. Mason, S. Moran, F. Onori, A. Sagués Carracedo, G. Valerin. (2019). *The transitional gap transient AT 2018hso: new insights on the luminous red nova phenomenon.* A&A Letter, In Press. DOI: https://doi.org/10.1051/0004-6361/201936749

Paper III, Cai et al. (2019b); Y-Z. Cai, A. Pastorello, ..., . (2019). *Intermediate-Luminosity Red Transients: Spectro-photometric Properties.* A&A, To be submitted.

Paper IV, Pastorello et al. (2019a); A. Pastorello, T.-W. Chen, **Y-Z. Cai**, A. Morales-Garoffolo, Z. Cano, E. Mason, E. A. Barsukova, S. Benetti, M. Berton, S. Bose, F. Bufano, E. Callis, G. Cannizzaro, R. Cartier, Ping Chen, Subo Dong, S. Dyrbye, N. Elias-Rosa, A. Flörs, M. Fraser, S. Geier, V. P. Goranskij, D. A. Kann, H. Kuncarayakti, F. Onori, A. Reguitti, T. Reynolds, I. R. Losada, A. Sagués Carracedo, T. Schweyer, S. J. Smartt, A. M. Tatarnikov, A. F. Valeev, C. Vogl, T. Wevers, A. de Ugarte Postigo, L. Izzo, C. Inserra, E. Kankare, K. Maguire, K. W. Smith, B. Stalder, L. Tartaglia, C. C. Thöne, G. Valerin, and D. R. Young. (2019). *The evolution of luminous red nova AT 2017jfs in NGC 4470.* A&A, 625, L8.

Paper V, Pastorello et al. (2019b); A. Pastorello, E. Mason, S. Taubenberger, M. Fraser, G. Cortini, L. Tomasella, M. T. Botticella, N. Elias-Rosa, R. Kotak, S. J. Smartt, S. Benetti, E. Cappellaro, M. Turatto, L. Tartaglia, S. G. Djorgovski, A. Drake, M. Berton, F. Briganti, J. Brimacombe, F. Bufano, **Y.-Z. Cai**, S. Chen, E. J. Christensen, F. Ciabattari, E. Congiu, A. Dimai, C. Inserra, E. Kankare, L. Magill, K. Maguire, F. Martinelli, A. Morales-Garoffolo, P. Ochner, G. Pignata, A. Reguitti, J. Sollerman, S. Spiro, G. Terreran, and D. E. Wright. (2019). *Luminous Red Novae: Stellar Mergers or Giant Eruptions?.* A&A, 630, A75.

Contents

List of Figures

List of Tables

Chapter 1

Introduction

1.1 Surveying the sky

Sky surveys are fundamental for astronomy, as new science originates from charting and monitoring the sky. The first survey, going back to the 2nd century BC, is attributed to Hipparchus, that created a catalog of 850 stars using his naked eyes. For almost two thousand years, sky surveys were performed using the naked eye or simple telescopes. However, the breakthroughs in sky surveys started from late 20th century thanks to the advent of new technologies and facilities, such as sensitive photo emulsions, high-efficiency CCD matrices, high-performance computers, and larger telescopes. These surveys widely increased our knowledge on the variety of transients, and led us to classify dozens new types of events.

1.1.1 Targeted surveys

In the past 30 years, there have been many successful surveys searching for supernovae (or other types of stellar transients). The most representative targeted survey is the Lick Observatory Supernova Search (LOSS) with the Katzman Automatic Imaging Telescope (KAIT [1]) (e.g., Filippenko et al. 2001; Li et al. 2000), whose first light is dated 1996. It targeted around 5000 nearby (usually $z < 0.03$) galaxies, most of which were nearby large galaxies. A scheduler automatically selected every night the objects to be observed according to their observational records. The LOSS focused on the SN search, although other types of astrophysical sources were observed, including variable stars, active galactic nuclei, etc. This type of survey is labelled "targeted survey".

1.1.2 Empty-field surveys

The Robotic Optical Transient Search Experiment (ROTSE; e.g., Marshall et al. 1997) is contemporary of LOSS. However, its scientific goal was to discover and observe fast-evolving transients, in particular the optical counterparts of Gamma-Ray Bursts (GRBs). The most recent configuration is ROTSE-III, which operated in four nodes: ROTSE-IIIa (Australia), ROTSE-IIIb (USA), ROTSE-IIIc (Namibia) and ROTSE-IIId (Turkey). Its survey strategy was to target a particular sky region with fully automated telescopes at different sites in the world. The ROTSE survey is an example of

[1] `http://w.astro.berkeley.edu/bait/kait.html`

"empty-field" surveys, where bright nearby galaxies are not the primary targets. Although the main goal of the ROTSE project is to observe rapid events, fruitful by-products were supernovae [2], novae [3] and variable stars [4]. The Texas Supernova Search program (TSS; e.g., Quimby 2006) at ROTSE found around 30 SNe in its first two years (from late 2004) of activity. Then, TSS evolved towards the ROTSE Supernova Verification Project (RSVP; e.g., Yuan et al. 2007), that discovered 46 SNe until September 2009. The first Super-Luminous Supernova (SLSN; 2005ap) was discovered by 0.45 m ROTSE-IIIb (Quimby et al. 2007, 2011).

1.1.3 Wide-field surveys

A new era of searching astrophysical transients in the Local Universe began with the construction of telescopes equipped with large field of view cameras. Active surveys, such as the Palomar Transient Factory (PTF; e.g., Law et al. 2009), the Pan-STARRS1 (PS1; e.g., Kaiser et al. 2010), the Catalina Real Time Survey (CRTS; e.g., Drake et al. 2009), and the SkyMapper survey (e.g., Keller et al. 2007), are usually a network of 0.7-2 m telescopes, equipped with cameras covering 5-10 square degrees. The typical exposure time of a single image taken during these surveys is 30-60 seconds, thus they are able to detect sources down to magnitudes 19 to 21, and scanning around 1000-6000 square degrees of sky every night.

The wide-field survey is defined when data come from sky areas that cover at least 1% of the entire sky (Djorgovski et al. 2013). We remark that "big data" is a time-evolving concept, which increases exponentially following Moore's law. A wide-field survey provides a broad variety of scientific objects, and this thesis will be focused on some of the most peculiar stellar transients.

1.1.4 Spectroscopic classification of new candidates

Once a new transient is found, a spectroscopic classification is required. Spectra of new targets are obtained with low-resolution spectroscopy performed with the available telescopes. A remarkable example of spectroscopic survey is the Public European Southern Observatory Spectroscopic Survey of Transient Objects (PESSTO; PI: S. J. Smartt; e.g., Smartt et al. 2015) started in 2012. It first classifies the transients provided by the main sky surveys. The evaluation criteria for transient selection are determined to match the scientific goals of PESSTO. The main facility for PESSTO is the 3.58-m New Technology Telescope (NTT), equipped with EFOSC2 (optical) and SOFI (near-infrared; NIR). By studying the optical and NIR photometry and spectroscopy datasets, we expand the knowledge of the physics regulating the explosion mechanisms and evolution of stellar transients.

1.1.5 Multi-domain surveys

With the development of instruments and new technologies, more extended surveys became possible. Beyond the classical optical, new surveys at different wavelengths started to produce useful data, in particular: in the gamma-ray, X-ray, IR, and radio domains.

[2] http://www.rotse.net/rsvp/
[3] http://www.rotse.net/rsvp/
[4] http://www.rotse.net/transients/

- Gamma-ray surveys

Gamma-ray bursts (GRBs) are transients with extremely high energy in the Universe. GRBs have short durations, ranging from 10 milliseconds to several hours, and can be classified as short (<2s), long (>2s), and ultra-long GRBs, according to their time scales (e.g., Mukherjee et al. 1998). Broad-line Type Ic supernovae (see Subsection 1.2.2) are associated with long-duration GRBs (e.g., Podsiadlowski et al. 2004; Mazzali et al. 2005; Woosley & Bloom 2006), and binary neutron star mergers are believed to produce short-duration GRBs (e.g., Abbott et al. 2008; Smartt et al. 2017; Granot et al. 2017; Drout et al. 2017). A GRB event is usually associated with an afterglow at longer wavelengths, after the initial gamma-ray flash. There are many questions still open on GRBs, such as the energy sources and the local environments. The Fermi Gamma-ray Space Telescope is one of the dedicated facilities to explore the Universe and to answer to these questions. The Large Area Telescope (LAT) equipped in Fermi detects GRBs with spectral energy of 30 MeV - 300 GeV, while another instrument Gamma-ray Burst Monitor (GBM) has a relatively lower energy coverage from 8 keV - 40 MeV (e.g., Atwood et al. 2009).

- X-ray surveys

X-ray transients pervade the Universe. However, X-rays are blocked by Earth's atmosphere and thus the X-ray telescopes have to be placed in space. The X-ray Multi-Mirror Mission (XMM-Newton) was launched by the European Space Agency's (ESA) on 1999 December 10th. XMM-Newton has a wide energy passband, and can simultaneously observe also at the optical and UV domains, providing three channels for imaging and spectroscopy. Thus, it allows us to study different classes of X-ray sources, such as tidal disruption events (TDE), supernova shock breakouts, and low-mass X-ray binaries (LMXBs).

- IR surveys

Some transients are faint in the optical region, but are luminous in the IR domain. This is because they are significantly obscured by the dust along the line of sight. The dust absorbs the shorter wavelength radiation and re-emits the photons at longer wavelengths. Or, they might also intrinsically red. In order to explore the landscape of IR transients, Kasliwal et al. (2017) started the SPitzer InfraRed Intensive Transients Survey (SPIRITS) in 2014. They observed IR-luminous transients in nearby galaxies (d< 35 Mpc) at CH1 (3.6 μm) and CH2 (4.5 μm). SPIRITS discovered the so-called eSPecially Red Intermediate-luminosity Transient Events (SPRITEs; e.g., Kasliwal et al. 2017, and references therein). The most distinguished properties for SPRITEs are that they have no or weak optical counterparts and their peak luminosities (CH2=4.5 μm) are between -11 and -14 mag. The timescale for their luminosity decline is between 55 and 480 days (Kasliwal et al. 2017).

- Radio surveys

Karl Jansky first detected radio signals from the Universe in the 1930s, and now, radio telescopes are widely used to detect the radio waves emitted from a variety of astrophysical events. Radio telescopes provide a new channel to understand the Universe, which is different from the optical view. Radio telescopes can be used individually and be linked together to form an interferometer network. Astronomers work with radio telescopes hearing the radio wave with high-time resolution. This allows us to detect gas and astrophysical sources obscured by cosmic dust. The Survey for Pulsars and Extragalactic Radio Bursts (SUPERB; e.g., Keane et al. 2010; Rane et al. 2016; Keane et al. 2018;

Bhandari et al. 2018b; Caleb et al. 2018) is a recent survey which searches radio transients (pulsars) and fast radio bursts (FRBs), with the Parkes radio telescope. The main radio transients are short-duration pulses. For example, pulsars have a few 10s to ms pulses, while FRBs have durations of milliseconds. The future Square Kilometre Array (SKA; e.g., Schilizzi et al. 2010; Norris et al. 2013; Bhandari et al. 2018a) will be able to observe the sky with faster cadence than any current telescope. An enormous number of short transients will be detected when SKA will be fully operational (e.g., Wang et al. 2015).

The above modern surveys provide us a global view of cosmic sources in the Local Universe (see Figure 1.1). We will discuss the most important types of transients in the following sections.

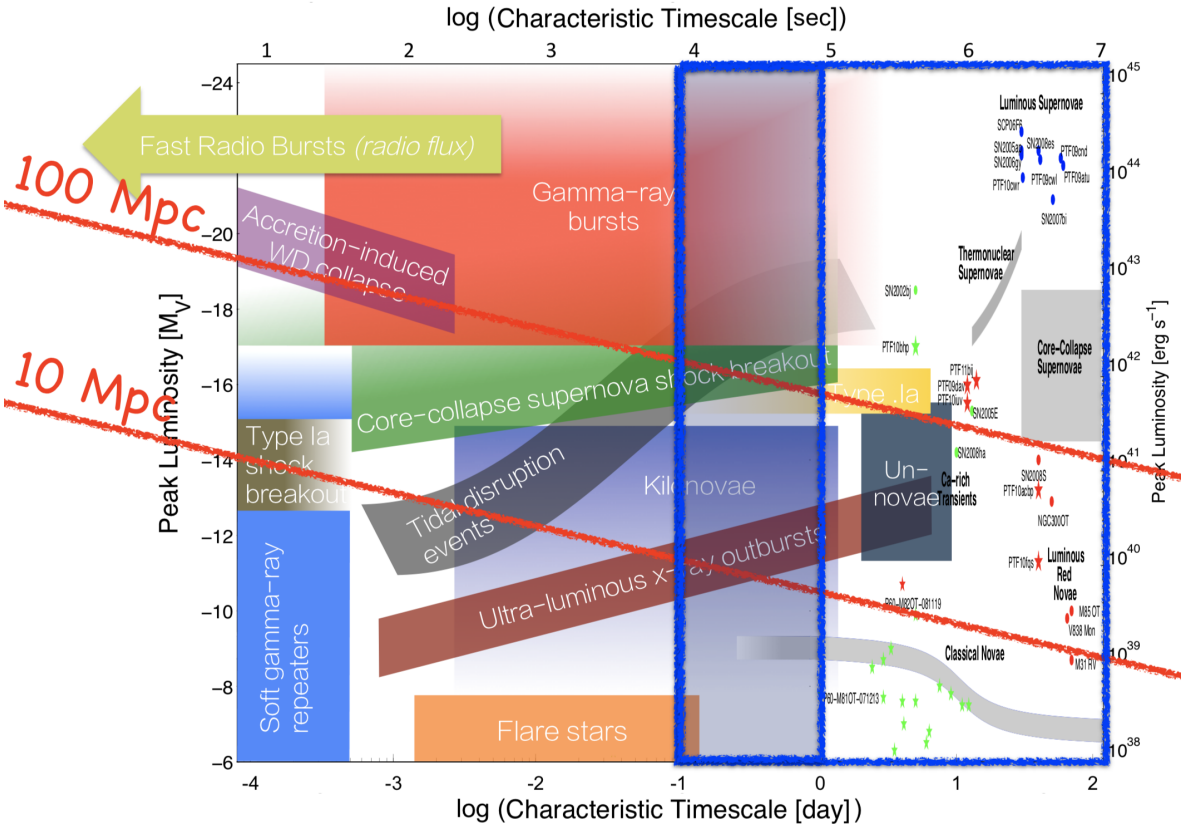

Figure 1.1: The zoo of cosmic sources. This is an extended version of Figure 1 of Kasliwal (2012). Two inclined red lines mark the distance at which usually each type of transients occur. The left part shows the transients evolving in short time scales (usually $\ll$ 1 day), the right one with blue edging presents traditional transients with longer evolutionary time scales (usually $\gg$ 1 day), and the middle blue area is an overlapping region, with transients evolving in 0.1-1 days. It intersects most of known transients (e.g., supernovae, kilonovae, intermediate luminosity optical transients, gamma-ray bursts, fast radio bursts). (Figure source: *http : //www.ioa.s.u − tokyo.ac.jp/kisohp/RES EARCH/symp*2018*/morokuma.pdf*)

1.2 Transients: Supernovae

Why we study Supernovae (SNe)? As a basic question for human beings, the origin of new light points in the sky is fascinating. Furthermore, SNe are associated with the end of life of a star, with a gigantic release of radiated energy. SNe have a peak luminosity comparable with a billion times that of the Sun, and the matter is ejected at extremely high speeds (a few percent of light speed). From the first SN discovery to now, we have found many tens of thousands events. With the development of observational technology and methods, ground and space facilities allowed us to find an increasing number of new SN types, which required an updated classification scheme.

First attempts to classify SNe date back to the late 1930s (e.g., Baade & Zwicky 1934; Zwicky 1938, 1940). Minkowski (1941) introduced a spectral classification scheme according to the presence/absence of hydrogen lines in their spectra, providing Type II and Type I, respectively. The classical Type I SNe (now named "Ia") had H- and He- free spectra, and showed prominent S II and Si II lines (see details in Section 1.2.1). Later, Elias et al. (1985) labelled as Type Ib SNe whose spectra showed He I features. Harkness et al. (1987) realised that the spectra of Type Ib were dominated by He I lines near the peak phase, showing weak Si II absorption. Later, Wheeler et al. (1994) introduced another sub-class termed Type Ic, whose spectra did not have signatures of He I, but strong O I and Ca II lines. When the sub-classification is controversial, SN Type Ib and Type Ic are referred to as "SN Ib/c" (see Section 1.2.2). A spectral characteristic of different SN categories (see Filippenko 1997, for a review on the SN spectral classification) is presented in Figure 1.2.

Among H-rich events, Barbon et al. (1979) proposed two subclasses of Type II, namely, Type II-P and Type II-L, based on the different shapes of their light curves. Type II-P SNe are characterised by a long period (3-4 months) of constant luminosity, called plateau; Type II-L SNe have a linear decline in the post-peak light curve. Filippenko (1988) introduced the Type IIb subclass, whose spectra have strong H lines at early times, and show intense He lines later. Both SN IIb and SN Ib/c are usually termed as "stripped-envelope supernovae" (Clocchiatti et al. 1996), because we believe that their progenitors had lost the H envelope prior to the explosion. Schlegel (1990) introduced another SN subclass, called Type IIn, whose spectra show strong and relatively narrow H emission lines a top of a broader base, suggesting an interaction between the ejecta and slow-moving pre-existing circumstellar material (CSM, Chugai & Danziger 1994). Similarly, Type Ibn SNe also show narrow He I lines in emission likely coming from the interaction with He-rich CSM (Pastorello et al. 2008). The detailed discussions are presented in Section 1.2.2, and the updated classification scheme (Athem Alsabti 2015) is shown in Figure 1.3.

In summary, the main spectral characteristics of Type I SNe are:

- Ia – no Hydrogen lines, but prominent S II and Si II lines.
- Ib – no Hydrogen, weak Si II lines, but dominant He I lines.
- Ic – no Hydrogen, weak Si II lines, and no He I lines.
- Ibn [5] – The spectra show prominent, narrow He I lines in emission.

Type II SNe show spectra with H, but:

- II-P – The light curve is characterised by a plateau, lasting about 80-120 days.

[5] They show a large variety of light curve shapes.

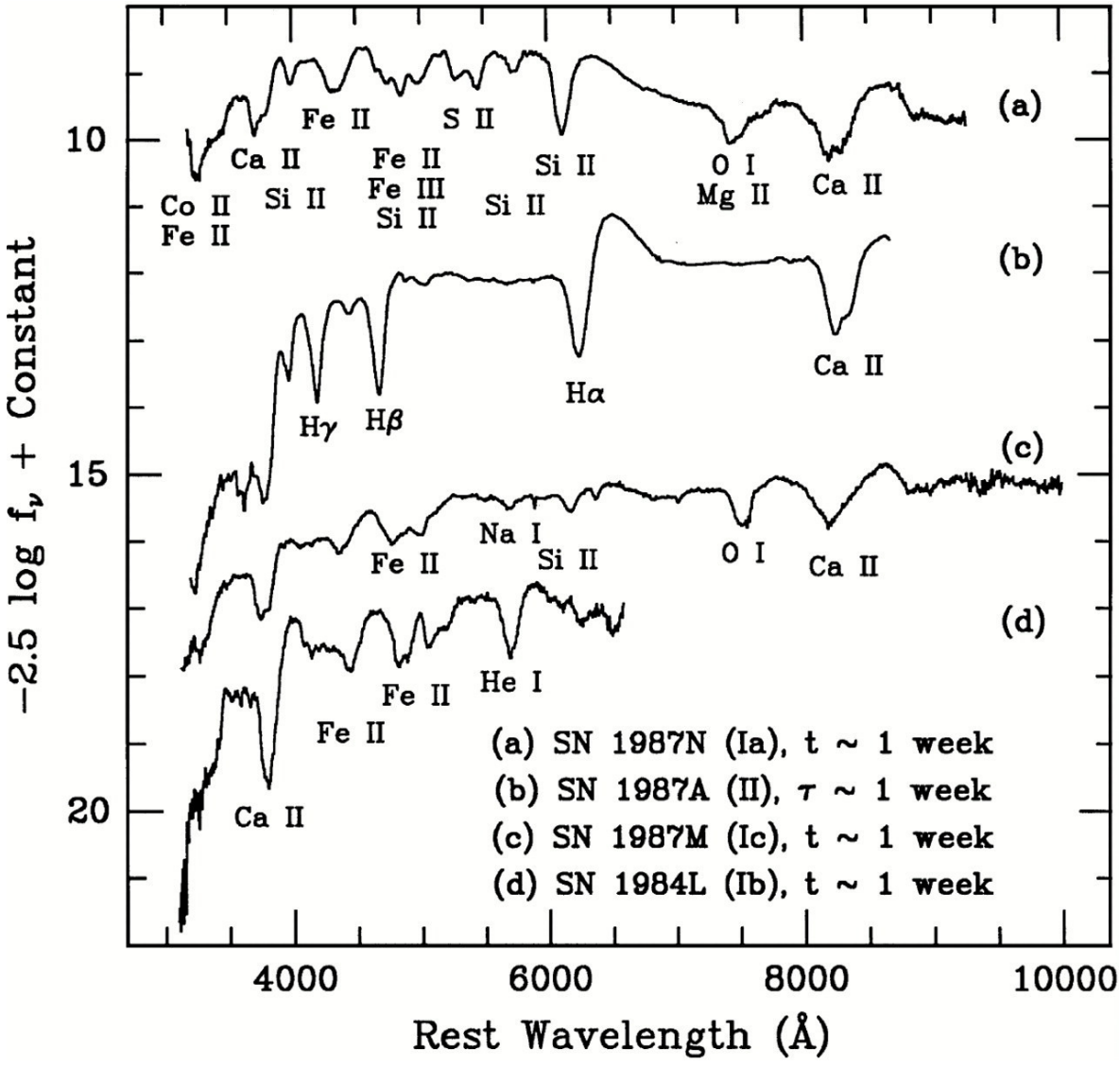

Figure 1.2: Spectral comparison between different SN types. (Figure from Filippenko 1997)

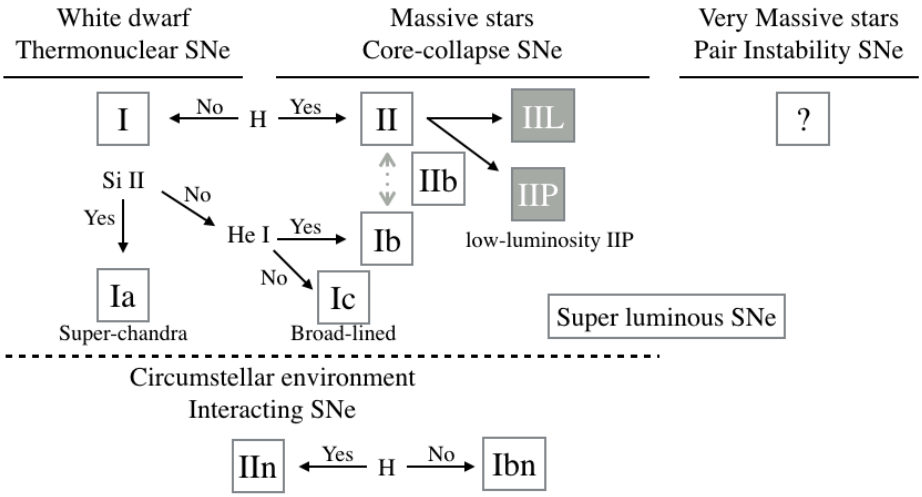

Figure 1.3: SN classification scheme based on photometric and spectroscopic features. Figure from Athem Alsabti (2015).

- II-L – The light curve has a linear decline rate after peak.
- IIb – The light curves resemble those of Type Ib/Ic SNe. The spectra show He I lines and have strong H I lines at early time (usually a few weeks), that become weak at later phases.
- IIn – They display a variety of light curves. The spectra have a blue pseudo-continuum, with Balmer series lines in emission, usually displaying multiple-components.

With the improvement of observational facilities, the catalogs of SN (or transient) families have tremendously enlarged in recent decades. Among new species, we mention broad-line SNe Ic (also known as SNe Ic-BL) sometimes connected with GRBs and X-Ray Flashes (XRFs) (Woosley & Bloom 2006). In addition, a newly-defined category of SLSNe challenged our knowledge on the fate of massive stars (e.g., Quimby et al. 2011; Gal-Yam 2012; Inserra et al. 2018b). The facts we gathered now led to an improved classification scheme, with a combination of physical and observational features.

In this Chapter, a basic review on the different SN species is presented in Section 1.2. The observational and theoretical properties of thermonuclear, core-collapse (CC) SNe, and SL SNe are illustrated in Section 1.2.1, 1.2.2, and 1.2.3, respectively. In Section 1.3, we describe some rare transients in the gap between thermonuclear and CC SNe.

1.2.1 Thermonuclear supernovae

Stars with an initial mass below 7-8 $M_\odot$ are expected to end their life as white dwarfs (WDs). At the late phase of its evolution, a star will shed its outer layers, leaving a stripped carbon (C) and oxygen (O) core. At this stage, the CO core is not hot enough to ignite the fusion of these high-mass elements. Thermonuclear SNe are believed to be the explosion of WDs in a binary system accreting mass from a companion star (e.g., Wang et al. 2018). When the WD reaches the Chandrasekhar limit (critical mass $\sim 1.44 M_\odot$), the electron degeneracy pressure no longer supports the stellar mass, the core temperature

increases and thus triggers thermonuclear reactions. These produce heavier elements, including ^{56}Ni that decays to ^{56}Co and finally to ^{56}Fe. The explosion does not leave compact remnants behind. Type Ia SNe contribute to the chemical enrichment of the galaxies, providing in particular iron peak elements. The radioactive energy powers the SN light curve to a peak luminosity comparable with that of the host galaxy. In the following sub-sections, we briefly describe the observational properties and theoretical scenarios for SNe Ia.

Observational category

Type Ia SNe are discovered in all types of galaxies, from the early to the late types (Barbon et al. 1999). A strong link of SN Ia sites with star-forming regions (i.e., the spiral arms) does not exist, suggesting that they can explode in any stellar population environments [6].

SNe Ia have relatively similar light curves (see Figure 1.4). In particular, their peak luminosity is homogeneous (with an average absolute magnitude $M_V = -19.48 \pm 0.07$ mag; Gibson et al. 2000), and thus they can be used to measure cosmological distances. Through the study of SNe Ia, S. Perlmutter, B. P. Schmidt, and A. G. Riess found the accelerated expansion of the Universe (Riess et al. 1998; Perlmutter et al. 1999), leading them to win the 2011 Nobel Prize in Physics. SNe Ia are used as Standardizable Candles (e.g., Phillips 2003; Krisciunas et al. 2004; Wang et al. 2006; Dhawan et al. 2018). We note that bright SNe Ia have broader light curves than faint ones, as seen in the top panel of Figure 1.3 of Ganeshalingam (2012). By analysing the light curve characteristics, Phillips (1993) found a relation between their luminosities and light curve widths, known as Phillips' relation (see details in the Figure 1 of Phillips 1993). Standardised light curves using Phillips' relation are shown in the left bottom panel. The light curves of SNe Ia are characterised by a pronounced secondary maximum in the red/NIR bands (e.g., Dhawan et al. 2015; Wang et al. 2009; Kasen 2006; Jack et al. 2012). Another important feature of the light curves is the late-time luminosity tail, which is typically steeper than the ^{56}Co decay (Kuchner et al. 1994; Varani et al. 1990). The multi-band light curves of a classical Type Ia SN 2005cf (Pastorello et al. 2007b; Wang et al. 2009) are shown in the right panel of Figure 1.4.

Broad bumps and valleys are dominant in the early spectra of SNe Ia (see an example in Figure 1.5). These features, in general, are attributed to the contribution of singly ionised metals, in particular intermediate-mass elements (e.g., O, Mg, S, Si, Ca). In addition, features of ionised iron-peak elements are strong in the near-UV region (e.g., Kirshner et al. 1993; Mazzali et al. 1993). In SN Ia optical spectra, the most prominent features are Si II (λ=6355 Å), the "W" feature of S II, and Ca II H&K ($\lambda_{1,2}$=3934 Å, 3968 Å) (e.g., Wang et al. 2009; Silverman et al. 2012). The contribution of intermediate-mass elements decreases with time, with iron-group elements becoming dominant at late phases. Fe II lines are strong at $\sim$ 2 weeks after the explosion, with Si II and Ca II lines remaining still visible. Forbidden Fe lines become dominant in the nebular phase in pure emission (Axelrod 1980). SN 1937C (Minkowski 1939; Greenstein & Minkowski 1973) is the first SN Ia with a long-term spectral monitoring, but well-sampled classical SNe Ia are also SN 1972E (Kirshner et al. 1973; Kirshner & Oke 1975), SN 1989B (Barbon et al. 1990; Wells et al. 1994), and SN 1994D (Meikle et al. 1996; Patat et al. 1996). As a representative object of this class, the spectral evolution of SN 1994D is shown

[6] However, in order to understand the birthplace vs. ejecta-velocity relation, Wang et al. (2013) investigated a sample of 188 well-defined SNe Ia. Their analysis suggest that SNe Ia may have two distinct populations.

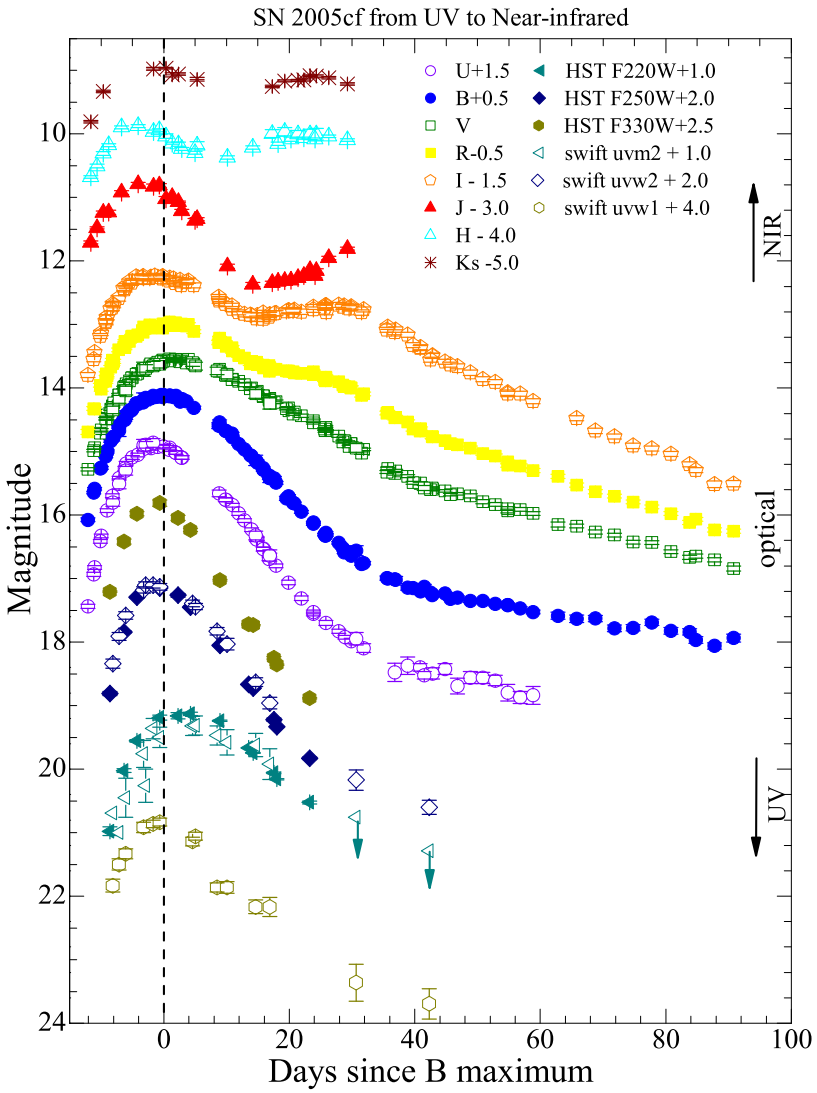

Figure 1.4: The UV (HST+*Swift* filters), optical (UBVRI), and NIR (JHK) light curves of a prototypical Type Ia - SN 2005cf. Figure source: Wang et al. (2009).

in Figure 1.5.

However, along with thousands of normal SNe Ia, a number of peculiar events (e.g. Zhang et al. 2016) have been discovered in the last three decades, challenging our knowledge on thermonuclear explosions, and their use as cosmological tools. The main classes of thermonuclear transients are presented in Figure 1.6, while we only mention a few highlighted subtypes as this topic is beyond the scope of this thesis.

- SN 1991T (e.g. Filippenko et al. 1992b; Ruiz-Lapuente et al. 1992; Phillips et al. 1992; Cappellaro et al. 1997, 2001) is the prototype of a SN group showing a luminous light curve, but with a broader width ($\Delta_{m15} < 1$ mag) [7]. The spectra do not exhibit prominent Si II or Ca II lines at pre-maximum phases, while a growing spectral similarity to the typical SNe Ia is observed two months past maximum. The presence of a light echo is occasionally found at late phases (e.g. Schmidt et al. 1994; Cappellaro et al. 2001; Patat et al. 2006).
  - SN 2000cx (e.g., Li et al. 2001; Candia et al. 2003; Thomas et al. 2004; Branch et al. 2004b; Sollerman et al. 2004) is the most famous example of a SN Ia subtype showing an asymmetric profile in the B band light curve, with fast pre-maximum rise, but a slow post-peak decline. It reveals an unusual colour evolution with (B-V) showing a plateau during 6-15 days and (V-R), (V-I) being very blue at around 30 days. Pre-maximum spectra of SN 2000cx resemble those of SN 1991T-like objects, but later spectra show a major evolution in the emergence of the Fe II lines and the weakness of the Si II lines.

- SN 1991bg (e.g. Filippenko et al. 1992a; Leibundgut et al. 1993; Turatto et al. 1996; Mazzali et al. 1997; Wang et al. 2005b) is the prototype of a sub-class of SNe Ia. It has a light curve with a sub-luminous maximum ($M_B \sim -16.54$ mag), and shows a rapid and monotonic decline without the classical red/NIR second maximum. The spectrum has strong Ti II lines already at the early times, while at late phases it shows strong [Ca II] emission lines. The SNe are observed only in old stellar population environments (early-type galaxies; e.g., Howell 2001; Neill et al. 2009; González-Gaitán et al. 2011).

- SN 2002es-like events are a sub-group of SNe Ia that do not follow Phillips' relation (Figure 1.6; see, also Ganeshalingam et al. 2012; Kromer et al. 2013, 2016). SN 2002es (e.g. Ganeshalingam et al. 2012) has a sub-luminous ($M_B \sim -17.78$ mag) and broad width ($\Delta_{m15} = 1.28 \pm 0.04$ mag) light curve peak. Its bolometric light curve shows an unexpected plummet at ~ 1 month after maximum. The spectra are reminiscent of SN 1991bg at around maximum, but with low expansion velocities (~ 6000 km s^{-1}).

- Type Iax (e.g. Foley et al. 2014, 2015; Liu et al. 2015a,b; Jha 2017; Lyman et al. 2018; Li et al. 2018) − A representative object is SN 2002cx (e.g. Li et al. 2003; Branch et al. 2004a; Jha et al. 2006) which is less luminous than normal SNe Ia, shows SN 1991T-like pre-maximum spectra but with slightly lower expansion velocities. Although Fe-group element lines are dominant in the spectra, the intermediate-mass elements are weak or even absent.

- Ca-rich gap transients own intrinsic luminosity between -10 and -15 mag, and are hence formally "gap transients" (see Section 1.3; Kasliwal 2012). The shape of their light curves re-

[7] Δ_{m15} is defined as the difference between $B-$band maximum and the magnitude at +15 days after the peak

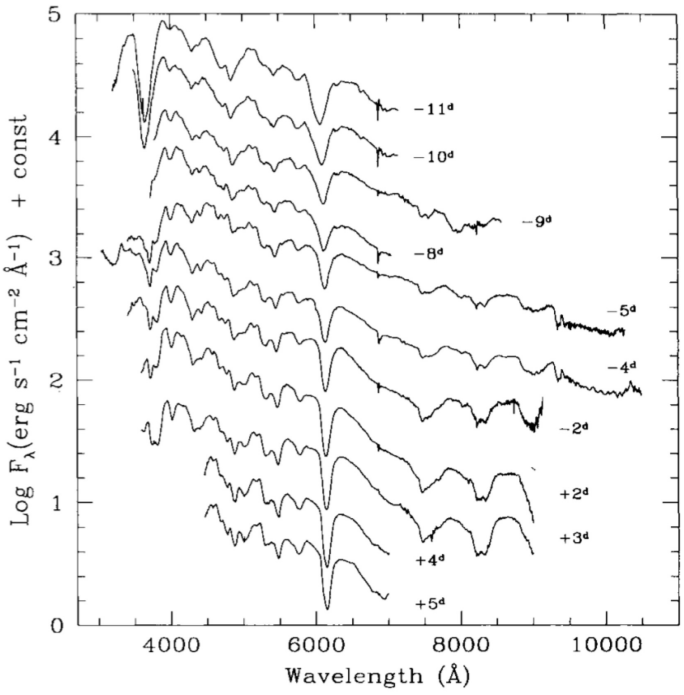

(a)

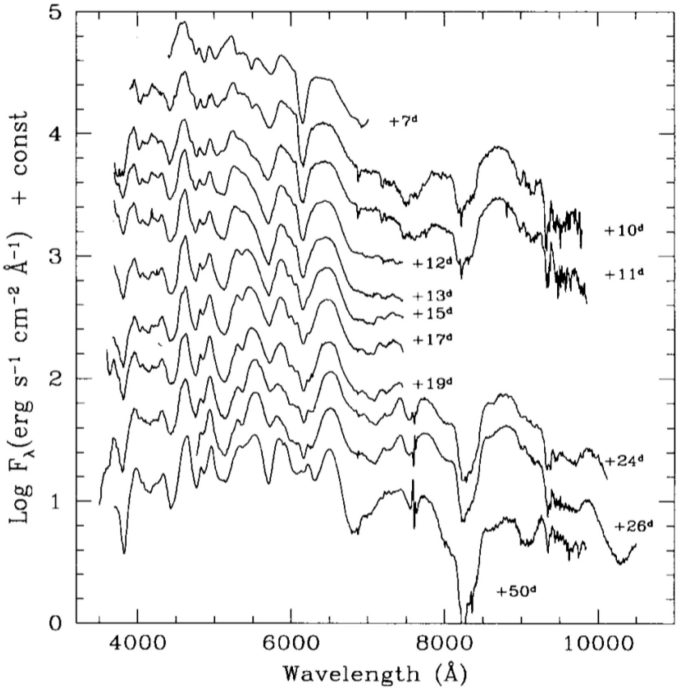

(b)

Figure 1.5: Spectral evolution of the classical Type Ia SN 1994D. Phases are relative to the $B-$band maximum (1994 March 21). Panel (a) shows spectra from −11 to +5 days. Panel (b) shows spectra from +7 to +50 days. The figure is from Patat et al. (1996)

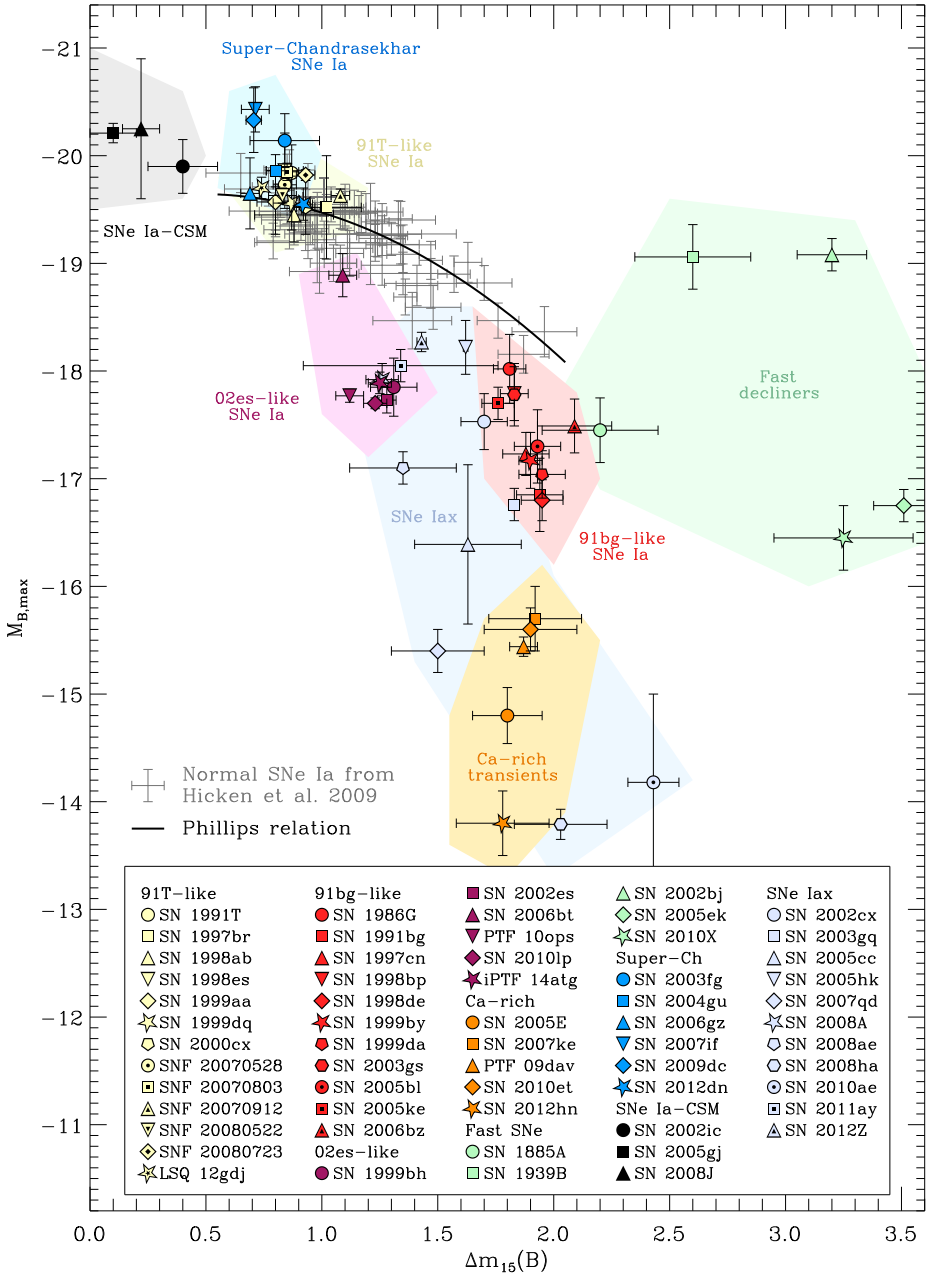

Figure 1.6: The distribution of likely thermonuclear SNe in the *B*-band absolute magnitude at peak vs. Δ_{m15}(B) diagram. The black solid line marks the Phillips' relation. The figure is from Taubenberger (2017).

semble those of SN 1991bg-like objects, or fast-declining SNe Ib/c (e.g., Perets et al. 2010; Kawabata et al. 2010; Valenti et al. 2014), but in general they decline faster in luminosity. They show He-rich and H-free spectra at early times, somewhat resembling SNe Ib. The nebular spectra are characterised by strong [Ca II] ($\lambda_{1,2}$ = 7291, 7323Å) emission lines, along with relatively weak Ca II NIR triplet (e.g., Kasliwal et al. 2012; Foley 2015).

- Super-Chandrasekhar-mass SNe Ia (e.g., Taubenberger et al. 2019) – The prototype, SN 2009dc (e.g., Yamanaka et al. 2009; Silverman et al. 2011; Taubenberger et al. 2011), has a light curve with a luminous peak of $M_B \sim -20.22$ mag, but with a broader width ($\Delta_{m15} \sim 0.71$ mag). The intermediate-mass elements are dominant in the early spectra, while the iron-group elements are prominent at late-time. All spectra show significantly lower ejecta velocities than normal SNe Ia. The SNe of this subclass explode preferably in low-mass host galaxies.

- SNe Ia-CSM (e.g., Wood-Vasey et al. 2004; Aldering et al. 2006; Taddia et al. 2012). The best observed example of this class is PTF 11kx (e.g., Dilday et al. 2012; Silverman et al. 2013b; Graham et al. 2017). They are thought to be thermonuclear explosions of WDs inside a dense H-rich CSM. This implies that their spectra resemble those of SNe IIn (e.g., see an ambiguous IIn/Ia-CSM object SN 2012ca; Inserra et al. 2016; Fox et al. 2015). For a review paper, see Silverman et al. (2013a).

Theoretical interpretations

Type Ia SNe are known to be thermonuclear explosions of a white dwarf (WD) star in a close binary system. In this system, the WD structure is determined by the balance between the gravitational pressure and electron degeneracy pressure (e.g., Koester & Chanmugam 1990; van Horn 1979; Althaus et al. 2010). This balance can be broken through the accretion of a certain amount of mass from the companion star. When the mass accretion reaches the Chandrasekhar Limit ($M \approx 1.44\ M_\odot$), the ignition of the carbon (typical ignition density $\rho_c \approx 3 \times 10^9$ g cm^{-3}) in degenerate conditions will cause the total disruption of the WD, leaving no compact remnant behind (Woosley et al. 1986; Woosley & Weaver 1986; Bychkov & Liberman 1995). Two possible competing scenarios have been proposed for thermonuclear explosions. One is detonation (e.g. Courant & Friedrichs 1948; Landau & Lifshitz 1975), in which the detonation propagates as a shock wave with a supersonic velocity. Thus the shock front compresses and heats the cool fresh materials at high density and pressure. The second is the deflagration (it also designated as "combustion wave" or "flame"; e.g. Zeldovich & Spalding 1985; Nomoto et al. 1986), in which the burning front propagates subsonically via thermal conduction. Both the density and pressure decrease behind the burning front. Although the above scenarios achieved successful arguments, they have some problems. Specifically, the pure detonation scenario could produce an overabundance of Fe-peak elements, while it fails to eject enough intermediate-mass elements. On the other hand, the pure deflagration model seems to fairly explain the expected observables, but it has an uncertainty in the transition between explosion and detonation. A combination of detonation and deflagration model has been proposed, where a slow, initial deflagration is followed by detonation (Khokhlov 1991). The density transition from deflagration to detonation is a critical parameter, which determines the nucleosynthesis and thus the ^{56}Ni production. The above "delayed-detonation" scenario well matches some observational parameters (Höflich 1995; Hoeflich & Khokhlov 1996; Hoeflich et al. 1996; Zhao et al. 2016), but a few aspects are still to be understood (Niemeyer 1999; Lisewski et al. 2000).

Two major progenitor systems can produce SN Ia: single-degenerate (SD) systems (e.g., Canal et al. 1996; Han & Podsiadlowski 2004; Justham 2011) and double-degenerate (DD) systems (e.g., Tanikawa et al. 2018; Rebassa-Mansergas et al. 2019; Martin et al. 2006). In the SD model, the WD accretes mass from a non-degenerate companion, such as a red giant, a sub-giant, or even a main sequence (MS) star. In the DD model, the SN explosion is due to the inspiralling approach with the final coalescence of two WDs. We note that in both scenarios, the carbon ignition of the WD degenerate core occurs, when the final WD gathers enough mass to reach the Chandrasekhar mass. The advantage of the DD model is that it predicts the absence of H lines in the spectra, in agreement with the observations.

1.2.2 Core-Collapse supernovae

Core-Collapse supernovae (CC SNe) are terminal explosions of massive stars (≥ 8 $M_\odot$), which may leave black holes or neutron stars as compact remnants (see a review, e.g., Heger et al. 2003). The fate of a massive star is determined by its initial mass, composition, and mass-loss history. Nonetheless, the core collapse mechanism is extremely complex, involving hydrodynamics and turbulence, particle physics, radiation mechanism, etc. In this thesis, we will present observational features and some basic physics of classical CC SNe.

- Type II supernovae (SNe II)

Type II SNe are CC events, showing H lines in the spectra (Minkowski 1941; Filippenko 1997). In particular, Hα (λ = 6563 Å) is the most prominent line, but other Balmer lines, such as H$_{\beta,\gamma,\delta}$ ($\lambda_{\beta,\gamma,\delta}$ = 4861, 4341, 4102 Å) are clearly detected. They explode in spiral or irregular galaxies (Barbon et al. 1999), being strongly associated to star-forming environments (Van Dyk et al. 1999). In a magnitude-limited sample, the observed Type II SNe comprise $\sim$ 17% of all types of SNe (see Figure 11, Li et al. 2011).

Type II SNe exhibit a wide variety of photometric properties, and different spectra (e.g., Inserra et al. 2013a). The sub-classification is based on their light curve shapes (Patat et al. 1994; Filippenko 1997; Gutiérrez et al. 2014b, 2017). SNe II-P show a plateau in the light curve lasting about 2-4 months, while SNe II-L have a faster decline rate (Barbon et al. 1979; Gutiérrez et al. 2014b, 2017). Some years later, new spectroscopic sub-classes have been added in the Type II group: Type IIn and Type IIb (e.g., Schlegel 1990; Turatto et al. 1993; Filippenko 1988; Filippenko et al. 1993).

The average peak magnitude of SNe II-P is $M_B \approx -16.7$ mag, and their luminosity remains nearly constant during the plateau phase (e.g., Huang et al. 2015). Many factors influence the plateau, including explosion energy, progenitor radius, ejected mass, and the H envelope recombination, while the light curve tail luminosity depends on the ejected ^{56}Ni mass (e.g., Inserra et al. 2011, 2012b; Zhang et al. 2014). SNe II-P are used to measure distances (e.g., Expanding Photosphere Method; EPM; Schurmann et al. 1979; Hamuy 2001; Jones et al. 2009; Takáts & Vinkó 2012; Rodríguez et al. 2019). The observations indicate that Type II-P are produced by massive stars, and the direct detection of progenitors in pre-explosion images confirms they are Red Super Giants (RSGs), consisting with theoretical expectations (Van Dyk et al. 2003b; Smartt et al. 2004; Wang et al. 2005a; Li et al. 2007; Maund et al. 2014a; Maund & Smartt 2009; Maund et al. 2014b; Rui et al. 2019). An example of a recent Type II-P SN 2014cx is in Figure 1.7, with its spectrophotometric evolution (Huang et al. 2016).

Type II-L SNe were first introduced by Barbon et al. (1979). They have H lines in spectra and display a linear decline after the light curve peak (see Figure 1.8). The main difference between SNe II-P and SNe II-L is in the photometric properties, although they have some differences in the spectra (e.g., absorption to emission strength ratios; Patat et al. 1994; Inserra et al. 2012a; Gutiérrez et al. 2014a). SNe II-L have an average magnitude at maximum ($M_B \approx -18$ mag) higher than SNe II-P ($M_B \approx -16.7$ mag) (e.g., Valenti et al. 2016; Arcavi 2017). Although a Yellow Super Giant (YSG) was possibly the progenitor of the Type II-L SN 2009kr (Elias-Rosa et al. 2010) and a YSG or an RSG was the possible progenitor of SN 2009hd (Elias-Rosa et al. 2011), the progenitors of SNe II-L remain debated [8] (e.g., Van Dyk et al. 2003a; Smartt et al. 2004; Valenti et al. 2016; Terreran et al. 2016; Van Dyk 2017; Williams et al. 2018; Ott et al. 2018).

Type IIn SNe are usually associated with stars exploding in a dense H-rich CSM, and being characterised by narrow H emission lines in the spectra (Schlegel 1990). The hydrogen emission lines are usually characterised by a narrow component (hence the label IIn), with FWHM from a few tens to a few hundreds of km s^{-1}, an intermediate one (a few thousands of km s^{-1}) and occasionally a broad base ($V_{FWHM} \sim 10^4$ km s^{-1}) (e.g., Zhang et al. 2012). SNe IIn span a large range of photometric properties with some objects displaying slow-evolving light curves, while others have more rapid declines ($\sim$ 3 - 7 mag $100d^{-1}$), comparable to SNe IIL. They usually explode in late-type galaxies (Taddia et al. 2015). However, a tight correlation with spiral arms and star-forming regions was not found (Habergham et al. 2014). Although many SNe IIn were discovered, their categorisation and physical mechanism are poorly understood. Recent studies suggest that massive luminous blue variable (LBV) stars are likely the progenitors for some SNe IIn, such as SN 2005gl (Gal-Yam et al. 2007; Gal-Yam & Leonard 2009), SN 2009ip (Smith et al. 2010; Foley et al. 2011; Mauerhan et al. 2013a; Pastorello et al. 2013; Fraser et al. 2013, 2015). The data of a Type IIn, SN 2009kn, are shown in Figure 1.9.

- Stripped-envelope supernovae (SE SNe)

SE SNe (i.e., Type Ib/c SNe) were proposed to be a new type of H deficient SNe (Type I), but characterised by weak Si II (λ=6355 Å) lines in the spectra (Bertola 1964, 1965). They arise from the core-collapse of massive stars, which had lost a large fraction of their envelope during the late phases of their evolution. Famous SE SNe are SN 1983N (Richtler & Sadler 1983) and SN 1984L (Wheeler & Levreault 1985). The light curves of a sample of well-studied SE SNe are shown in Figure 1.10, while the spectral evolution is presented in Figure 1.11.

The Type Ib SN label was introduced by Elias et al. (1985) by studying NIR spectra of Type I SNe. In contrast with SNe Ia, SNe Ib show neither a secondary photometric peak in the NIR light curves nor the 1.2 μm absorption in the NIR spectra, which are characteristic features of SNe Ia (Branch & Wheeler 2017). Then, their early spectra always show He I lines. Moreover, the light curve decline is slower than those of SNe Ia and the average maximum absolute magnitude of SNe Ib is M_B = -17.54 ± 0.33 mag in volume-limit distributions (Richardson et al. 2014). SNe Ib synthesised lower ^{56}Ni mass ($\sim$ 0.1 $M_\odot$) than typical Type Ia ($\sim$ 0.6 $M_\odot$). An evidence that SNe Ib are CC SNe comes from the nebular spectra, which have a remarkable resemblance with SNe II (see Section 1.2.2). In summary, the absence of hydrogen, the weakness of Si II, and the presence of He I lines are ubiquitous features

[8] According to the limited pre-explosion archive progenitor detections and SN rates models, the Zero Age Main Sequence (ZAMS) masses of SN IIL progenitors tend to be around 20 $M_\odot$ (Branch & Wheeler 2017).

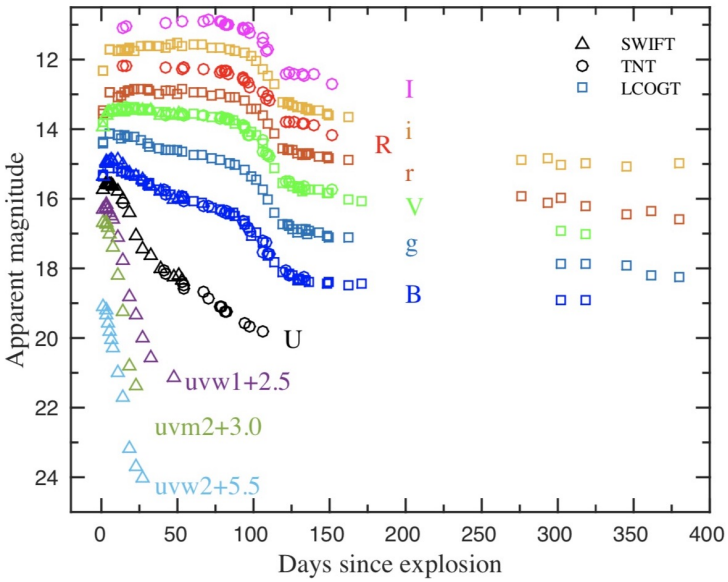

(a)

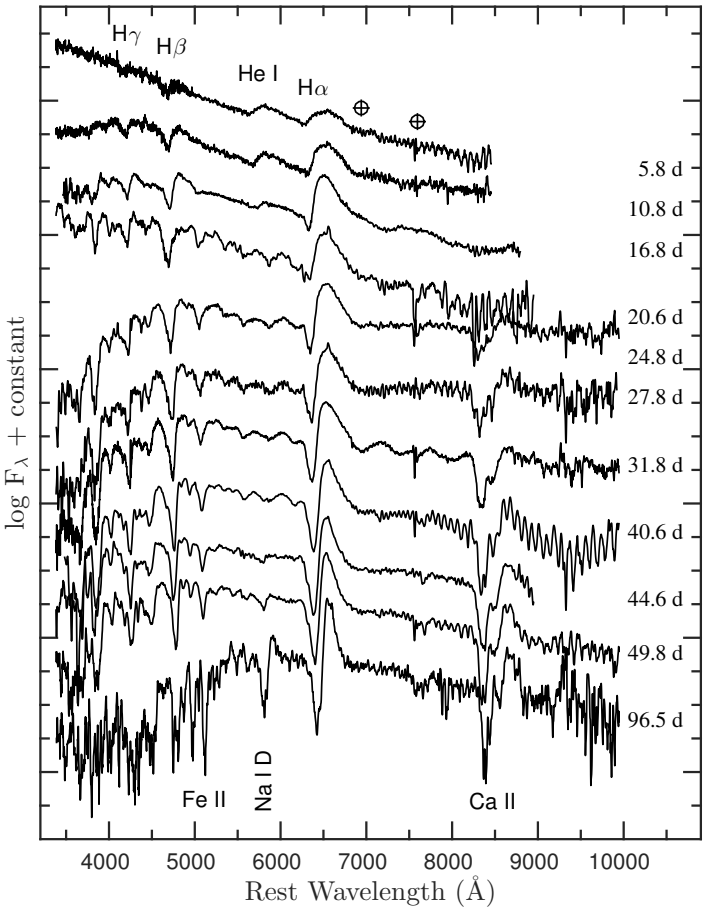

(b)

Figure 1.7: Spectrophotometric evolution of the Type II-P SN 2014cx. Panel a): Ultraviolet and optical light curves of SN 2014cx. Panel b): Spectral evolution of SN 2014cx. Figures are from Huang et al. (2016).

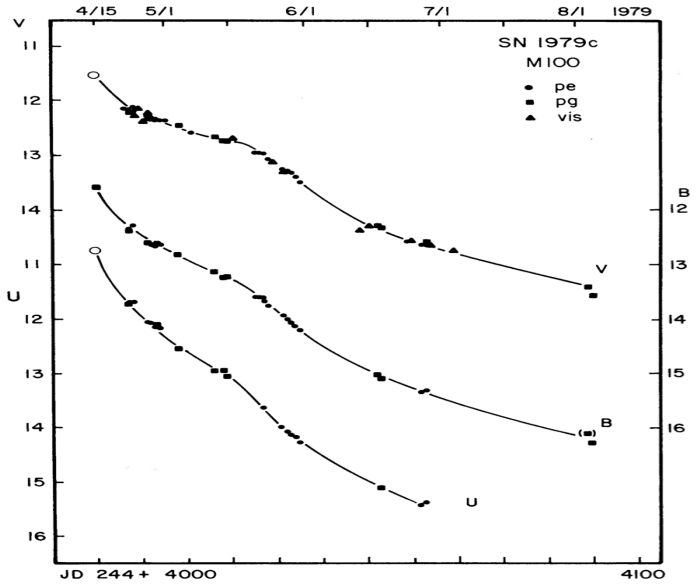

(a)

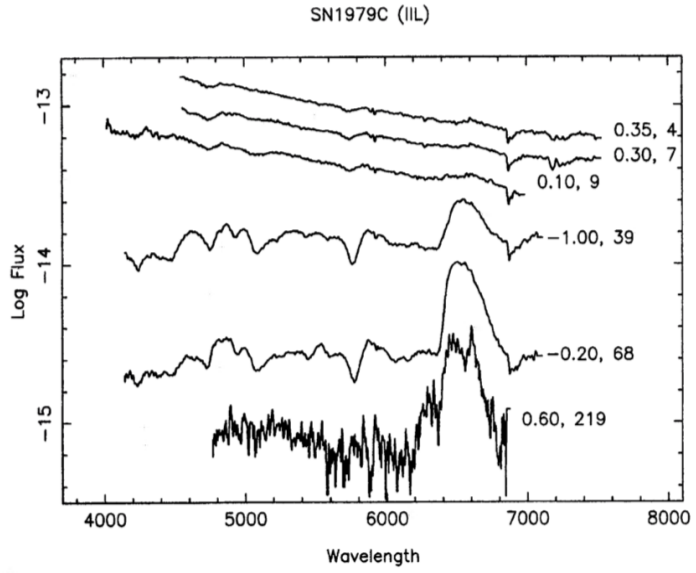

(b)

Figure 1.8: Spectrophotometric evolution of the prototypical Type II-L SN 1979C. Upper panel: the optical (U,B,V) light curves of SN 1979C. The open circles mark the extrapolated U, V maximum. (Figure source: de Vaucouleurs et al. 1981). Lower panel: the optical spectral evolution of SN 1979C. The numbers report the vertical offsets and the observational epochs, respectively. (Figure source: Schlegel 1996).

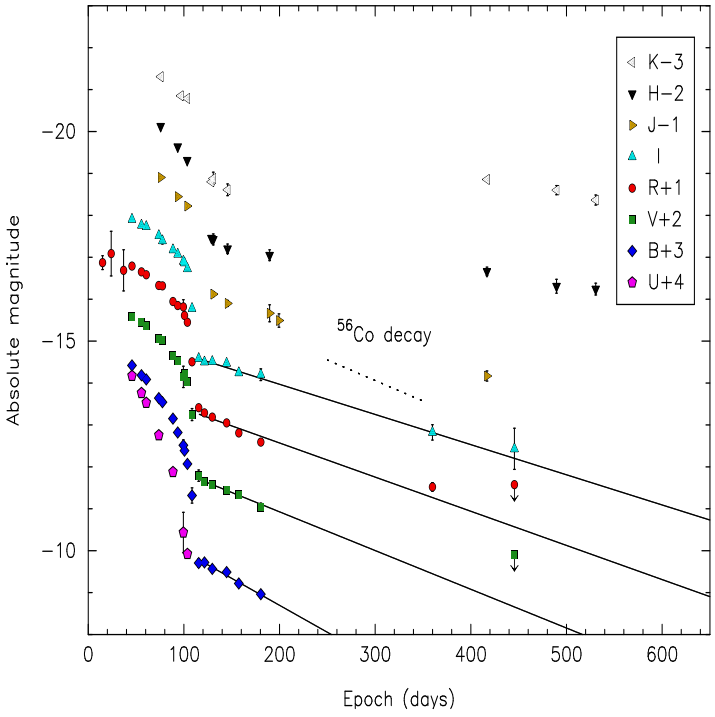

(a)

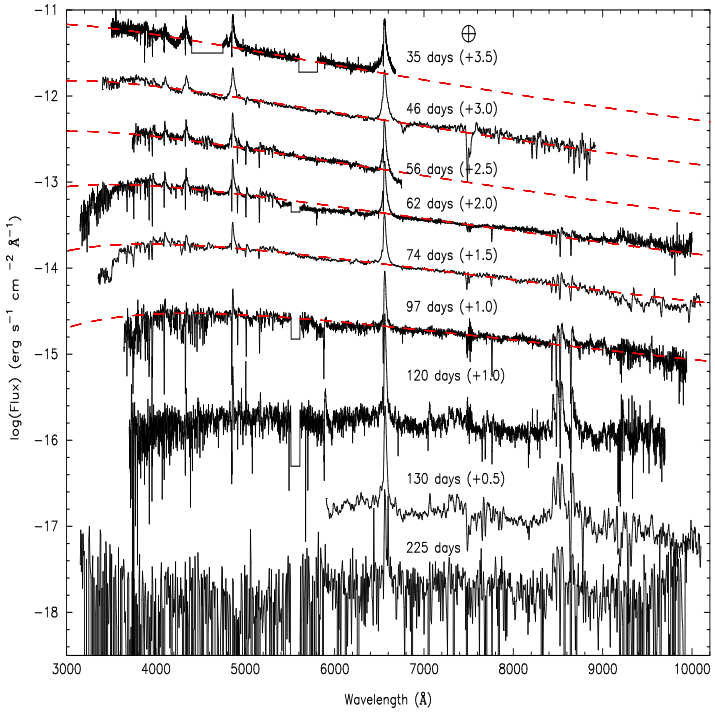

(b)

Figure 1.9: Spectrophotometric evolution of the Type IIn SN 2009kn. Panel a): multi-band (UBVRI+JHK) light curves. Panel b): spectral evolution. (Data are from Kankare et al. 2012)

of SNe Ib.

Type Ic SNe show a strong absorption of O I (λ=7774 Å) and prominent Ca II lines near the peak luminosity, without showing He lines (e.g., Wheeler et al. 1994; Matheson 2001; Chen et al. 2014; Liu et al. 2015b). We remark that this spectral classification depends on the observation epochs, as a few traces of helium may be detected at early phases in some spectra of SNe Ic (e.g., Filippenko et al. 1990; Wheeler et al. 1994; Hamuy et al. 2002; Terreran et al. 2019). SNe Ic usually have an average maximum light M_B = -17.67 ± 0.40 mag in volume-limit distributions (Richardson et al. 2014). Type Ic events occur in metal-rich and higher star-formation host galaxies than Type Ib and Type II SNe (e.g., Kelly et al. 2008, 2014; Levesque 2014). We note that observations revealed the existence of broad-lined Type Ic (Type Ic-BL), sometimes labelled as hypernovae (see an overview; Woosley & Bloom 2006, and references therein). These are sometimes connected to long and soft GRBs, with broad line features being associated to high energy ejecta (e.g., Mesler 2013; Levan et al. 2016; Sobacchi et al. 2017). Type Ib/Ic SNe are approximately 4% of all types of SNe in magnitude-limited sample (see Figure 11, from Li et al. 2011).

Type IIb SNe constitute another sub-class of SE SNe. One of the first SNe IIb was SN 1987K, which revealed the spectral transition from a Type II to a Type Ib (Filippenko 1988). The distinguishing spectral feature of SNe IIb is the emergence of He I lines with strong P-Cygni after the H-dominated spectral phase. Furthermore, the nebular spectra of SNe IIb are reminiscent of SNe Ib/c, showing intense [Mg I] (λ = 4571Å), [O I] ($\lambda_{1,2}$ = 6300, 6364Å), and [Ca II] ($\lambda_{1,2}$ = 7291, 7323Å) emission lines.

All SE SNe show nebular spectra with prominent [O I], [Mg I], and [Ca II] lines. The presence of α-elements such as O, Mg, Ca and the weakness of [Fe II] lines clearly support the CC SN nature of SE SNe (e.g., Inserra et al. 2014). Type Ib/Ic spectral features are explained with the total (Ic) or partial (Ib) stripping of H/He layers. There are two progenitor scenarios for SE SNe: a single massive Wolf-Rayet (WR) star, and a stripped star in a binary system. In the former, the progenitor star has a high mass at Zero Age Main Sequence (ZAMS; $\geq 20 - 30 M_{\odot}$), and loses the envelope through strong winds (e.g., Woosley et al. 1993; Crowther 2007; Georgy et al. 2009). In the second scenario, the progenitor is an interacting binary, in which the star loses the envelope via interaction with its companion (e.g., Johnson et al. 2017; Kim et al. 2015). Both scenarios have their observational support (for a review, see Eldridge et al. 2013). The attempts to directly identify SNe Ib/c progenitors have been mostly unsuccessful (e.g., Gal-Yam et al. 2005; Maund et al. 2005; Elias-Rosa et al. 2013). However, reliable progenitors have been detected for the Type Ib iPTF13bvn (a single WR star; Cao et al. 2013) and the Type Ic SN 2017ein [9] (see Van Dyk et al. 2018; Xiang et al. 2019). SNe IIb progenitors, with initial mass likely ranging from 10 - 18 $M_{\odot}$, stripped their H envelope through Roche-lobe overflow rather than via severe wind loss, hence they are likely He-rich stars in binary systems (Ensman & Woosley 1988; Podsiadlowski et al. 1993; Stancliffe & Eldridge 2009; Dessart et al. 2016; Yoon et al. 2017; Kilpatrick et al. 2017).

[9] If the progenitor is a single star, possibly with initial mass ~ 49 $M_{\odot}$, and if it is in a binary system, may even higher to 80 $M_{\odot}$.

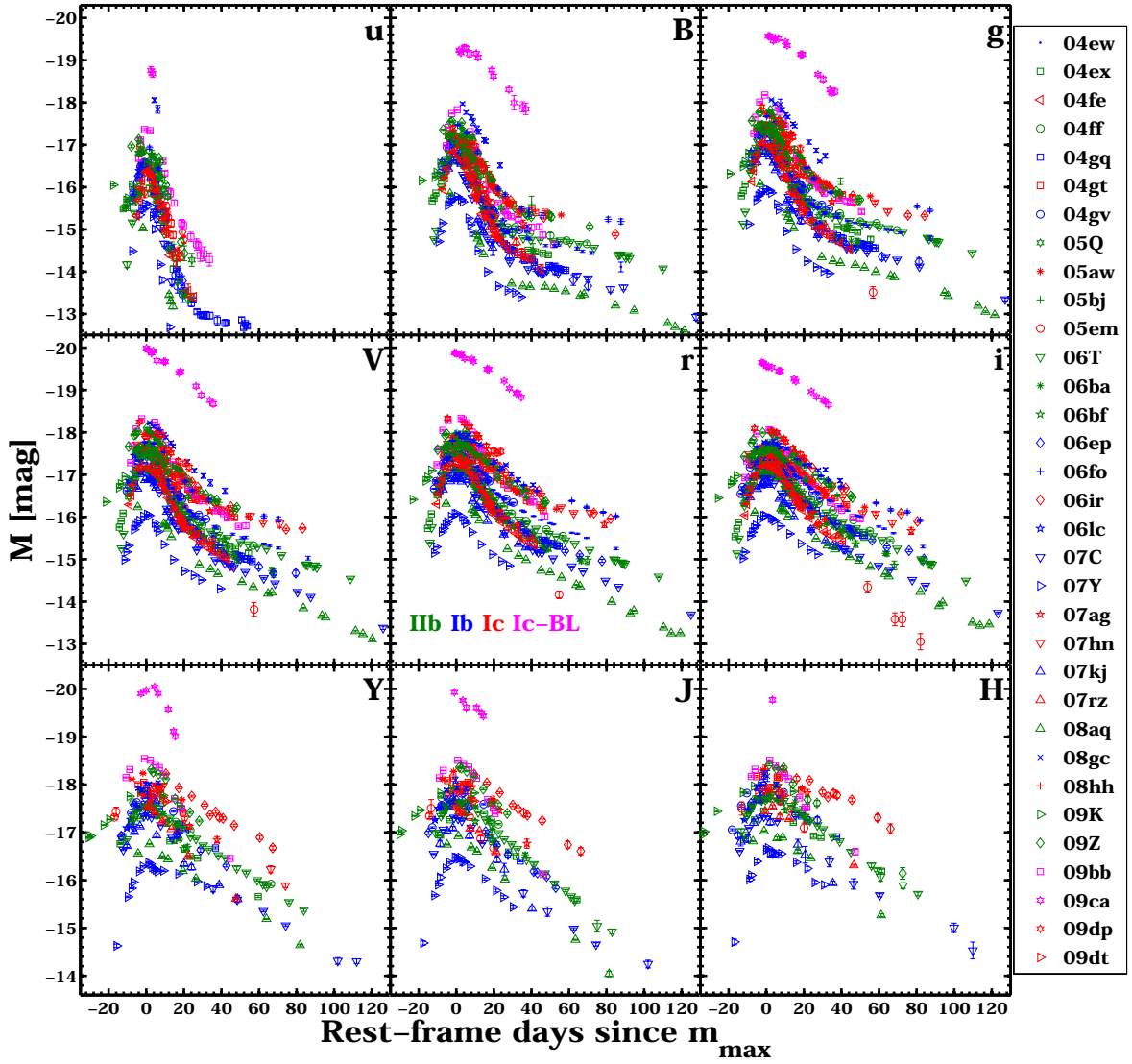

Figure 1.10: Absolute magnitude light curves (u-to-H bands) of 33 SE SNe. The blue, red, green, and magenta colours represent SNe IIb, Ib, Ic, and broad-line Ic, respectively. The figure is from Taddia et al. (2018).

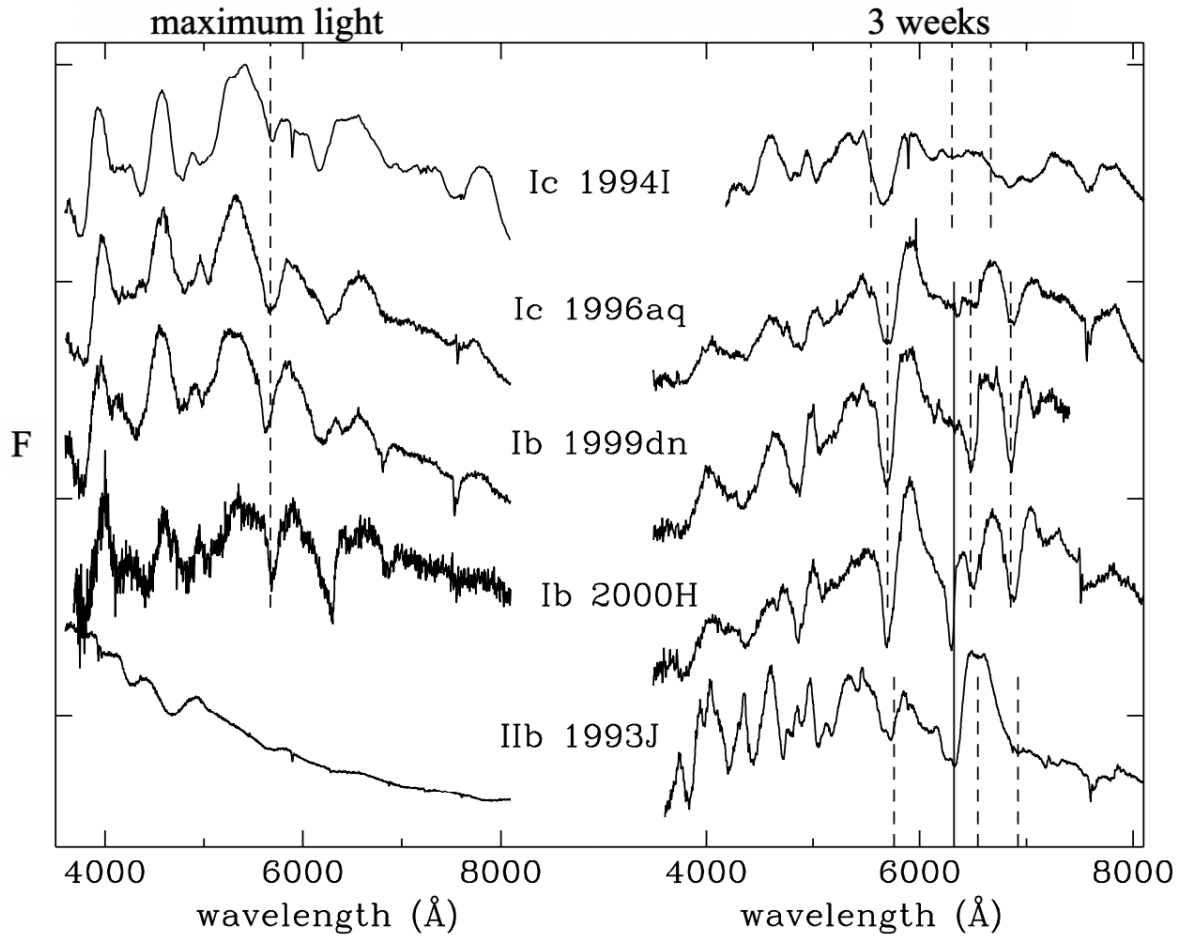

Figure 1.11: The spectral comparison of SNe Ib, Ic, and IIb. The spectra were obtained at maximum (Left) and about 3 weeks after maximum (Right). The figure is from Turatto (2003).

Theoretical interpretations

CC SNe are the end-point of life of massive stars (> 8 $M_\odot$; for a review, see Smartt 2009). In order to understand CC SN models, different branches of physics are involved, such as plasma physics, general relativity, nuclear physics, and transport theory. In this section, I will give a brief overview about the CC SN explosion mechanism.

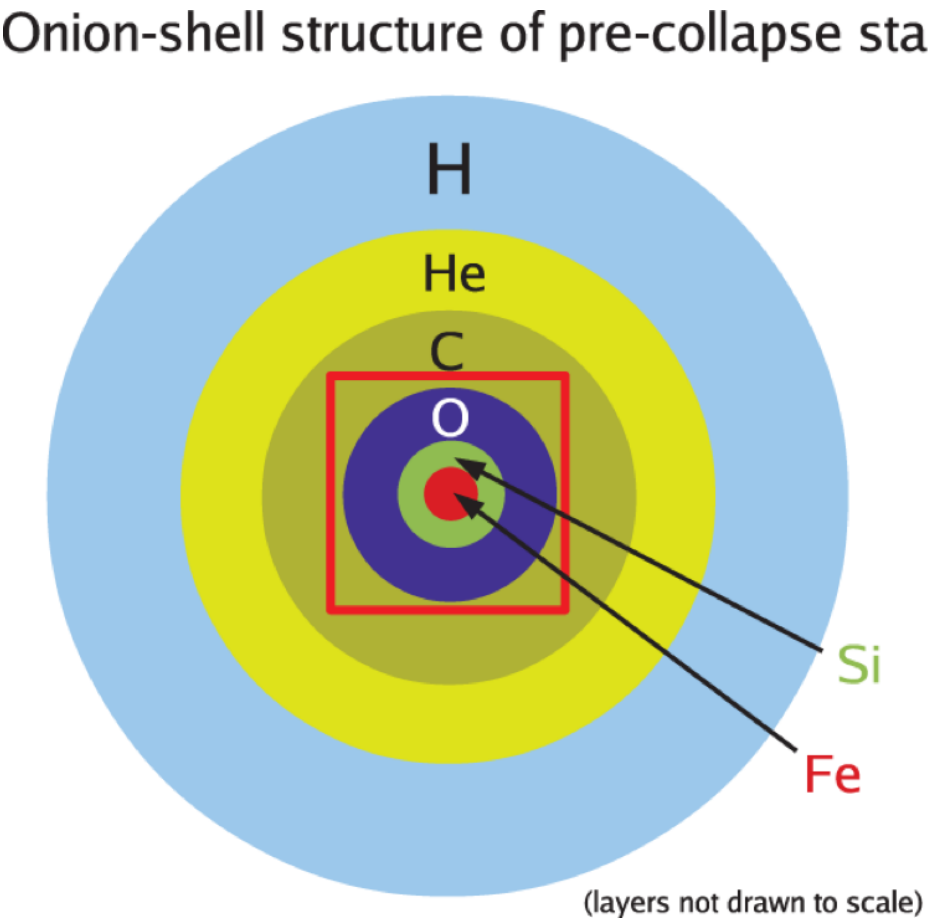

Figure 1.12: A schematic onion-like structure of a pre-collapse star. The figure is from Janka et al. (2012).

Modern stellar evolution theory suggests that stars at the lower mass end (8 – 10 $M_\odot$) for core collapse generate O-Ne-Mg cores, where electron capture may trigger the core collapse without producing an Fe core, producing an electron-capture supernova (EC SN) (e.g., Mazurek et al. 1974; Miyaji et al. 1980; Müller et al. 2017; Leung & Nomoto 2019; Takahashi et al. 2019). The details on the physics of EC SNe are discussed in Sect. 1.3.1.

Stars more massive than 10 – 12 $M_\odot$ are likely to produce iron cores. In this phases, the star forms an onion-like structure (see Figure 1.12), in which the inner iron core is supported by electron degeneracy pressure, and is surrounded by lighter-element shells. The outer envelope is C-O in the precursors of SNe Ic, He in progenitors of SNe Ib and H in the progenitors of SNe II. The Si shell burning continues to promote the Fe core growth up to reaching the Chandrasekhar mass, which is

usually governed by two parameters, accounting for the relation (Baron & Cooperstein 1990; Couch 2017):

$$\mathrm{M_{calib}} \approx 1.44\,(\frac{Y_e}{0.5})^2\,[1 + (\frac{s_e}{\pi Y_e})^2] \tag{1.1}$$

where Y_e is the electron number per baryon and s_e is the entropy per baryon at the collapse. It produces a degenerate iron core in the mass range of $\sim$ 1.3 - 1.7 $\mathrm{M_\odot}$. Once an iron core reaches its critical mass, this triggers the gravitational collapse. Both the photodissociation reactions and electron capture speed up the core collapse, leading temperatures and core densities to increase. The inner part of the core ($\sim$ 0.4 - 0.6 $\mathrm{M_\odot}$) contracts homogeneously with sub-sonic velocity, while the outer part collapses with super-sonic velocity.

The neutrino-driven mechanism in one dimension is explored to model CC explosions. In this scenario, neutrinos are radiated from the accretion layer surrounding the proto-neutron star (PNS), transporting some energy to the loosely surrounding layer (e.g., Janka 2017a,b; Janka et al. 2016; Pejcha & Thompson 2012). The gravitational collapse releases a large amount of gravitational binding energy, following the relation (Couch 2017):

$$\Delta \mathrm{E_b} = GM_{core}^2(\frac{1}{R_{PNS}} - \frac{1}{R_{core}}) \approx 1.2 \times 10^{53}\mathrm{erg}\,(\frac{M_{core}}{1.5\mathrm{M_\odot}})^2\,(\frac{50\ \mathrm{km}}{R_{PNS}} - \frac{2000\ \mathrm{km}}{R_{core}}) \tag{1.2}$$

This generates a hundred times the energy enough to drive the canonical CC ($E_{KIN} \sim 10^{51}$ erg [10]). Most of this energy is emitted as neutrinos. Once the collapse halts, CC in less than 1s, usually about 0.25s, a shock wave develops and ejects the collapsing material (e.g., Couch 2017). The propagation of this shock wave rebounds through the stellar mantle and compresses its material, producing heavier elements, including some elements heavier than iron (e.g., Au, Hg, Pb; Truran et al. 1967; Aufderheide et al. 1991). Finally, when the shock wave reaches the stellar surface, original material and newly synthesised elements are expelled into the interstellar medium (ISM). The fate of the core can either be a neutron star or a black hole, depending on the initial mass of the progenitor star, specifically, below or above the critical mass of $\sim$ 20-25 $\mathrm{M_\odot}$ (e.g., Zampieri et al. 1998; Heger et al. 2003; Georgy et al. 2012; Yusof et al. 2013). Progress has been made in modelling CC SNe through the numerical methods, simulating in 1, 2, and 3 spatial dimensions. Beyond the 1D spherical symmetry simulations for CC SNe, 2D simulations include non-spherical instabilities and convection into the explosion mechanism (Wilson & Mayle 1988), or even more sophisticated 3D ones (e.g., Murphy & Burrows 2008; Rosswog & Liebendörfer 2003; O'Connor & Ott 2010; Couch & Ott 2015; Hanke et al. 2012; Murphy et al. 2013).

1.2.3 Super-Luminous Supernovae

Super-Luminous Supernovae (SLSNe) are extremely luminous ($\mathrm{M}_V < -21$ mag; see Figure 1.13) transients, over a hundred times brighter than normal SNe (total radiated energies $\geq 10^{51}$ erg, see Gal-Yam 2012; Inserra 2019, for reviews). In recent years, they are generally classified as two distinct groups (i.e., SLSNe I and SLSNe II; Gal-Yam 2012; Inserra et al. 2017, 2018b,c), based on their individual spectroscopic properties instead of using a trivial magnitude threshold (e.g., Prajs et al. 2017; Lunnan et al. 2016; Papadopoulos et al. 2015). Hydrogen-free SLSNe I are the most common

[10] It may have a large range from around 10^{50} to 10^{52} erg. KIN=kinetic energy.

type of SLSNe, showing a blue continuum and a distinctive "W"-like O II (~ 4200 Å) feature in the spectra at maximum (e.g., Quimby et al. 2011; Gal-Yam 2012). At around 30 days after maximum, their spectra resemble those of normal or broad-lined SNe Ic (Pastorello et al. 2010), and hence are also labelled as SLSNe Ic (Inserra et al. 2013b). They are usually discovered in dwarf, low-metallicity, and star-forming galaxies (Quimby et al. (2011); Lunnan et al. (2014); Leloudas et al. (2015); Chen et al. (2017); but see Bose et al. 2018). Inserra & Smartt (2014) analysed a sample of sixteen well-observed SLSNe Ic, distributed from redshift 0.1 to 0.2, and proposed their use as promising distance indicators (for the high-redshift Universe, see Inserra et al. 2018a). The SLSNe II are characterised by hydrogen-rich features in the spectra, but with heterogeneous photometric properties and multiple types of host environments (e.g., Schulze et al. 2018; Leloudas et al. 2015; Gal-Yam et al. 2009). The explosion mechanism is debated, and the powering source for the enormous luminosity of SLSNe is controversial. Several models have been proposed to explain the SLSNe, such as pair-instability SNe (e.g., Woosley et al. 2007), magnetar spin-down (e.g., Kasen & Bildsten 2010; Inserra et al. 2013b, 2018c), and CSM-ejecta interactions (e.g., Blinnikov 2010), but none of them is entirely consistent with observations. A combination of the above scenarios is also a plausible explanation for the large radiated energy observed in SLSNe.

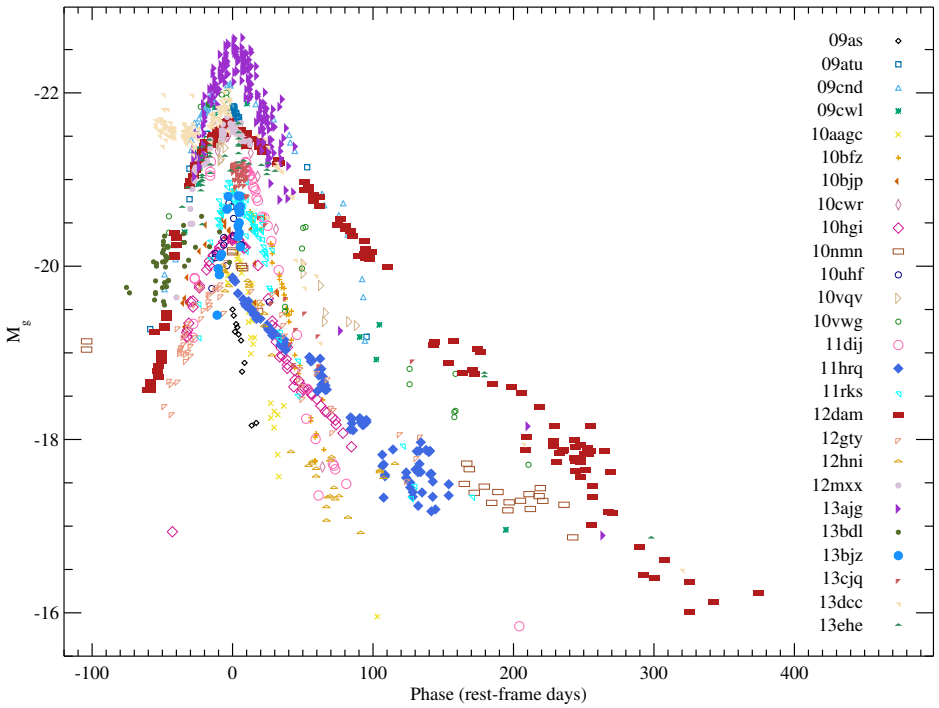

Figure 1.13: The *g*-band light curves for a sample of SLSNe. The figure is from De Cia et al. (2018).

1.3 Intermediate-Luminosity Optical Transients

Modern surveys discovered a harvest of stellar transients (see Figure 1.14); some of them have peak absolute magnitudes intermediate between those of CC SNe and classical novae, in the range −10 to −15 mag. They are labelled "Intermediate Luminosity Optical Transients" (ILOTs; e.g., see Berger et al. 2009a) or Gap Transients (GTs; Kasliwal 2012; Pastorello & Fraser 2019). The Gap Transient zoo includes ultra-faint SNe (e.g., faint CC SNe, Ca-rich transients, .Ia explosions can fall in the gap transient domain; see e.g., Pastorello et al. 2004; Valenti et al. 2009; Spiro et al. 2014; Lyman et al. 2014; Mulchaey et al. 2014), Luminous Blue Variable (LBV) and LBV-like outbursts (de Groot 1988; Humphreys & Davidson 1994; Humphreys et al. 1999; Smith et al. 2011), Intermediate-Luminosity Red Transients (ILRTs; e.g., see Botticella et al. 2009; Bond et al. 2009; Kasliwal et al. 2011; Kulkarni et al. 2007; Pastorello et al. 2007a; Adams et al. 2018; Cai et al. 2018), and Luminous Red Novae (LRNe; e.g., see Pastorello et al. 2019a,b; Lipunov et al. 2017; MacLeod et al. 2017; Pejcha et al. 2017, 2016a; Smith et al. 2016b; Kochanek et al. 2014). When transients have similar observational features as real SNe but do not undergo terminal explosions, they are usually labelled "SN impostors" (e.g., Van Dyk et al. 2000; Maund et al. 2006; Kochanek et al. 2012).

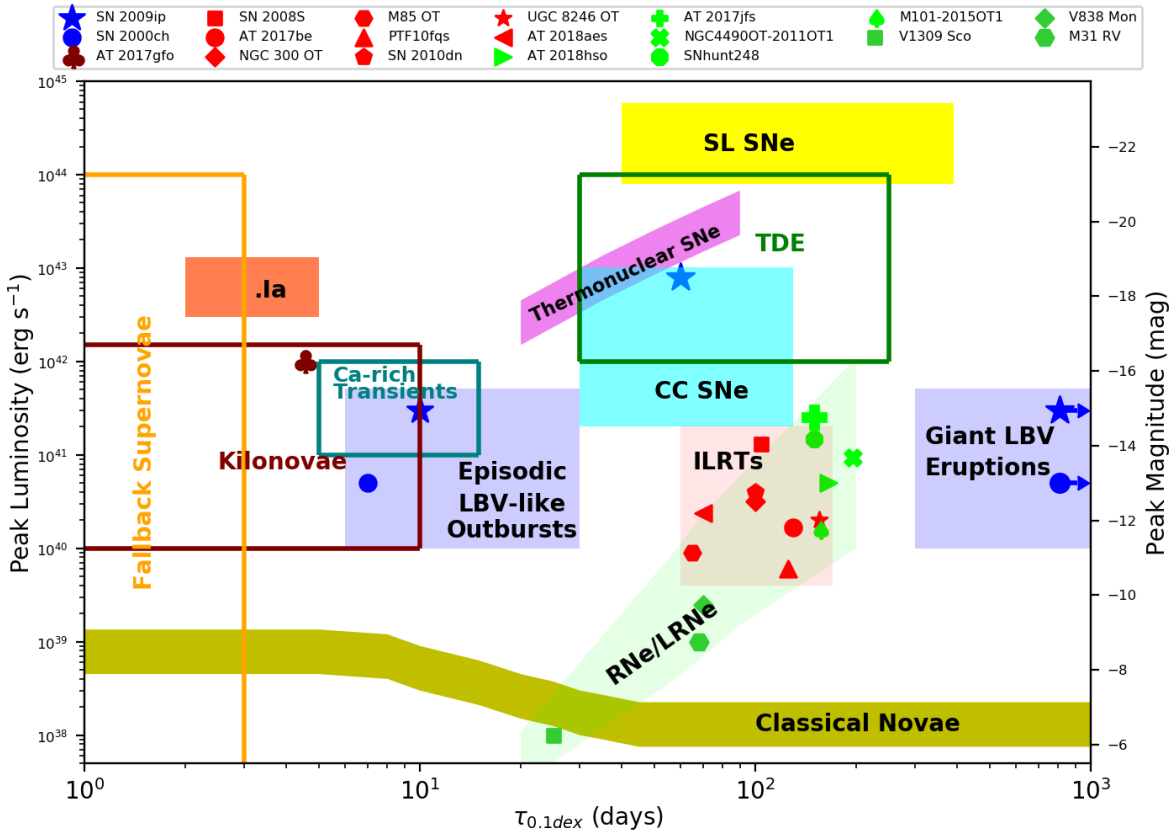

Figure 1.14: Transients in the Local Universe. Peak luminosity (L_{peak}) vs. time scale ($\tau_{0.1dex}$) diagram. $\tau_{0.1dex}$ is the decay time from $1L_{peak}$ to $0.1L_{peak}$. (Image was created by Cai & Pastorello.)

In the following, we will present observational properties and theoretical interpretations of the above transients.

1.3.1 Intermediate-Luminosity Red Transients

Intermediate-Luminosity Red Transients (ILRTs) are a sub-class of Gap Transients. Their peak absolute magnitudes varies from −12 to −14.5 mag. They have single-peaked light curves, which are similar to those of faint SNe IIP (e.g., PTF10fqs, M85 OT2006-1) or SNe IIL (e.g., SN 2008S, NGC300-2008OT1) (see Figure 1.15). The late-time light curves show a flattened tail, which is barely consistent with the ^{56}Co decay rate (whose theoretical decline rate is around 0.98 mag/100d). Their spectra show prominent Hα and other Balmer emission lines, along with weak Fe II lines, Na I D and Ca II lines (the [Ca II] doublet and the Ca II NIR triplet; see Figure 1.16). In particular, the [Ca II] doublet ($\lambda1$, $\lambda2$ = 7291, 7324 Å), visible in the spectra at all phases, is a typical feature of ILRTs (Pastorello 2012). In quiescent stage, the progenitors of ILRTs are usually embedded in extended dusty cocoons. They are invisible in the optical and NIR domains, but are luminous in the mid-IR region (see Figure 1.17).

The EC SN from an H-rich super-AGB star scenario has been proposed to ILRTs (e.g., Botticella et al. 2009; Pumo et al. 2009; Thompson et al. 2009). Although the accurate precursor mass is still controversial, it is commonly believed that a star with initial mass ∼8-10 $M_\odot$ may die as an EC SN (see, e.g., Miyaji et al. 1980; Nomoto 1984, 1987; Miyaji & Nomoto 1987). This type of CC is triggered by EC in the strongly electron-degenerate O-Ne-Mg core, reducing the electron pressure and then giving rise to an EC SN (e.g., Hashimoto et al. 1993; Kitaura et al. 2006; Poelarends et al. 2008). The trigger threshold depends on the competition between mass loss and core growth (e.g., Woosley et al. 2002; Herwig 2005). As the O-Ne-Mg core grows to the critical mass (i.e., $M_C \sim 1.38\,M_\odot$; and $\rho \sim 4 \times 10^{12}$ kg m^{-3}), electrons are captured by ^{24}Mg and ^{20}Ne nuclei, the degenerate pressure decreases, and the core subsequently collapses into a neutron star (e.g., Nomoto et al. 2014; Doherty et al. 2017; Leung & Nomoto 2017). An alternative LBV-eruption scenario was proposed by Smith et al. (2011). However, very late-time *Spitzer* IR observations reported that SN 2008S and NGC300-2008OT1 were much fainter than their quiescent progenitors (i.e., over 15 times), suggesting the disappearance of the progenitors (Adams et al. 2016). It gives a strong argument favouring the terminal core-collapse for ILRTs.

Remarkable Objects

SN 2008S shows a single-peaked light curve and reaches an *R*-band absolute magnitude at maximum M_R=−14.17 ± 0.16 mag after ∼17 days from the explosion. Its peak bolometric luminosity is approximately 10^{41} erg s^{-1}, which is comparable to the faintest SNe IIP, but fainter than classical CC SNe. At late times, SN 2008S shows a flat light curve, which follows the ^{56}Co decay. Assuming a terminal SN explosion, Botticella et al. (2009) constrained a ^{56}Ni mass of 0.0014 ± 0.0003 $M_\odot$. In addition, the bright mid-infrared (mid-IR) source was found soon after the explosion, suggesting a light echo from pre-existing dust grains. Late-time (∼ 120 days after explosion) spectral energy distribution (SED) analysis indicated the emergence of the contribution from newly-formed dust grains. The spectrum shows a blue continuum at early phases, and becomes redder with time, suggesting that the photospheric temperature decreases with time. This is consistent with the temperature evolution obtained through the SED blackbody fit. Strong emission lines, including Hα, the [Ca II] doublet and the Ca II NIR triplet, are detected in the spectra of SN 2008S. The spectral measurements indicate that the Hα profile has multiple (narrow, intermediate, and broad) components corresponding to Full-Width Half Maximum (FWHM) velocities of $v_n \sim 250$ km s^{-1}, $v_i \sim 1000$ km s^{-1}, and $v_b \sim 3000$ km s^{-1},

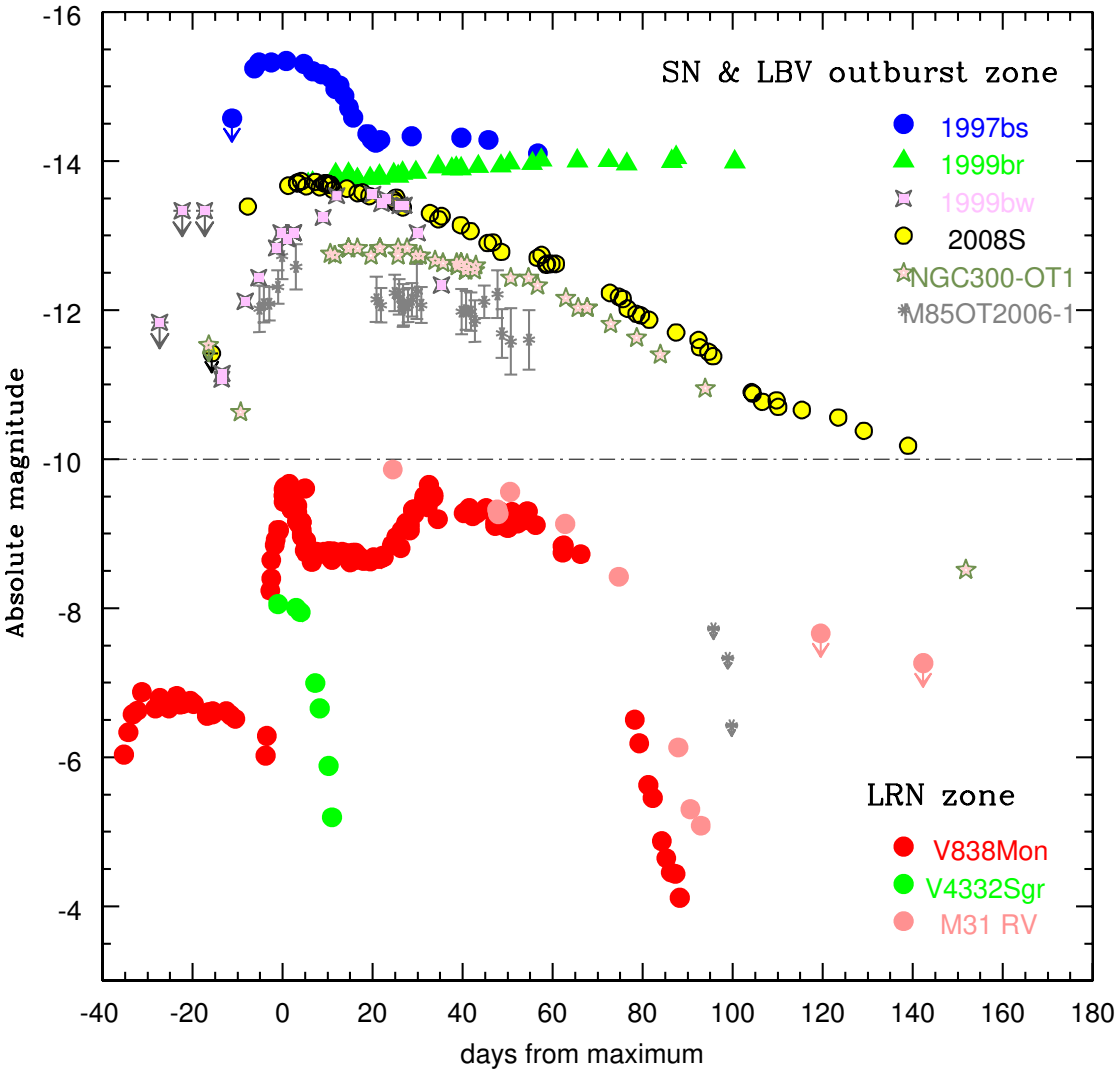

Figure 1.15: Absolute light curves of sub-luminous transients, including three ILRTs (SN 2008S, NGC300-2008OT1, 1999bw, and M85-2006OT1), a possible giant outbursts of LBVs (see Section 1.3.3), the sub-luminous SN IIP 1999br (upper panel), and Luminous Red Novae (see Section 1.3.2) (bottom panel). The figure is from Pastorello (2012).

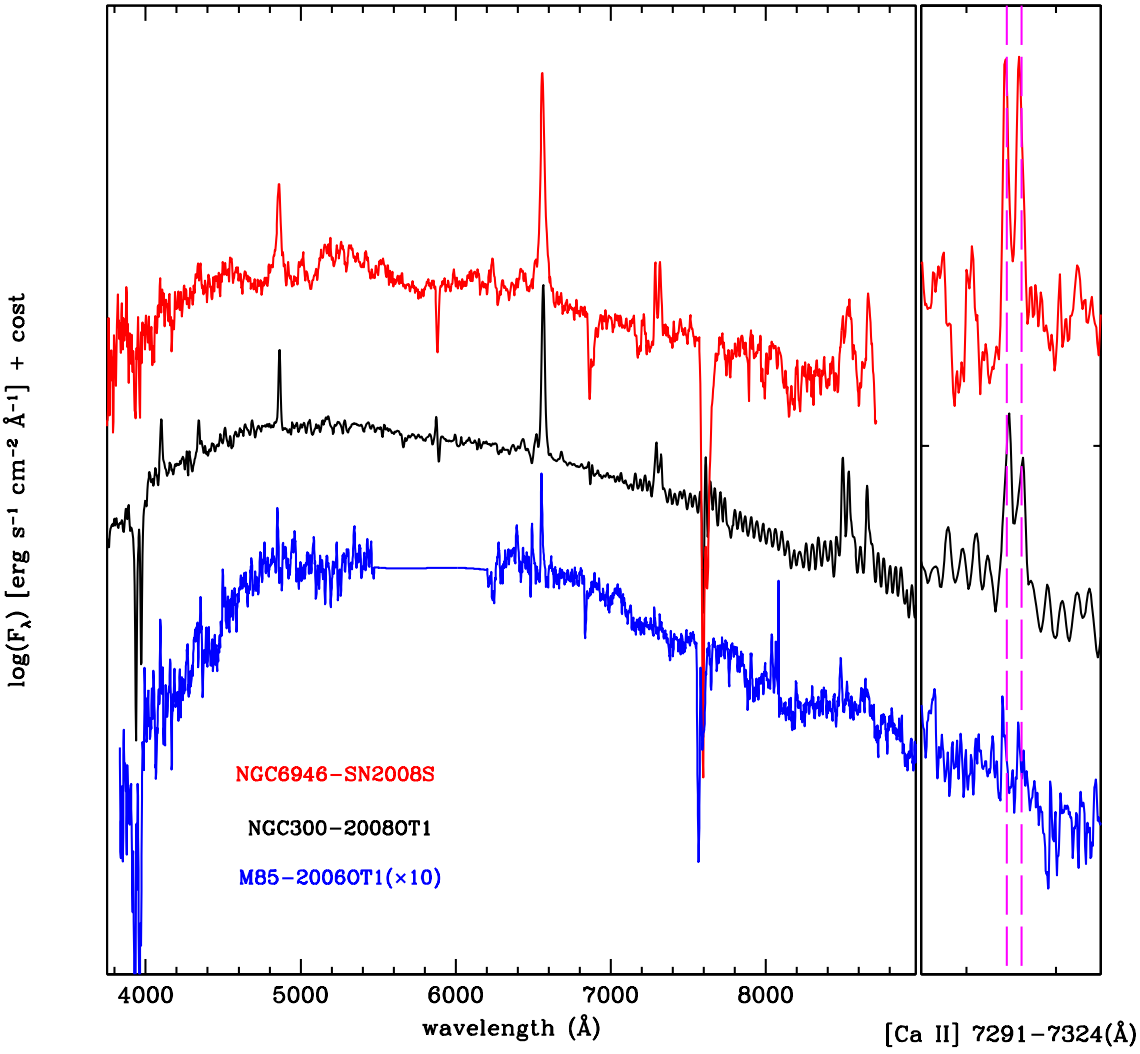

Figure 1.16: Spectral comparison among three ILRTs: SN 2008S, NGC300-2008OT1, and M85-2006OT1. The right panel show a zoom-in of the [Ca II] doublet region. This figure is from Pastorello (2012).

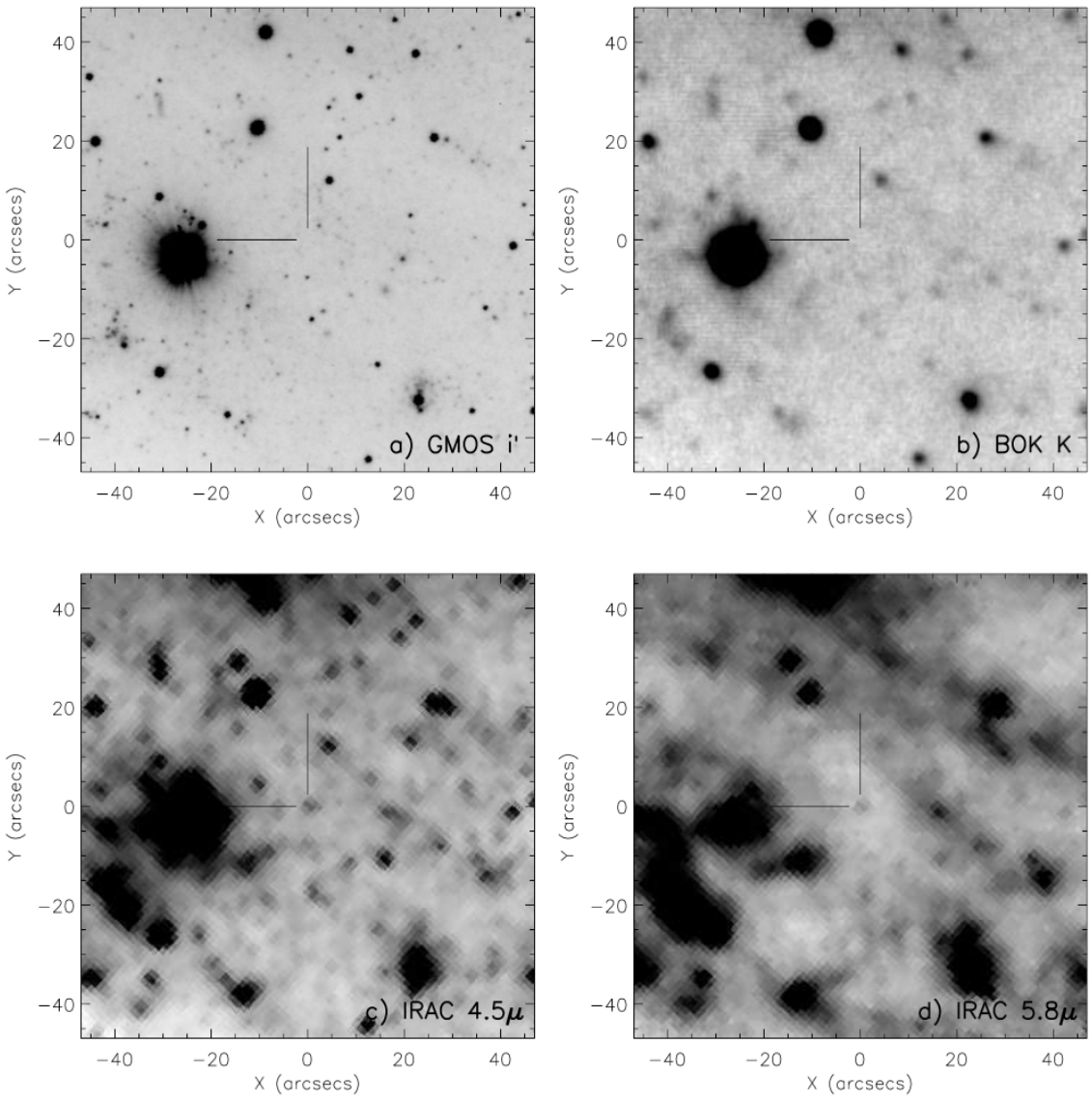

Figure 1.17: Pre-explosion images of the SN 2008S site from the optical to the mid-IR bands. Figure from Botticella et al. (2009).

respectively. The intermediate width component of Hα is likely produced by shocked material from the collision between fast-moving ejecta and slowly expanding CSM. The [Ca II] doublet shows a constant FWHM velocity of $\sim$ 250 km s^{-1}, suggesting it was emitted by slow, low-density CSM. Further analysis of the pre-explosion images (optical, NIR and mid-IR bands) implies that the central star has a luminosity of $\sim 10^{4.6} L_{\odot}$ and is surrounded by two dusty shells with radii of 90 AU (inner shell) and 450 AU (outer shell), respectively. Above observational parameters led Botticella et al. (2009) to propose for SN 2008S an EC SN scenario from a super-AGB progenitor exploded in an optically-thick, dusty cocoon.

ILRT NGC300-2008OT1 (hereafter NGC 300 OT) was discovered in the nearby galaxy NGC 300 on 2008 May 14.1 UT (Monard 2008). This object has a peak absolute magnitude $M_V \simeq -13$ mag and releases approximately 10^{47} erg during the eruption, with most of the radiated energy being emitted in the first two months (Bond et al. 2009). The $B - V$ colour becomes redder ($\sim$ 1.2 mag) as the object evolves, but late-phase colour turns back to be bluer. The $V - K$ colour progressively increases to redder colours ($\sim$ 6.8 mag) until 2008 September 1st, and then evolves more slowly to $\sim$ 7.2 mag (Humphreys et al. 2011). The late-time light curve becomes flat, following the ^{56}Co decay rate. Berger et al. (2009b) first investigated the spectroscopic properties of an ILRT through high-resolution spectra. The spectra show prominent hydrogen lines, Ca II H&K in absorption, the [Ca II] doublet and the NIR Ca II triplet in emission. The complex profiles of these lines suggest a complicate CSM environment. Bond et al. (2009) analysed the pre-outburst images from the Hubble Space Telescope (HST) and Spitzer Space Telescope (SST). They found no optical source brighter than V=28.5 mag in the HST archival images, but *Spitzer* data revealed the detection of a luminous mid-IR progenitor of 10-15 $M_{\odot}$. Prieto et al. (2009) inspected a low-resolution mid-IR *Spitzer*/IRS spectrum (5-14 μm) of NGC 300 OT, and found a mid-IR excess. It accounted for about 20% of total radiated energy and could be interpreted as the emission from pre-existing dust ($M_{dust} \sim 3 \times 10^{-4}$ $M_{\odot}$; T$\sim$ 400K). Moreover, the SED analysis presented a NIR excess, suggesting also some new dust formed in the ejecta. Both the NIR and mid-IR excesses indicate the transient had a dusty, thick CSM. Therefore, Prieto et al. (2009) concluded that the progenitor was embedded in a dusty shell, and could be a super-AGB star with a moderate mass of about 6-10 $M_{\odot}$.

PTF10fqs was discovered by the Palomar Transient Factory (PTF [11]) on 2010 April 16.393 UT, with a magnitude $V = 20.0 \pm 0.2$ mag (Kasliwal & Kulkarni 2010). Soon after discovery, Kasliwal et al. (2011) observed PTF10fqs with X-ray (on 2010 April 20.466 and 22.024), ultraviolet (on 2010 April 20.19-20.26) and radio observations (on 2010 April 24.387), but did not detect any point source at the site of the transient at those wavelengths. In the optical domain, it has a peak absolute magnitude M_r=$-$12.1 mag, and a red colour $g - r = 1.0$ mag. The light curves have a sort of plateau of around 30 days and a relatively slow evolution ($\sim$ 1.47 mag/100d). The spectra are dominated by an intermediate component of Hα ($v_{FWHM} \sim 930\ km\ s^{-1}$) and other narrow emission lines, in particular the [Ca II] doublet and the Ca II NIR triplet. In order to constrain the progenitor of PTF10fqs, Kasliwal et al. (2011) searched in archived pre-explosion images from ground telescopes (i.e., Katzman Automatic Imaging Telescope[12] and DeepSky[13]) and space facilities (i.e., HST and SST). No source was found at the position of object. While the non-detection in optical/NIR HST observations is expected, the non-detection in the mid-IR domain from SST observations is likely due to the far distance or the

[11] https://www.ptf.caltech.edu
[12] http://w.astro.berkeley.edu/bait/kait.html
[13] https://c3.lbl.gov/nugent/deepsky.html

insufficient exposure time. Nonetheless, the above observational properties suggest that PTF10fqs is an ILRT, similar to SN 2008S and NGC 300 OT.

A puzzling transient is M85 OT in the S0 galaxy Messier 85. It was announced by Kulkarni et al. (2007) on 2006 January 7, and had a peak luminosity of M_R=−12 mag. The radiated energy was around 10^{47} erg during the first two months. Its light curves showed a plateau with a duration of approximately 70 days. The Palomar spectral continuum had a blackbody temperature $\sim$ 4600 K. The strongest emission lines were Hα and Hβ, and a FWHM velocity (after instrumental resolution correction) of 350 ± 140 km s^{-1} for Hα. The [Ca II] doublet is marginally detected in the spectra. Kulkarni et al. (2007) did not find any source at the location of M85 OT in archival HST images and provided a limiting magnitude (F475W = −4.3 mag). LBVs are massive ($\geq$ 20 $M_\odot$) and luminous ($\geq$ 10^5 $L_\odot$) stars, hence we expect a precursor detection in pre-outburst optical/NIR images (Smith et al. 2004, 2011). This progenitor inspection disfavours an LBV outburst classification. Kulkarni et al. (2007) proposed a stellar merger scenario and designated it as a "luminous red nova". However, this interpretation was questioned by Pastorello et al. (2007a) after an independent analysis of Kulkarni et al. datasets, and favoured an extremely faint SN II-P scenario. The SN would have a low kinetic energy ($\sim$ $5-10\times10^{49}$ erg), very small ^{56}Ni mass ($\ll$ 0.001 $M_\odot$), and an ejected mass of 6-9 $M_\odot$. Although the nature of M85 OT is still controversial, current classification supports it to be an ILRT (Cai et al. 2018).

This thesis is mostly focused on ILRTs. A detailed study of AT 2017be (published in Cai et al. 2018) will be presented in Chapter 3; a systematic study of a new, extended ILRT sample (i.e., SN 2010dn, PSN J14535395+0334049, PSN J15213475-0722183, PSN J13100734+3410514 and AT 2018aes; Cai et al. 2019) will be presented in Chapter 4.

1.3.2 Luminous Red Novae

In the past few years, we have observed about 10 gap transients with intrinsic magnitudes in the range of -10 to -15 mag. They are characterised by double or even triple-peaked light curves, which are inconsistent with those of ILRTs (e.g., Pastorello et al. 2019a,b; Kankare et al. 2015). Their spectra usually reveal significant evolution during the monitoring period. Early spectra have a blue continuum with superposed prominent Balmer emission lines, resembling those of ILRTs. Then, the spectra become redder with Hα becoming barely visible, and a forest of narrow metal lines are detected in absorption. These spectra are remarkably similar to those of late G to K-type stars. Very late spectra present broad molecular absorption bands (e.g., TiO, VO, CaH, CN), while the narrow Hα emission line becomes prominent again. In this phase, the spectra mimic those of late M-type stars. These events are labelled as "Luminous Red Novae" (LRNe) (e.g., Blagorodnova et al. 2017; Lipunov et al. 2017; Smith et al. 2016b). Galactic Red Novae (RNe) are fainter and have an enormous range of luminosities, including faint transients with $M_V \sim$ -4 - -6.5 mag (e.g., V1309 Sco; Mason et al. 2010; Tylenda et al. 2011; McCollum et al. 2014) and more luminous events with $M_V \leq$ -10 mag (e.g., V838 Mon; Munari et al. 2002; Loebman et al. 2015; Kimeswenger et al. 2002). LRNe and RNe have similar observables, and thus are thought to be produced by the same mechanism (e.g., Pastorello et al. 2019a,b; Smith et al. 2016b; Mason et al. 2010).

Although several scenarios have been proposed to explain LRNe, such as thermonuclear runaway (e.g., M31 RV; Iben & Tutukov 1992), or a post-asymptotic giant branch He-shell flash (e.g., Munari et al. 2002; Kimeswenger et al. 2002), growing evidence supports a common-envelope ejection

in a binary, with possibly the final merging event. A sketch outlining the possible LRN scenarios presented by Pastorello et al. (2019b) is shown in Figure 1.18. It is natural to explain LRNe/RNe in a framework of binary interaction (e.g., Pastorello et al. 2019b; Kochanek et al. 2014; Smith et al. 2016b; Mason et al. 2010), in particular thanks to the unequivocal observational evidence of V1309 Sco, a sub-luminous Galactic RN (e.g., Tylenda et al. 2011; Pejcha 2014; Pejcha et al. 2016a, 2017). Specifically, during the pre-outburst phases, its luminosity showed a slow rise superposed on a periodic modulation (P $\sim$ 1.4 d) (Pejcha et al. 2016b). Then, the photometric period started to decline following an exponential law, which may be attributed to orbital shrink of the two stars (e.g., Tylenda et al. 2011; Pejcha et al. 2016a). After a minimum, a sharp luminosity rise was observed, due to the common envelope ejection. Finally, a further brightness increase lasting less than 2 weeks was observed, likely a consequence of the final coalescence. After this first sharp blue peak, a broad red peak or even a plateau is observed, which is a typical characteristic of LRNe. Finally, light curves experience a fast luminosity drop, likely due to dust formation. Nonetheless, the physical mechanisms regulating the structured light curve of LRNe is still debated. Lipunov et al. (2017) pointed out that H recombination may occur in the expansion of the gas. While this may explain the second long-lasting peak or the plateau, it fails in explaining the first blue peak, as mentioned by MacLeod et al. (2017). Metzger & Pejcha (2017) proposed that the first blue peak originates from the thermal release of hot gas, which freely expands along the polar direction. The second, red peak results from the shock-heated material, resulting from the interaction between the fast shell and the equatorial wind. This likely generates a cool dense shell, which is the ideal condition for dust consideration. This has been observed in most of LRNe (e.g., AT 2017jfs; Pastorello et al. 2019a).

LRNe are not fully understood yet, due to their limited sample, incomplete datasets, and imperfect models. With the help of future instruments (e.g., the Large Synoptic Survey Telescope; LSST[14]), an increasing number of objects monitored with high cadences in both optical and IR domains, high-resolution spectra, and local environmental investigations, will shed light on the nature of LRNe.

AT 2017jfs, a remarkable object

A well-defined LRN, AT 2017jfs, was discovered by *Gaia* on the 2017 December 26.13 (UT time) in the early-type spiral galaxy NGC 4470 (Delgado et al. 2017). The optical and NIR light curves are shown in Figure 1.19. Its optical light curves reveal the typical double-peaked shape of LRNe, with a first narrow peak, followed by a broad, second maximum. The *r*-band light curve reaches its first maximum at -15.59 mag in 5 days, followed by a sharp decline. Later, it rises again, following a broad peak until around 110 days. Finally, the object declines faster ($\sim$ 3.9 mag/(100d)) in the *r*-band until its brightness fades below the detection threshold. The evolution in the Sloan *i* and *z* bands is very similar to the *r* band. In contrast, the blue-band (B, g, V) light curves show a low-contrast second peak that is similar to a plateau. NIR light curves resemble those in the red bands, but at the very late time (from $\sim$ 170 days) they show a moderate re-brightening until the object disappears behind the sun. This late-time NIR excess may be associated to dust formation or IR light echoes (e.g., Banerjee et al. 2015; Exter et al. 2016; Smith et al. 2016b). The spectral evolution of AT 2017jfs is shown in Figure 1.20. The spectra reveal a major evolution during the monitoring period. At the first peak, the spectra have a blue continuum with H, Fe II emission lines. During the second peak, the continuum becomes cooler with time, with metal lines in absorptions. About 5-6 months later, the nebular spectra

[14] https://www.lsst.org

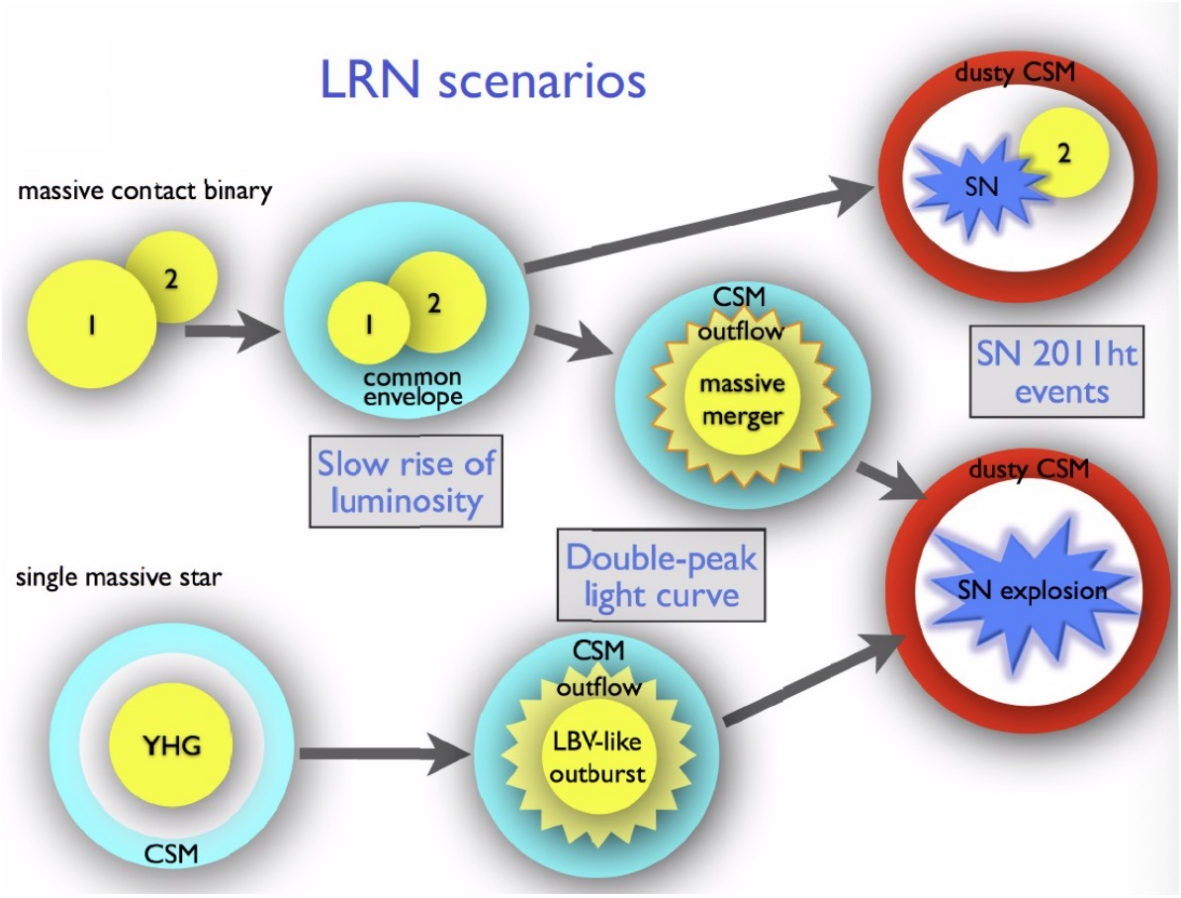

Figure 1.18: Schematic illustration of the possible evolutionary paths of LRNe. Plausible scenarios include a single massive star and a massive contact binary. The figure is from Pastorello et al. (2019b).

become extremely red resembling those of M-type stars, with prominent molecular absorption bands (e.g., TiO, VO, CaH, CN; Pastorello et al. 2019a).

Pastorello et al. (2019b) analysed a big sample of LRNe including NGC4490-2011OT1, NGC3437-2011OT1, UGC12307-2013OT1, M101-2015OT1, and SNhunt248, constraining their observational properties and correlating their physical parameters. Their work favours a coalescence of binary systems for LRNe. The recent discovery of an unprecedented transient AT 2018hso (or ZTF18acbwfza) reveals transitional spectrophotometric properties between those of ILRTs and LRNe, fueling again the interest on LRNe. This object will be discussed in Chapter 5.

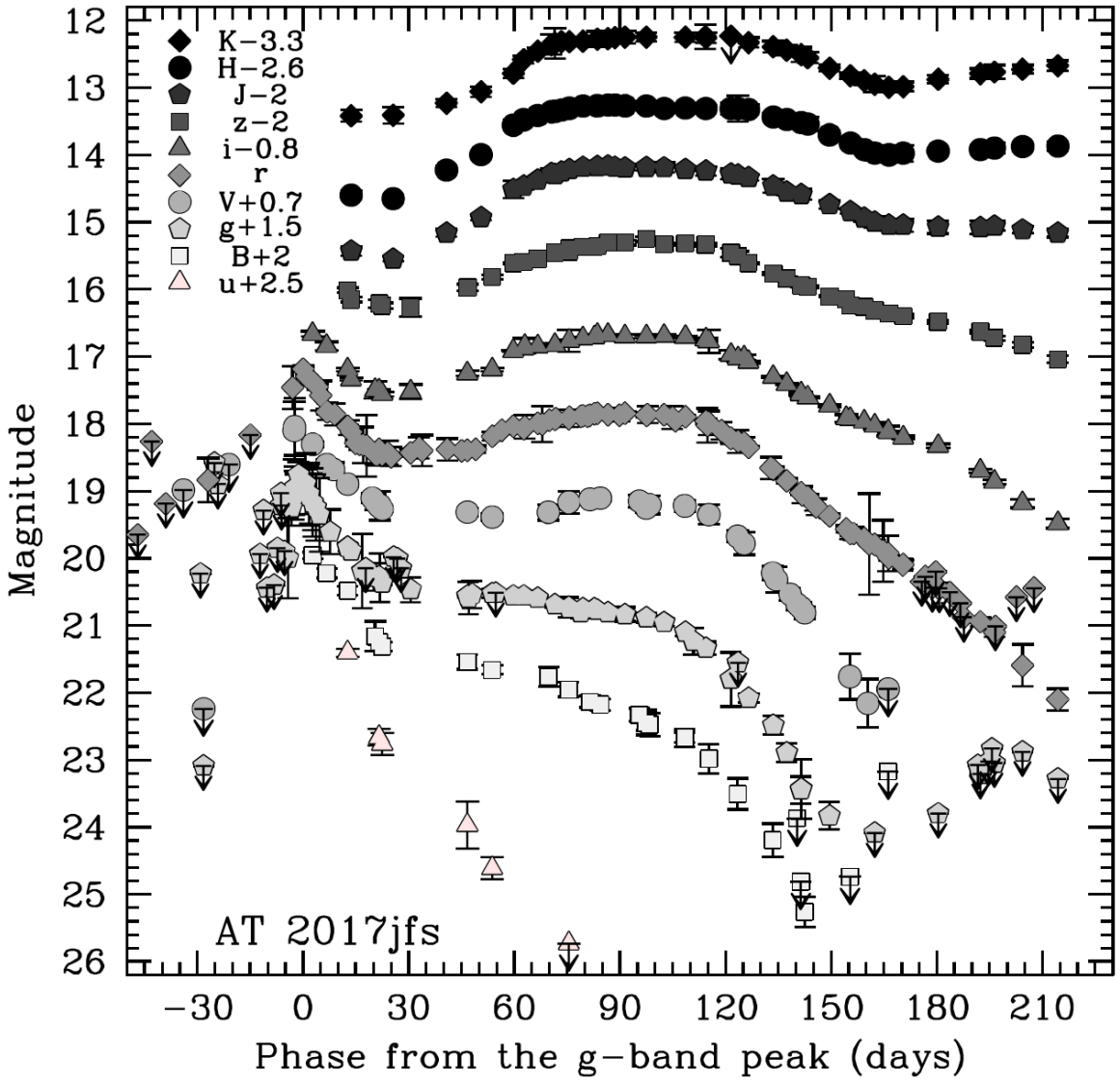

Figure 1.19: Multi-band (*uBgVrizJHK*) light curves of AT 2017jfs. Phases are relative to *g*-band first peak (MJD=58114.8 ± 1.8). The figure is from Pastorello et al. (2019a).

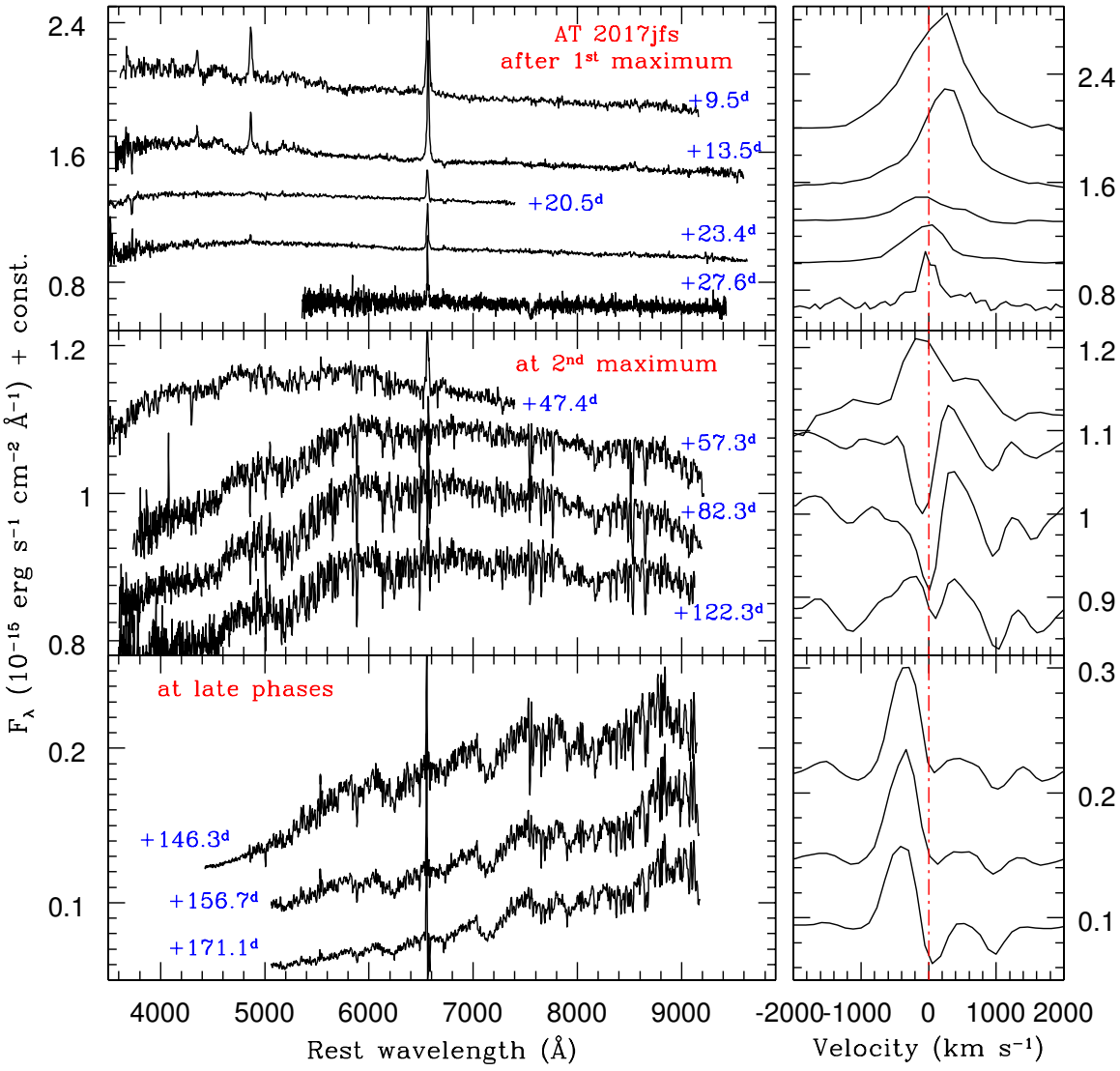

Figure 1.20: Left panel: Spectral evolution of AT 2017jfs at the first peak (top), at the second maximum (middle), and at late phases (bottom). Right panel: Evolution of the Hα profile in the velocity space. The red vertical lines mark the Hα rest wavelength position at the same epochs as the left spectra. All spectra have been redshift corrected with the z=0.007809. The figure is from Pastorello et al. (2019a).

1.3.3 Eruptions of massive stars: Supernova Impostors

Some Gap Transients may mimic the SN behaviour without being SN explosions. Specifically, these events are giant eruptions of massive stars, in particular LBVs. For this reason, these non-terminal events are dubbed "SN Impostors" (Van Dyk et al. 2000; Maund et al. 2006; Van Dyk 2007).

LBVs (sometimes also named "Hubble-Sandage Variables"; Wolf & Zickgraf 1986; Lamers 1986) are luminous evolved stars with a bolometric luminosity of $-9.7 \leq M_{bol} \leq -11.5$ mag, hence over $10^5 L_{\odot}$ (Humphreys et al. 2016). They usually show irregular light curves and spectra resembling those of SNe IIn during eruptions. Very massive stars ($M > 40\ M_{\odot}$) are thought to proceed through a short-duration LBV stage accompanied by severe mass loss. During a giant eruption, they may expel up to few tens $M_{\odot}$, and release over 10^{50} erg of energy. In light of their high luminosities, they may sometimes exceed the classical Eddington limit, defined as:

$$L_{Eddington} \equiv \frac{4\pi cGM}{\kappa} \tag{1.3}$$

where M is the stellar mass, κ is the opacity per unit mass and $L_{Eddington}$ is the maximum luminosity for a given star in hydrodynamic equilibrium. When the star exceeds this limit, an eruption driven by Super-Eddington winds is observed.

Figure 1.21 shows some confirmed and presumed LBVs in the Hertzsprung-Russell (HR) diagram. In quiescence stage, LBVs lie in a temperature-dependent luminosity region, with a mass-loss rate of around 10^{-7} to $10^{-6}\,M_{\odot}\ yr^{-1}$. However, during the eruption, LBVs move to the region above the evolved supergiant luminosity limit. At this phase, LBVs have essentially the same minimum temperature (near 8000-8500 K), and the mass-loss rate can reach 10^{-5} to $10^{-4}\,M_{\odot}\ yr^{-1}$, but it may even exceed $10^{-3}\,M_{\odot}\ yr^{-1}$ (Smith & Hartigan 2006). We note that this shift in the HR diagram is due to the outermost layer changes. In Figure 1.21, the LBV instability strip (it is also designated as "S Dor instability strip"; Wolf 1989a,b) is marked, with the temperature increasing with the luminosity. This indicates the existence of an amplitude-luminosity relation for LBV eruptions.

LBV spectra have typically strong emission lines, such as H, He I, Fe II, often with P-Cygni features due to gas expanding with velocity of few hundreds km s^{-1} (Humphreys & Davidson 1994). The spectra vary with the photometric evolution. In quiescence (at the visual minimum), LBVs are hot, with temperatures around 12000 to 30000 K, and spectroscopically they resemble OB stars. Occasionaly, at minimum some LBVs are similar to Of/WN9 stars (Conti & Frost 1977; Bohannan & Walborn 1989; McGregor et al. 1989; Smith et al. 2018). However, during the eruption (at the visual maximum), the expanded pseudo-photosphere is optically thick, resembling that of a colder supergiant of spectral type A or F (Leitherer et al. 1985), and the temperature decreases to about 7000-8000K.

The best-known LBV major eruptions are two Galactic events, shown in Figure 1.22: Eta Carinae (Humphreys & Davidson 1994) and P Cygni (de Groot 1969a,b, 1988). Eta Carinae appears embedded into the spectacular Homunculus nebula, while the P Cygni nebula is composed by some spherically symmetric shells (Nota et al. 1995). In recent years, a growth in the sample of LBVs (or LBV candidates) has been observed, some of which are reported in Figure 1.21.

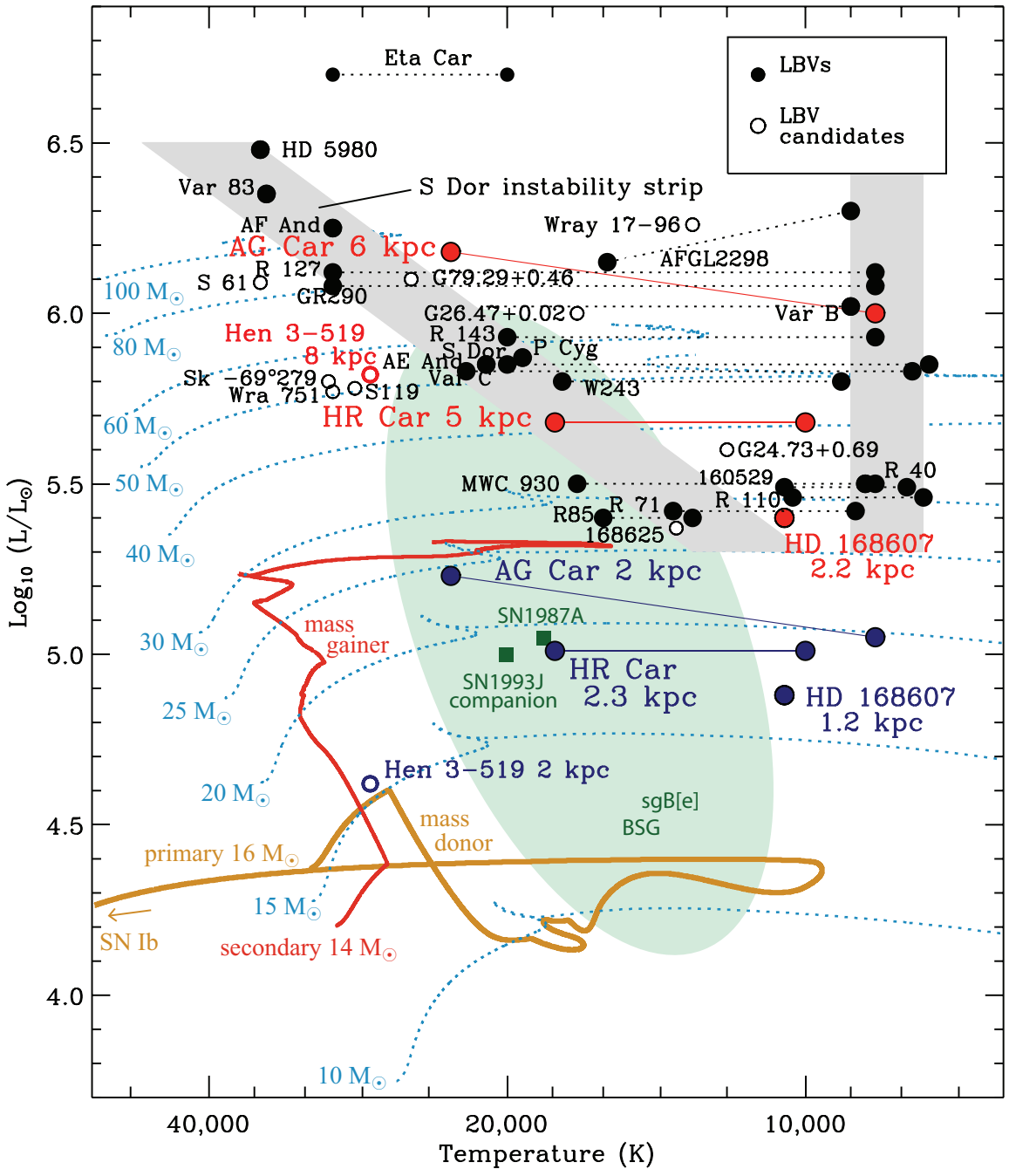

Figure 1.21: The HR diagram of confirmed LBVs (black dots) and LBV candidates (empty dots) in the Local Universe. The dashed lines connecting two dots mark the transitions from quiescence to the eruptive phase. The figure is from Smith & Stassun (2017).

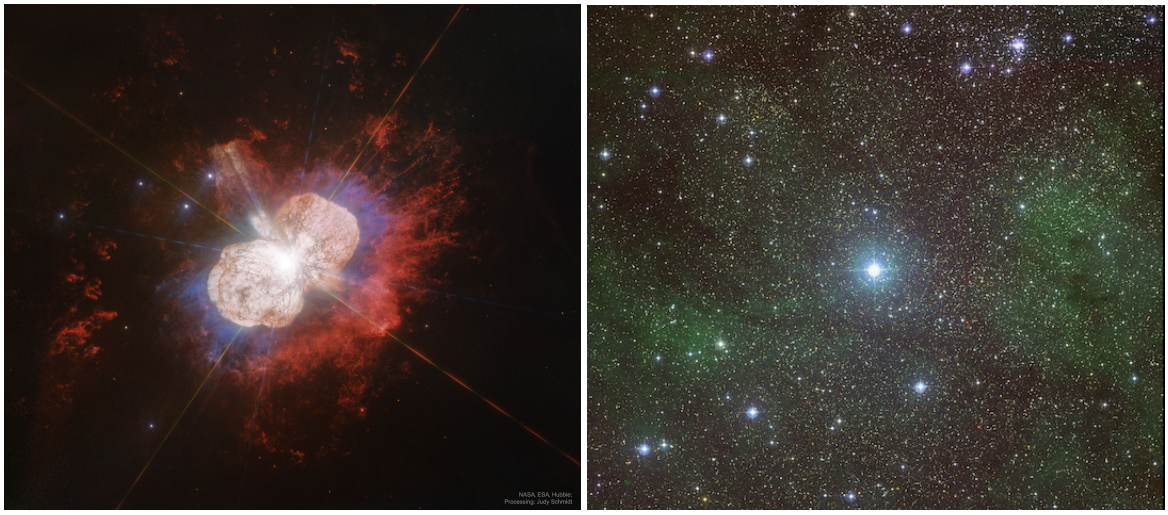

(a) (b)

Figure 1.22: The nebulae surrounding two Galactic LBVs: Eta Carinae and P Cygni. Panel a): The Homunculus nebula of Eta Carinae, produced by the 19th century Giant Eruption. (Image Source: NASA, ESA, Hubble Space Telescope; Processing & License: Judy Schmidt; *https* : //*apod.nasa.gov*/*apod*/*ap*190220.*html*). Panel b): The P Cygni region. (Image Source: *http* : //*www.cxielo.ch*/*gallery*/*v*/*nebulae*/*p* − *cygni* − *cx.jpg.html*?*g*2¡*mageViewsIndex* = 1).

Chapter 2

Data Reduction

Spectroscopical data were reduced with standard IRAF[1] tasks (Tody 1986, 1993). Photometric data reduction was performed using the *SNoOpy* [2] pipeline written by E. Cappellaro. *SNoOpy* is a PYTHON-based package, which makes use of a series of programmes for photometric measurements (e.g., SEXTRACTOR[3], DAOPHOT[4], HOTPANTS[5]).

2.1 Photometry

.

The photometric data of our transients were obtained using several instruments equipped with broad-band Johnson-Cousins *UBVRI* (Cousins 1976; Johnson & Morgan 1953; Bessell 2005) and Sloan *ugriz* (Thuan & Gunn 1976; Doi et al. 2010) filters. Figure 2.1 shows the transmission curves of the above filters. In addition, we collected observations in the NIR *JHK* bands (Bessell & Brett 1988; Wainscoat & Cowie 1992).

Two methods are normally used to perform photometry of point-like sources: aperture photometry and Point-Spread-Function (PSF) photometry. Aperture photometry is suitable for isolated stars or very bright sources with a relatively flat background. Aperture photometry measures the counts inside a region, which is generally a circle centred on the target, with a radius of 3 times the FWHM. At the same time, the background contamination is estimated by integrating the flux in an outer annulus, extended to the target circle, and still centered on the target. Finally, the subtraction between the total and the background flux provides the net counts attributed to the transient.

PSF-fitting photometry is more useful for faint objects, or targets exploded in very complex environments. With this method, we build a model PSF by measuring the PSF profiles of many bright stars in the target's field. Then, the source is extracted with a PSF equal to the modelled one. The transient background is estimated through a low order (2nd or 3rd order) polynomial function before

[1] IRAF is written and supported by the National Optical Astronomy Observatories (NOAO) in Tucson, Arizona. NOAO is operated by the Association of Universities for Research in Astronomy (AURA), Inc. under cooperative agreement with the National Science Foundation.

[2] *SNOoPy* is a package for SN photometry using PSF fitting and/or template subtraction developed by E. Cappellaro. A package description can be found at `http://sngroup.oapd.inaf.it/snoopy.html/`

[3] `www.astromatic.net/software/sextractor/`

[4] `http://www.star.bris.ac.uk/~mbt/daophot/`

[5] `http://www.astro.washington.edu/users/becker/v2.0/hotpants.html/`

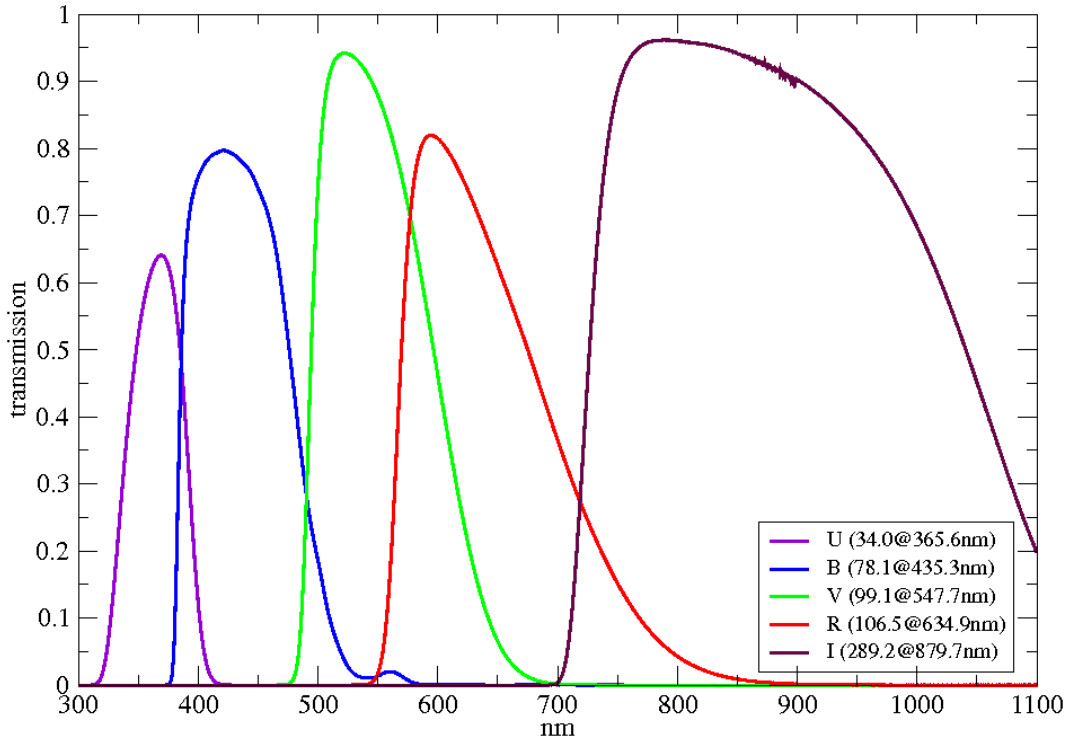

(a)

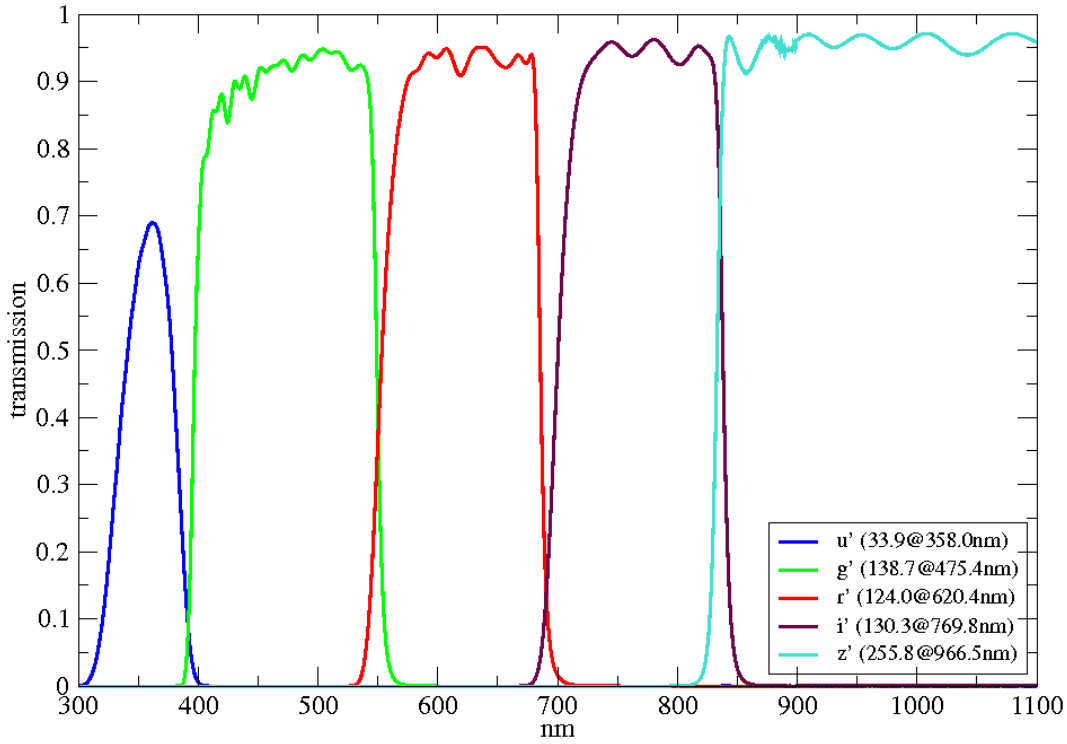

(b)

Figure 2.1: Schematic transmission curves of a) broad-band Johnson-Cousins U, B, V, R, I and b) Sloan u, g, r, i, z filters. (Figure source: *http* : *//user.astro.columbia.edu/ jules/UN*2002/).

subtracting the modelled PSF.

Template subtraction provides more accurate results. A good quality image is adopted as a template showing the host without the transient. We generally select templates with good seeing and deep exposure times. In order to perform template subtraction, astrometry, PSF and flux matchings need to be done for the target and template images. A good subtracted image will have a flat background with the clean target source. The aim of template subtraction is to remove the contaminating flux, leaving only the variable source.

Once we have obtained instrumental magnitudes, the final step is the photometric calibration. The instrumental magnitudes are transformed into apparent magnitudes in a standard photometric system (Johnson-Cousins or Sloan system). Calibration is usually done with a colour correction. If the instrumental system well matches the standard photometric system, the colour correction is negligible and the calibrated magnitudes are obtained as follows:

$$\mathrm{m_{calib}} = \mathrm{m_{inst}} + ZP + \kappa X \tag{2.1}$$

where $\mathrm{m_{calib}}$ is the calibrated magnitude, $\mathrm{m_{inst}}$ is the instrumental magnitude, ZP is a photometric zero point defined as the magnitude of an object producing one count per second, κ is the atmospheric extinction coefficient, and X is the airmass at the moment of the observation.

As, in general, the broad-band filters of the instrument do not match with those of the standard photometric system, a colour term correction is needed for the calibration of the magnitudes. The basic algorithm of calibration with colour correction is similar to Equation 2.1, but an additional colour term should be accounted. Consequently, Equation 2.1 has to be modified as follows:

$$\mathrm{m_{calib}} = \mathrm{m_{inst}} + ZP + \kappa X + \text{Colour Correction} \tag{2.2}$$

In particular, for the Johnson-Bessell UBV system, it becomes:

$$U_{calib} = U_{inst} + ZP_U + \kappa_U X + CT_U(U - B) \tag{2.3}$$
$$B_{calib} = B_{inst} + ZP_B + \kappa_B X + CT_B(B - V) \tag{2.4}$$
$$V_{calib} = V_{inst} + ZP_V + \kappa_V X + CT_V(B - V) \tag{2.5}$$
$$\tag{2.6}$$

where U_{calib}, B_{calib}, and V_{calib} are the calibrated magnitudes, U_{inst}, B_{inst}, and V_{inst} are the instrumental magnitudes, ZP_x (x=U, B, V) is the photometric zero point, CT_x (x=U, B, V) is the colour term in the three bands, κ_x (x=U, B, V) is the atmospheric-extinction coefficient, and X is the airmass.

Photometric errors are estimated via artificial star tests, in which several fake stars are placed near the transient position. The resulting dispersion of individual magnitudes, combined in quadrature with the errors from the PSF-fit measurements and those from the photometric calibrations, provides the final photometric errors.

2.1.1 Pre-reduction

Preliminary steps for measuring photometric data consist of bias removal, overscan correction, image trimming, and flat-field correction. The aim is removing instrumental patterns from raw frames. After performing pre-reduction steps, we obtain clean science images for data measurements. The above steps are detailed as follows:

- **Bias Removal.** The bias is the CCD count offset introduced by the electronics to keep the Analogue-to-Digital Converter (ADC) output always with a positive value. The ADC counts the charge accumulated in a pixel and converts it to a digital value (the number of Analogue-to-Digital Units; ADUs). This is equal to the number of electrons detected in the pixel. The gain is defined as the numbers of photo-excited electrons per ADU (e.g., Gain = 3 e^-/ADU), which is typically used in the conversion from counts to number of incident photons. The common practice is to create a 'master bias' image by averaging individual bias frames, that will be subtracted to all images. The single bias image is obtained with the shutter closed and 0 second exposure time. The IRAF command ZEROCOMBINE is used to obtain the master bias.

- **Overscan Correction.** The overscan correction is a second-order effect to be removed from the bias level. It is a mere offset and varies from frame to frame, due to changes in the CCD temperature with time. To determine the overscan section, we normally average an unexposed region of the frame (typically a few tens columns or rows wide). In IRAF, we use IMEXAMINE or IMPLOT to identify the overscan region, then we subtract it from all frames with the IRAF command CCDPROC.

- **Trimming.** This operation is done to reduce the physical dimension of the frame, cutting unexposed CCD regions or those that have an irregular response to the light. The overscan correction and trimming should be performed in all images prior to any other process, using CCDPROC.

- **Flat-field Correction.** Once previous processes are completed, the final step is the flat-field correction. The sensitivity of individual pixels is different due to non-uniform transmission (e.g., vignetting or dust grains on the CCD) and quantum efficiency (QE) inhomogeneities. In order to correct these effects, one needs a fully illuminated frame. Dome flats are obtained pointing the telescope to a diffusing screen on the dome, and twilight flats are taken pointing to the illuminated twilight sky. The exposure time for a single flat has to be calculated to obtain the highest counts avoiding the saturation or the non-linearity response levels, and separate flats should be prepared for each filter. We median-combine flat fields for one filter, to remove spurious sources (e.g., stars in sky flat images). The IRAF commands CCDPROC and FLATCOMBINE allow the image correction and perform a combination to obtain the master flat, respectively. Finally, science frames are flat-corrected using CCDPROC.

For some specific instruments, dedicated pipelines have been developed to speed up the reduction process. In particular, the Public ESO Spectroscopic Survey for Transient Objects (PESSTO) uses a pipeline[6] (with several PYTHON-based tasks/packages) for EFOSC2 and SOFI mounted on the New Technology Telescope (NTT) (see, Smartt et al. 2015). This pipeline reduces quickly the photometric and spectral data from both instruments.

[6] http://wiki.pessto.org/pessto-operation-groups/data-reduction-and-quality-control-team

Foscgui [7] is divided in the *ekargui* and *alfoscgui* pipelines, for the AFOSC instrument at the 1.82-m Copernico telescope in Asiago and for the ALFOSC instrument at the 2.56-m NOT telescope on La Palma, respectively. It is a useful tool to perform both photometric and spectral reductions with a FOSC-like instrument [8]. The *Foscgui* is written in PYTHON and is based on *anaconda/astroconda* PYTHON distribution. As an example, the user interface of *alfoscgui* is shown in Figure 2.2. Following the tutorials in the *help* button, one can complete the reduction of the transient images with a much more efficient approach. Detailed information on the *Foscgui* is available on the website of the Padova-Asiago Supernova Group [9].

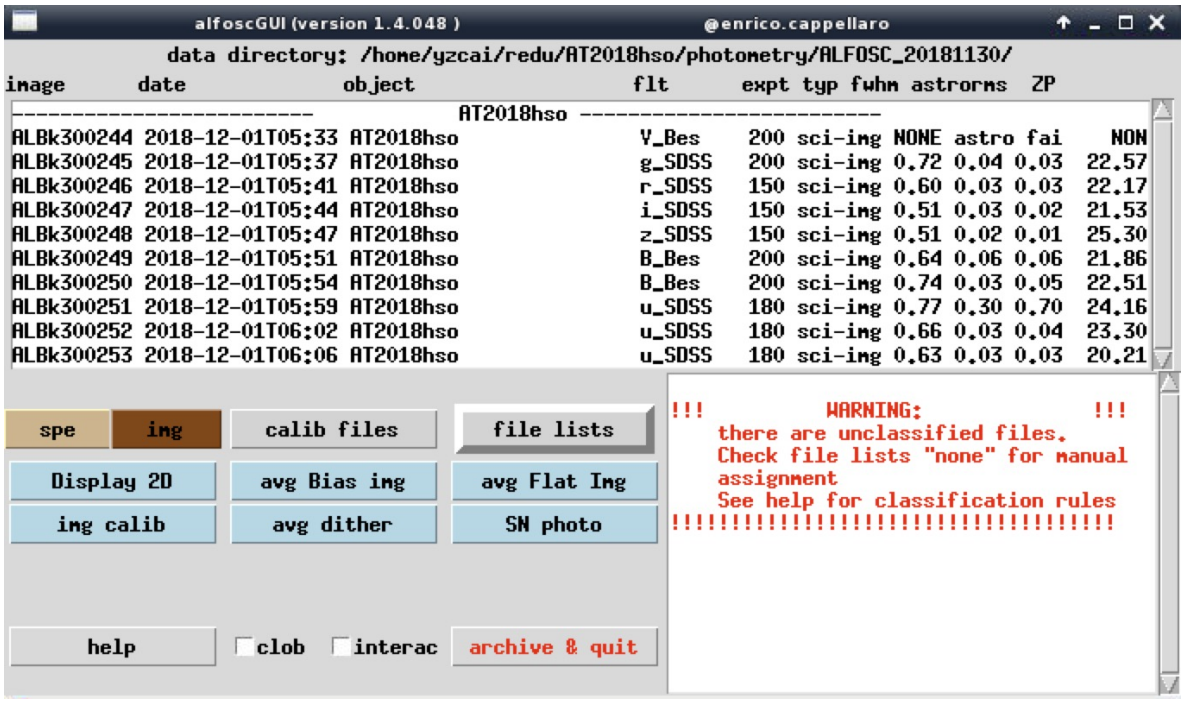

Figure 2.2: The graphic user interface of the *alfoscgui* pipeline, written for the reduction of photometric and spectroscopic data taken with the ALFOSC instrument.

Another IRAF script *notcam.cl* [10] is devoted to a quick pre-reduction of NIR data obtained with NOTCam at the Nordic Optical Telescope (NOT). The current version has been updated to 2.6 in December 2014.

[7] `http://sngroup.oapd.inaf.it/foscgui.html`. Foscgui is a graphic user interface aimed at extracting transient spectroscopy and photometry obtained with FOSC-like instruments. It was developed by E. Cappellaro.

[8] A FOSC instrument is a focal reducer, and that FOSC stands for Faint Object and Spectrograph Camera

[9] `http://sngroup.oapd.inaf.it/foscgui.html`

[10] `http://www.not.iac.es/instruments/notcam/guide/observe.html#reductions`

2.1.2 Photometry with *SNoOpy*

SNoOpy is a pipeline which allows us to perform photometric measurements on images taken at different telescopes. It is a combination of PYTHON scripts that use IRAF standard tasks via *pyraf* and other photometric softwares. Specifically, *SNoOpy* consists of SEXTRACTOR (Bertin & Arnouts 1996) for target source extraction, DAOPHOT (Stetson 1987) for PSF fits, and HOTPANTS (Becker 2015) for image difference.

Preparation

When we starting to use *SNoOpy*, we set basic instrumental parameters (e.g., *gain*, *scale*, *readout noise*, etc) in a file called "*snoopy.default*". An example is shown for NOT/ALFOSC and NOTCAM.

ALFOSC
site: Roque
datamin: -100
datamax: 80000
epadu: 0.33
readnoise: 4.2
object: OBJECT
exposure: EXPTIME
mjd: MJD
dateobs: DATE-OBS
airmass: AIRMASS
filter: FILTER
scale: 0.19
seeing: SEEING
UBVRI: U_Bes 362_60, B_Bes 440_100, V_Bes 530_80, R_Bes 650_130, i_int 797_157
ugriz: u_SDSS, g_SDSS, r_SDSS, i_SDSS, z_SDSS

NOTCAM
site: Roque
datamin: -3000
datamax: 3000.
epadu: 2.6
readnoise: 8.9
object: OBJECT
exposure: EXPTIME
mjd: MJD-OBS
dateobs: DATE-OBS
airmass: AIRMASS
filter: FILT2
scale: 0.24
seeing: SEEING
JHK: J,H,Ks

Table 2.1: The key-words in the header of science images

file name	object	instrument	dateobs	mjd	filter	band	expos	airm	seeing
ALFOSC_u	AT2018hso	ALFOSC	2018-11-15	58437.200	u	ERROR	180	1.62	2.17
ALFOSC_g	AT2018hso	ALFOSC	2018-11-15	58437.210	g_SDSS	g	180	1.60	ERROR
ALFOSC_r	AT2018hso	ALFOSC	2018-11-15	ERROR	r_SDSS	r	90	1.58	1.88
ALFOSC_i	AT2018hso	ALFOSC	2018-11-15	58437.210	i_SDSS	i	90	1.57	1.91

After the standard pre-reduction steps, we need to verify if all parameters are correctly set in the image header. This is done using the *SNoOpy* command *eclist* (Table 2.1). If the output of *eclist* gives some errors, this implies there is a mismatch between the header and the keywords combined in the *snoopy.default* file, that needs to be corrected. As an example, the keyword "filter" in the header of *ALFOSC_u.fits* image does not match the parameter in *snoopy.default* (Table 2.1).

Occasionally, multiple images are observed for individual bands. This happens when the source is faint, in order to increase the final image Signal-to-Noise Ratio (SNR), or to avoid single image saturation when the source is bright. The final image is obtained by mean combining the dithered single frames. This operation can be performed using ECDITHER and it can be done manually or automatically.

When the MJD keyword is missing in the header of an image (see, for instance, *ALFOSC_r.fits* image in Table 2.1), one can use the ECMJD command to calculate the Modified Julian Date (MJD). The calculation is based on some time parameters recorded in the header (e.g., *DATE-OBS*, *TIMESTART*, *EXPTIME*).

The header of the *ALFOSC_g.fits* image in Table 2.1 does not contain the SEEING keyword. The task ECSEEING measures the FWHM of isolated non-saturated stars, selecting manually or automatically the field stars.

Astrometry has to be done before any photometric measurements. We have two choices to perform astrometry, including the manual and automatic options. The task ECASTRO is used to do astrometric calibration by hands, selecting at least three reference stars and comparing them with USNO-A2.0 or 2MASS catalogs. Another solution is using the ECASTROAUTO command, which automatically calculates an astrometric solution for the target image according to star coordinates. If an image is astrometrised, it can be used as a reference for other frames with a similar astrometric solution.

PSF fit

In order to achieve precise photometry, the PSF fitting method is a valuable tool to obtain instrumental magnitudes, particularly suitable for transient located in relatively crowded fields. The PSF model is produced by fitting the profiles of several local stars in the target's frame. Many factors can determine the PSF construction, such as weather conditions, detector artefacts, and field distortion. To build an effective PSF, we have to define a sample of good stars that have high SNRs and isolated locations. Although *SNoOpy* allows us to build the PSF automatically, it is better to inspect individual PSF profiles, and manually select good quality stellar PSFs. For instance, Figure 2.3 shows different types of PSFs.

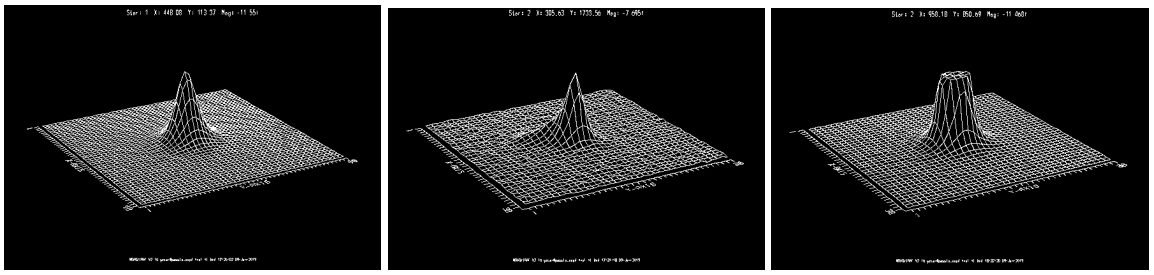

(a) (b) (c)

Figure 2.3: Examples of different PSF profiles. Panel (a) shows an output with good PSF. Panel (b) shows an elongated PSF profile, which may be caused by telescope tracking issues. Panel (c) shows a saturated PSF profile, which should not be selected to build the PSF model.

ECPSF performs automatically or manually the PSF model construction, using the DAOPHOT algorithm. The output of ECPSF includes two files, namely, **.psf.fits* and **.sn*. Specifically, **.psf.fits* contains the analytical model of the final PSF and the residuals, while **.sn* is an *ascii* file consisting of key information on the target image, including the instrumental magnitudes of all measured stars. In addition, other important parameters are also included in this file, such as the instrument, the MJD, the filter name, the exposure time, the airmass, etc (see below).

2018hso IO:O 2018-12-26T03:13:00.036 58478.13 r
Exptime 120.0 Airmass 1.365378 FWHM[pix] 4.5 Ap.Corr. -0.038 +/- 0.011

RA	DEC	magp9(2)	magph(3)	err	mph(4)	magfit	err	diff
11:33:29.494	53:02:53.85	-10.842	-10.958	0.001	-10.973	-10.854	0.056	-0.104
11:33:45.848	53:04:16.24	-7.952	-7.988	0.008	-8.002	-7.957	0.006	-0.031
11:34:21.237	53:03:41.03	-8.646	-8.674	0.004	-8.681	-8.617	0.004	-0.057
11:34:14.010	53:03:39.87	-7.701	-7.730	0.010	-7.747	-7.698	0.006	-0.032
11:34:18.272	53:10:16.49	-10.902	-10.942	0.001	-10.952	-10.908	0.047	-0.034

After the PSF construction, we extract the transient PSF using ECSNFIT. Firstly, the program asks the user if the trim section around the SN position is suitable. In general, the astrometry does not exactly match the coordinates of the target (listed in the file *sn.coo*), hence we have to select the option *-r* to fine-tune the position. Secondly, we mark the target's location in the trimmed image, and we can set the box width in FWHM units and fit the background with low-order polynomials along the x, y axes (see the left panel in Figure 2.4). When the background parameters are fixed, the resulting PSF of the target is computed (see the right panel of Figure 2.4). A resulting file **.res.fits* is simultaneously created, consisting of the PSF-fit residuals.

It is useful to fix an acceptable SNR to determine the detectability and photometric accuracy for a very faint target, and a 3-sigma criterion (i.e., SNR~3) is a common detection threshold. The standard SNR equation for determining the limiting magnitudes is:

$$\mathrm{SNR} = \frac{R_* \times t}{[(R_* \times t) + (R_{sky} \times t \times n_{pix}) + (RN^2 + (\frac{G}{2})^2 \times n_{pix}) + (D \times n_{pix} \times t)]^{1/2}}. \tag{2.7}$$

In Equation 2.7, all contributing factors are independent, hence they are accounted in quadrature.

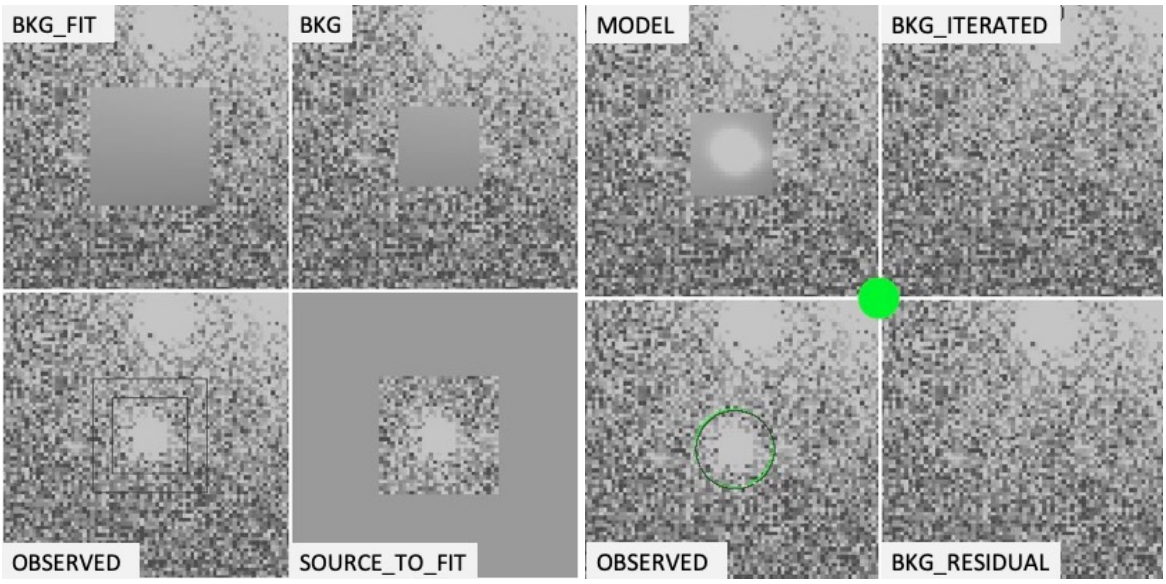

(a) (b)

Figure 2.4: The interactive response of ECSNFIT, including background estimation, its subtraction (Panel a), the transient fit and the residuals (Panel b). The black circle marks the original position computed from the *sn.coo* file, while the green open circle marks the measured location of the object via fine-tuning fit. The green filled circle marked in the middle of the image indicates that the transient has a SNR ≥ 10.

R_* (e^-/s) is the count rate of the target, R_{sky} ($e^-/s/pixel$) is the count rate of the background, t (s) is the exposure time, r ($pixel$) is the aperture radius, n_{pix} ($\pi \times r^2$) is the number of pixels of the aperture, G (e^-/DN) is the inverse gain, D ($e^-/pixel/s$) is the dark current, and RN is the read-out noise. In ECSNFIT, a green circle is marked in the middle of a frame when SNR ≥ 10 (see Figure 2.4 panel b); a blue square is printed when $3 \leq$ SNR ≤ 10, and a red triangle when the SNR is below 3. The specific task ECLIMIT is applied to give a limiting magnitude at the location of the object when the source is invisible. The default SNR limit value is 2.5 but we can set it to different values (e.g., 1, 1.5, or 2). An example of a limiting magnitude measurement is shown in Figure 2.5.

The instrumental errors are combined in quadrature with the PSF-fit errors (provided by DAOPHOT), as they are independent error sources to provide the total uncertainty on the photometric point. The instrumental errors are estimated through an artificial star technique, in which fake stars (with the same PSF and magnitude as the target) are placed near the real location of the object. The RMS of the magnitudes of a number of fake stars provides an averaged value for the instrumental errors. Figure 2.6 shows an example of fake star tests.

Template Subtraction

When the source has a very complex background, or it is very faint with a magnitude comparable to that of the local environment (e.g., at early and late phases), we can use the template subtraction technique to measure instrumental magnitudes. The templates are usually collected from archival pre-

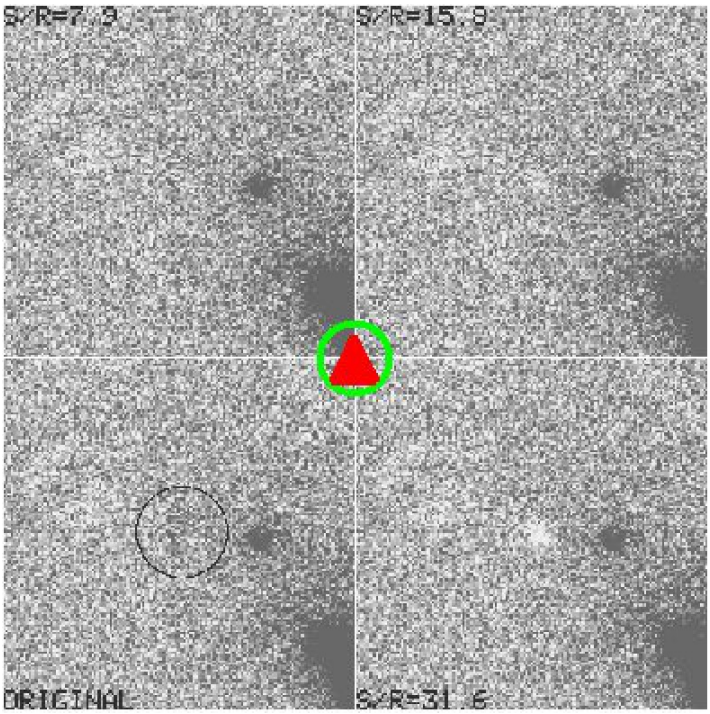

Figure 2.5: Example of a limiting magnitude measurement. The target position is marked with a black circle. A circle-centred red triangle indicates the object is not detected in this frame. We adopt the default SNR = 2.5.

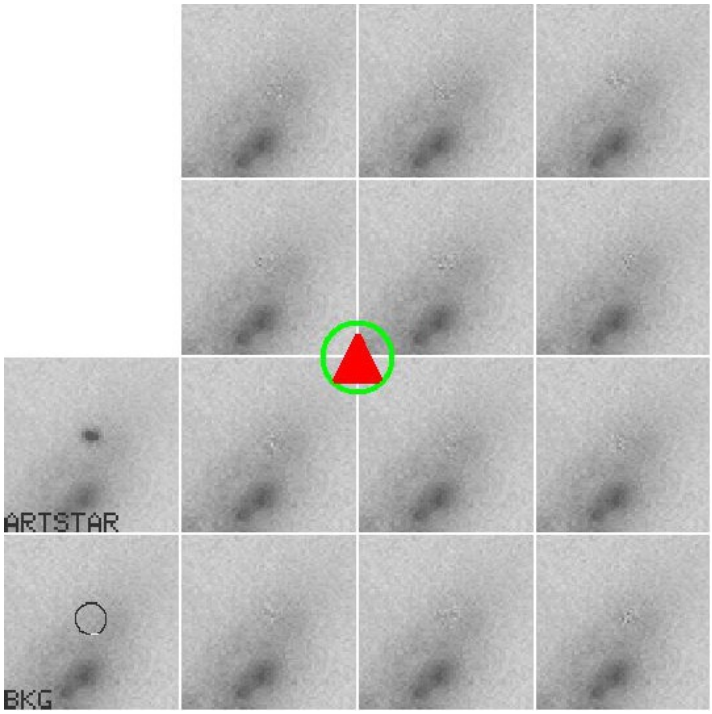

Figure 2.6: Example of an artificial star experiment. The fake star is shifted by a default value of 2.0 *pix* from the position of the object.

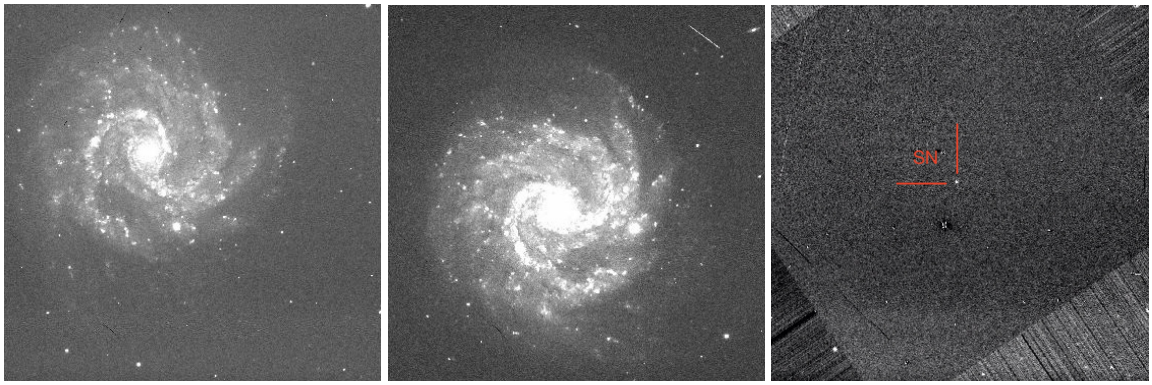

(a) (b) (c)

Figure 2.7: An example of template subtraction technique. Panels (a) and (b) show the original and template images, respectively; Panel (c) shows the subtracted frame, which also presents the image rotation between original and template images. The SN is marked with red lines in panel (c).

explosion images or are taken after the object has disappeared. A good template should be obtained with a good seeing, deep exposure time, and with high SNR. In *SNoOpy*, the command ECSNDIFF performs the template subtraction, in which the image is subtracted by HOTPANTS, and the source magnitude is obtained with the PSF fitting technique. *SNoOpy* performs the template subtraction following these steps:

1. It first scales the astrometrised template frame to the science image to be measured, and simultaneously compute the geometric transformation using some reference stars in common in the two frames.

2. After the best seeing image is degraded to the worse one, the template is subtracted to the science image.

3. The subtracted image contains the clean transient and some background residuals (e.g., hot pixels or residuals from saturated stars). Then, we can perform either aperture or PSF fitting photometry on the subtracted frames to obtain the instrumental magnitudes. In the default mode adopted by *SNoOpy*, we use PSF-fitting photometry.

An example of template subtraction is shown in Figure 2.7. A good light curve obtained after template subtraction is shown in Figure 2.8. The colour dashed lines are the multi-band light curves of UGC 8246 OT with the PSF-fitting technique, while the colour points are the measurements obtained with the template-subtraction technique. The light curve with template subtraction has a plateau signature, while the normal PSF-fitted one does not show a clear plateau. This is because of the strong background contamination in the original images. In addition, the late-time light curves with template subtraction decline much faster.

Magnitude Calibration

Once we obtained the instrumental magnitudes with the methods illustrated before, the apparent magnitudes are calibrated using Equations 2.2. There are two crucial terms we need to know: the night ZP and the instrumental CT. We derive ZPs through standard fields observed in photometric nights.

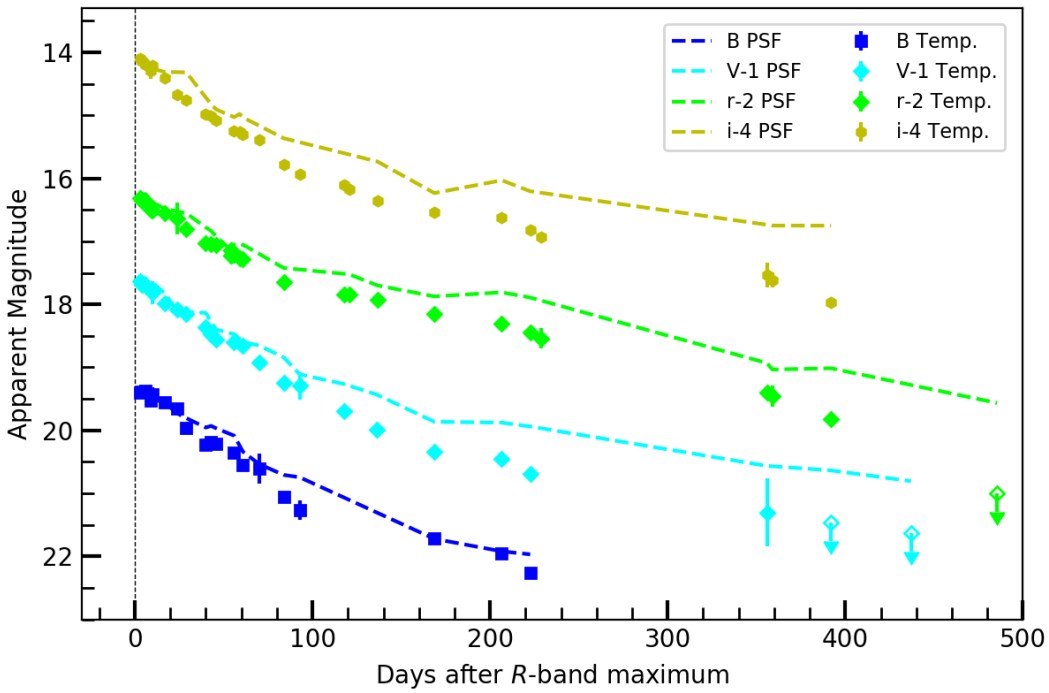

Figure 2.8: Light curve comparison with template-subtraction (filled points) and PSF-fitting (dashed lines) methods.

The term "Standard Fields" indicates a catalog of field of stars, whose components have well-known magnitude and colour information. ZPs and CTs for specific instruments and nights are determined by directly comparing the measured and catalogue magnitudes. Specifically, we use standard stars in the Landolt (1992) catalogue for Johnson-Cousins filters, and the Sloan Digital Sky Survey (SDSS) or PanStar catalogues for Sloan-band data. The ECPH command allows us to derive ZPs and CTs for each night of observation.

An *ascii* file named *photo.ph* containing the ZP and CT values (and their errors) is the output of this command. An example is shown below for the Johnson-Cousins and Sloan bands for the ALFOSC instrument.

```
###  ALFOSC_FASU   2015-04-29   57141.21
U    UB    24.992   0.043   0.100   0.048
B    BV    26.708   0.025   0.011   0.019
V    BV    26.556   0.004  -0.059   0.003
V    VR    26.551   0.005  -0.089   0.007
R    VR    26.405   0.005  -0.136   0.006
R    RI    26.410   0.003  -0.144   0.004
I    RI    25.582   0.035  -0.072   0.044
u    ug    25.718   0.259  -0.003   0.108
g    gr    27.033   0.062   0.049   0.028
r    gr    26.666   0.137   0.035   0.060
r    ri    26.664   0.321   0.057   0.231
```

```
i    ri    26.170   0.755   0.072   0.262
z    iz    24.856   0.025   0.018   0.027
```

To obtain an accurate calibration, a sequence of reference stars in the transient field (secondary standards) are used to correct the ZPs in the non-photometric nights. To this aim, we first use the ECREFSTAR command to obtain the apparent magnitudes of the secondary standards. In addition, ECZEROPOINT is an alternative command to obtain calibrated magnitudes, both in Johnson-Cousins and Sloan filters. This command can automatically convert the Sloan magnitudes to Johnson-Cousins ones, following the relations of Chonis & Gaskell (2008) (see their Equations 1 - 5) using the option *-w*. Examples of Johnson-Cousins and Sloan filter magnitudes of local sequence stars for the target (AT 2017be) field are reported below:

```
#  ra          dec           U             B             V             R             I
8:13:00.079 45:52:19.96 22.603 0.763 19.601 0.075 18.036 0.037 17.072 0.075 16.034 0.154
8:12:33.234 45:56:20.81 16.726 0.013 16.631 0.036 15.961 0.017 15.569 0.027 15.184 0.052
8:12:32.995 45:59:14.77 19.429 0.057 18.327 0.056 17.147 0.027 16.472 0.040 15.884 0.079
8:14:05.509 45:46:16.64 18.174 0.021 18.237 0.033 17.655 0.017 17.302 0.027 16.915 0.052
8:14:18.475 45:54:01.59 17.179 0.014 16.426 0.045 15.493 0.022 14.951 0.034 14.445 0.067
                                      ......

#  ra          dec           u             g             r             i             z
8:13:00.079 45:52:19.96 23.457 0.763 18.906 0.010 17.442 0.006 16.665 0.005 16.244 0.008
8:12:33.234 45:56:20.81 17.580 0.011 16.256 0.004 15.772 0.004 15.609 0.004 15.550 0.006
8:12:32.995 45:59:14.77 20.283 0.057 17.770 0.006 16.728 0.004 16.373 0.004 16.179 0.008
8:14:05.509 45:46:16.64 19.028 0.020 17.894 0.006 17.506 0.006 17.341 0.006 17.281 0.013
8:14:18.475 45:54:01.59 18.033 0.012 15.958 0.004 15.186 0.004 14.908 0.004 14.751 0.005
                                      ......
```

In order to calibrate non-photometric nights, ZP corrections have to be applied to them. Comparing the night magnitudes of secondary standards with those obtained in photometric nights allows us to obtain ZP corrections. The ECNIGHTCAL command provides the ZP corrections for non-photometric nights. Figure 2.9 shows the process of deriving ZP corrections for a poor-quality night. In that case, the correction is large (-0.7 mag). In addition, the list of ZP corrections for Johnson-Cousins and Sloan filters for all nights are archived in a file "*zerocor.dat*" as follows:

```
################## output zerocor.dat ##################
ALFOSC_FASU   57769.975      B -0.815 0.021      V -0.955 0.026
ALFOSC_FASU   57776.150      B -0.793 0.013      V -0.811 0.043
ALFOSC_FASU   57781.870      B -0.849 0.065      V -1.006 0.027
ALFOSC_FASU   57809.910      B -0.770 0.032      V -0.890 0.025
ALFOSC_FASU   57821.015      B -0.702 0.046      V -0.797 0.023
                                  ......
ALFOSC_FASU  57769.980  g 0.124 0.011   r 0.015 0.022   i 0.041 0.022   z 0.010 0.036
ALFOSC_FASU  57781.870  g -0.101 0.029  r -0.027 0.038  i -0.239 0.027  z -0.011 0.039
ALFOSC_FASU  57803.070  g 0.008 0.021   r 0.009 0.016   i 0.002 0.041   z 0.001 0.014
```

```
ALFOSC_FASU  57809.900  g 0.013 0.021   r 0.035 0.017   i 0.026 0.023   z 0.023 0.024
ALFOSC_FASU  57864.890  g -0.005 0.015  r 0.061 0.042   i 0.020 0.020   z 0.247 0.027
ALFOSC_FASU  57875.875  g 0.116 0.024   r -0.016 0.014  i 0.016 0.017   z 0.113 0.013
                                    .....
```

Final ZPs and CTs are applied to instrumental magnitudes, and the calibrated apparent magnitudes of the transient are written in an *ascii* file named *snlc.dat*. The ECSNCAL command completes this step.

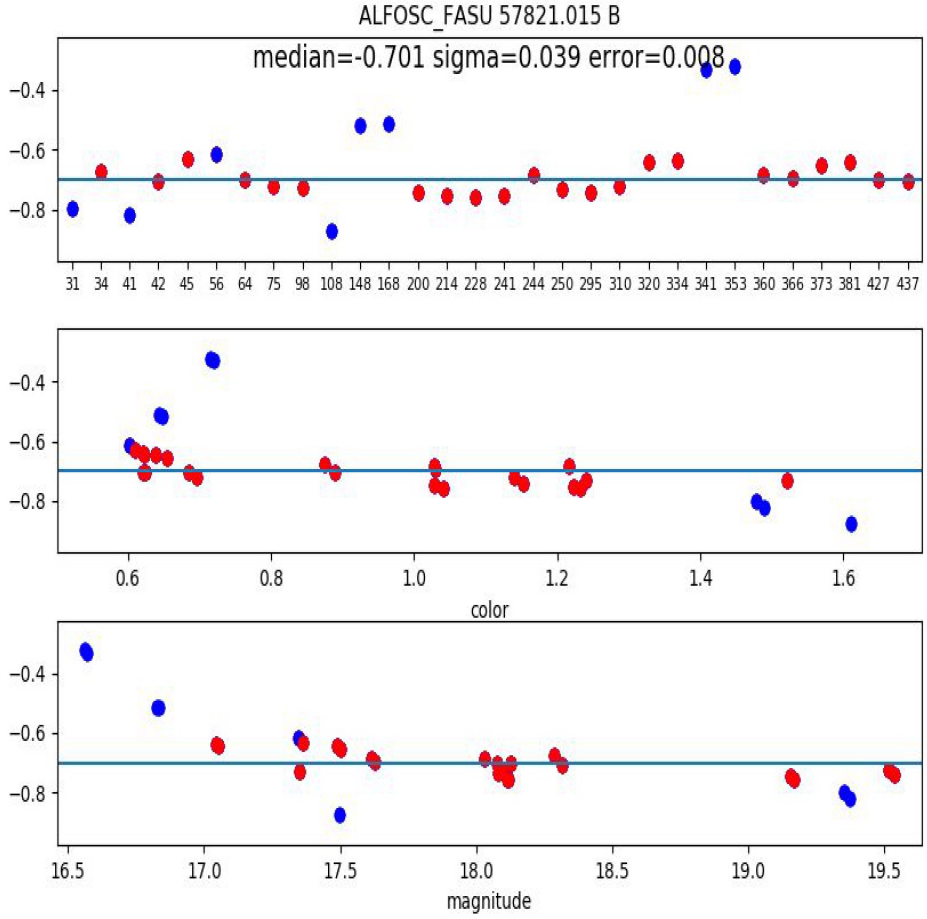

Figure 2.9: Comparison between measured magnitudes and catalogued ones of local standard stars in the transient (AT 2017be) field during a non-photometric night. The blue dots mark stars that have large discrepancies, and are automatically rejected by *SNoOpy* or removed by hands. Red points are adopted to calculate the ZP corrections, in which the computed parameters, such as median, sigma, error for this specific night and instrument are also reported.

2.2 Spectroscopy

2.2.1 Pre-reduction

The spectral pre-reduction steps are similar to those applied to imaging frames. They still need bias, overscan, trimming, and flat-field corrections. The *response* IRAF task allows us to do the normalisation through an interactive fit of the flats with a high order function (typically over 30) along the dispersion direction.

2.2.2 Spectroscopy with IRAF

After the pre-reduction, the spectra of the targets are reduced through standard IRAF tasks, mainly contained in the CTIOSLIT package. First, one dimensional (1-D) spectra are extracted from the two-dimensional (2-D) frames along the dispersion axis.

Then wavelength calibration is applied via a comparison with arc lamp spectra obtained during the same night, and with an identical instrumental configuration. Generally, there are some available lamps for a specific instrument, such as Ar, Ne, Hg, and He. Once the wavelength is calibrated, the accuracy of the calibration should be checked by measuring the wavelengths of some prominent night sky lines (e.g., [O I] at λ=5577 Å, 6300 Å, 6364 Å). In case of mismatch, a constant shift has to be applied, to obtain an accuracy within 1 Å. The spectral resolution is calculated by measuring the FWHM of night sky lines.

The flux calibration is performed using spectrophotometric standard stars available in the European Southern Observatory (ESO) website [11]. The spectra of standard stars allow us to obtain sensitivity function curves to flux calibrate the spectrum of the targets. We remark that the wavelength-dependent extinction at the different telescope sites has to be accounted for an accurate flux calibration. The calibrated spectra then need to be fine-tuned against simultaneous broad-band photometry, and a scaling factor should be eventually applied. This scaling factor is calculated from the Pogson formula:

$$\frac{\mathrm{F_{Spectra}}}{\mathrm{F_{Photometry}}} = 10^{0.4(m_{Photometry}-m_{Spectra})} \tag{2.8}$$

We finally use the spectra of spectrophotometric standard stars to remove the telluric absorption bands (e.g., O_2, H_2O, etc). The final spectra have to be corrected for the redshift and reddening. A spectrum reduced following the above prescriptions is shown in Figure 2.10.

In the specific case of FOSC-like instruments, both *ekargui* and *alfoscgui* were implemented with full steps of spectroscopic reduction (see Figure 2.2). A SN classification tool is also implemented in the package (*snid*; Blondin & Tonry 2007).

[11] https://www.eso.org/sci/observing/tools/standards/spectra.html

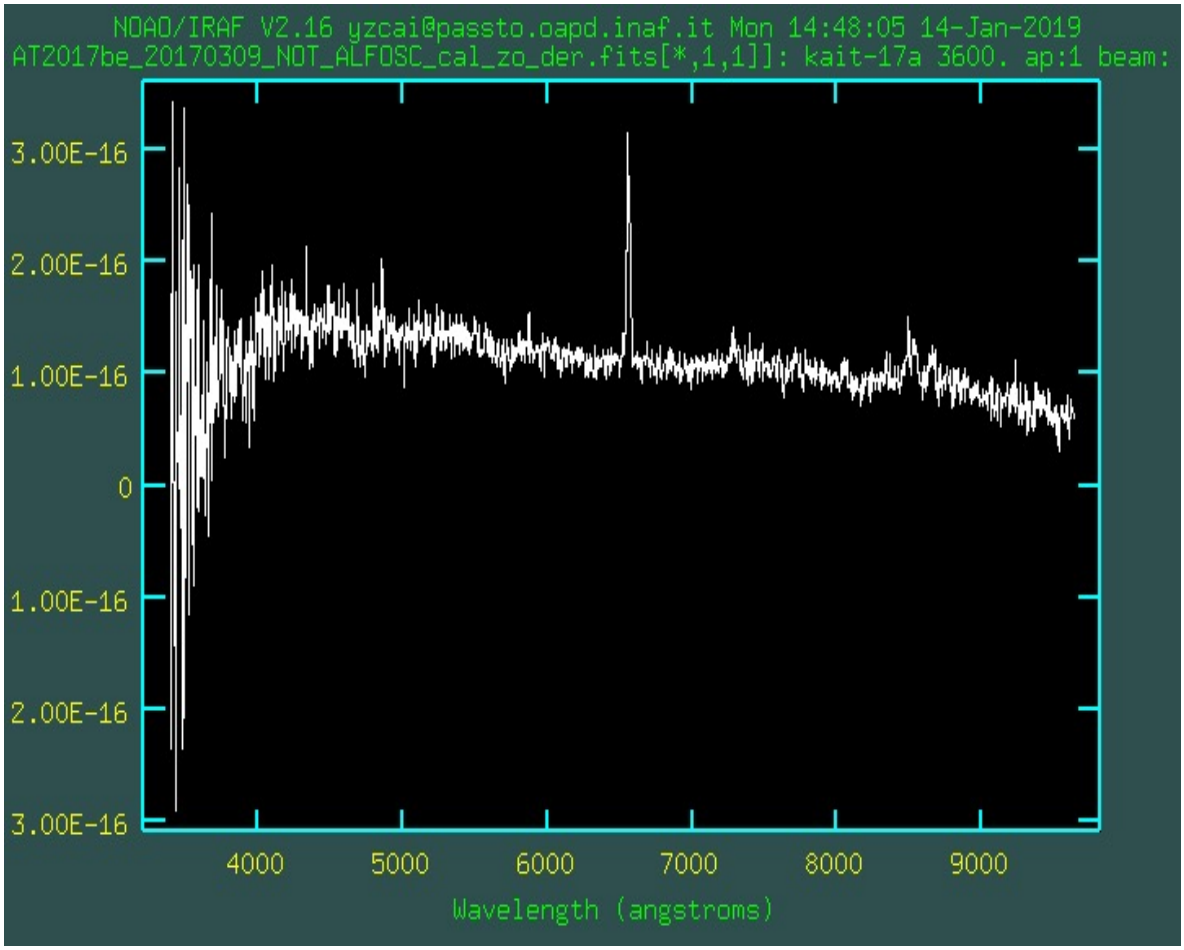

Figure 2.10: A spectrum of AT 2017be obtained on 2017 March 9 with NOT/ALFOSC. This spectrum was redshift and reddening corrected.

Chapter 3

A very faint, red transient in NGC 2537

As discussed in Chapter 1.3, the proliferation of wide-field sky surveys has led to the discovery of a large variety of transients of various luminosities. In particular, ILOTs are challenging our understanding of standard scenarios of stellar evolution.

A sub-set of ILOTs are designated "SN impostors" (Van Dyk et al. 2000), and mimic the observables of real SN explosions, although their progenitor stars survive the outburst (see Chapter 1.3.3). An LBV scenario has been proposed to explain many SN impostors (see details in Chapter 1.3.3). According to several authors (e.g., Smith et al. 2009), ILRTs can be SN impostors, i.e., LBV-like outburst of moderately massive stars. In this chapter, we show that the explosion of a S-AGB star as an ECSN is viable alternative explanation for ILRTs.

S-AGB stars are usually surrounded by a thin circumstellar shell and an extended hydrogen envelope (Nomoto 1987), and may experience major mass-loss accompanied by significant outbursts. It has been proposed that when a star's initial mass is in the range $\sim$ 8-10 $M_{\odot}$, it can die as an ECSN (Miyaji et al. 1980; Nomoto 1984, 1987; Miyaji & Nomoto 1987; Hashimoto et al. 1993; Kitaura et al. 2006; Poelarends et al. 2008; Wanajo et al. 2011, see also Chapter 1.3.1). We note however, that the precise mass range for ECSN progenitors is controversial and is likely limited to $\Delta M \sim 1\,M_{\odot}$ or less (Siess 2007; Doherty et al. 2015, 2017).

Recently, Kankare et al. (2012) proposed that CSM interaction following an ECSN can explain the Type IIn SN 2009kn (peak $M_B \approx -18$ mag). A similar suggestion has been given by Smith (2013) and Mauerhan et al. (2013b) for the Type IIn SN 2011ht[1]. However, ECSNe are expected to be fairly faint events (e.g., Tominaga et al. 2013). Therefore, candidates are expected to have modest luminosities and type IIn SN like spectra if a mass loss event happened a short time before the SN explosion (Pumo et al. 2009). The faint SN 2008S is an appealing ECSN candidate. In fact, a possible S-AGB progenitor has been proposed by several authors (Botticella et al. 2009; Szczygieł et al. 2012; Adams et al. 2016), based on pre-outburst archival Spitzer images which revealed a candidate in the correct mass range, and embedded in a dusty cocoon. Other famous ILRTs (NGC 300 OT2008-1, M85 OT2006-1, PTF10fqs; see Chapter 1.3.1), along with some faint SE SNe such as SN2008ha, SN 2005E and SN2005cz, have been proposed to be ECSNe (Pumo et al. 2009).

[1]Pastorello et al. (2019b) proposed an alternative explanation that SN 2011ht is likely a final CC SN explosion, after an outburst event. It shows a striking similarity with LRN evolutionary channel (see Chapter 1.3.2).

In this chapter, we present a study of a newly discovered ILRT, AT 2017be (also known as KAIT-17A or iPTF17be). AT 2017be was discovered on 2017 January 06.508 (UT will be used hereafter) by the Lick Observatory Supernova Search (LOSS), at an unfiltered magnitude of 18.5 (Stephens et al. 2017). We note that Hosseinzadeh et al. (2017) initially classified AT 2017be as an LBV, and Adams et al. (2018) recently presented some followup observations of AT 2017be, also supporting an LBV eruption scenario for this event. This work presents a more extensive dataset, with higher-cadence spectro-photometric coverage, and a monitoring window covering all phases of the transients evolution, from which we reach a somewhat different conclusion on the nature of AT 2017be.

This chapter is organised as follows: in Section 3.1, we characterise the host galaxy NGC 2537. In Section 3.2, we describe the photometric data reduction techniques and present the lightcurves of AT 2017be. In Section 3.3, the spectroscopic data are shown and analysed. In Section 3.4, we examine the pre-explosion frames, in particular *Hubble Space Telescope* (*HST*) archival images, and characterise the quiescent progenitor star a few years before the AT 2017be event. A discussion on the nature of AT 2017be and a short summary are presented in Section 3.5. The results of this study have been published in Cai et al. (2018).

3.1 The host galaxy

AT 2017be was discovered in NGC 2537 at RA = $08^h13^m13.38^s$, Dec = $+45°59'29.54''$ [J2000] (see Figure 3.1). The host galaxy is also known as Mrk 86, Arp 6 or the Bear's Paw Galaxy. According to the standard morphological classification scheme (Hubble 1926; de Vaucouleurs 1959), NGC 2537 is a blue SB(rs) galaxy. Detailed information on the host galaxy taken from the NASA/IPAC Extragalactic database[2] (*NED*) is reported in Table 3.1.

The distance to NGC 2537 has been estimated with multiple methods, including using the brightest stars in the galaxy (Sharina et al. 1999) and the Tully-Fisher technique (Bottinelli et al. 1984). However, the reported estimates are largely discrepant. In particular, different estimates based on the Tully-Fisher method give a wide range of values ($\sim$ 9 - 20 Mpc). From the radial velocity (cz) corrected for local group infall into Virgo (V_{Vir} = 571 ± 4 km s^{-1}) from LEDA[3] (Makarov et al. 2014) and adopting standard cosmological parameters (H_0 = 73 km s^{-1}Mpc^{-1}, Ω_M = 0.27, Ω_Λ = 0.73), we derive a luminosity distance $d_0 = 7.82 \pm 0.54$ Mpc [4]. The resulting distance modulus, $\mu = 29.47 \pm 0.15$ mag, will be used throughout this chapter. We note that this kinematic distance is in good agreement with that inferred from the absolute magnitude of the brightest stars in NGC 2537 (Sharina et al. 1999).

We adopt a Milky Way reddening $E(B-V)_{\rm Gal}$ = 0.048 mag (NED; Schlafly & Finkbeiner 2011), assuming R_V = 3.1 (Cardelli et al. 1989), towards AT 2017be. A narrow Na I D absorption is visible in our spectra at the redshift of the host galaxy NGC 2537, but with low signal-to-noise (S/N) ratio. We increased the S/N by averaging the early spectra, and measured for the blended doublet an equivalent width (EW) of $\simeq 0.57 \pm 0.17$ Å. Following the relation in Turatto et al. (2003) (i.e., $E(B-V) = 0.16 \times$ EW(Na I D)), and assuming R_V = 3.1 (Cardelli et al. 1989), we obtain a

[2] http://nedwww.ipac.caltech.edu/

[3] http://leda.univ-lyon1.fr/

[4] This value is obtained using Ned Wright's Cosmological Calculator http://www.astro.ucla.edu/~wright/CosmoCalc.html/; see Wright (2006)

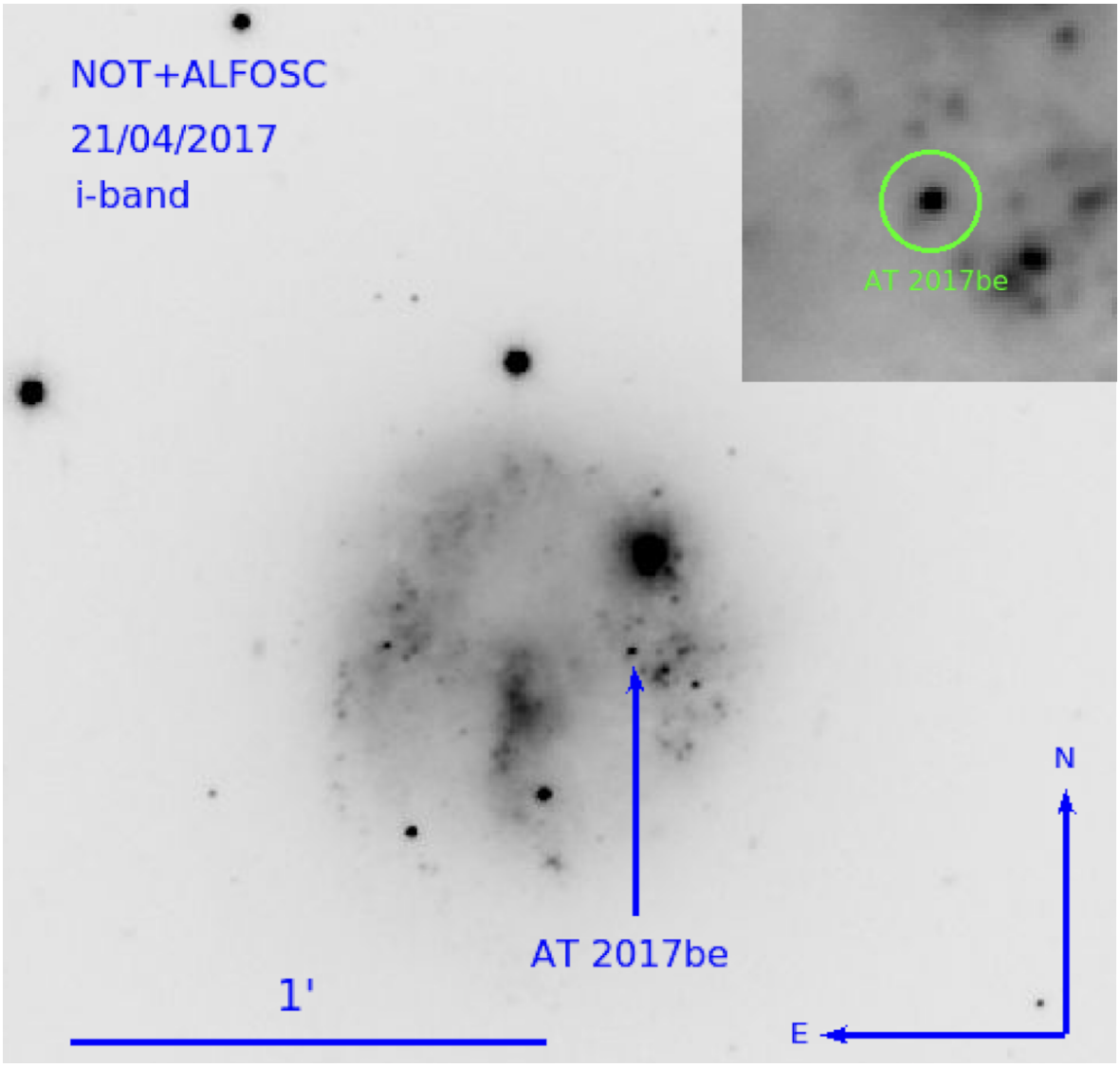

Figure 3.1: The field of AT 2017be. A zoom in on the location of AT 2017be is shown in the inset.

Table 3.1: Basic parameters of NGC 2537.

α (J2000)	$08^h13^m14.64^s$
δ (J2000)	$45°59'23.3''$
Major Axis (arcmin)	$1.7'$
Minor Axis (arcmin)	$1.5'$
Morphological Type	SB(rs)dm
Apparent Magnitude (V)	12.32 mag
Redshift	0.001438 ± 0.000003
$v_{\rm Heliocentric}$	431 ± 1 km s^{-1}
Adopted Distance	7.82 ± 0.54 Mpc
Galactic Absorption	$A_B = 0.195$ mag

host galaxy reddening value of $E(B-V)_{\rm host} = 0.04 \pm 0.02$ mag and a total line-of-sight colour excess $E(B-V)_{\rm total} = 0.09 \pm 0.03$ mag.

Our highest resolution spectrum (+30.2 d from the *r*-band maximum, see Section 3.3) allows us to deblend the narrow Galactic and host galaxy Na ID absorption line components, which appear to have similar strengths. This supports our claim of a similar reddening contribution from the the Milky Way and NGC 2537. A final check has been performed by computing the Balmer decrement (which is the ratio of the Hα and Hβ line intensities) in our spectra. We obtained decrements roughly in agreement with the classical value of Hα/Hβ = 2.86 for typical gas conditions (Osterbrock & Bochkarev 1989) adopting an $E(B-V)_{\rm total} = 0.09$ mag. This total reddening estimate will be used throughout the chapter.

3.2 Photometry

3.2.1 Observations and data reduction

As previously mentioned, AT 2017be was first found by the Lick Observatory Supernova Search (LOSS; reported in *TNS*[5]). An early-phase photometric measurement was also obtained by the Intermediate Palomar Transient Factory (iPTF[6]). We included these data in our lightcurve. Our multi-band monitoring campaign started on 2017 January 6, soon after the classification, when we triggered systematic follow-up observations of the target, with a more aggressive strategy during the first month, when the evolution of the transient was more rapid. Later, we slightly relaxed the cadence of the campaign, which went on to span a period of approximately one year. Detailed information on the observations including the photometric measurements are provided in Table 1 (Appendix 7).

The optical follow-up campaign of AT 2017be was performed using the following instruments: the 1-m telescope of the Las Cumbres Observatory (LCO[7]) at McDonald Observatory (Texas, USA) equipped with a Sinistro (labelled in this chapter as fl05) camera; the 2.56-m Nordic Optical Telescope

[5] https://wis-tns.weizmann.ac.il/object/2017be

[6] https://www.ptf.caltech.edu/iptf/

[7] LCO is a global robotic network of telescopes; see http://lco.global/

(NOT[8]) equipped with ALFOSC and the 10.4-m Gran Telescopio Canarias (GTC[9]) with OSIRIS, both located at Roque de los Muchachos Observatory (La Palma, Canary Islands, Spain); and the 1.82-m Copernico Telescope of the INAF - Padova Observatory at Mt. Ekar (Asiago, Italy)[10] with the AFOSC camera. A complementary near-infrared (NIR) photometric campaign started on 2017 February 7 (approximately one month after the discovery) and ended on 2018 January 4. The NIR data were obtained using the NOT equipped with NOTCam.

All optical imaging frames were first pre-processed using standard tasks in IRAF[11] for overscan, bias and flat field corrections, and trimming of unexposed frame regions (see Section 2.1.1 in Chapter 2). The steps necessary to obtain the SN magnitude (PSF-fitting technique) were performed using the dedicated pipeline SNoOpy, following the descriptions in Section 2.1.2 of Chapter 2. However at late phases, when the transient became too faint to obtain reliable measurements with the PSF-fitting technique, we used template subtraction to properly remove the flux contamination of the host galaxy (see details in Section 2.1.2 of Chapter 2). The template images of the host galaxy were observed as part of the Sloan Digital Sky Survey (SDSS[12]) on 2000 May 4, and were subtracted from the late-time *griz* images. This procedure was needed in particular for the LCO images, because the seeing was typically poor and hence background contamination more severe. The final optical magnitudes of AT 2017be are reported in Table 1 (Appendix 7). We note that very few observations were obtained using the Johnson-Cousins *R* and *I* filters, hence these data were converted to Sloan-*r* and *i* SDSS systems following again the relations given in Chonis & Gaskell (2008).

NIR reductions include differential flat-field correction, sky subtraction and distortion correction. The reductions were based on a modified version of the external IRAF package NOTCam version 2.5[13] (see Chapter 2). To improve the S/N, for each filter we combined multiple individual dithered exposures. NIR instrumental magnitudes of AT 2017be were measured with SNoOpy, and then calibrated using sources in the field from the Two Micron All Sky Survey (2MASS[14]) catalogue. The resulting NIR magnitudes (in the Vegamag system) for AT 2017be are reported in Table 2 (Appendix 7).

3.2.2 Lightcurves

The last pre-discovery non-detection with a limiting magnitude $\sim$ 18.5 mag (Vegamag) reported by the KAIT is from 2016 December 29.479 UT (MJD = 57751.479), while the discovery epoch is 2017 January 6.508 UT (MJD = 57759.508) with a detection of unfiltered mag of 18.5 (Vegamag). Therefore, it is reasonable to assume that the explosion of AT 2017be occurred between these two epochs. In the absence of more stringent indications, we adopt an explosion epoch of MJD = 57755 ± 4. Soon after the discovery of AT 2017be, we initiated a photometric followup campaign which lasted for around one year. The resulting multi-band lightcurves of AT 2017be are shown in Figure 3.2. In the forthcoming discussion, we will adopt the epoch of the *r*-band peak magnitude (MJD = 57769.8 ± 0.1) as the reference time for the light and colour curves (see Section 3.2.3). This was obtained by

[8] http://www.not.iac.es/
[9] http://www.gtc.iac.es/
[10] http://www.oapd.inaf.it/
[11] http://iraf.noao.edu/
[12] http://www.sdss.org/
[13] http://www.not.iac.es/instruments/notcam/guide/observe.html#reductions/
[14] http://irsa.ipac.caltech.edu/Missions/2mass.html/

Table 3.2: Parameters for the peak and the plateau.

Filter	m_{peak} (mag)	$m_{plateau}$ (mag)	Δm (mag) [a]
B	18.46 ± 0.07	20.07 ± 0.06	1.61 ± 0.09
V	18.05 ± 0.05	19.03 ± 0.05	0.98 ± 0.05
g	18.21 ± 0.05	19.33 ± 0.04	1.12 ± 0.06
r	17.70 ± 0.04	18.63 ± 0.04	0.93 ± 0.04
i	17.73 ± 0.03	18.38 ± 0.03	0.65 ± 0.03
z	17.45 ± 0.35	18.12 ± 0.03	0.67 ± 0.35

[a] Δm is the magnitude difference between the averaged plateau and the peak.

fitting a 3rd-order polynomial to the early *r*-band lightcurve from 6 January to 6 February.

The apparent magnitudes of AT 2017be in the different bands at maximum are listed in Table 3.2, while the decline rates in different phases of the evolution obtained through linear fits are reported in Table 3.3. Similar to other ILRTs, AT 2017be rises rapidly and reaches the peak magnitude in all bands in less than two weeks. The blue-band lightcurves reach their luminosity peaks a few days earlier than the red-band ones (see Figure 3.2). After maximum, the luminosity of AT 2017be decays quite rapidly in all bands until day $\sim$ 30, with the blue band (e.g., *BgV*) lightcurves usually fading more rapidly than the red bands (e.g., *ri*). Subsequently, the luminosity settles onto a plateau phase lasting approximately 30 days. The averaged plateau apparent magnitudes are also reported in Table 3.2. After the plateau phase, all lightcurves fade again more rapidly. From a morphological point of view, we can hence split the lightcurve evolution in three phases: from the peak to $\sim$ 30 days there is an initial fast decline ($\gamma 1 \approx$ 1-3 mag/100d, see Table 3.3); from $\sim$ 30 days to $\sim$ 70 days a plateau ($\gamma 2 \approx$ 0.6-0.9 mag/100d), and from $\sim$ 70 days to the latest detections before solar conjunction a faster late decline ($\gamma 3 \approx$ 1.3-2.8 mag/100d). The transient was followed in photometry up to late phases, but only upper limits were obtained in all optical bands after solar conjunction (which lasted $\sim$ 100 days). Complementary NIR photometry is shown in Figure 3.2 and the data are reported in Table 3.3. Unfortunately, we did not follow the transient in the NIR during the first month, hence the lightcurve rise and the subsequent NIR peak have not been monitored, while the initial decline, and the late decline phases have been observed. The NIR decline rates $\gamma 2$ (optical plateau-like period) and $\gamma 3$ are reported in Table 3.3. We included the earliest photometric points in our measurements of $\gamma 2$, and this may explain the relatively large decline rates found in the NIR lightcurves during the intermediate plateau phase (up to $\sim$ 80 days). We also note that the measured *K*-band decline rate at very late phases in the *K* band is around 1.02 mag/100d, which is consistent with the theoretical ^{56}Co decay of 0.98 mag/100d assuming complete gamma-ray and positron trapping. However, this is not a strong argument to support the ^{56}Co decay powering mechanism at late times, as the spectral energy distribution (SED; see Section 5.4) suggests the presence of a clear near-IR excess at these epochs probably due to emission from pre-existing dust in the CSM of AT 2017be. For this reason, we believe that the observed K-band decline match with the ^{56}Co decay rate is likely a coincidence.

3.2.3 Colour and Absolute Lightcurves

Figure 3.3 shows the $B - V$ (upper panel), $R - I/r - i$ (middle panel), $J - K$ (lower panel) colour evolution of AT 2017be along with that of other ILRTs, including SN 2008S (Botticella et al. 2009), NGC 300 OT2008-1 (Humphreys et al. 2011), M85 OT2006-1 (Kulkarni et al. 2007) and PTF10fqs (Kasliwal et al. 2011).

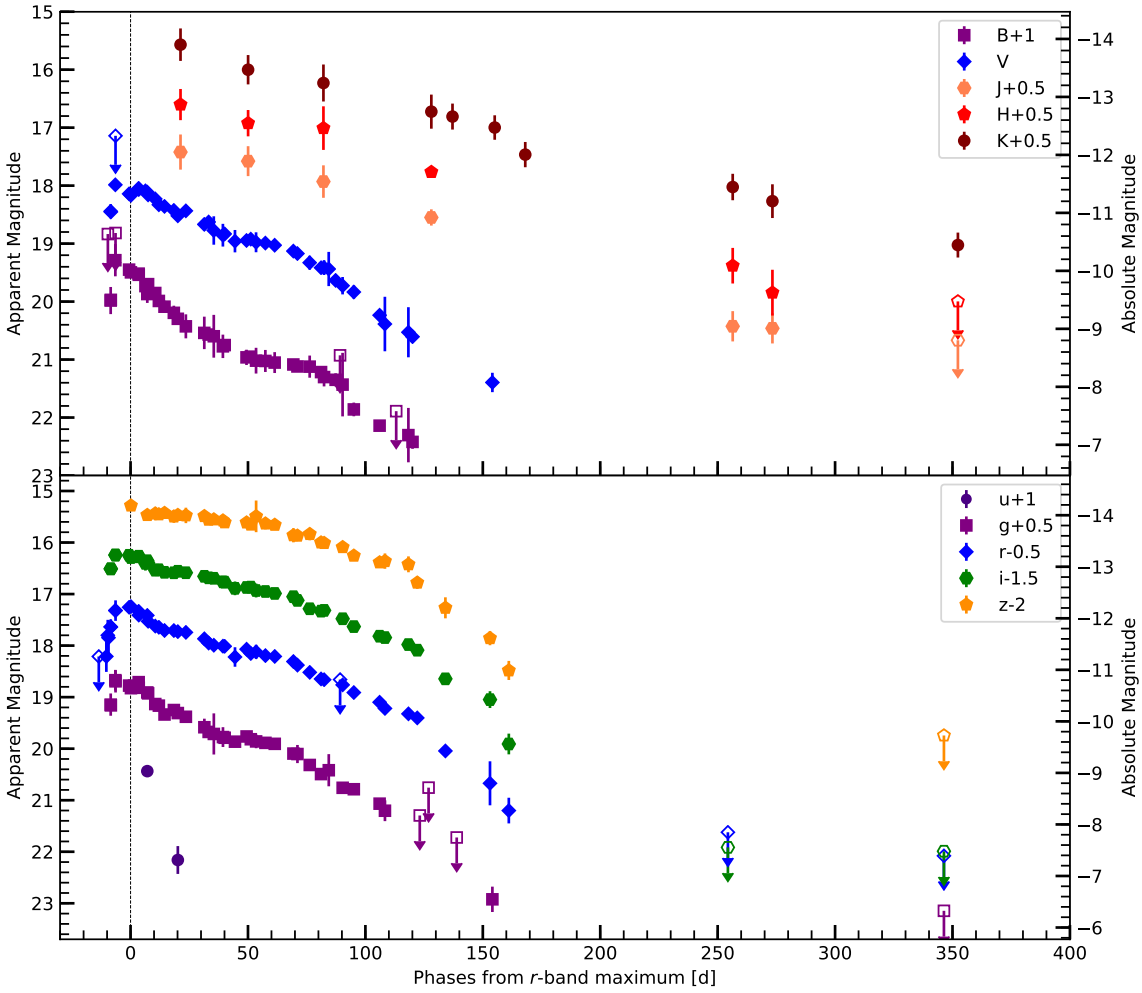

Figure 3.2: Multi-band lightcurves of the transient AT 2017be. Both the optical and NIR observations are shown in this Figure. Note that the *ugriz* magnitudes are in the AB magnitude scale, while *BV* and *NIR* magnitudes are calibrated to the Vega magnitude scale. Some points are taken from published values (as reported in Table 1 (Appendix 7)). Detection limits at early and late phases are indicated with an empty symbol with a down-arrow. The errors for most data points are smaller than the marked symbols.

Table 3.3: Decline rates in mag/100d for the lightcurves.

Filter	γ_1 (mag/100d)	γ_2 (mag/100d)	γ_3 (mag/100d)
B	3.22 ± 0.04	0.61 ± 0.06	2.80 ± 0.07
V	1.90 ± 0.03	0.74 ± 0.05	2.84 ± 0.05
g	2.67 ± 0.03	0.40 ± 0.04	2.77 ± 0.07
r	1.81 ± 0.02	0.60 ± 0.04	2.29 ± 0.03
i	1.18 ± 0.02	0.89 ± 0.03	2.12 ± 0.03
z	0.54 ± 0.03	0.61 ± 0.03	2.31 ± 0.04
J	–	0.84 ± 0.14	1.35 ± 0.28
H	–	0.66 ± 0.14	1.64 ± 0.27
K	–	1.08 ± 0.15	1.31 ± 0.12

In order to further study the observational properties of AT 2017be, we compared it with other well-studied ILRTs. These ILRTs show similar observational features with AT 2017be, and they are likely regulated by the same physical mechanism. The basic parameters of them are reported as follows: For SN 2008S, we adopted a distance modulus $\mu = 28.78 \pm 0.08$ mag, a Galactic reddening $E(B-V)_{\rm Gal} = 0.36$ mag and a host galaxy reddening $E(B-V)_{\rm host} = 0.32$ mag (Botticella et al. 2009). For NGC 300 OT2008-1, we adopted a distance modulus of $\mu = 26.37 \pm 0.14$ mag (e.g., Bono et al. 2010; Tully et al. 2013; Bhardwaj et al. 2016, averaging several values available in the literature with Cepheid estimations), a Galactic reddening $E(B-V)_{\rm Gal} = 0.01$ mag (Schlafly & Finkbeiner 2011) and a host galaxy reddening $E(B-V)_{\rm host} = 0.25$ mag (Na I D measurement), which agree with the estimates of Humphreys et al. (2011). For M85 OT2006-1, Kulkarni et al. (2007) estimated a distance modulus of $\mu = 31.33 \pm 0.14$ mag and a total reddening $E(B-V)_{\rm total} = 0.14$ mag. Here we updated the distance modulus of $\mu = 31.05 \pm 0.12$ mag (Tully et al. 2013) and used the same reddening estimate. Finally, for PTF10fqs, Kasliwal et al. (2011) adopted Galactic reddening $E(B-V)_{\rm Gal} = 0.04$ mag only. Note that a non-negligible contribution from host galaxy reddening cannot be ruled out, although the host galaxy is an S0-type, as there is evidence of low level star formation (Pastorello et al. 2007a). Here we adopt the Kasliwal et al. (2011) extinction and update the distance modulus to $\mu = 30.76 \pm 0.20$ mag (Tully et al. 2013). All the distance moduli are adopted in the framework of the same cosmology ($H_0 = 73$ km s^{-1}Mpc^{-1}, $\Omega_M = 0.27$, $\Omega_\Lambda = 0.73$).

At early phases, the transients included in our sample show a homogeneous colour evolution, which can be indicative of similar temperatures. The $B-V$ colour of AT 2017be evolves to progressively redder colours reaching 0.9 mag at about 60 days after maximum, which suggests a significant decrease in the ejecta temperature. This is confirmed through the inspection of the spectral blackbody temperature (Section 3.3). Later on, the $B-V$ index moves back to a bluer colour and remains between 0.5 mag and 0.9 mag at later phases. This evolution of AT 2017be is similar to that of NGC 300 OT2008-1. Figure 3.3 (middle) shows the $R-I/r-i$ colour evolution of the five ILRTs. The $r-i$ colour of AT 2017be has very little evolution to redder colours (reaching 0.3 mag) until about day 30, while $B-V \sim 0.7$ mag at the same epoch (see the upper panel of Figure 3.3). The $r-i$ colour of AT 2017be experiences a monotonic rise from 0.1 mag to 0.5 mag during the entire follow-up campaign. We note that a significant dispersion is observed in the colour evolution of AT 2017be in the data presented by (Adams et al. 2018, see their figure 1), while our data define a clearer colour evolution. However, the maximum colour of ~ 0.5 mag in our $r-i$ colour curve is in agreement with their measurement. A comparison at later phases is more difficult due to the larger dispersion in the Adams et al. (2018) data. The $J-K$ colour curves for our ILRT sample are shown in Figure 3.3 (lower panel). We note that AT 2017be shows a NIR colour minimum of 1.5 mag at the phase of around 50 days, then it becomes progressively redder with time, reaching 2.2 mag. The overall trend with $J-K$ colours becoming redder with time seems to be a common property for all ILRTs.

Figure 3.4 shows the absolute r-band lightcurve of AT 2017be, compared with those of the ILRTs mentioned above. AT 2017be reached an absolute peak magnitude of $M_r = -11.98 \pm 0.09$ mag as measured using a 3rd-order polynomial fit to the lightcurve. A multi-band absolute lightcurve of AT 2017be was also shown in (Adams et al. 2018, see their Figure 15). Their measurement of the Sloan r-band peak is around -11.4 mag. This difference of over half a magnitude is mainly due to different adopted distances and (more marginally) to the different extinction estimates. The Adams et al. apparent magnitude lightcurves are in good agreement with our data. The above value is intermediate between those of luminous novae and classical CC SNe (i.e., $-10 > M_V > -15$ mag), and

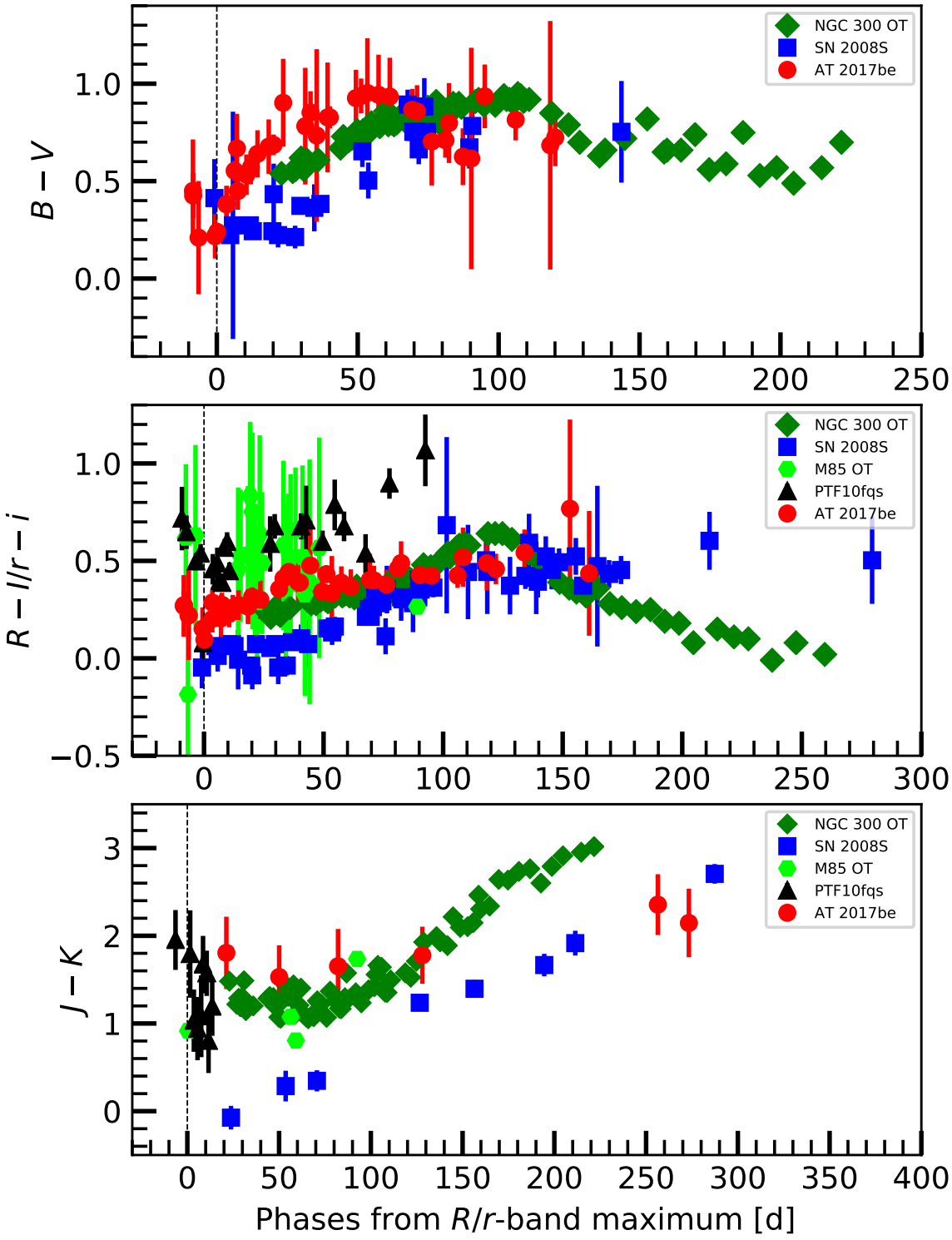

Figure 3.3: Comparison of $B-V$, $R-I/r-i$ and $J-K$ colour curves of AT 2017be, SN 2008S, NGC 300 OT2008-1, M85 OT2006-1 and PTF10fqs. The data of SN 2008S are from Botticella et al. (2009), those of NGC 300 OT2008-1, M85 OT2006-1, PTF10fqs are from Humphreys et al. (2011), Kulkarni et al. (2007) and Kasliwal et al. (2011), respectively. The adopted reddening values are given in the main text. The $r-i$ colours shown here are obtained from Sloan magnitudes, conveted to the Vega system. The errors on $J-K$ colour were not included in the NIR dataset for NGC 300 OT2008-1.

is consistent with that expected for an ILOT (Smith et al. 2011; Tartaglia et al. 2016). The r-band lightcurve of AT 2017be has an asymmetric lightcurve peak, with a rapid rise but a modest post-peak decline, with the lightcurve settling onto a sort of plateau. AT 2017be is fainter than SN 2008S ($M_R = -14.24 \pm 0.03$ mag) and NGC 300 OT2008-1 ($M_R = -13.23 \pm 0.05$ mag), and nearly the same luminosity as M85 OT2006-1 ($M_R = -12.60 \pm 0.50$ mag) and PTF10fqs (absolute peak magnitude $M_R = -11.55 \pm 0.30$ mag; see the upper panel of Figure 3.4). Figure 3.4 (lower panel) shows the R/r-band absolute magnitude evolution of AT 2017be and PTF10fqs in the ABmag scale (Oke & Gunn 1983). The comparison shows the striking similarity in the early lightcurve evolution for these two ILRTs, which reach approximately the same maximum magnitudes.

3.2.4 Quasi-bolometric Lightcurve

Quasi-bolometric luminosities are obtained by converting the available magnitudes to flux densities, then correcting these fluxes with the adopted extinction coefficients, and finally integrating the SED over the entire wavelength range. We assume that the flux at the integration limits (at effective wavelengths shorter than the u band and longer than the K band) is zero. At some epochs, in a given filter, in which the photometric data are not available, we estimate the flux contribution of the missing bands by interpolating between epochs with available data or through an extrapolation from the earlier or later available epochs, assuming a constant colour evolution. We calculated the pseudo-bolometric lightcurve of AT 2017be and other ILRTs using only the *BVRIgri* bands. This allows for meaningful comparisons among ILOTs, for which often u, z or *NIR* bands were not available. In the case of AT 2017be we also computed a more complete quasi-bolometric lightcurve including the contribution to the total luminosity of the u and the NIR (z, J, H, K) bands. The resulting quasi-bolometric lightcurves are shown in Figure 3.5.

The quasi-bolometric lightcurve peak of AT 2017be is $\sim 8 \times 10^{39}$ erg s^{-1}, including the optical bands only; this value increases to $\sim 1.8 \times 10^{40}$ erg s^{-1} including also the u and NIR bands contributions ($\sim 55.6\%$). The peak luminosities of SN 2008S, NGC 300 OT2008-1, M85 OT2006-1, and PTF10fqs (considering optical bands only) are about 6×10^{40} erg s^{-1}, 1.8×10^{40} erg s^{-1}, 10^{40} erg s^{-1} and 6×10^{39} erg s^{-1} respectively. The lightcurve shape of AT 2017be is different from those of SN 2008S and NGC 300 OT2008-1, having a somewhat narrower peak and a post-peak plateau, and is very similar to those of M85 OT2006-1 and PTF10fqs, in overall shape, peak luminosity and post-peak lightcurve flattening. The main difference is in the duration of the plateau. While the post-plateau decline in AT 2017be begins about 70 days after maximum light, and at a similar phase in PTF10fqs, for M85 OT2006-1 the plateau only lasts for around 30–35 days. The post-plateau decline of AT 2017be is very rapid, with a rate that is faster than the decay of ^{56}Co (see Figure 3.5). Unfortunately, we could not follow the object to observe an optical flattening onto the radioactive tail, because the transient disappeared behind the sun. However, we observed again the field a few months later, when it became visible again before the sunrise, and noticed that AT 2017be was no longer visible in the optical bands, while it was clearly detected in the NIR bands.

As we have a limited lightcurve information for AT 2017be at late phases, we cannot securely estimate its bolometric light curve, which is essential to constrain the ejected ^{56}Ni mass. In addition, AT 2017be has no mid-IR monitoring, and we know that similar objects like SN 2008S and NGC 300 OT2008-1 have a non-negligible mid-IR contribution at late phases, with the peak of their SEDs shifting from the optical to the mid-IR (Kochanek 2011). Given that SN 2008S and

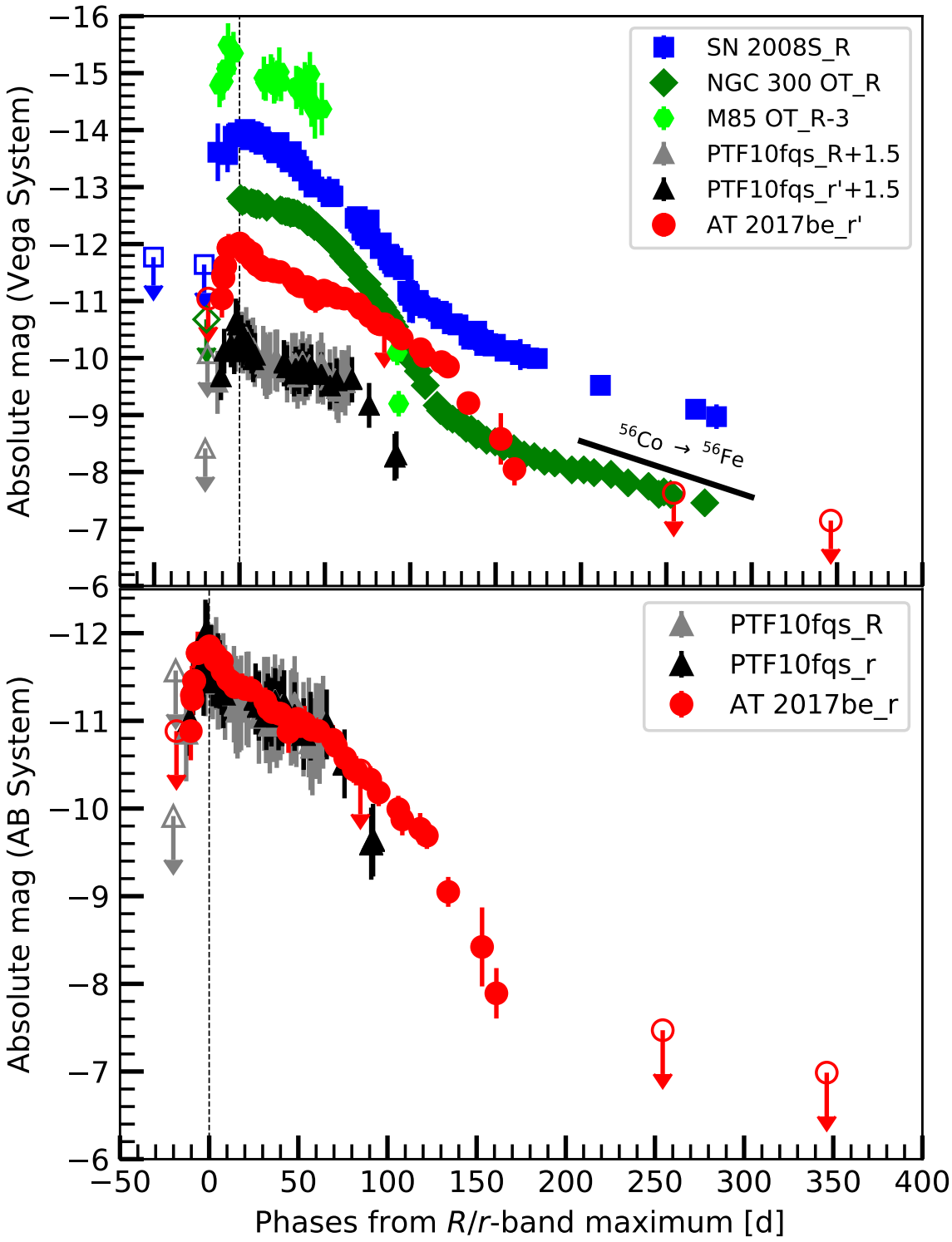

Figure 3.4: *R*/*r* band absolute lightcurves of AT 2017be and other ILRTs, including SN 2008S (Botticella et al. 2009), NGC 300 OT2008-1 (Humphreys et al. 2011), M85 OT2006-1 (Kulkarni et al. 2007) and PTF10fqs (Kasliwal et al. 2011). In order to improve visualisation, arbitrary shifts are applied to M85 OT2006-1 and PTF10fqs as per the legend. We adopt the time of the *R*/*r* band lightcurve peaks as our reference epoch.

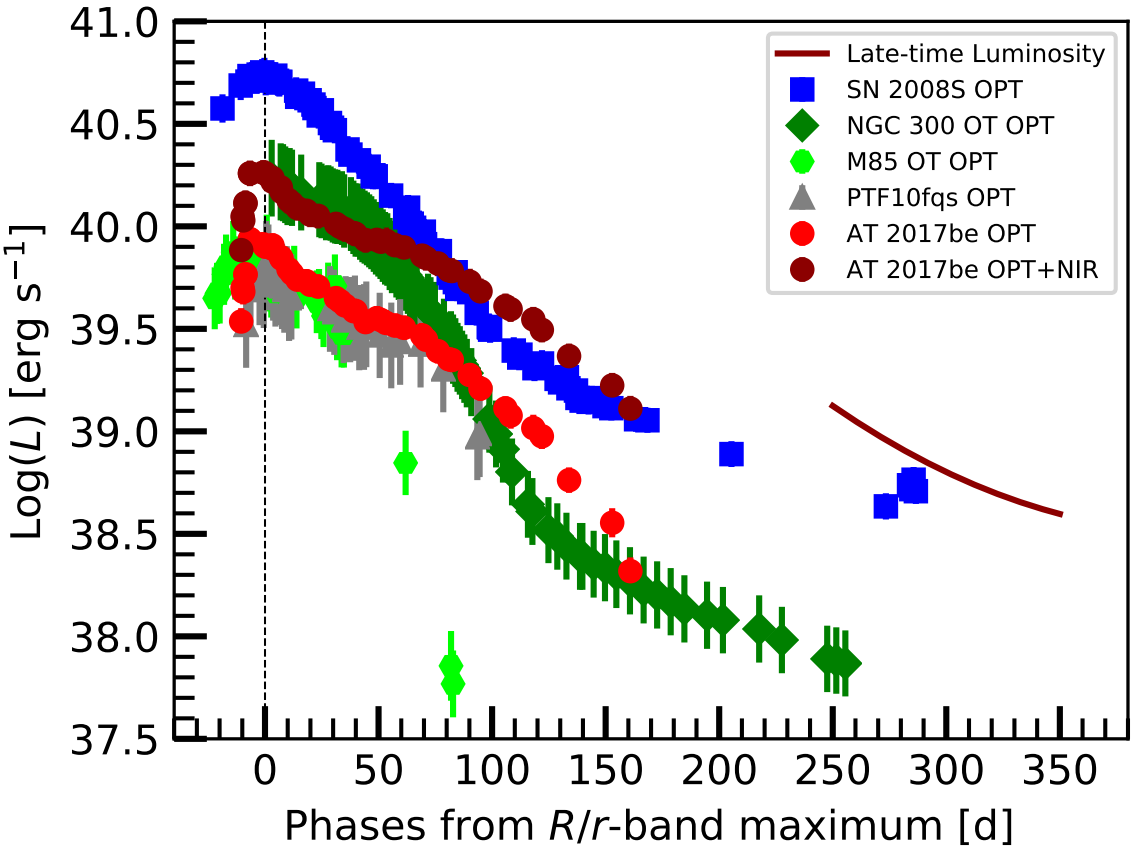

Figure 3.5: Quasi-bolometric lightcurves of AT 2017be, SN 2008S (Botticella et al. 2009), NGC 300 OT2008-1 (Humphreys et al. 2011), M85 OT2006-1 (Kulkarni et al. 2007)and PTF10fqs (Kasliwal et al. 2011). For the purpose of comparison, only the Johnson/Cousins *BVRI*and SDSS *gri* filters were used. Note that for AT 2017be we also computed the *u*-to-*K* band lightcurve (shown with dark red dots). Errors shown account for the uncertainties on photometric measurements, distance and reddening estimates, and SED fitting.

NGC 300 OT2008-1 have relatively complete datasets spanning from the optical to mid-IR and extended to late phases, we use their SEDs to estimate the relative flux contribution of the different wavelength regions. Assuming that the SED evolution of AT 2017be is similar to that of the two template objects, we can in this way constrain the contribution of the missing bands and estimate a reliable bolometric light curve also for the former object.

We first used SN 2008S as template for AT 2017be, in view of the similar $J - K$ colour evolution [15]. We estimated the NIR luminosity of SN 2008S from its light curve, and adopted its model bolometric lightcurve obtained by Kochanek (2011) through the relation: $L_{bol} = L_0 \exp(-t/t_0) + L_1$, with $L_0 \simeq 10^{7.3} L_\odot$, $L_1 \simeq 10^{5.8} L_\odot$ and $t_0 \simeq 48$ days. Hence we computed the L_{NIR}/L_{bol} ratio for SN 2008S to be ≈ 0.31 - 0.36, from ~ 245 to 345 days after maximum. Finally, we obtained the bolometric light curve of AT 2017be using its L_{NIR} values obtained from the light curve at late phases assuming the same L_{NIR}/L_{bol} ratio as SN 2008S. The resulting bolometric lightcurve for AT 2017be at late phases is also shown in Figure 3.5 with a solid line.

Assuming that the energy from γ rays and positrons is fully trapped and thermalised, we constrain the ^{56}Ni mass deposited by AT 2017be by comparing its late-time bolometric luminosity with that of SN 1987A at the same epochs ($\sim$ 260-360 days after their explosion). The luminosity of SN 1987A was calculated by Whitelock et al. (1988), including the U- to M-band contribution (we will assume that the contribution to the total luminosity from the regions outside this range is negligible). The ^{56}Ni mass systhesized by AT 2017be ($\sim 7 \times 10^{-4}$ M$_\odot$) is obtained through the relation:

$$M(^{56}Ni)_{AT\ 2017be} \ = \ 0.073 M_\odot \times (\frac{L_{AT\ 2017be}(t)}{L_{SN\ 1987A}(t)}). \tag{3.1}$$

As a further test, we can use the SED of NGC 300 OT2008-1 as a template, adopting the same algorithm as SN 2008S, and we find M(^{56}Ni) $\sim 9 \times 10^{-4}$ M$_\odot$. Averaging the above estimates, we infer M(^{56}Ni) = 8 ($\pm$ 1) $\times 10^{-4}$ M$_\odot$ for AT 2017be. However, we remark that additional contributions to the late bolometric lightcurve from interaction between ejecta and CSM, or even IR echoes cannot be definitely ruled out (see the further discussion in Section 5.4). In that case, the above M(^{56}Ni) value should be regarded as an upper limit.

Integrating the bolometric lightcurve over the entire observational campaign ($\sim$ 370 days) of AT 2017be, we can estimate a reliable value for the total radiated energy. We have a good early time coverage in the optical and NIR bands at early phases. Hence, we can estimate the contribution of the missing bands using again both SN 2008S and NGC 300 OT2008-1 templates. In the two cases, we obtain $\sim 1.19 \times 10^{47}$ erg and $\sim 1.31 \times 10^{47}$ erg as energy radiated by AT 2017be, with an average of 1.25 ($\pm$ 0.06) $\times 10^{47}$ erg.

Although ECSNe are expected to arise from stars in a very narrow range of masses, and the mass of ^{56}Ni only marginally affect the observed luminosity (in particular, at early phases), the quasi-bolometric lightcurves of ILRTs are expected to be reasonably similar (e.g., Moriya & Eldridge 2016; Pumo et al. 2009; Kitaura et al. 2006). Indeed, as shown in Figure 3.5, the lightcurves of all our ILRTs are indeed broadly similar. The differences between these events can potentially be explained

[15] A caveat that such similarity might not be true up to 50 days after maximum as observed in the $J - K$ colour evolution in the bottom panel of Figure 3.3

by a number of factors, including the mass-loss history (hence the geometric distribution and density profile of the CSM), the H recombination timescale, and the influence of ^{56}Ni distribution inside the ejecta.

3.2.5 Spectral energy distribution analysis

The temporal evolution of the SED of AT 2017be is shown in Figure 3.6. We did not collect NIR observations until about three weeks after maximum, so our SED at early epochs is based solely on optical data. These early epochs are well represented by a single blackbody, which is fit to the optical data, whose temperature declines rapidly from $\sim$ 6500 K to $\sim$ 5500 K by $\sim$+20 days (see the upper panel of Figure 3.7). The first optical+NIR SED is obtained at +21 days from maximum, which reveals a notable NIR excess over a single black body (see inset in the upper-right corner of Figure 3.6). To investigate the nature of the NIR excess, we carried out a simultaneous two-component fit to the optical+NIR SEDs consisting of two (hot plus warm components) black-body functions. Occasionally, for some epochs fluxes for unobserved bands were estimated through an interpolation procedure. At these later epochs (after +20 days), the temperature of the hot component slowly declines from about 5500 K to 4300 K at about 160 days. As expected, the above temperature estimates are in agreement with those obtained from the blackbody fit to the continuum of the spectra obtained at the similar epochs (see Section 3.3.1, and Figure 3.7, upper panel). Furthermore, the derived temperature is consistent with the hydrogen recombination temperature. The temperature of the warm blackbody is apparently constant over the 3 months (from $\sim$ 20 days to 150 days) of monitoring, within substantial errors, T = 1200 $\pm$ 200 K, indicative that this component is very likely due to thermal emission from surrounding dust.

From luminosity and temperature we derive the radius of AT 2017be using the Stefan-Boltzmann law. The evolution of the wavelength-integrated luminosity of the hot component is shown in the middle panel of Figure 3.7. It decreases from $\sim 1.7\times10^{40}$ erg s^{-1} at $-$6.5 days to $\sim 4.5\times10^{38}$ erg s^{-1} at about three months from maximum. The radius of the hot component (see the lower panel of Figure 3.7) slowly increases from 1.1×10^{14} cm near maximum light to 1.3×10^{14} cm at about one month after peak luminosity (see lower panel in Figure 3.7). After this until about four months past-maximum the radius decreases from about 1.4×10^{14} cm to 1.2×10^{14} cm, before dropping more rapidly to about 4×10^{13}cm at 161 days. The time evolution of the luminosity as well as the blackbody radius and hot temperature are reported in Table 3.4, and shown in Figure 3.7.

NIR excess emission has been observed in several SNe and is often attributed to the thermal emission from warm dust heated by the SN. On the other hand, Kochanek (2011) investigated the evolving SEDs of SN 2008S and NGC 300 OT2008-1, extending to mid-IR wavelengths, and found that the transient SEDs are largely determined by the dust reformation beyond the shock front.

Assuming the near-infrared emission is indeed due to dust, we fit a modified black-body function (Hildebrand 1983) to the optical+NIR SEDs. We fit for the dust temperature, $T_{\rm d}$, and dust mass, $M_{\rm d}$ adopting the formalism as described in (Gall et al. 2017), which assumes that the dust mass absorption coefficient, $\kappa_{\rm abs}(\nu, a)$ (in units of [cm^2 g^{-1}]) behaves as a λ^{-x} power law in the wavelength range 0.9–2.5 μm, with x as the power-law slope. Here we perform fits for either x = 1.2 or 1.5 and adopt $\kappa_{\rm abs}(\lambda$ = 1 μm) = 1.0×10^4 cm^2 g^{-1} (appropriate for carbonaceous dust, e.g. Rouleau & Martin (1991)).

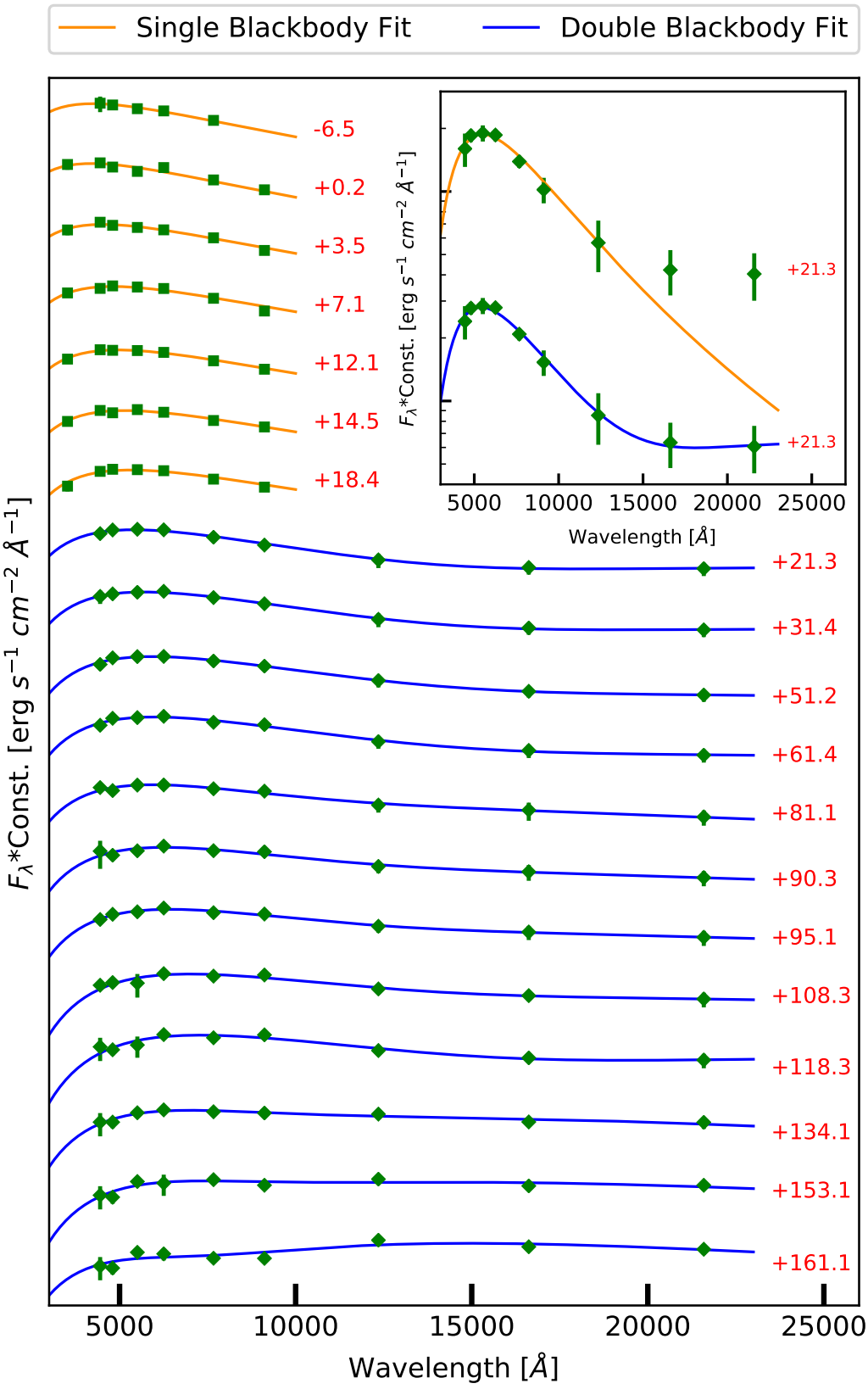

Figure 3.6: The observed SED evolution of AT 2017be. The fluxes have been corrected for reddening. We adopt the value of MJD = 57769.8 ± 0.1 (Sloan *r*-band maximum) as our reference epoch.

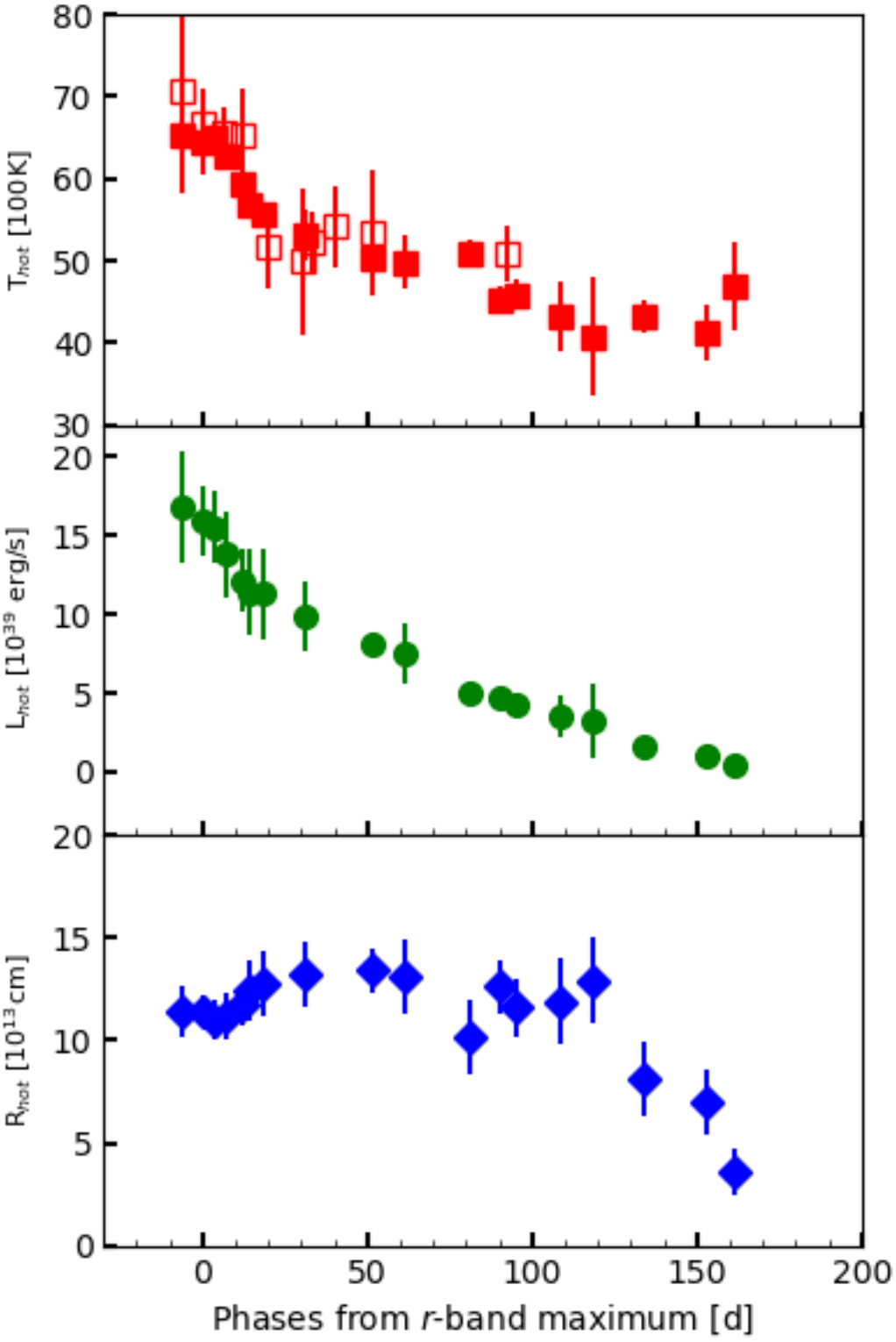

Figure 3.7: Temporal evolution of parameters determined from the SED of AT 2017be. In the upper panel, empty squares indicate the temperature evolution deduced from the blackbody fit to the spectral continuum. The uncertainty in the inferred blackbody temperature has been estimated based on the uncertainties in flux in each bandpass. We adopt MJD = 57769.8 ± 0.1 (Sloan *r*-band maximum) as our reference epoch.

The results for the temperature and radius of the black body function for the supernova are identical to the results obtained from the pure hot and warm black body fits. However, here we obtain a slightly lower temperature ($\sim$ 1000 K) for the dust component which also shows no evolution over time. The amount of dust decreases over time from a few times 10^{-5} $M_{\odot}$ to a few times 10^{-6} $M_{\odot}$ in the case of carbonaceous dust. However, the low dust temperatures do not rule out other dust species such as silicates. In the case of silicate dust the estimate of the dust mass would be about an order of magnitude larger.

Unfortunately, in the absence of longer wavelength observations to better constrain the dust component we can only derive an upper limit to the dust temperature and a lower limit on the dust mass. From the analysis of the SED of AT 2017be SED, we infer that pre-exisisting dust from the progenitor likely survived in the circumstellar environment, and was probably heated by the SN. This dust has to be distributed far from the progenitor and such that it does not contribute to additional extinction along the line of sight towards the SN (see the extinction discussion in Section 3.1). This implies that either the dust mass is only slightly above our lower limit, or that the dust distribution of AT 2017be may be similar to that of V838 Mon (e.g., Tylenda 2004; Tylenda & Kamiński 2012), in form of clumpy, complex structure.

3.3 Spectroscopy

Our spectroscopic follow-up campaign started on 2017 January 10, and lasted until 2017 April 18, hence covering almost 100 days. Spectroscopic observations were performed using the 2-m Faulkes North Telescope of LCO with FLOYDS, the 2.56-m NOT with ALFOSC and the 10.4-m Gran Telescopio Canarias (GTC) with OSIRIS. Details on the instrumental configurations and information on our spectra of AT 2017be are reported in Table 4.3.

The spectra of AT 2017be were reduced using standard tasks in IRAF[16], following the standard steps as detailed in Section 2.2 of Chapter 2. In order to properly analyse our spectra of AT 2017be, we applied a correction to account for the line-of-sight reddening contribution (see Section 3.1), and a Doppler shift to place the spectra in the host galaxy rest frame. The spectral resolutions, reported in Table 4.3, were obtained by measuring the average widths of night sky lines.

3.3.1 Spectral evolution

The spectra of AT 2017be show little evolution over the entire monitoring period (from 7 days to almost 100 days after the explosion, see Figure 3.8). All spectra consist of a nearly featureless continuum with strong Balmer emission lines. The [Ca II] doublet at 7291,7324 Å and the Ca II NIR triplet are also detected. The P-Cygni absorption troughs, which usually characterise SN explosions or the presence of CSM material if narrow, are observed in our highest resolution GTC (R2500R) spectra. The Hα line possibly shows a multicomponent profile, although in most spectra of AT 2017be the line is well reproduced by fitting a single Lorentzian profile (see Section 3.3.3).

[16]NOT+ALFOSC spectra were reduced using a dedicated graphical user interface (ALFOSC GUI) developed by E. Cappellaro (http://sngroup.oapd.inaf.it/foscgui.html).

Table 3.4: Properties of the hot blackbody component fit to the uBVgrizJHK bands of AT 2017be. The warm component does not show a significant evolution within its uncertainties. Uncertainties are given in parentheses.

Date	MJD	Phase[a] (d)	Luminosity (hot) (10^{39}erg s^{-1})	Temperature (hot) (K)	Radius (hot) (10^{13} cm)
20170110[b]	57763.3	−6.5	16.8 (4.0)	6530 (190)	11.4 (1.0)
20170116[b]	57770.0	+0.2	15.9 (2.0)	6430 (390)	11.4 (1.0)
20170120[b]	57773.3	+3.5	15.5 (2.0)	6510 (170)	11.0 (1.0)
20170123[b]	57777.0	+7.1	13.8 (3.0)	6280 (170)	11.2 (1.0)
20170128[b]	57781.9	+12.1	12.1 (2.0)	5930 (70)	11.7 (1.0)
20170131[b]	57784.3	+14.5	11.4 (3.0)	5680 (130)	12.4 (2.0)
20170204[b]	57788.3	+18.4	11.3 (3.0)	5580 (140)	12.8 (2.0)
20170207	57791.1	+21.3	10.9 (3.0)	5540 (220)	12.8 (1.0)
20170217	57801.2	+31.4	9.9 (2.0)	5310 (300)	13.2 (2.0)
20170309	57821.0	+51.2	8.1 (1.0)	5020 (100)	13.4 (1.0)
20170319	57831.2	+61.4	7.6 (2.0)	4990 (320)	13.1 (2.0)
20170407	57850.9	+81.1	5.0 (1.0)	5100 (170)	10.2 (2.0)
20170417	57860.1	+90.3	4.8 (1.0)	4530 (160)	12.6 (1.0)
20170421	57864.9	+95.1	4.3 (1.0)	4590 (200)	11.6 (1.0)
20170505	57878.1	+108.3	3.5 (1.0)	4320 (420)	11.9 (2.0)
20170515	57888.1	+118.3	3.3 (2.0)	4070 (720)	12.9 (2.0)
20170530	57903.9	+134.1	1.6 (0.3)	4310 (200)	8.1 (2.0)
20170618	57922.9	+153.1	1.0 (0.3)	4130 (330)	7.0 (2.0)
20170626	57930.9	+161.1	0.4 (0.2)	4690 (540)	3.6 (1.0)

[a] Phases are relative to *r*-band maximum lightcurve, on MJD = 57769.8 ± 0.1.
[b] Data are obtained by fitting a single blackbody function, as we have no contemporaneous NIR observations.

Table 3.5: Log of the spectroscopic observations of AT 2017be.

Date		Phase[a] (d)	Telescope+Instrument	Grism	Spectral range (Å)	Resolution (Å)	Exp. time (s)
20170110	57763.4	−6.4	LCO+FLOYDS	Channels red+blue	3600-10000	15.5	3600
20170117	57770.0	+0.2	NOT+ALFOSC	gm4	3400-9700	15	3600
20170123	57776.2	+6.4	NOT+ALFOSC	gm4	3390-9650	18	3512
20170128	57781.9	+12.1	NOT+ALFOSC	gm4	3500-9590	15	3600
20170205	57790.0	+20.1	NOT+ALFOSC	gm4	3400-9650	18	3600
20170216	57800.0	+30.2	GTC+OSIRIS	R2500R	5580-7680	3.5	1800
20170219	57803.0	+33.2	NOT+ALFOSC	gm4	3400-9700	14	3600
20170225	57809.9	+40.1	NOT+ALFOSC	gm4	3700-9650	19	3600
20170308	57821.0	+51.2	NOT+ALFOSC	gm4	3400-9650	18	3600
20170418	57861.9	+92.1	GTC+OSIRIS	R1000R	5100-10400	8	2×900

[a] Phases are relative to *r*-band maximum light, on MJD = 57769.8 ± 0.1.

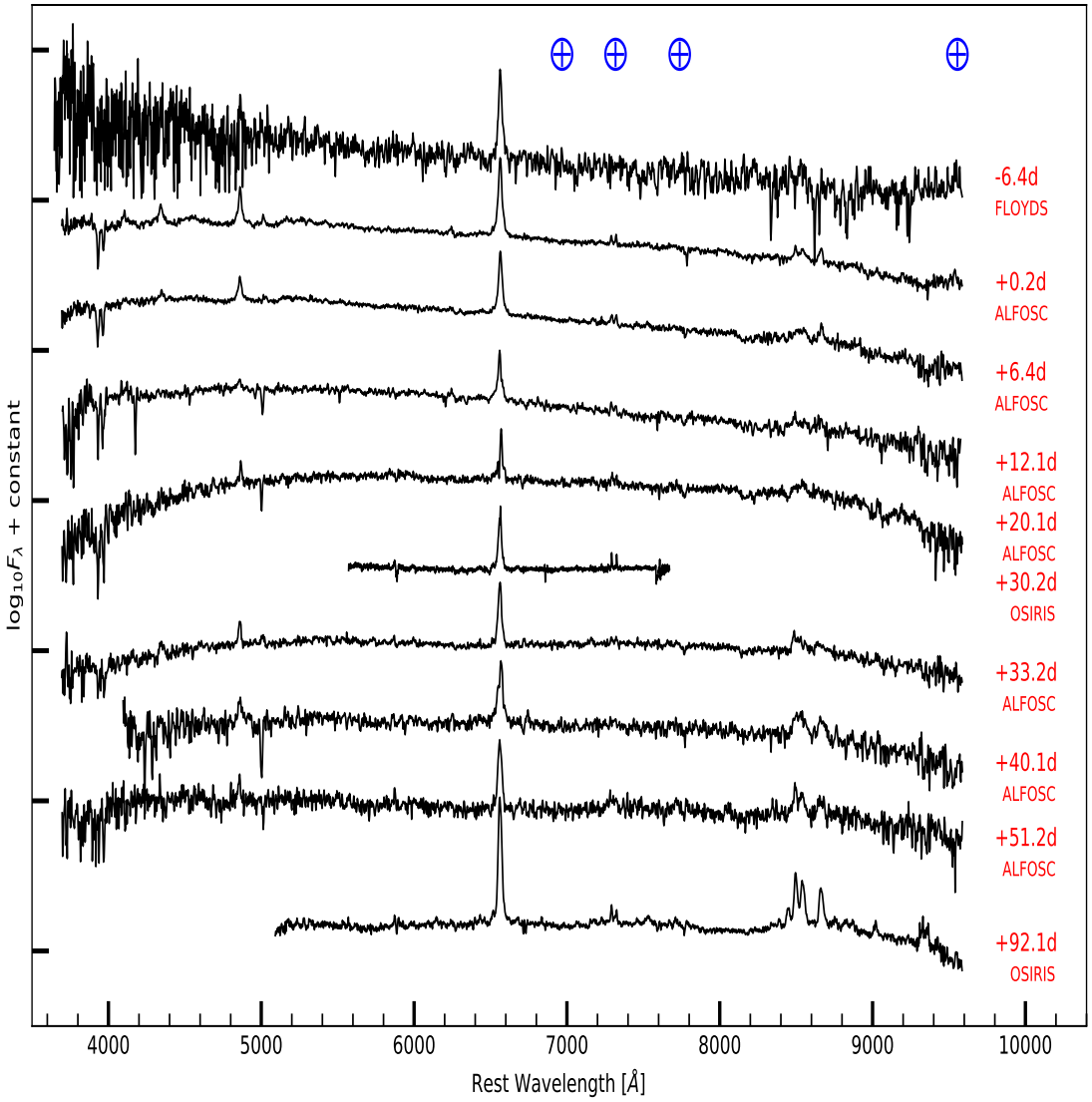

Figure 3.8: Spectroscopic evolution of AT 2017be from 2017 January 10 (MJD = 57763.38) to April 18 (MJD = 57861.93). The epochs reported to the right of each spectrum are relative to the Sloan r band maximum. The positions of the strongest telluric absorption bands are marked with the $\oplus$ symbol; all spectra have been redshift-corrected.

The spectra are characterised by a significant contribution of the continuum to the total flux, hence we estimated the temperature of the photosphere through a black-body fit. The black-body temperatures from spectra and imaging are consistent within the errors (see the upper panel of Figure 3.7). We note that this temperature evolution is consistent with that of hydrogen recombination in normal Type II CC SNe (e.g., Filippenko 1997). The spectral blackbody temperature values are reported in Table 4.4 and are plotted in Figure 3.7 (upper panel).

3.3.2 Line identification

The line identification was performed on two high S/N spectra: an early epoch (+0.2 days) ALFOSC spectrum, and a late-time (92.1 days) GTC spectrum. The identification is shown in Figure 3.9. Hα and other Balmer series emission lines are clearly present. Paschen series lines are also visible at the reddest wavelengths in our highest S/N spectra. Additionally, weak lines of Fe II, Na I D, O I , Ca II H&K and the Ca II NIR triplet are identified at their rest wavelengths. A possible Fe II line is visible from first spectrum up to three weeks after maximum light (see the question mark in the upper panel of Figure 3.9).

We also identify prominent [Ca II] doublet lines at $\lambda\lambda$7291,7324, which are visible in all spectra of AT 2017be (see Figure 3.8), and which are seen in all the ILRTs. In Figure 3.10, we compare spectra of AT 2017be and other four ILRTs at similar phases (marked with red labels in the figure). The striking spectral match of AT 2017be with the SN 2008S-like family is evident not only from the detection of the [Ca II] doublet (see right panel in Figure 3.10), but also from the presence of other shared spectral features (both in absorption and emission), providing further observational evidence to support our classification of AT 2017be as an ILRT.

3.3.3 Evolution of the line profiles

In order to search for signatures of ejecta-CSM interaction we analysed the evolution of the line profiles, along with the velocity and the luminosity of Hα at different phases. Multiple line components in spectra are normally associated with interaction between supernova ejecta and circumstellar wind, with the different components resulting from multiple emitting gas regions (Turatto et al. 1993). The classical interpretation is that the narrow component of Hα is emission from unshocked CSM, while broader line components are signatures of shocked material and/or freely-expanding SN ejecta.

- **Hα line**
  The profile of Hα is characterized by a narrow component which dominates in all our spectra of AT 2017be. Its profile is usually well reproduced by a simple Lorentzian fit. We first fitted the Hα profile with a single Lorentzian function using standard IRAF tasks, and measured the full-width-at-half-maximum (FWHM) and flux values. In order to account for the instrumental limitations, we corrected the FWHM values for the spectral resolution ($width = \sqrt{FHWM^2 - resolution^2}$), and finally we computed the Hα FWHM velocities (v_{FWHM}). The resulting velocities and luminosities are reported in Table 4.4, and the Hα luminosity evolution is plotted in Figure 3.11.

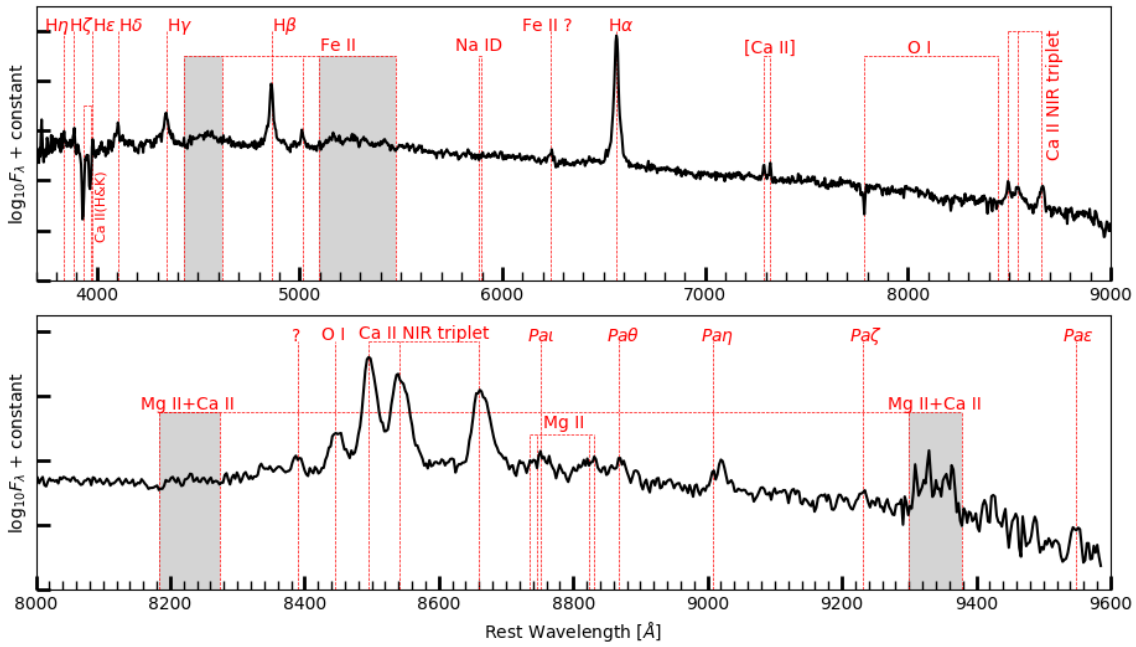

Figure 3.9: Upper panel: Identification of the strongest emission lines in the early-time (~1 day) NOT+ALFOSC spectrum of AT 2017be. Lower panel: Identification of the most prominent emission lines in the late-time (~90 days) GTC+OSIRIS spectrum of AT 2017be. Both the spectra have been redshift-corrected.

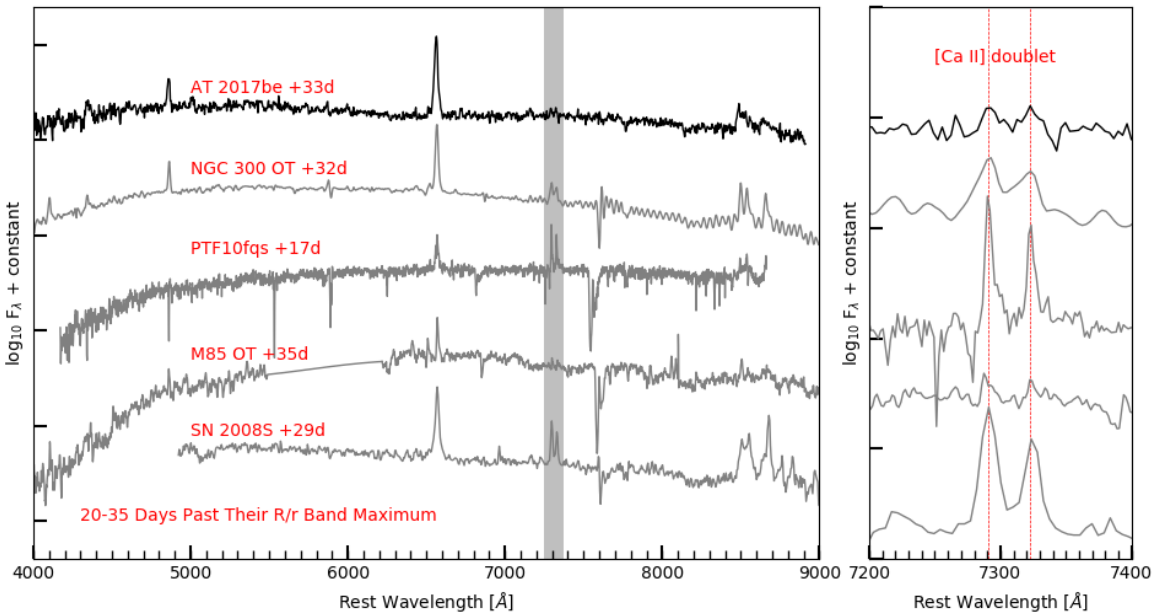

Figure 3.10: Comparison of spectra of those of ILRTs obtained around the same epoch after their R/r band maximum. All the spectra are taken from Cai et al. in prep, Kasliwal et al. (2011), Kulkarni et al. (2007) and Botticella et al. (2009). The [Ca II] doublet lines are marked in the grey shaded area in the left panel. The right panel shows the detailed profiles. The spectra are all redshift-corrected and extinction-corrected.

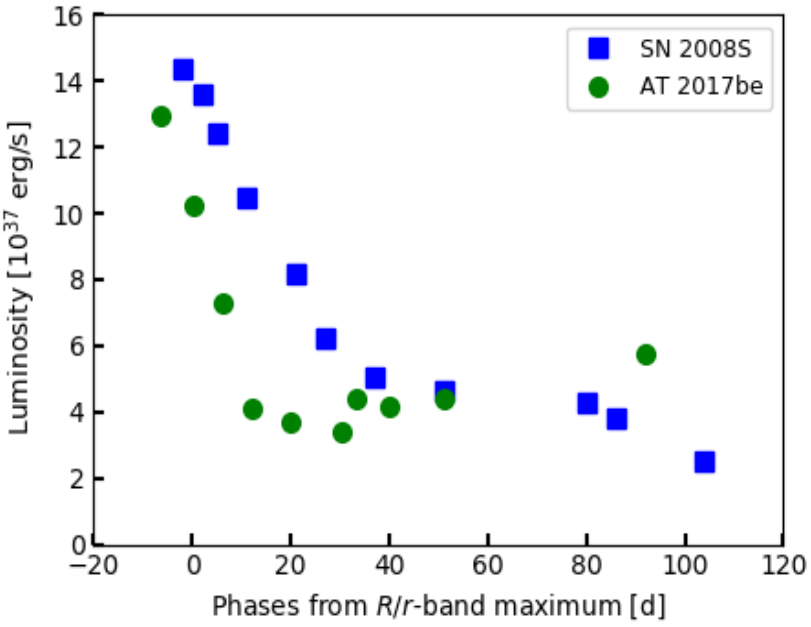

Figure 3.11: Comparison between Hα luminosity evolution in AT 2017be and SN 2008S. Values for SN 2008S are taken from the literature (Botticella et al. 2009, see their Table 10). We conservatively estimate the uncertainties to be around 20 percent.

The velocity ranges from $v_{\rm FWHM} \sim 300$ to ~ 850 km s^{-1} in a rather erratic way. However, we should note that in most spectra the FWHM of Hα is close to the instrumental resolution, hence these values are unreliable for determining the velocity of the emitting H-rich material. From our highest quality and best resolution GTC+OSIRIS spectra, we infer $v_{\rm FWHM} \sim 820$ km s^{-1} and $v_{\rm FWHM} \sim 730$ km s^{-1} at phases +30.2 and +92.1 days respectively, which we regard as our most reliable values for the line velocity. During the first ~ 30 days, the Hα luminosity decreases from $\sim 13{\times}10^{37}$erg s^{-1} to $\sim 3{\times}10^{37}$erg s^{-1}. Later on, it settles onto slightly higher values, around 4-6$\times10^{37}$erg s^{-1}. It is unclear if this apparent Hα luminosity increase at later phases is real or is rather due to systematic errors (such as slit losses). However, as the Hα luminosity increases by nearly a factor of two, we tentatively attribute it to a progressive strengthening of the interaction of ejecta with CSM.

Unfortunately, the modest resolution of our spectra is insufficient to reveal very narrow components in the Hα profile. The only exception is the spectrum at +30.2 days, that can resolve features down to a limit of 160 km s^{-1}. This spectrum will be discussed separately later on (Section 3.3.4). The evolution of the Hα profile during the three months of spectral coverage is shown in Figure 3.12 (left panel). We note that there is no significant change in the wavelength position of the Hα emission peak.

- **Ca II lines**
  The evolution of the Ca II NIR triplet line profiles in the wavelength window 8300-8800 Å for AT 2017be is shown in Figure 3.12 (right panel). In all spectra we mark the individual positions of Ca II triplet lines at 8498 Å, 8542 Å, and 8662 Å. These are produced through radiative de-excitation from the upper $4p^2P_{1/2,3/2}$ levels to the lower metastable $3d^2D_{3/2,5/2}$ levels (Mallik 1997). This triplet is a very common feature observed in the spectra of many types of transients. In our low-resolution spectra, the 8498 Å and 8542 Å members of the Ca II triplet are usually blended. In order to estimate the FWHM velocity of the Ca II lines, we considered the two spectra with the highest S/N: the NOT (phases +0.2 days) and GTC (phases +92.1 days) spectra. These spectra exhibit narrow features with velocity of 700-800 km s^{-1}, which are consistent with the values obtained for Hα. This is consistent with the Ca II triplet arising from the same region as the main Hα emission. On the other hand, the Ca II H&K absorptions are also clearly discernible in some epochs (the spectra at +0.2 days, +6.4 days, +12.1 days, +20.1 days and 33.2 days in Figure 3.8), with a velocity of ~ 180 km s^{-1} (as measured from two minima of the Ca II H&K lines).

  The [Ca II] doublet lines at 7291,7324 Å are always visible in our spectra, and appear to be slightly narrower than Hα, hence in most cases these lines are unresolved. The [Ca II] doublet is unblended in all our spectra, although the two components show different relative intensities and widths. The intensity ratio of the two [Ca II] components (λ 7291 vs. λ 7328) slightly increases from ~ 0.9 in our early spectra to ~ 1.3 in our late spectra. However, we remark that the uncertainty in the flux ratio measurements is on the order of 20 per cent.

  As in most spectra the [Ca II] lines are unresolved, we consider only the two moderate resolution GTC spectra (at phases +30.2 days and +92.1 days, respectively). Also in these spectra, however, the FWHMs of the [Ca II] doublet are close to the spectral resolution limit, therefore any velocity measurement is affected by a significant uncertainty. For the two spectra, we obtain ~ 115 km s^{-1} and ~ 250 km s^{-1} for the individual components of the doublet. The [Ca II]

doublet lines are produced in a relatively low density gas, from radiative de-excitation related to the metastable $3d^2D$ level (Chevalier & Fransson 1994). A major implication of the above analysis is that the [Ca II] and Ca II H&K lines form in a different region as the Ca II NIR triplet (and Hα). In particular, [Ca II] and Ca II H&K lines are likely forming in a slowly expanding (100-200 km s^{-1}) circumstellar shell, while the bulk of the Ca II NIR triplet and Hα emission comes from faster-moving ejected material.

3.3.4 Constraining the CSM using the +30 days spectrum

The GTC+OSIRIS spectrum at phase +30.2 days (resolution $v_{\rm FWHM} \approx 160$ km s^{-1}) reveals that the Hα line exhibits a more complex profile than what appears from the inspection of other lower resolution spectra shown in Figure 3.12. Note, however, that some bumps likely due to blends of Fe II lines (see Figure 3.13), are visible slightly above the flux level of the continuum. Most of these features were observed in SN 2008S (Botticella et al. 2009, see their Figure 9) and classified as Fe II lines (multiplets 40, 74, 92). Hence, they are not weak Hα components. In particular the bump peaking (in the Doppler-corrected spectrum) at 6518 Å (v = 2100 km s^{-1}) is inconsistent with a blue-shifted tail of Hα, whose profile is, in fact, well-fitted by a single Lorentzian emission component with $v_{\rm FWHM}$ $\sim$ 820 km s^{-1}. Superimposed on the Lorentizian component, we note a very narrow P-Cygni feature (see Figure 3.13), which is marginally resolved, and that can be attributed to a slow-moving circumstellar shell. From the position of the narrow P-Cygni absorption, we estimate an upper limit velocity of $\sim$ 70 km s^{-1} for this H-rich shell. We note that this velocity is barely consistent with the $v_{\rm FWHM}$ that we infer for the [Ca II] doublet lines in the same spectrum. In fact, the average velocity obtained after instrumental resolution correction for the two lines of the doublet is $v_{\rm FWHM} \sim 115 \pm 8$ km s^{-1} (the error on the line fit is only accounted for here). It likely suggests that the narrow Hα P-Cygni and the [Ca II] doublet are both produced in slow-moving material ($\leq$ 70-115 km s^{-1}) expelled by the progenitor star years before the explosion. This modest wind velocity allows us to disfavour an LBV-like outburst as the origin for this mass-loss event, and is more consistent with CSM produced by a RSG or a super-AGB star.

Berger et al. (2009b) investigated the environmental properties of the archetypal ILRT NGC 300 OT2008-1 through high-resolution spectroscopy. They discussed the complex profile of prominent spectral features such as the Balmer lines, the [Ca II] doublet and Ca II NIR triplet (visible in emission) and Ca II H&K (in absorption). These high-quality spectra of NGC 300 OT2008-1 showed also weaker features of He I, [O I] λ6300, λ6364, O I λ7774 and λ8446, along with Fe II multiplets. The Hα emission line was symmetric, but accompanied by narrow absorption features superimposed on the main emission, one (weaker) blue-shifted by -130 km s^{-1}, and another more prominent red-shifted by 30 km s^{-1}. A similar narrow P-Cygni absorption is visible in our GTC+OSIRIS spectrum (blue-shifted by -70 km s^{-1}). As in the case of NGC 300 OT2008-1, the [Ca II] doublet has a strongly asymmetric profile without a blue wing, while the Ca II NIR triplet has a broad absorption feature, supporting the existence of multiple line components. The features of Berger et al.'s high resolution spectra suggest that NGC 300 OT2008-1 has a complex circumstellar environment, marked by outflows and inflows from different gas components, including the wind from a possible companion star (a Wolf-Rayet star or a blue supergiant). Our spectral analysis of AT 2017be are in agreement with NGC 300 OT2008-1 in emission/absorption lines, Hα velocities, and complex CSM environment.

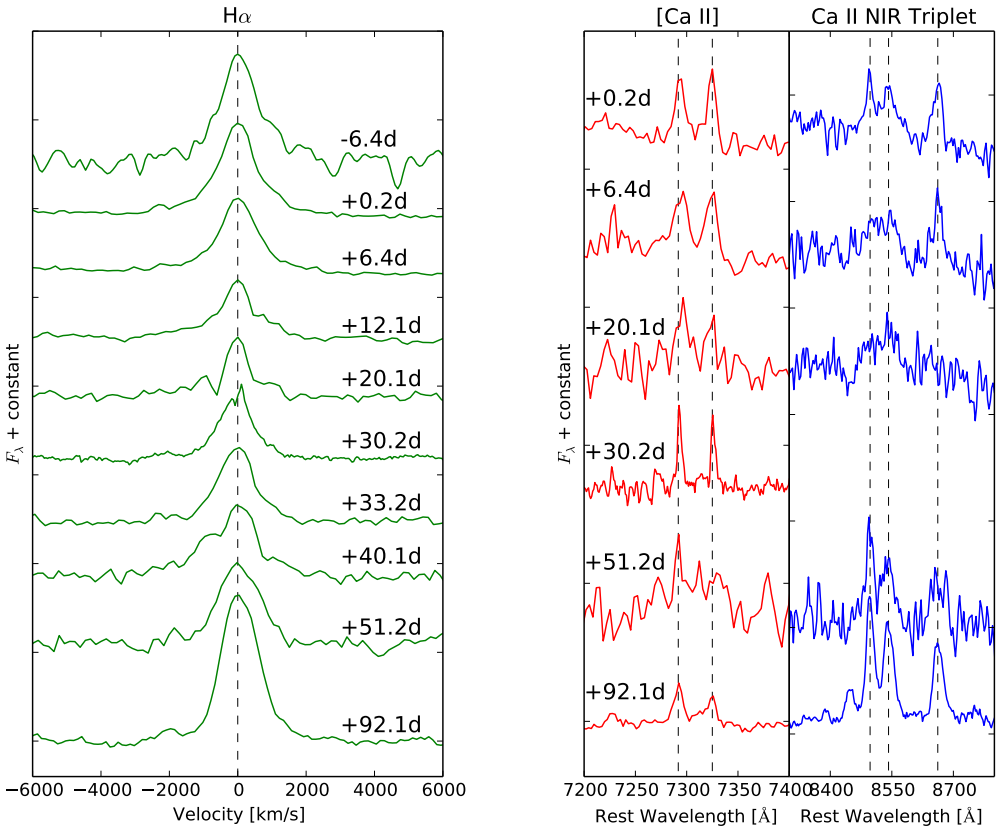

(a) Evolution of the Hα line profiles

(b) Evolution of the Ca II line profiles

Figure 3.12: Evolution of the Hα (left panel), [Ca II] doublet and Ca II NIR triplet (right panel) line profiles. The vertical black dashed lines mark the rest-wavelength position of these emission lines.

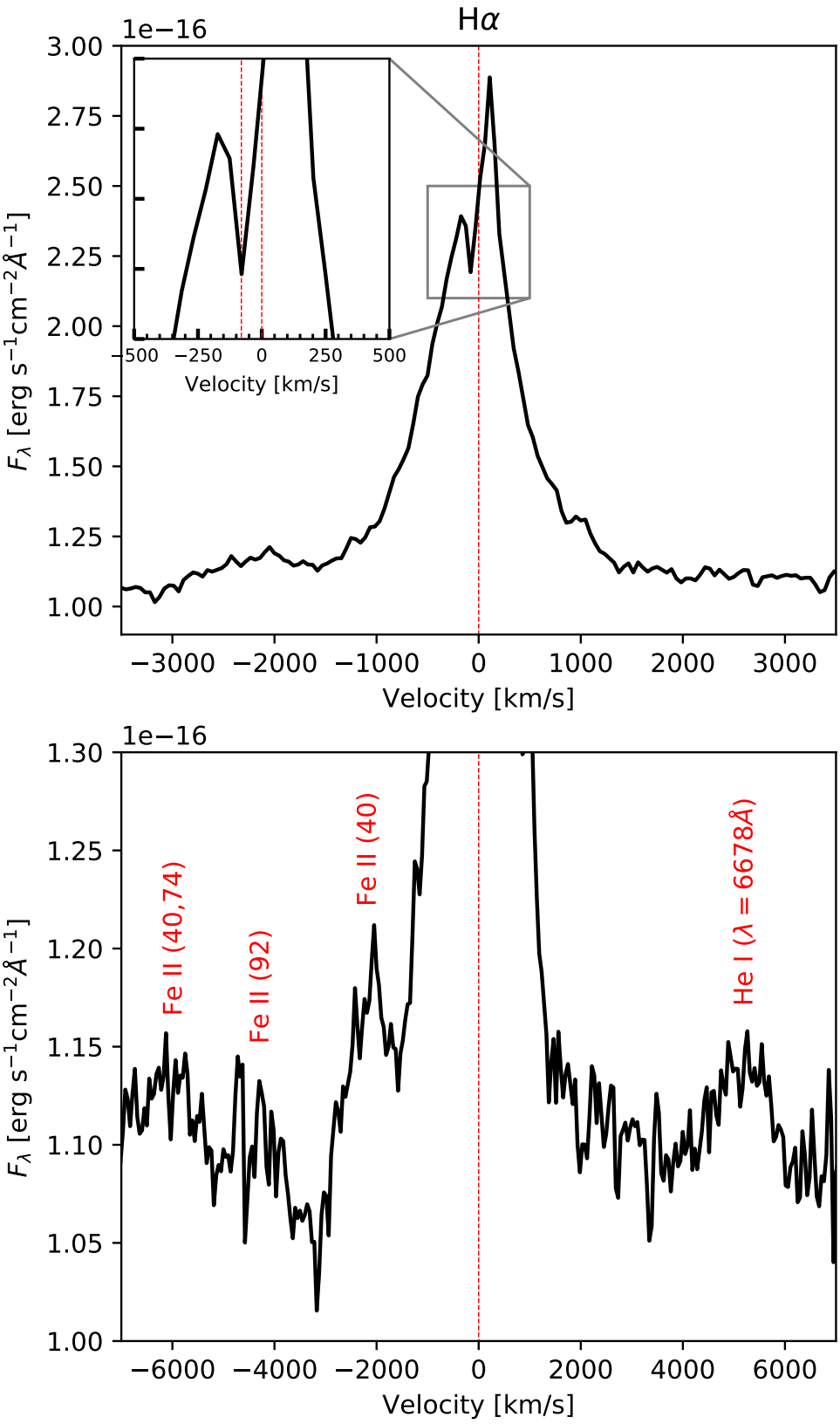

Figure 3.13: The profile of Hα in our highest resolution spectrum (GTC, phase 30.2 d) in velocity space. The vertical red dashed line marks the rest-velocity position of Hα. Lower contrast Fe II lines and He I λ6678 are also identified in the lower panel.

Table 3.6: Main parameters inferred from the spectra of AT 2017be.

Date	MJD	Phase[a] (d)	FWHM Hα (Å)	Velocity Hα (km s^{-1})	Luminosity Hα[d] (10^{37}erg s^{-1})	Temperature (K)
20170110[c]	57763.4	−6.4	19.9	570	13.0	7650 ± 1250
20170117[c]	57770.0	+0.2	19.8	590	10.2	6650 ± 400
20170123[c]	57776.2	+6.4	20.8	480	7.3	6550 ± 300
20170128[c]	57781.9	+12.1	18.6	500	4.1	6550 ± 550
20170205[c]	57790.0	+20.1	19.2[b]	310	3.7	5150 ± 500
20170216	57800.0	+30.2	18.4	820	3.0	5000 ± 900
20170219[c]	57803.0	+33.2	19.3	610	3.8	5250 ± 350
20170225[c]	57809.9	+40.1	24.9	740	5.3	5400 ± 500
20170308[c]	57821.0	+51.2	22.0	580	4.3	5650 ± 750
20170418	57861.9	+92.1	17.9	730	5.9	5100 ± 350

a Phases are relative to *r*-band maximum light, on MJD = 57769.8 ± 0.1.
b There is a hot pixel close to the Hα position, affecting the recovered line profile and making the above measurement uncertain.
c These measurements are close to the instrumental resolution, hence after correcting for instrumental resolution the resulting velocity has a large uncertainty.
d We assume conservative errors on the luminosity of about 20 per cent.

3.4 Progenitor analysis

In the attempt to detect (or place stringent detection limits) to the quiescent progenitor star, we searched pre-explosion images of the field of AT 2017be in ground based and space telescope archives. Unfortunately while the host galaxy is relatively nearby, very few deep images are available in the archives. The most constraining image is a *HST + NICMOS* frame taken on 2002 October 14, using the NIC3 camera and the F160W filter ($\sim$ *H* band). A narrow band NIR image taken at the same epoch does not place useful magnitude limits to the progenitor.

To identify the position of AT 2017be in the NICMOS data, we aligned the image to good seeing images taken at the NOT. We aligned the NICMOS data to both an *i*-band image taken on 2017 April 21, and a *H*-band image taken on April 8, using 10 sources in the former and 7 in the latter that were also present in the NICMOS frame. Rotation, translation and a scale factor between each pair of images were fitted for, and the resulting transformation had an RMS scatter of 69 mas and 53 mas when using either *i* band or *H* band, respectively, as our reference image. In both cases, we obtained an almost identical position for AT 2017be on the NICMOS image (see the left panel of Figure 3.14).

To determine a limiting magnitude for the progenitor of AT 2017be, we performed artificial star tests on the NICMOS data (see the middle and right panels of Figure 3.14). A model point spread function was created from sources in the field, and then scaled in flux and inserted at the SN position. The 3σ limiting magnitude was taken to be the value at which the source was recovered with a photometric uncertainty of 0.2 mag. We determine a flux limit for the progenitor with this technique of $F < 2.04 \times 10^{-18}$ erg s^{-1} cm^{-2} Å^{-1}, or a limiting magnitude in the ABmag system of $F160W > 20.8$ mag.

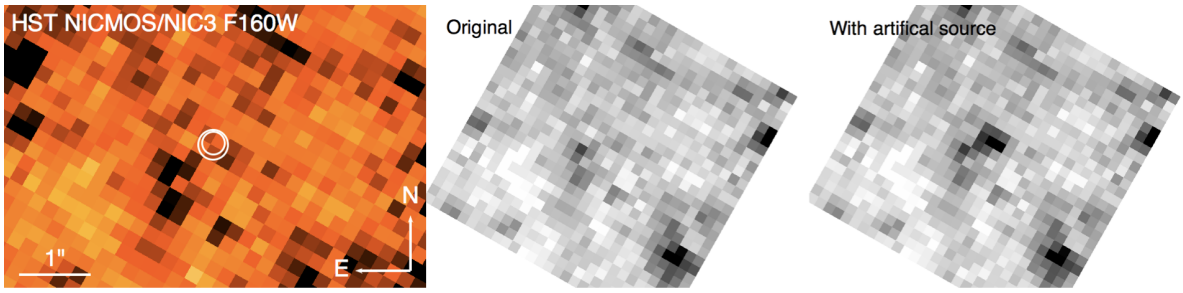

Figure 3.14: A section of the archival HST+NICMOS F160W image of the site of AT 2017be. The circles mark the location of AT 2017be as determined from *i*- and *H*-band images of the SN; the radii of the circles correspond to 3x the RMS scatter in the astrometric transformation (left).The HST+NICMOS F160W image of the site of AT 2017be (middle), and the same region with an artificial source at 3σ significance (right)

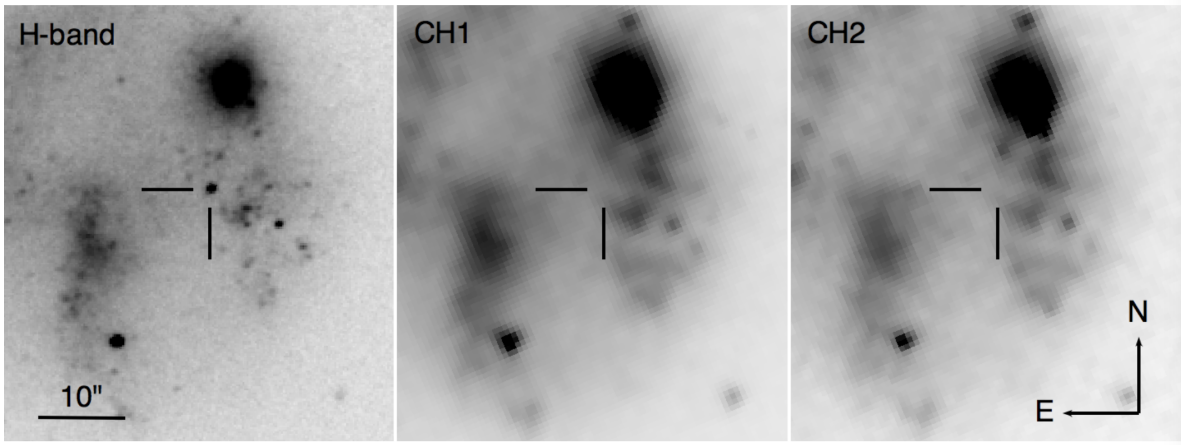

Figure 3.15: *H* band post-explosion and Spitzer IRAC CH1 (3.6μm) and CH2 (4.5μm) pre-explosion images of the site of AT 2017be. The position of the transient is indicated with tick marks in all panels.

We used the same techniques to determine limiting magnitudes for the Spitzer IRAC images (2004-04-01.5 UT, see the Figure 3.15) as were used for the NICMOS data. Limits of $M_{3.6\mu} > 15.80$ mag and $M_{4.5\mu} > 15.82$ mag (Vega mag) were found in IRAC CH1 and CH2 respectively.

The limits we can place on the progenitor of AT 2017be are unfortunately not particularly constraining. The implied absolute magnitude of the progenitor given a distance modulus of $\mu = 29.47$ mag is fainter than $H = -10.1$ mag (converting to Vegamag). For comparison, the progenitor of SN 2008S, which was detected in the MIR with Spitzer, had a *K*-band limit of > -10.8 mag (Botticella et al. 2009).

Adams et al. (2018) performed an independent analysis on pre-explosion archive images, although they did not describe in depth the methods used to infer their limits. While the *H*-band limit inferred by Adams et al. from the HST + NICMOS data, is similar to ours, their IRAC limits are significantly deeper (Adams et al. 2018, almost 1.5 mag discrepancy for CH1 and CH2, respectively; see their

Table 4). We note that the putative progenitor was blended with an IR-luminous extended source, and this can possibly explain the discrepancy. However, as it is unclear from Adams et al. exactly what data were used in their analysis, and how their limiting magnitudes were determined, we cannot investigate this discrepancy further.

3.5 Discussion and Summary

3.5.1 Comparison with other ILRTs

In recent years, the number of discovered ILRTs has grown significantly, and includes SN 2008S (Botticella et al. 2009), NGC 300 OT2008-1 (Humphreys et al. 2011), M85 OT2006-1 (Kulkarni et al. 2007) and PTF10fqs (Kasliwal et al. 2011). The latest addition is AT 2017be, whose absolute magnitude at peak lies in the same range ($-10 > M_V > -15$ mag) as several putative classes of ILOTs.

More specifically, AT 2017be exhibits the characteristic properties of an ILRT, having a relatively slow spectro-photometric evolution, along with a lightcurve that resembles those of faint Type II SNe. In addition, the spectra of AT 2017be are dominated by prominent and narrow H emission lines ($v_{\rm FWHM} < 1000$ km s^{-1}), weak Fe II features, Ca II H&K, and the Ca II NIR triplet, similar to other ILRTs. Most importantly, the [Ca II] doublet (see Figure 3.10, right), which is a typical marker of ILRTs, is visible in all our spectra.

The lightcurve of AT 2017be is very similar to that of PTF10fqs, and shares some similarity with M85 OT2006-1. Their lightcurves show a sort of short-duration plateau. The colour evolution of AT 2017be in the optical bands matches that of NGC 300 OT2008-1, especially the $B-V$ and $R-I/r-i$ colours. The $J-K$ colour of AT 2017be, SN 2008S, NGC 300 OT2008-1 and M85 OT2006-1 becomes redder with time. The Sloan r-band absolute magnitude at maximum of AT 2017be is $M_r = -11.98 \pm 0.09$ mag, and is almost equal to that of PTF10fqs. The constraint on the ^{56}Ni mass inferred from the late phase bolometric lightcurve, implies that very little ^{56}Ni was ejected in the explosion of AT 2017be ($\sim 8 \times 10^{-4}$ M$_\odot$ or less), which is less than that estimated by Botticella et al. for SN 2008S.

A common characteristic of ILRTs is their MIR luminous pre-explosion progenitors, with the quiescent star being embedded in a dusty CSM (Botticella et al. 2009, see their Figure 17). The best-studied cases indicate moderate-mass (8-15 M$_\odot$) progenitors, although in some cases the studies point to slightly lower-mass stars (e.g. M85 OT2006-1, Pastorello et al. 2007a; Rau et al. 2007; Ofek et al. 2008). Unfortunately, we cannot set stringent constraints on the AT 2017be progenitor star in pre-explosion archive images.

3.5.2 Plausible scenarios for ILRTs and conclusions

The nature of ILRTs is debated. Several scenarios have been proposed in the attempt to interpret their peculiar observables. For SN 2008S, a scenario invoking a weak ECSN explosion of a super-AGB star embedded in an optical thick dusty envelope has been proposed (Prieto et al. 2008; Botticella et al. 2009; Thompson et al. 2009). Alternatively, the LBV-like super-Eddington outburst of a highly obscured, massive progenitor (~ 20 M$_\odot$) has been suggested by Smith et al. (2009). Another well-studied object is NGC 300 OT2008-1, which has been proposed to be both an ECSN (Prieto et al.

2008; Thompson et al. 2009) or an LBV-like eruption of a moderate-mass star (Smith et al. 2011).

Berger et al. (2009b) investigated NGC 300 OT2008-1 with high-resolution spectroscopy, and proposed that the observed outburst was produced by a $\sim$ 10 - 20 $M_{\odot}$, relatively compact progenitor (a blue supergiant or a Wolf-Rayet star), obscured by a dusty cocoon. An alternative explanation involved interaction in a binary system. Bond et al. (2009) proposed NGC 300 OT2008-1 to be an eruption of a dust-enshrouded, IR-luminous and relatively massive star ($\sim$ 10-15 $M_{\odot}$), likely an OH/IR source, which began its evolution on a blue loop toward higher temperatures. Both SN 2008S and NGC 300 OT2008-1 are slightly more luminous than other ILRTs, and have lightcurves similar to those of SNe II-L. From an observational point of view, ILRTs appear to be scaled-down analogs of faint Type II SNe.

Therefore, we now discuss three possible scenarios (LRN nature, LBV-like eruption, and EC SN explosions) for ILRTs.

1. The typical observational features of LRNe such as AT 2017jfs and NGC4490-2011OT1 are double-peaked lightcurves, low ejecta velocities ($\sim$ 100-300 km s^{-1}), no evidence of [Ca II] features, and very late-time spectra dominated by molecular bands (TiO, VO) in the optical domain (Pastorello et al. 2019a,b). All of this makes AT 2017be quite different from LRNe, we agree with Adams et al. (2018) in ruling out a LRN classification for this transient.

2. LBVs are erupting massive stars that may experience severe mass-loss. Multiple outbursts can be observed during a single eruptive phase that may lasts even decades (like the Great Eruption of η Carinae). During these outburst, no ^{56}Ni is expected to be ejected. In addition, the ejected gas expands at velocities of a few hundreds km s^{-1}, occasionally exceeding 10^4 km s^{-1} during a giant eruption, which are inconsistent with our spectroscopic observations (e.g., $\sim$ 820 km s^{-1} and 730 km s^{-1} at epoch of +30.2 days and +92.1 days, respectively). An LBV outburst scenario for AT 2017be has been recently proposed by Adams et al. (2018). However, we do not find robust arguments to support this, as we did not detect any luminous progenitor in pre-explosion data (in contrast with expectations from a massive LBV). A caveat here is that lower luminosity LBVs may have initial masses down to about 20 $M_{\odot}$, as claimed by Smith et al. (2010, 2016a). In particular, UGC 2773-OT is a moderate-mass LBV of $\sim$ 20 $M_{\odot}$, sharing some observational properties with ILRTs (in particular, the overall spectral evolution and the detection of the [Ca II] doublet). However, the light curve is totally different, showing a luminosity rise lasting over a decade, which is a clear signature of a long-lasting eruptive phase. AT 2017be and ILRTs have short-duration light curves, resembling that of some CC SNe, and the best-followed objects (SN 2008S and NGC 300 OT2008-1) show a late-time decline rate consistent with the ^{56}Co decay into ^{56}Fe, suggesting a dim SN explosion (see below).

3. Pumo et al. (2009) described the expected properties of EC SNe from super-AGB progenitors combining theoretical models with observational evidence. This type of CC SNe are triggered by electron-capture in the core of a progenitor which has evolved to reach the super-AGB phase. The threshold to trigger an EC SN explosion is determined by the competition between core growth and mass loss (see, e.g., Woosley et al. 2002; Herwig 2005). If the core grows to reach the Chandrasekhar limit (i.e., $M_{CH}\sim$ 1.37 $M_{\odot}$; Nomoto 1984), electron-capture reactions

are triggered, allowing the super-AGB star to explode as faint (^{56}Ni-poor) ECSN. In contrast, if envelope mass loss is large enough, electron-capture reactions fail, and the super-AGB star evolves to become an ONe white dwarf (WD). Although the ECSN mechanism in super-AGB is a plausible explanation, several uncertainties still exist. Nonetheless, as a major support to the ECSN scenario for ILRTs, Adams et al. (2016) obtained late-time Hubble and Spitzer Space Telescope imaging of SN 2008S and NGC 300 OT2008-1, and detected both transients at a mid-IR luminosity much fainter than those of their quiescent progenitors, with no detection in the optical and NIR bands.

Unfortunately, in contrast with SN 2008S and NGC 300 OT2008-1, a tight constraint on the progenitor of AT 2017be does not exist. However, we favour an ECSN scenario on the basis of the following supporting observational arguments:

- The lightcurves of ILRTs resemble sub-luminous counterparts of SNe.

- The expansion velocity of the ejecta inferred from broader resolved H and Ca II lines of AT 2017be is significantly lower than those of canonical CC SNe, but only slightly slower than those observed in some faint Type II SNe (Pastorello et al. 2004; Spiro et al. 2014). The wind velocity expected in the super-AGB stars is low, $\sim$ 100 km s^{-1} or even less (e.g., Weaver & Woosley 1979; Winters et al. 2003, 2007; Höfner & Olofsson 2018; Yasuda et al. 2019). This agrees with the velocities inferred for the slow-moving CSM in the highest resolution spectra of NGC 300 OT2008-1 (Berger et al. 2009b), and in the GTC spectrum of AT 2017be at phase +30.2 d.

- AT 2017be was photometrically monitored until very late epochs. Although already below the detection threshold in the other monitoring bands, in the K-band it was visible up to $\sim$ 350 days from maximum. The late time photometric data allow us to constrain to about 8×10^{-4} M$_\odot$ for the ejected ^{56}Ni mass. This ^{56}Ni limit is marginally lower than the amount estimated for other ILRTs ($\lesssim 10^{-3}$ M$_\odot$). The above limit is still consistent with the predictions for an EC SN explosion, such as $M_{^{56}Ni} < 0.015$ M$_\odot$ (hydrodynamics simulation; see Kitaura et al. 2006), $M_{^{56}Ni} \sim 2.5 \times 10^{-3}$ M$_\odot$ (analytical model; see Moriya et al. 2014), and $M_{^{56}Ni} \approx 1.2 \times 10^{-3}$ M$_\odot$ (observations; see Botticella et al. 2009). However, on the other hand, we can not exclude a totally ^{56}Ni-free outburst.

- For a few ILRTs, the progenitor stars were recovered in pre-explosion archive images, and in all cases they were moderate mass stars (in the mass range $\sim$ 8-15 M$_\odot$) embedded in a dusty environment, consistent with super-AGB star scenario.

- Adams et al. (2016) reported the mid-IR fading of some ILRTs at very late phases to be more than 15 times fainter than the luminosity of the quiescent progenitor detection. This is a crucial argument to support a terminal SN explosion of ILRT progenitor stars. A deep IR limit with James Webb Space Telescope (JWST) can determine if there is a surviving star following AT 2017be.

It is evident that high-resolution spectroscopy at early phases, the availability of deep pre-discovery images in the optical and IR archives (ideally with high spatial resolution), and deep late-time obser-

vations in the IR domain are crucial for better constraining the explosion scenario of AT 2017be and other ILRTs. In the following Chapter 4, we will further study a sample of ILRTs, in our attempts to systematically constrain their observational and physical parameters. One major goal of our study is the construction of a set of templates for future surveys. Identifying ILRT candidates in the millions of new transients discovered every night by future surveys is a priority. The next generation of optical and NIR facilities, such as the Large Synoptic Survey Telescope (LSST; see LSST Science Collaboration et al. 2009; Foley et al. 2018) and the Wide Field Infrared Survey Telescope (WFIRST; e.g., Spergel et al. 2015), will discover a larger number of new ILRTs, enabling us to unequivocally unveil the nature of their stellar progenitors and their explosion mechanism.

Chapter 4

A large sample of ILRTs

4.1 Introduction

As discussed in previous chapters, modern surveys are discovering a large number of gap transients. A fraction of them are "SN Impostors", and giant eruptions of LBVs are considered a plausible interpretation for classical SN impostors (see details in Chapter 1.3.3). Another sub-class, conventionally designated as LRNe, displays double-peaked (or even multiple) light curves and fast-evolving spectra, showing SN IIn-like spectra at early times but changing to M-type spectra at late phases, with molecular band absorptions (e.g., Chapter 1.3.2; see also Pastorello et al. 2019a,b).

Another sub-group of ILOTs/GPs, i.e., ILRTs, shows observational signatures resembling those of SN Impostors, but have SN-like light curves, with 8-15 $M_{\odot}$ progenitors embedded in dusty cocoons (see Botticella et al. 2009; Thompson et al. 2009; Prieto et al. 2008, also in Chapter 1.3.1). They have been proposed to be LBV-like outburst of moderate-mass stars, or stellar mergers. A more appealing possibility is that we are actually observing faint core-collapse SN explosions, in particular EC SNe from S-AGB stars (Pumo et al. 2009). In recent years, a number of objects have been studied, including SN 2008S (see, e.g., Prieto et al. 2008; Smith et al. 2009; Botticella et al. 2009; Kochanek 2011; Szczygieł et al. 2012; Adams et al. 2016), NGC 300 OT2008-1 (e.g., Bond et al. 2009; Berger et al. 2009b; Prieto et al. 2009; Humphreys et al. 2011), PTF10fqs (Kasliwal et al. 2011), M85 OT2006-1 (see, e.g., Kulkarni et al. 2007; Pastorello et al. 2007a; Rau et al. 2007) and AT 2017be (Stephens et al. 2017; Adams et al. 2018; Cai et al. 2018), as reported in Chapter 3.

In this chapter, we analyse a sample of five ILRTs, including SN 2010dn, PSN J14535395+0334049, PSN J15213475-0722183, PSN J13100734+3410514 and AT 2018aes. Usually, they were initially classified as LBV outbursts or, more generically, SN Impostors. Subsequent follow-up campaigns allowed us to fine tune the classifications as ILRTs. General information on these transients is given in Section 4.2. The photometric and spectroscopic analyses are reported in Section 4.3 and Section 4.4, respectively. A discussion on the observational and theoretical properties of ILRTs is given in Section 4.5.

4.2 Basic information of sample

4.2.1 Host galaxies: distance, reddening and metallicity

SN 2010dn was discovered by the amateur astronomer K. Itagaki on 2010 May 31.523 UT (hereafter UT will be used throughout this chapter) with unfiltered magnitude 17.5 (CBAT [1]). The object was detected at RA=$10^h18^m19.89^s$, Dec=+41°26′28.80″ [J2000], 61″ north and 33″ east of the center of NGC 3184. We adopt a distance to the host galaxy d = 14.40 ± 0.33 Mpc (μ = 30.79 ± 0.05 mag; adopting a standard cosmological model, H_0 = 73 km s^{-1}Mpc^{-1}, Ω_M = 0.27, Ω_Λ = 0.73) as obtained with the Cepheids method (Ferrarese et al. 2000). The Galactic reddening $E(B-V)_{Gal}$ = 0.017 mag is from Schlafly & Finkbeiner (2011). On the other hand, the presence of the narrow interstellar Na I D ($\lambda\lambda$ 5890,5996 Å) feature at the host galaxy redshift is usually considered as a proxy for additional internal extinction (Pozzo et al. 2006; Sahu et al. 2006; Poznanski et al. 2011). However, in this case, the equivalent width (EW) of Na I D varies with time, suggesting that this dust is likely due to circumstellar material (CSM). For this reason, we adopt a total reddening E$(B-V)_{Total}$ = E$(B-V)_{Gal}$ = 0.017 mag, in agreement with Smith et al. (2011).

PSN J14535395+0334049 is also designated as NGC 5775-2012OT1 and SNhunt120. Hereafter, for simplicity, the object will be named as NGC 5775 OT. It was found by S. Howerton and the Catalina Real-Time Transient Survey (CRTS [2]) on 2012 March 27.460 UT (Berger et al. 2012; Howerton et al. 2012). Its coordinates are: RA=$14^h53^m53.95^s$, Dec=+03°34′04.90″ [J2000], and is located 85″ north and 55″ west of the center of NGC 5775. A distance of d = 18.62 ± 1.12 Mpc (hence μ = 31.35 ± 0.13 mag) is inferred. The above value is the weighted average of several estimates using the Tully-Fisher method (e.g., Tully et al. 2013; Sorce et al. 2014; Tully et al. 2016, from the NASA/IPAC Extragalactic database[3]). The above estimates have been scaled to the same cosmological model (H_0 = 73 km s^{-1}Mpc^{-1}, Ω_M = 0.27, and Ω_Λ = 0.73). A Galactic reddening E$(B-V)_{Gal}$ = 0.037 mag (Schlafly & Finkbeiner 2011) is adopted. We measure $EW \simeq 0.9$ Å for the Na I D absorption at the redshift of NGC 5775 in the early spectra of the transient. Following Turatto et al. (2003) and assuming R_V = 3.1 (Cardelli et al. 1989), we obtain a host galaxy reddening of $E(B-V)_{Host}$ = 0.144 mag. Hence, the total extinction is $E(B-V)_{Total}$ = 0.181 mag.

The discovery of PSN J15213475-0722183 (NGC 5917-2013OT1, hereafter NGC 5917 OT for brevity) was announced by the CHilean Automatic Supernovas sEarch on 2013 January 27.340 UT (CHASE [4], Margheim et al. 2013). The coordinates are RA=$15^h21^m34.75^s$, Dec=-07°22′18.30″ [J2000], and 19″ north and 31″ east of the center of NGC 5917. For this galaxy, we compute a kinematic distance. From the radial velocity corrected for Local Group infall onto the Virgo Cluster V_{Vir} = 2024 ± 7 km s^{-1} (see Sandage & Tammann 1990; Theureau et al. 1998; Terry et al. 2002, reported by *H*yperLeda [5]) and a standard cosmology model (H_0 = 73 km s^{-1}Mpc^{-1}, Ω_M = 0.27, Ω_Λ = 0.73), we obtain a luminosity distance d = 27.73 ± 1.90 Mpc (μ = 32.21 ± 0.15 mag). A Galactic reddening $E(B-V)_{Gal}$ = 0.085 mag (Schlafly & Finkbeiner 2011) is reported for this object. Additionally, spectroscopy indicates a negligible local environment extinction.

[1] http://www.cbat.eps.harvard.edu/iau/cbet/002200/CBET002299.txt
[2] http://crts.caltech.edu/index.html
[3] NED; http://nedwww.ipac.caltech.edu/
[4] http://www.das.uchile.cl/proyectoCHASE
[5] http://leda.univ-lyon1.fr/

PSN J13100734+3410514 (PS1-14ln, hereafter UGC 8246 OT) was discovered by B. Wang and X. Gao on 2013 December 20.932 UT, at RA=$13^h10^m07.34^s$, Dec=+34°10′51.40″ [J2000]. The object is 0.8″ south and 32.7″ east of the center of UGC 8246. Averaging several recent Tully-Fisher estimates (e.g., Tully et al. 2013; Sorce et al. 2014; Tully et al. 2016), we obtain $d = 15.21 \pm 0.11$ Mpc (hence, $\mu = 30.91 \pm 0.02$ mag) for UGC 8246 in the framework of a standard cosmology ($H_0 = 73$ km s^{-1}Mpc^{-1}, $\Omega_M = 0.27$, $\Omega_\Lambda = 0.73$). We adopt the same line-of-sight extinction as Barsukova et al. 2014, $E(B-V)_{Total} = 0.009$ mag. We note, in analogy with SN 2010dn, the variable EW of Na I D suggests the presence of some additional circumstellar dust, which is not accounted for reddening estimates. We hence adopt $E(B-V)_{Total} = E(B-V)_{Gal}$.

AT 2018aes (Kait-18M) was discovered by the Lick Observatory Supernova Search[6] (LOSS) on 2018 March 11.535 (Yunus et al. 2018). It was detected at RA=$13^h48^m17.76^s$, Dec=+03°56′44.20″ [J2000], 18.9″ south and 25.7″ east of the nucleus of NGC 5300. We average a few recent Tully-Fisher distances estimates from *NED* (e.g., Tully et al. 2013; Sorce et al. 2014; Tully et al. 2016), obtaining a weighted average distance $d = 18.02 \pm 0.61$ Mpc ($\mu = 31.28 \pm 0.07$ mag, obtained adopting $H_0 = 73$ km s^{-1}Mpc^{-1}, $\Omega_M = 0.27$, $\Omega_\Lambda = 0.73$). As there is some spectroscopic signature of interstellar Na I D at the host galaxy redshift, following Turatto et al. (2003), we estimate an internal reddening $E(B-V)_{Host} = 0.160$ mag, while we adopt a Milky Way contribution $E(B-V)_{Gal} = 0.020$ mag (Schlafly & Finkbeiner 2011) for AT 2018aes. Hence, we obtain a total colour excess $E(B-V)_{Total} = 0.180$ mag.

Although we did not perform precise estimates of metallicity at the ILRTs location, an estimate of the characteristic oxygen abundance at $0.4R_{25}$ (where R_{25} is the Holmberg radius [7]) can be done through a statistical approach, using the following relation from Pilyugin et al. (2004):

$$12 + log(O/H) \;=\; 6.93\,(\pm\,0.37) \;-\; 0.079\,(\pm\,0.018) \;\times\; M_B \tag{4.1}$$

which links the characteristic oxygen abundance to the B-band absolute magnitude M_B of the galaxy. The results for ILRT host galaxies are in Table 4.1. Their oxygen abundances span a very narrow range, from 8.2 to 8.6 dex, which is nearly solar (or marginally sub-solar).

A summary of the ILRT parameters is in Table 4.1, while in Figure 4.1 we show the location of the transients in their galaxies.

4.2.2 Data reduction

Routine follow-up campaigns were triggered soon after the announcement of the ILRT discoveries, using the instruments available to our collaboration. Information on the instrumental configurations is in Table 3 (Appendix 7). For some transients, additional early unfiltered data were collected from

[6] http://w.astro.berkeley.edu/bait/kait.html

[7] Holmberg radius is defined as a measure of a galaxy radius along the semi-major axis, based on its surface brightness. Specifically, the radius to the galaxy region where the surface brightness is 26.5 magnitudes per square arcsecond in B-band filtered light (e.g., Mo et al. 2010).

Table 4.1: Basic information for ILRT host galaxies.

Object	Host Galaxy[a]	m_B[b]	Redshift	Distance[c]	Distance Modulus	Position[d]	Metalicity	$E(B-V)_{Gal}$	$E(B-V)_{Host}$
		mag		Mpc	mag	kpc	dex	mag	mag
SN 2010dn	NGC 3184 [SABc]	10.3	0.00198	14.40 (0.33)	30.79 (0.05)	4.8 (0.1)	8.55	0.017	0
NGC5775 OT	NGC 5775 [SBc]	12.2	0.00561	18.62 (1.12)	31.35 (0.13)	9.1 (0.5)	8.44	0.037	0.144
NGC5917 OT	NGC 5917 [Sb]	13.7	0.00635	27.73 (1.90)	32.21 (0.15)	2.7 (0.1)	8.39	0.085	0
UGC8246 OT	UGC 8246 [SBc]	14.6	0.00271	15.21 (0.11)	30.91 (0.02)	4.0 (0.3)	8.22	0.009	0
AT 2018aes	NGC 5300 [SABc]	12.1	0.00391	18.02 (0.61)	31.28 (0.07)	2.8 (0.1)	8.45	0.020	0.160
SN 2008S	NGC 6946 [SABc]	8.2	0.00013	5.70 (0.21)	28.78 (0.08)	5.6 (0.2)	8.56	0.360	0.320
NGC300 OT	NGC 0300 [Scd]	8.8	0.00048	1.88 (0.12)	26.37 (0.14)	2.5 (0.2)	8.32	0.011	0.250
PTF10fqs	NGC 4254 [Sc]	10.2	0.00803	14.19 (1.31)	30.76 (0.20)	6.9 (1.7)	8.56	0.040	0
AT 2017be	NGC 2537 [SBm]	13.1	0.00144	7.82 (0.54)	29.47 (0.15)	-	8.22	0.048	0.040
M85 OT	NGC 4382 [S0-a]	10.1	0.00243	16.20 (0.90)	31.05 (0.12)	2.5 (0.1)	8.58	0.027	0.113

[a] Galaxy type from *H*yperLeda.
[b] *B*-band apparent magnitude of the host galaxy, from NED.
[c] All the distances adopted in these objects are in the framework of the standard cosmology (H_0 = 73 km $s^{-1}Mpc^{-1}$, $\Omega_M = 0.27$, $\Omega_\Lambda = 0.73$).
[d] Distance projection of the ILRT location from the host galaxy nucleus.

amateur astronomers. We also collected historical data available in public archives.

The raw images were first pre-reduced, applying overscan, bias and flat-field corrections using standard IRAF[8] tasks (Tody 1986, 1993), following the descriptions in Chapter 2.1.1. In order to increase the SNR, multiple-exposure frames were median-combined. Photometric measurements were performed through a dedicated pipeline *SNoOpy*, following the standard steps in Chapter 2.1.1. We note that the template subtraction technique was applied to remove the background contamination from our measurements, in particular some objects were faint or had a complex background. Specifically, we applied it to SN 2010dn, UGC 8246 OT and AT 2018aes measurements. The final magnitudes of the transients are reported in Tables 4, 6, 7, 9, and 10 (Appendix 7).

As described in Chapter 2, NIR data reduction includes flat fielding, distortion correction and sky subtraction. We performed pre-reduction on NOT/NOTCam and NTT/SOFI raw images using dedicated pipelines for NOTCam (version 2.5) and SOFI (PESSTO pipeline, version 2.2.10) respectively. Standard IRAF tasks were used to reduce LT/SupIRCam and TNG/NICS images. Instrumental magnitudes were measured via *SNoOpy*, and then calibrated using the Two Micron All Sky Survey (2MASS[9]) catalogue (assuming negligible colour corrections). The resulting NIR measurements are reported in Tables 5, 8, and 11 (Appendix 7).

4.3 Photometry

Our monitoring observations of the above transients started soon after the discovery, and lasted several months. Magnitudes of the transients are reported in Tables 4, 5, 6, 7, 8, 9, 10, and 11 (Appendix 7, while individual light curves are shown in Figs. 1, 3, 5, 7, and 9 (Appendix 7). As a reference epoch,

[8] http://iraf.noao.edu/
[9] http://irsa.ipac.caltech.edu/Missions/2mass.html/

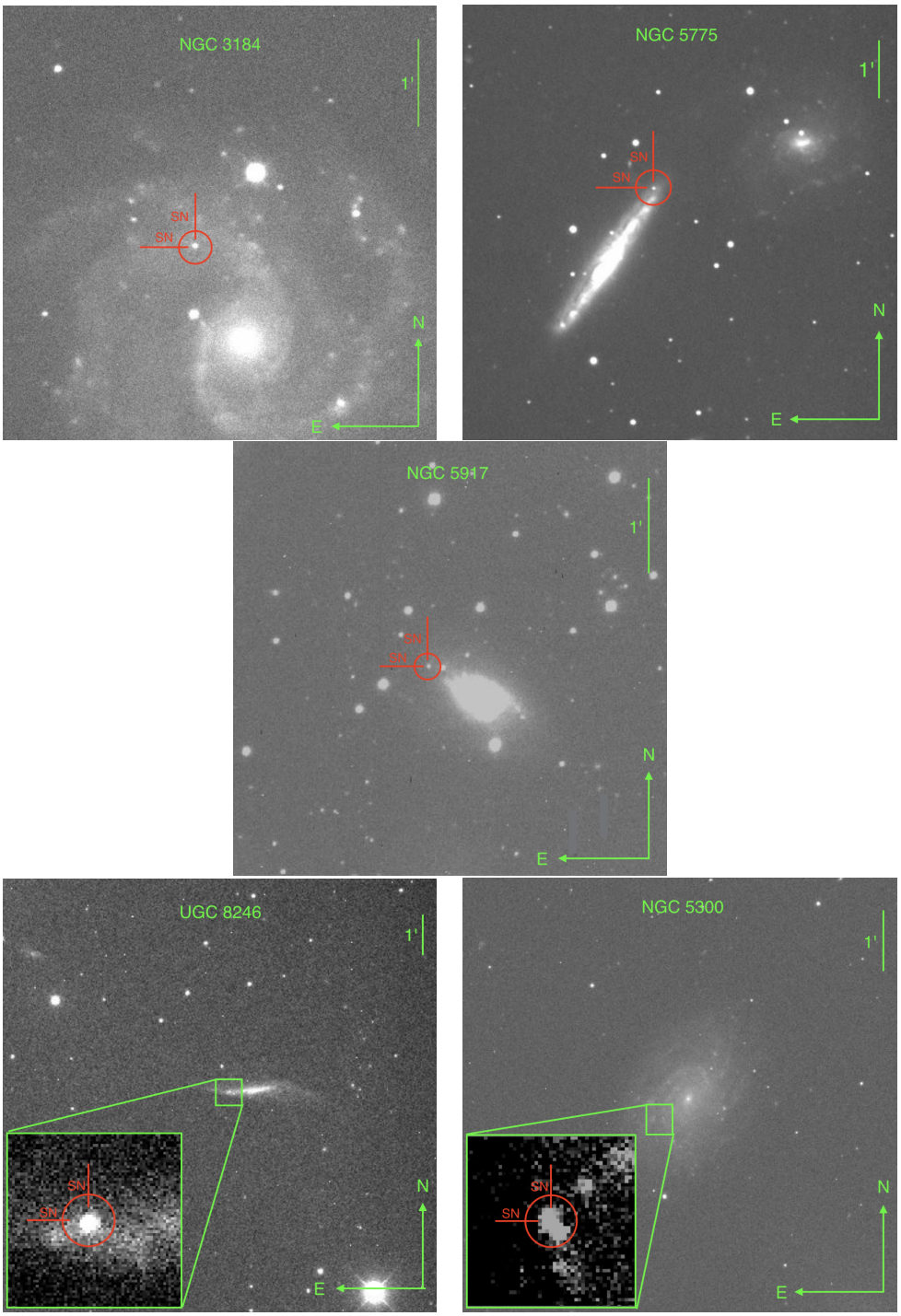

Figure 4.1: Top-left: SN 2010dn in the spiral arm of the host galaxy. Sloan *r*-band image taken on 2010 June 19 with the 2-m robotic Faulkes Telescope North (FTN; LCO network). Top-middle: NGC 5775 OT at the north edge of its host galaxy. Johnson-Cousins *R*-band image obtained on 2012 April 06 with the 0.41-m PROMPT5 telescope. Top-right: NGC 5917 OT in the host galaxy NGC 5917. Johnson-Cousins *R*-band image obtained on 2013 February 20 with the 2-m fully automatic Liverpool Telescope (LT) with RATCam. Bottom-left: UGC 8246 OT at the east edge of its galaxy. A zoom-in is shown in the lower-left corner. Sloan *r*-band image obtained on 2014 February 12 with the LT equipped with IO:O. Bottom-right: AT 2018aes and its host galaxy. LT/IO:O Sloan *r*-band image obtained on 2018 May 17 with a blow-up in the lower-left inset.

we selected the R/r-band maximum, obtained through a 3^{rd} order polynomial fit to the observed light curves (see below).

4.3.1 Individual light curves

SN 2010dn - Its light curves are shown in Figure 1. The r-band light curve rises to maximum in about 12 days and the peak is reached on $MJD = 55354.9$, at a magnitude $r = 17.2$ mag. Then the light curve fades until 25d, with a rate of 1.69 ± 0.68 mag/100d, before disappearing behind the sun. The light curve declines much faster in the blue-band than in the red bands: 4.02 ± 0.38 mag/100d in B, 2.08 ± 0.21 mag/100d in V, 1.19 ± 0.18 mag/100d in i, 0.57 ± 0.23 mag/100d in z. The late-time observations show a light curve flattening from about 160 to 210 days, with the V band declining by ~ 0.08 mag/100d. The NIR light curves have a similar evolution as in the optical bands, although with a slightly faster decline (on average, ~ 2.6 mag/100d) from ~ 170 to 200 days.

NGC 5775 OT - Also in this case, the light curves rise in about 16 days to the maximum light, reached on $MJD = 56023.5$ in the R band, at $R \approx 17.2$ mag. Then, at about 20d past-maximum, the light curve settles onto a plateau. The plateau signature is more evident in the red bands (the I-band decline rate is ~ 0.09 mag/100d) than the blue bands (~ 3.21 mag/100d in B). The plateau lasts nearly 20 days (Figure 3). Unfortunately, observations at phases later than ~ 80 days are not available.

NGC 5917 OT - The R-band peak magnitude reached on $MJD = 56324.5$ is around 18.7 mag. Then, the light curve slowly fades until ~ 60 days (1.17 ± 0.12 mag/100d). Later, a more rapid decline is observed, with a rate of 5.13 ± 0.18 mag/100d (see Figure 5). Initially, the blue bands have fast decline rates (e.g., 3.23 ± 0.11 mag/100d in B and 1.90 ± 0.12 mag/100d in V) than in the red bands (1.17 ± 0.12 mag/100d in R and 0.59 ± 0.10 mag/100d in I). Also in this case, late-time data are not available. Unfortunately, our NIR observations do not cover the pre-maximum phase. A linear decline is observed after peak, with an indicative rate of 0.79 ± 0.11 mag/100d (this is the weighted average of the three NIR bands). Finally, at ~ 70 days, the object was no longer visible, because it went in solar conjunction.

UGC 8246 OT - As shown in Figure 7, the r-band light curve has a maximum light of $r \approx 17.8$ mag on $MJD = 56652.0$. Then the light curve declines with a rate of 1.69 ± 0.05 mag/100d. A short plateau (0.50 ± 0.05 mag/100d) is observed in the r-band light curves starting from ~ 100 days, in analogy with other objects (e.g., AT 2017be, NGC 5775 OT). However, Sloan-u and Johnson-B light curves decline at faster rates, viz. ~ 2.2 and 2.1 mag/100d, respectively. Later, from ~ 230 to 350 days, the object was in solar conjunction. Finally, the transient became visible again, with the late-time r, i-band light curves having decline rates of 1.17 ± 0.12 and 1.14 ± 0.09 mag/100d respectively, slightly fast than the expected decline rate of ^{56}Co.

AT 2018aes - Optical and NIR band light curves have a similar behaviour. After an over 30 day raise, the r-band light curve peaks on $MJD = 58211.1$, at $R \approx 18.6$ mag. The past-maximum decline rate is 4.18 ± 0.15 mag/100d in r (see Figure 9). Very sparse NIR data are available, with only four epochs observed, with an average cadence of ~ 40 days. The NIR light curves show a linear decline, with a weighted average value of 2.06 ± 0.35 mag/100d. The monitoring was interrupted at around 140 days, when the object was below the detection threshold in the K band.

The light curves of the five transients are similar to those of other known ILRTs, and in some

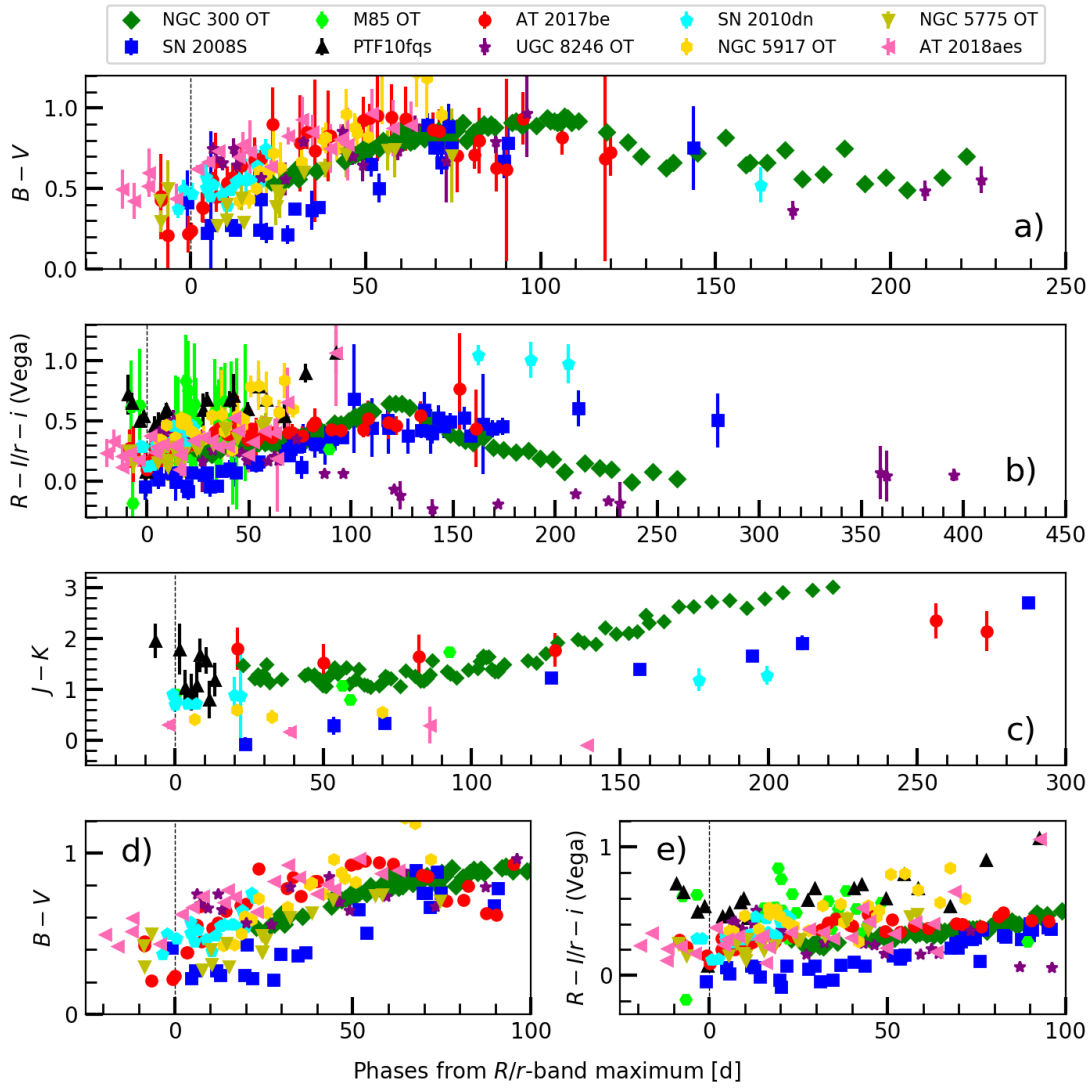

Figure 4.2: The colour evolution of ILRTs. a) panel: $B-V$ colour curves of ILRTs; b) panel: $R-I/r-i$ colour curves; c) panel: $J-K$ colour curves; d) and e) panels are the blow-up of panels a) and b), showing the colour curves during the first 100 days. The reference time is the R/r-band maximum epoch.

cases (e.g. SN 2008S, NGC 300 OT, SN 2010dn, UGC 8246 OT) late-time observations are available, showing a flatter decline light, consistent with that expected from the ^{56}Co decay. We will discuss the implications of this in Sect. 4.3.4.

4.3.2 Colour evolution

The colour evolution of the five transients presented in this chapter is shown in Figure 4.2, along with those of known ILRTs. The $B-V$ colour evolves rapidly from $\sim$ 0.2 - 0.4 mag at early phases to $\sim$ 0.7 - 1.0 mag at around 100 days past maximum, suggesting that the temperature decreases with time (see panel *a* in Figure 4.2). At the later phases (>100 days), $B-V$ turns back to bluer colours, from 0.5 to 0.8 mag. At the similar epochs, the $R-I/r-i$ colours increase from $\sim$ 0.1 - 0.3 mag to 0.5 - 1.0 mag (Figure 4.2, panel b). Very late-time colours show a large dispersion. UGC 8246 OT is somewhat discrepant, with $r-i$ colour becoming bluer (reaching ~ -0.2 mag) than at early epochs. The $J-K$ colour usually shows a NIR minimum at 30-70 days. The best NIR dataset is that of NGC 300 OT, that allows us to estimate a minimum value of $\sim$ 1.1 mag. Later, $J-K$ rises to 3.0 mag at $\sim$ 230 days (Figure 4.2, panel c).

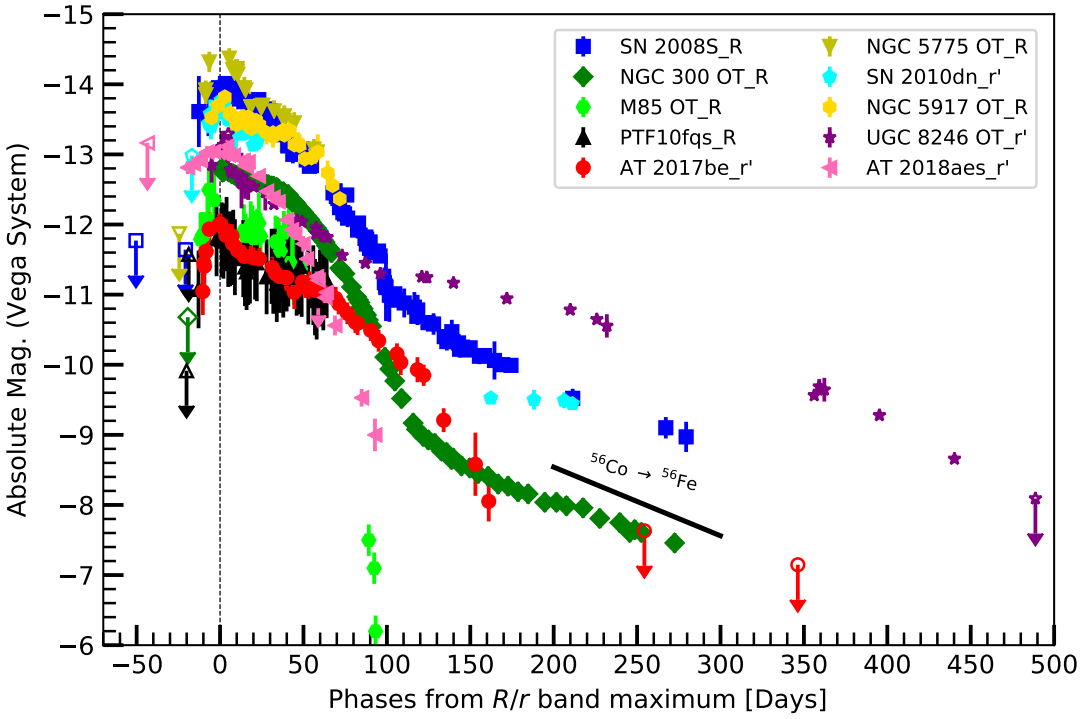

Figure 4.3: R/r band absolute light curves of ILRTs. All light curves are referred to their R/r-band peaks.

4.3.3 Absolute light curves

The R/r-band absolute light curves of our ILRT sample, calibrated in the Vega system, are shown in Figure 4.3. We used 3rd order polynomials fits to estimate the R/r-band peak absolute magnitudes, and

Table 4.2: Light curve parameters for ILRTs: last non-detection MJD (column 2), explosion MJD (column 3), first detection MJD (column 4), maximum MJD (column 5), peak magnitude (column 6), peak luminosity (columns 7) and ^{56}Ni mass (in column 8).

Object	$MJD_{non.d.}$	$MJD_{exp.}$	$MJD_{first.d.}$	$MJD_{R/r,peak}$	$M_{R/r,peak}$ mag	L_{peak} 10^{40} $erg\ s^{-1}$	^{56}Ni Mass $M_\odot$
SN 2010dn	55338.00	55343 ± 5	55348.04	55354.9	-13.83 (0.04)	4.0	$2.5 \times 10^{-3} - 2.7 \times 10^{-3}$
NGC 5775 OT	56003.39	56008 ± 5	56013.49	56023.5	-14.54 (0.32)	8.5	-
NGC 5917 OT	56112.03	–	56319.34	56324.5	-13.78 (0.27)	4.8	-
UGC 8246 OT	56463.22	–	56646.93	56652.0	-13.29 (0.08)	2.0	$> 4.8 \times 10^{-3}$
AT 2018aes	58167.57	58178 ± 10	58188.54	58211.1	-13.22 (0.04)	2.4	-
SN 2008S	54481.50	54486 ± 4	54489.50	54502.5	-14.24 (0.03)	6.0	$3.2 \times 10^{-3} - 3.5 \times 10^{-3}$
NGC 300 OT	54504.00	–	54580.15	54600.0	-13.23 (0.05)	1.8	$> 1.4 \times 10^{-3}$
PTF10fqs	55295.20	55299 ± 4	55302.39	55315.3	-11.55 (0.30)	0.6	-
AT 2017be	57751.48	57755 ± 4	57759.51	57769.8	-11.98 (0.09)	0.8	$6.7 \times 10^{-4} - 7.2 \times 10^{-4}$
M85 OT	52672.00	–	53742.00	53755.6	-12.60 (0.50)	0.9	$< 1.0 \times 10^{-3}$

the resulting values are in Table 4.2. All transients have short rise times to their maximum ($\lesssim 2$ weeks), although AT 2018aes reaches the light curve peak in ~ 3 weeks. The peak absolute magnitudes span from ~ -11.5 to -14.5 mag, still within the range expected for gap transients ($-10 < M < -15$ mag). If we consider the ten objects whose data are available in the literature, we obtain mean absolute magnitude at peak of $M_R = -13.23 \pm 0.95$ mag.

4.3.4 Pseudo-bolometric light curves

The bolometric light curve is computed by integrating the spectral energy distribution (SED) over the whole spectromagnetic spectrum. However, in most cases, we observations at wavelengths shorter than the u band, and longer than the I/i-band are not available. For this reason, to achieve meaningful comparisons among ILRTs, we computed pseudo-bolometric light curves including only the contribution from the B to the I/i bands. We first converted the extinction-corrected available magnitudes to flux densities, and finally integrated the SEDs at their effective wavelengths, assuming negligible flux contribution outside the extremes of the integration region. The resulting pseudo-bolometric light curves are presented in Figure 4.4, while peak luminosities are reported in Table 4.2. They show faint peak luminosities ranging from 0.6×10^{40} erg s^{-1} to 8.5×10^{40} erg s^{-1}. The pseudo-bolometric light curves of ILRTs share some similarities with faint Type II SNe.

In order to provide reliable estimates for the ejected ^{56}Ni masses, we need to compute truly bolometric light curves. Unfortunately, most objects have no mid-IR observations, and optical or NIR light curve information is sometimes incomplete at late times. SN 2008S and NGC 300 OT are somewhat exceptions, as they were followed until late phases, and also in the mid-IR domain. They revealed that the SED of ILRTs shifts from the optical to mid-IR domains, with the mid-IR being dominant at late phases (e.g., Botticella et al. 2009; Kochanek 2011). To by-pass the limited observational information available for most objects, we adopted SN 2008S as a template for other ILRTs, and assumed that all of them have similar SED evolution. Hence, we used SN 2008S to apply bolometric corrections for all ILRTs that had incomplete wavelength coverage. We estimated the optical and NIR luminosity contribution of SN 2008S, using the bolometric light curve model ($L_{bol} = L_0 \times \exp(-t/t_0) + L_1$, with $L_0 \simeq 10^{7.3} L_\odot$, $L_1 \simeq 10^{5.8} L_\odot$ and $t_0 \simeq 48$ days) from Kochanek (2011). We first computed the $\frac{L_{opt}}{L_{bol}}$,

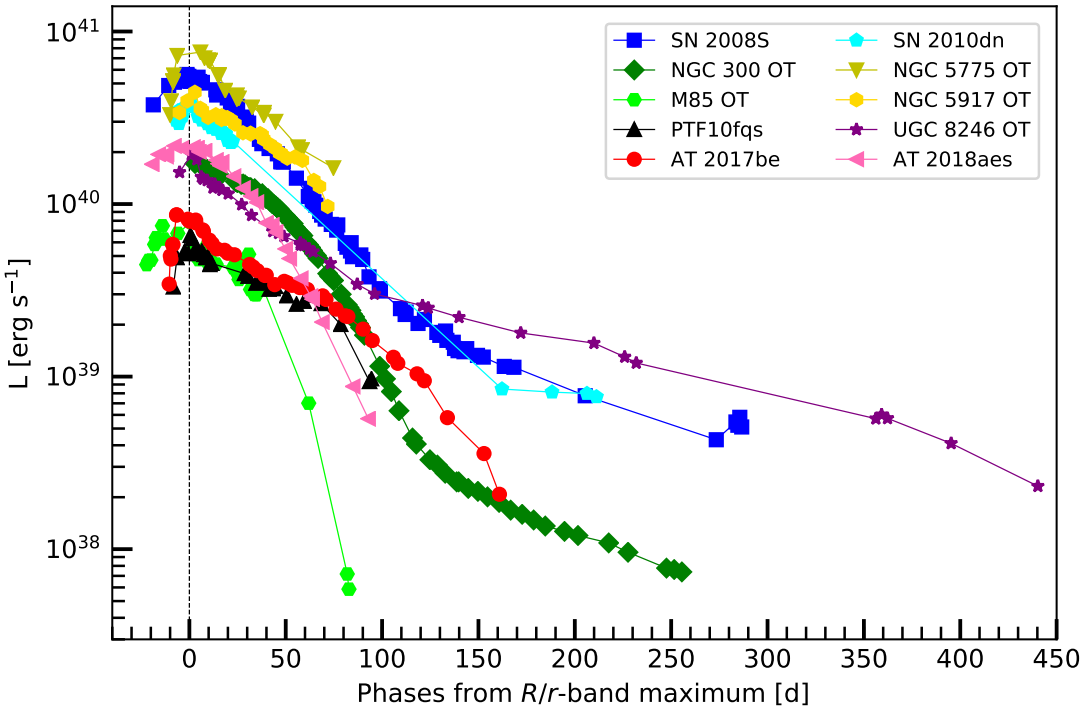

Figure 4.4: Pseudo-bolometric light curves of ILRTs. All light curves are referred to their R/r-band peaks.

$\frac{L_{NIR}}{L_{bol}}$, and $\frac{L_{opt}+L_{NIR}}{L_{bol}}$ ratio at late phases for SN 2008S. Then the L_{opt}, L_{NIR}, and L_{opt} + L_{NIR} contributions for some ILRTs at the same phases were calculated, assuming the same ratios as SN 2008S. Specifically, L_{bol} was computed starting from the measured L_{opt} + L_{NIR} for SN 2010dn, from L_{opt} for UGC 8246 OT, and L_{NIR} for AT 2017be, and than by applying the adopted bolometric corrections.

With the assumption that gamma rays produced by the radioactive decay chain ^{56}Ni to ^{56}Co to ^{56}Fe are fully thermalised and trapped, the late-time luminosity of ILRTs can be used to constrain the synthesised ^{56}Ni mass. As the Type II SN 1987A was observed from the U to the MIR bands, for this object we have a quite reliable bolometric light curve (Catchpole et al. 1988; Whitelock et al. 1988; Catchpole et al. 1989). This can be a template to estimate the ejected ^{56}Ni mass of ILRTs, calculated using Equation 4.2:

$$M(^{56}Ni)_{ILRT} = M(^{56}Ni)_{SN\ 1987A} \times (\frac{L_{ILRT}(t)}{L_{SN\ 1987A}(t)}). \quad (4.2)$$

where M(^{56}Ni)$_{\rm SN\ 1987A}$ $\sim$ 0.073 M$_\odot$ is the ^{56}Ni mass synthesised by SN 1987A, $L_{\rm ILRT}$ and $L_{\rm SN\ 1987A}$ are late-time luminosities of an individual ILRT and SN 1987A, respectively. Hereafter, we will only consider five ILRTs that have observations in the nebular phase. Due to the poor constraints on the explosion epoch of ILRTs, we use the last non-detection and the first detection to fix the earliest and the latest possible extremes for the explosion epochs. Hence, we obtain upper and lower limits of ^{56}Ni masses for the ILRTs, reported in Table 4.2. SN 2008S ejected the largest amount of ^{56}Ni (3.2 - 3.5 $\times$ 10^{-3} M$_\odot$), while AT 2017be has the lowest ^{56}Ni mass (6.7 - 7.2 $\times$ 10^{-4} M$_\odot$). All inferred ^{56}Ni masses are of the order of 10^{-4} to 10^{-3} M$_\odot$, in agreement with EC SN scenario

predictions (see Sect. 4.5).

4.4 Spectroscopy

Our spectral sequences of SN 2010dn, NGC 5775 OT, NGC 5917 OT, UGC 8246 OT and AT 2018aes were obtained using multiple instrumental configurations, whose basic information is listed in Appendix 7 (Table 3). Basic parameters for the above spectra are reported in Table 4.3.

The spectra were processed with the standard procedures in IRAF, including pre-reduction, spectral extraction, wavelength calibration, flux calibration, photometric fine tuning, and telluric corrections (see details in Chapter 2.2). The resulting ILRT spectra are shown in the Appendix 7 (Figs. 2, 4, 6, 8, and 10).

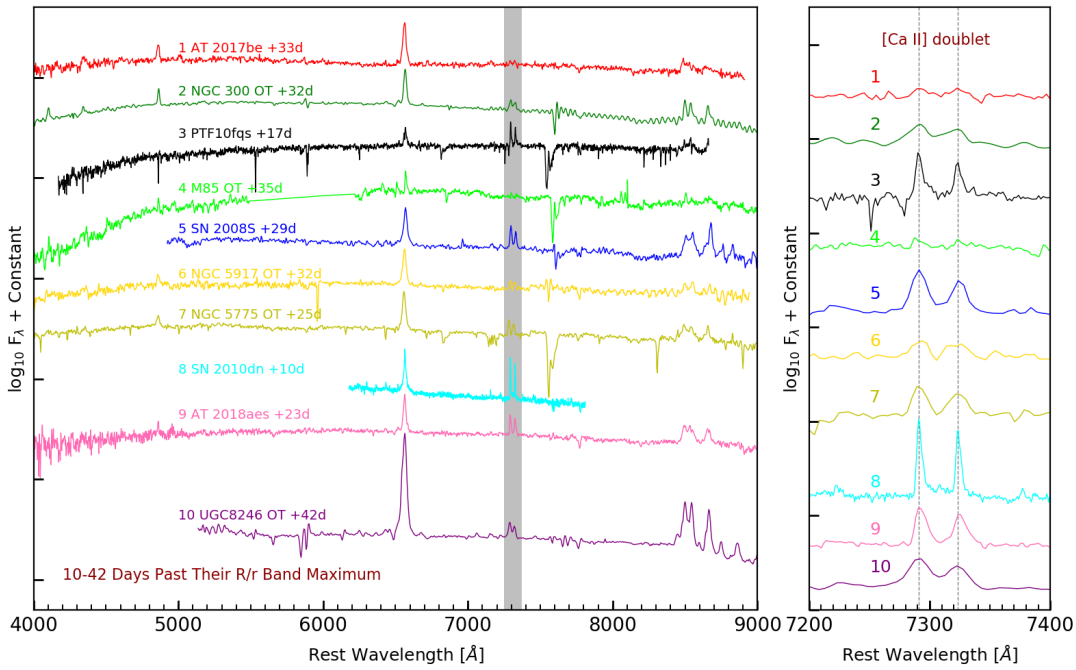

Figure 4.5: The spectral comparison of a sample of ILRTs. The published spectra of SN 2008S, PTF10fqs, M85 OT, and AT 2017be are taken from Botticella et al. (2009), Kasliwal et al. (2011), Kulkarni et al. (2007) and Cai et al. (2018). The right panel shows the region of [Ca II], marked with the grey-shaded region in left panel. All spectra were obtained at similar epoch from the R/r-band maxima, and were Doppler- and reddening-corrected.

4.4.1 Spectroscopic evolution and line identification

The five objects of our sample have spectra showing little evolution over the period of their spectral monitoring (from $\sim$ 25 to 1 year after maximum). All spectra have a nearly featureless continuum, which is relatively blue at early phases, becoming redder with time. Narrow emission lines of the

Table 4.3: Spectroscopic log of ILRTs.

Date	MJD	Phase[a] (d)	Telescope+Instrument	Grism	Spectral range (Å)	Resolution (Å)	Exp. time (s)
SN 2010dn							
20100602	55349.9	-5.0	TNG+LRS	LR-R	5090 - 8340	10.5	2100
20100603	55350.9	-4.0	TNG+LRS	LR-B	3300 - 7990	13.5	3000
20100604	55351.9	-3.0	TNG+LRS	VHR-R	6170 - 7780	3.2	2700
20100605	55352.9	-2.0	TNG+LRS	VHR-I	7290 - 8870	3.5	2700
20100607	55354.9	+0.0	WHT+ISIS	R300B/R158R	3160 - 10300	4.1/6.8	1800/1800
20100609	55356.9	+2.0	NOT+ALFOSC	gm4	3630 - 8960	18	3600
20100611	55358.9	+4.0	TNG+LRS	LR-B	3520 - 7990	11	2700
20100616	55363.9	+9.0	TNG+LRS	VHR-R	6190 - 7820	3.2	3000
20100617	55364.9	+10.0	TNG+LRS	VHR-R	6190 - 7820	3.2	3000
20100707	55384.9	+30.0	WHT+ISIS	R300B/R316R	3160 - 8860	4.1/3.1	1200/1200
NGC5775 OT							
20120329	56015.1	−8.4	Ekar1.82 + AFOSC	gm4	3500 - 8060	24	3600
20120331	56017.3	−6.2	Irénée du Pont + WFCCD	blue (400/mm)	3600 - 9120	5.3	1500
20120414	56031.2	+7.7	NTT + EFOSC2	Gr#11/Gr#16	3340 - 9920	21.3/21	1800
20120501	56048.3	+24.8	NTT + EFOSC2	Gr#11/Gr#16	3340 - 9920	14/13	1800
20120623	56101.2	+77.7	Magellan II + LDSS-3	VPH-All	3940 - 10300	6.5	900
NGC5917 OT							
20130207	56330.1	+5.6	Ekar1.82 + AFOSC	gm4	3900 - 8200	14	2700
20130207	56330.4	+5.9	NTT + EFOSC2	Gr#13	3650 - 9090	17	1213
20130207	56330.4	+5.9	Gemini-S + GMOS-S	IFU-R	4210 - 8440	?	900
20130209	56332.3	+7.8	NTT + EFOSC2	Gr#11	3340 - 7460	22	1394
20130220	56343.3	+18.8	NTT + EFOSC2	Gr#11	3340 - 7460	22	2700
20130305	56356.3	+31.8	NTT + EFOSC2	Gr#11/Gr#16	3340 - 9990	14/13	2700
20130422	56404.3	+79.8	Gemini-S + GMOS-S	IFU-R	4210 - 8440	?	450
UGC8246 OT							
20140108	56665.2	+13.2	Ekar1.82 + AFOSC	gm4	3400 - 8200	14	1800
20140115	56672.2	+20.2	Pennar1.22 + B&C	300tr	3350 - 7930	10	1800
20140203	56692.2	+40.2	TNG+LRS	LR-B	3430 - 8050	10.5	3600
20140205	56694.2	+42.2	GTC + OSIRIS	R500R	5150 - 9990	15.5	2700
20140228	56717.2	+65.2	GTC + OSIRIS	R1000B	3650 - 7850	7	900
20140322	56739.1	+87.1	TNG+LRS	LR-B	3430 - 8050	10.5	2700
20140716	56854.9	+202.9	GTC + OSIRIS	R1000B	3650 - 7850	7	1500
20140814	56883.9	+231.9	GTC + OSIRIS	R1000B	3650 - 7850	7	1900
20141220	57012.3	+360.3	GTC + OSIRIS	R1000B	3650 - 7850	7	1800
AT 2018aes							
20180331	58208.1	−3.0	GTC + OSIRIS	R1000B/R	3630 - 10080	7.5	600/600
20180426	58234.1	+23.0	GTC + OSIRIS	R1000B/R	3630 -10340	7.5	600/600

[a] Phases are relative to their R/r-band peak: MJD = 55354.9 for SN 2010dn, MJD = 56023.5 for NGC 5775 OT, MJD = 56324.5 for NGC 5917 OT, MJD = 56652.0 for UGC 8246 OT, and MJD = 58211.1 for AT 2018aes.

Table 4.4: Physical parameters inferred from the spectra of ILRTs.

Date	MJD	Phase[a] (d)	V (Hα) [b] (km s^{-1})	L (Hα) [c] (10^{38}erg s^{-1})	Temperature (K)
SN 2010dn					
20100602	55349.9	−5.0	695	2.12	7095 ± 30
20100603	55350.9	−4.0	671	1.85	6890 ± 240
20100604	55351.9	−3.0	588	3.47	6540 ± 20
20100605	55352.9	−2.0	–	–	6435 ± 30
20100607	55354.9	+0.0	577	2.29	6760 ± 120
20100609	55356.9	+2.0	<823	2.63	6830 ± 80
20100611	55358.9	+4.0	563	1.86	6690 ± 195
20100616	55363.9	+9.0	442	2.12	6820 ± 320
20100617	55364.9	+10.0	438	1.81	6710 ± 280
20100707	55384.9	+30.0	857	0.58	5020 ± 80
NGC5775 OT					
20120329	56015.1	−8.4	<1097	5.30	8380 ± 180
20120331	56017.3	−6.2	614	5.30	7385 ± 740
20120414	56031.2	+7.7	<960	5.27	7995 ± 205
20120501	56048.3	+24.8	<617	2.97	6780 ± 155
20120623	56101.2	+77.7	842	2.36	5445 ± 525
NGC5917 OT					
20130207	56330.1	+5.6	<640	3.33	6865 ± 685
20130207	56330.4	+5.9	<777	3.36	6450 ± 645
20130207	56330.4	+5.9	–	3.29	6250 ± 315
20130209	56332.3	+7.8	<1006	–	5850 ± 585
20130219	56343.3	+18.8	<1006	2.29	6388 ± 640
20130304	56356.3	+31.8	<617	1.87	6450 ± 50
20130422	56404.3	+79.8	–	2.33	4377 ± 45
UGC8246 OT [d]					
20140108	56665.2	+13.2	<640	6.31	5880 ± 110
20140115	56672.2	+20.2	<457	5.92	7110 ± 1420
20140203	56692.2	+40.2	778	–	6050 ± 1210
20140205	56694.2	+42.2	<709	5.33	5345 ± 160
20140228	56717.2	+65.2	400	4.99	5290 ± 140
20140322	56739.1	+87.1	<480	5.04	6005 ± 1200
20140716	56854.9	+202.9	446	3.98	5055 ± 135
20140814	56883.9	+231.9	503	3.87	4285 ± 45
20141220	57012.3	+360.3	499	2.68	4485 ± 180
AT 2018aes					
20180331	58208.1	−3.0	708	0.85	6620 ± 110
20180426	58234.1	+23.0	609	0.77	5675 ± 55

[a] Phases are relative to the R/r-band light curve peaks: MJD = 55354.9 for SN 2010dn, MJD = 56023.5 for NGC 5775 OT, MJD = 56324.5 for NGC 5917 OT, MJD = 56652.0 for UGC 8246 OT, and MJD = 58211.1 for AT 2018aes.

b Most of our measurements are limited by the instrumental resolution constraints, hence the FWHM velocities may have large error bars, and in many cases they should be regarded as upper limits.

c We adopt conservative errors of ∼20% for the Hα luminosity.

d Hα has a complex profile in UGC 8246 OT, hence it was fit with multiple components. The narrowest Gaussian emission and absorption components are usually below the instrumental resolution limit. For this reason, only the FWHM velocities of the broader Lorentzian components are reported here.

Balmer series are superposed to the continuum, with Hα and Hβ being the most prominent spectral features. Weak Fe II lines are also observed, along with Na I D and Ca H&K in absorption. After the H lines, the most prominent spectral features are the [Ca II] doublet ($\lambda\lambda$ 7291, 7324 Å) and the Ca NIR triplet ($\lambda\lambda\lambda$ 8498, 8542, 8662 Å). The lines of the [Ca II] doublet are visible in all spectra shown in this chapter. This is considered a feature characterizing ILRTs, visible at any time during their evolution. In Figure 4.5, all ILRTs show basically the same spectral features, further supporting an overall homogeneity in their observables.

Detailed line identification, performed on the best quality spectra of the five transients, is given in Figure 4.6. We present Balmer lines in emission, along with OI, Fe II, [Ca II], the Ca II NIR triplet, while Ca H&K and Na I D are visible in absorptions. Taking UGC 8246 OT as a representative object, the spectra collected covers its complete evolutionary phases. The spectral continuum evolves quite slowly, being initially blue (e.g., at phase $\sim$ +12.9 d), to then become much redder at late phases (+360.0 d). It resembles other ILRT spectral properties, but showing additional strong He I (λ 5876 Å) absorption in all GTC/OSIRIS high-resolution spectra at +41.9 d, +64.9, +202.6 d, +231.6 d, +360.0 d, respectively (see Figure 8 in Appendix 7). We note that narrow P-Cygni absorption troughs are also detected in the highest resolution spectra (see, e.g., the GTC/OSIRIS spectra of UGC 8246 OT in Figure 4.8 and Figure 8 in Appendix 7). The blue-shifted absorption component atop of the Hα emission (see, Figure 4.8) may originate from a dense, slow-moving wind. This will be more widely discussed in Sect. 4.4.2.

We assume the radiation of SN photosphere is approximated as a blackbody. We therefore may estimate the temperature through a blackbody fit to the spectral continuum. The inferred continuum temperatures are reported in Table 4.4, while the temperature evolution is shown in the top panel of Figure 4.7. For all objects of our sample, the temperature rapidly declines from $\sim$ 7000 - 8500 K near maximum, to nearly 5000 K at $\sim$ 100 days. At late phase, the temperature decreases more slowly to $\sim$ 4200 - 4500 K at about 1 year after maximum. Figure 4.7 probes that ILRTs have a similar temperature evolution.

4.4.2 Hα and Ca II line evolution

In order to inspect the evolution of individual spectral feature, we analyse in detail spectra of our ILRT sample at three critical phases [10]: around 0, +30, +70 days from maximum (see Figure 4.8). We measure the FWHM of Hα through a single Lorentzian function fit, as the profile wings are mostly produced by electron scattering (e.g. Huang & Chevalier 2018). This type of fit is frequently performed for SNe with narrow-line spectra (i.e. SNe IIn; see Taddia et al. 2013; Smith 2017; Nyholm et al. 2017). Its profile is dominated by a narrow component in the spectra of most objects (e.g., SN 2010dn, NGC 5775 OT, NGC 5917 OT, and AT 2018aes). However, our GTC/OSIRIS spectra of UGC 8246 OT show Hα with a more complex profile, with a narrow, blue-shifted P Cygni absorption. Instead, we fitted the dominant emission with a broader Lorentzian plus a narrow Gaussian components for a modest resolution GTC/OSIRIS spectrum at +42.2d, while other four high-resolution GTC/OSIRIS spectra (+65.2d, +202.9, +231.9, +360.3d) were reproduced via multiple components of an intermediate-width Lorentzian profile, a narrow Gaussian emission and a Gaussian absorption. The narrow component of Hα arises from the un-shocked photo-ionised CSM, while the intermediate-

[10] These critical phases are fixed on the basis of relatively large changes in the colour evolution.

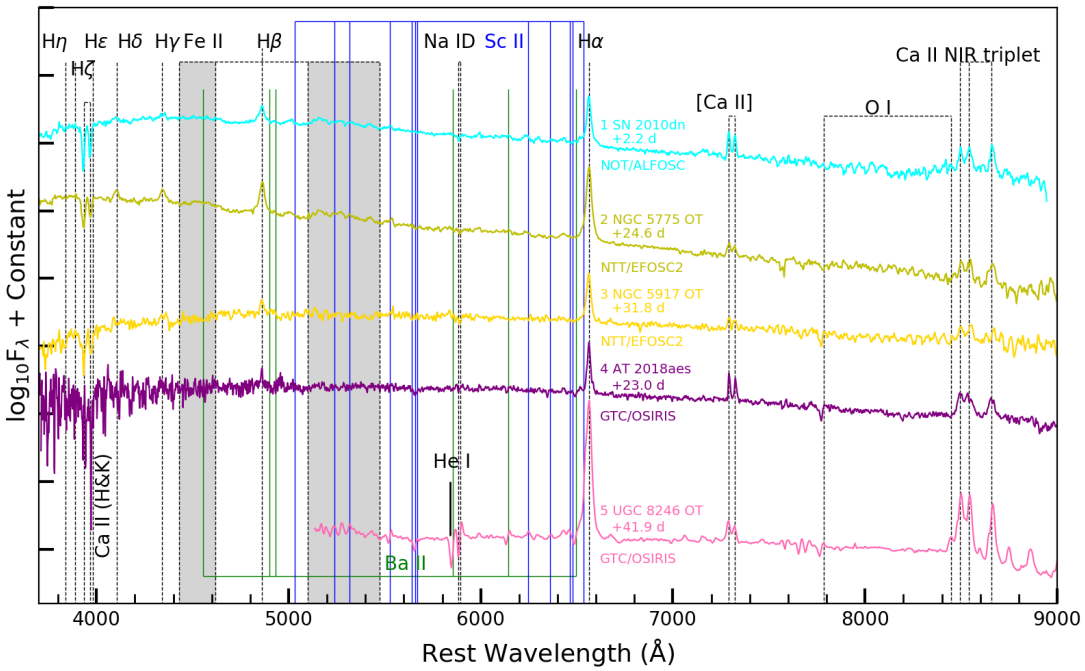

Figure 4.6: Line identification in the spectra of the five transients presented in this chapter. The spectra have been corrected for Doppler shift and reddening.

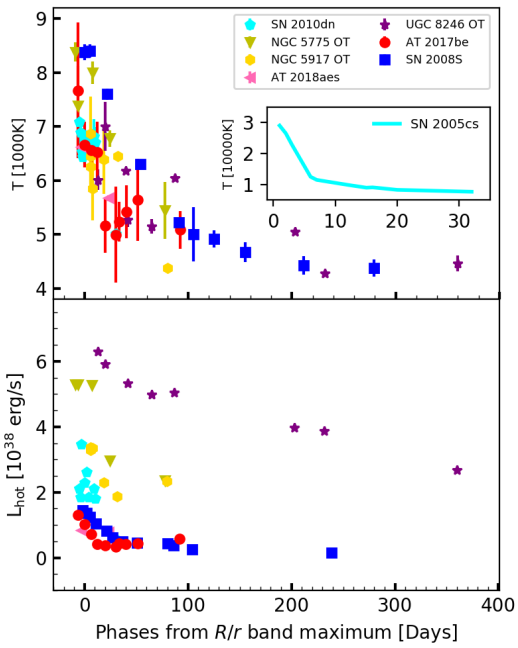

Figure 4.7: The spectral parameters inferred for a sample of ILRTs. The temperature and the Hα luminosities of SN 2008S, AT 2017be, and SN 2005cs are taken from Botticella et al. (2009), Cai et al. (2018) and Pastorello et al. (2006), respectively.

width component is likely emitting from the shocked CSM and the broad component is produced by faster ejecta. The resulting FWHM velocities (v_{FWHM}) of Hα, after correcting the instrumental resolution (Width = $\sqrt{FHWM^2 - Resolution^2}$), are reported in Table 4.4. We note that most FWHM velocities are very close to the resolution limits, and only upper velocity limits for the expanding gas can be inferred.

The profile of individual [Ca II] doublet and Ca II NIR triplet lines were fitted with a single Gaussian function. The [Ca II] doublet are produced by quadrupole transitions from $4s^2S$ to the metastable $3d^2D$ level, in which $\lambda1$ at 7291 Å and $\lambda2$ at 7324 Å are associated to $^2S_{1/2}$ - $^2D_{5/2}$ and $^2S_{1/2}$ - $^2D_{3/2}$ transitions (e.g., Osterbrock 1951; Lambert et al. 1969; Chevalier & Fransson 1994). The [Ca II] doublet likely originates from extremely low density gas regions, possibly in a slow-moving circumstellar shell. The Ca II NIR triplet lines with $\lambda_{1,2,3}$= 8498, 8542, 8662 Å are common features in many cool transients, and are produced by transitions from higher levels $4p^2P_{1/2,3/2}$ to lower levels $3d^2D_{3/2,5/2}$ (e.g., Mallik 1997, 1998; Andretta et al. 2005; Busà et al. 2007; Martin et al. 2017).

At early phases (see Figure 4.8, left panel), the Hα FWHM velocities of the transients presented in this chapter are 600-700 km s^{-1}(with upper limits to nearly 1000 km s^{-1}in case of unresolved features), which is comparable with those features for ILRTs (e.g. ∼750 km s^{-1}per SN 2008S and ∼600 km s^{-1}for AT 2017be. Therefore, all the Hα velocities indicated that in ILRT ejected material expands with similar velocities, of a few hundreds km s^{-1}. As in most cases the [Ca II] doublet is below the resolution limits, we do not have reliable estimates for the outflow velocity inferred from this feature. But the doublet is resolved in two spectra of SN 2010dn obtained with TNG/LRS at −2.8 d and −1.8 d, providing average [Ca II] FWHM velocities of 196 km s^{-1}and 171 km s^{-1}, in the two spectra. The feature was also resolved in a spectrum of NGC 5775 OT at phase -6.4 d from the duPont telescope, where we measured $v_{FWHM} \sim 220$ km s^{-1}. For AT 2018aes, GTC/OSIRIS spectra obtained at -3.0 d show a [Ca II] feature with $v_{FWHM} \sim 300$ km s^{-1}. All of this supports the idea that the [Ca II] doublet originates in a slow-moving CSM (∼ 170 - 300 km s^{-1}), while the broader Hα component forms in fast-expanding ejected gas.

At 3-5 week after maximum (Figure 4.8, middle panel), the spectra become redder. We also see a strengthening of a narrow P-Cygni superposed to Hα in UGC 8246 OT, although we cannot rule out that the non-detection of this feature in other objects is a mere resolution effect. The FWHM velocities of Hα are in the range 600-850 km s^{-1}for all objects, with M85 OT being the only outlier with $v_{FWHM} \sim 350$ km s^{-1}for additional object. A reliable [Ca II] velocity at this phase is reported for AT 2017be to be 115 km s^{-1} (Cai et al. 2018).

At late phases (70-80 d; Figure 4.8, right panel, the Hα velocity does not change significantly, still ranging from 400 (in UGC 8246 OT) up to 850 km s^{-1}(in other objects). The available spectra for UGC 8246 OT also provide an averaged [Ca II] $v_{FWHM} \sim 500$ km s^{-1}. In most cases, the modest-resolution or the low Signal-to-Noise ratio (SNR) of our spectra do not allow us to probe in detail the Ca II triplet lines (e.g., in above two phases), with an exception being the Magellan spectrum of NGC 5775 OT obtained on 2012 June 23 (phase +77.5 d), where the triplet emission lines show a symmetric profile, with an average $v_{FWHM} \simeq 1100$ km s^{-1}. The [Ca II] profile appears to shown very little evolution in the FWHM and/or the profile until ∼ 70 days, and this is a further argument to claim that these lines form in the circum-stellar environment.

A few spectra with high SNR are used to investigate the evolution of the Hα and the [Ca II] lumi-

nosity ratio. The values for the different ILRTs are reported in Table 4.5, and shown in Figure 4.9. The ratio for two objects (NGC 5775 OT and NGC 5917 OT) show a major decline (by a factor of three) from maximum (when Hα largely dominates) to one month later. However, for other two objects (SN 2010dn and AT 2018aes) the above ratio shows a much flatter evolution (from about 3 to 2) over the same temporal window. Interestingly, in these two ILRTs, [Ca II] are very luminous relatively to Hα.

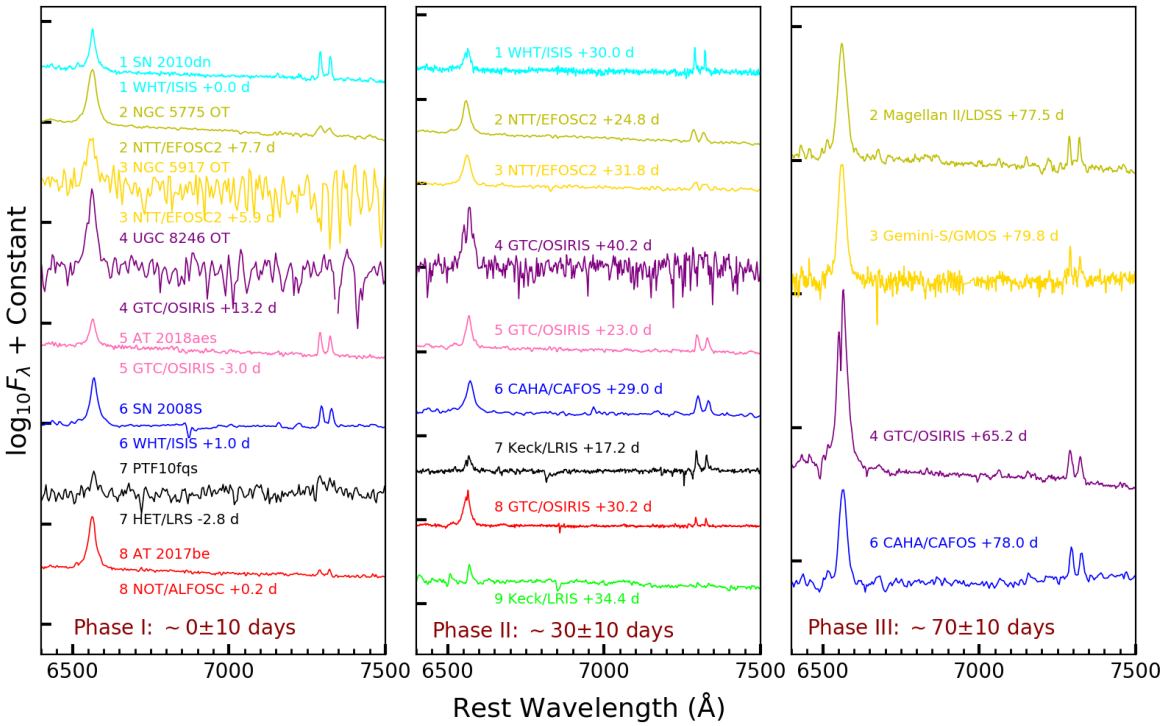

Figure 4.8: The spectral evolution with Hα and [Ca II] of ILRTs. The spectra of SN 2008S, PTF10fqs, M85 OT, and AT 2017be, downloaded from *W*ISeREP website [12], which were published by Botticella et al. (2009), Kasliwal et al. (2011), Kulkarni et al. (2007) and Cai et al. (2018). All spectra were Doppler-corrected and reddening-corrected.

4.5 Discussion and Summary

4.5.1 Observables and Parameter Correlations

In this chapter, we systematically analyse a large sample of ILRTs. They show relatively homogeneous spectrophotometric properties, that can be summarised as follows:

(i) They show single-peaked light curves, resembling those of Type IIP/IIL SNe but scaled-down in luminosity. The duration of plateau would be determined by the effective recombination time of the hydrogen envelope (e.g., see Grassberg et al. 1971; Eastman et al. 1994; de et al. 2010).

[12] https://wiserep.weizmann.ac.il/

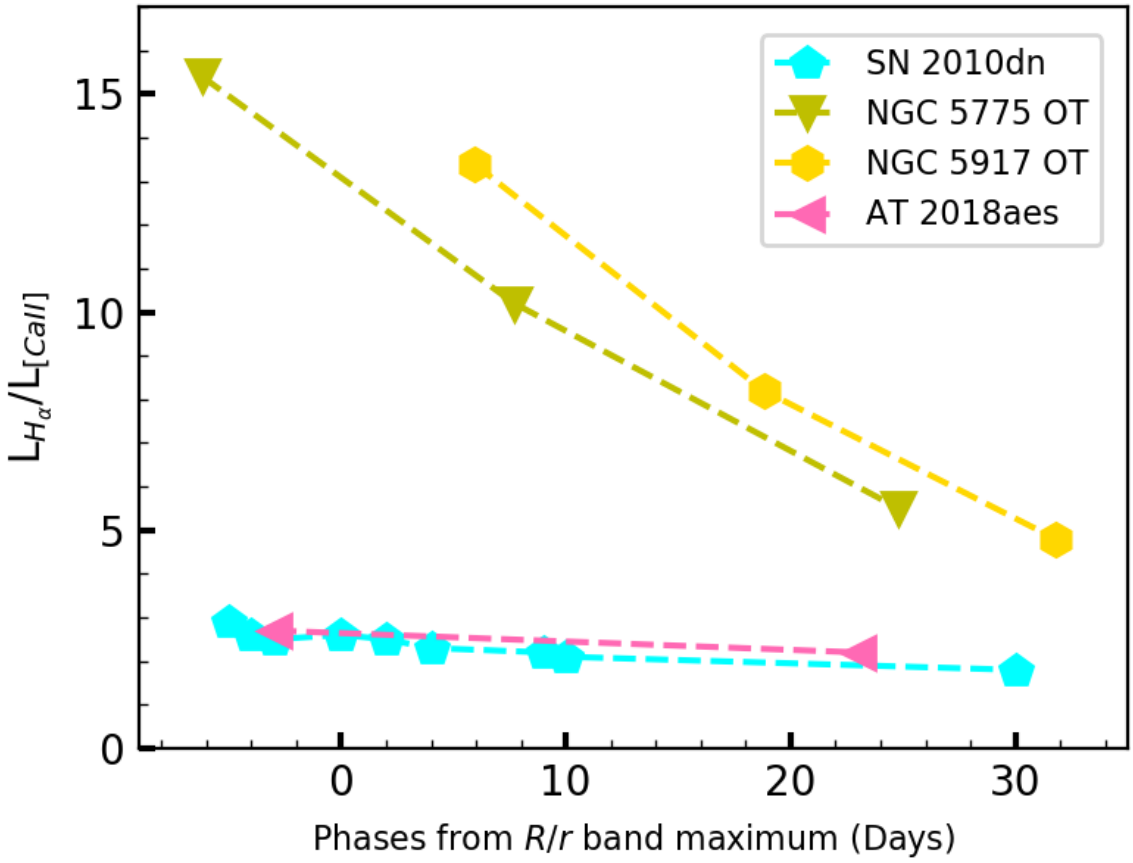

Figure 4.9: The ratio Hα to [Ca II] luminosities until phase $\sim$ 30 d.

Table 4.5: Hα to [Ca II] luminosity ratio. The luminosity of [Ca II] is from the total of the doublets.

Date	MJD	Phase[a] (d)	$L_{H_\alpha}/L_{[Ca\ II]}$
SN 2010dn			
20100602	55349.9	−5.0	2.9
20100603	55350.9	−4.0	2.6
20100604	55351.9	−3.0	2.5
20100607	55354.9	+0.0	2.6
20100609	55356.9	+2.0	2.5
20100611	55358.9	+4.0	2.3
20100616	55363.9	+9.0	2.2
20100617	55364.9	+10.0	2.1
20100707	55384.9	+30.0	1.8
NGC5775 OT			
20120331	56017.3	−6.2	15.4
20120414	56031.2	+7.7	10.2
20120501	56048.3	+24.8	5.5
NGC5917 OT			
20130207	56330.4	+5.9	13.4
20130219	56343.3	+18.8	8.2
20130304	56356.3	+31.8	4.8
AT 2018aes			
20180331	58208.1	−3.0	2.7
20180426	58234.1	+23.0	2.2

(ii) They have a homogeneous colour (hence temperature) evolution. The temperature evolution shows an initial fast decline (usually lasting <30 days), and is followed by a much slower decline trend which lasts until the end of the follow-up. This is similar to what observed in the Type IIP SN 2005cs (e.g., see the inset of Figure 4.7; top panel). Remarkably, the temperature evolution of ILRTs is in good agreement with that expected for the hydrogen recombination of classical Type II SNe (see (i)).

(iii) Their peak magnitudes range between −12 to −14.5 mag. Their quasi-bolometric light curve peaks in the range $\sim 6 \times 10^{39}$ to $\sim 8.5 \times 10^{40}$ erg s^{-1}.

(iv) The late-time light curves of SN 2008S, NGC 300 OT2008-1, and SN 2010dn decline roughly following the ^{56}Co theoretical decay rate $\sim$ 0.98 mag/(100day). The estimated ^{56}Ni mass inferred from the bolometric light curve are of the order of 10^{-4} to 10^{-3} $M_\odot$.

(v) The spectra experience relatively slow evolution during the monitoring period. Prominent lines are those of Balmer series, along with Ca II (e.g., Ca H&K, [Ca II] doublet, and Ca NIR triplet), Na I D, Fe II, and possibly O I. The [Ca II] doublet is still visible along the entire monitoring campaign. However, the study of AT 2019abn challenges this claim (see Figure 5 of Chapter 5).

(vi) The expansion velocities of ejecta inferred from the Hα FWHM lie between about 400 to 800

km s^{-1}. In addition, the [Ca II] feature width suggests the existence of slow-moving CSM with v_{FWHM} ~ 170 - 300 km s^{-1}.

(vii) The investigation of archive optical and NIR images of the SN site, obtained years before the explosion, suggests that the ILRT progenitors are moderately massive, in the range between 8 and 15 $M_{\odot}$. In addition, they are embedded in dusty cocoons (see Botticella et al. 2009; Prieto et al. 2009, and also Chapter 1.3.1).

(viii) The inspection of the SN site a few years after the explosion suggests that the SN remnant is about 15 times fainter than the quiescent progenitors (Adams et al. 2016). This is strong argument to support a terminal SN explosion.

In order to better characterise ILRTs, we looked for possible correlations among the physical parameters. In Figure 4.10, we plot peak luminosity (L_{peak}; reported in Table 4.2) vs. multiple physical parameters of ILRTs, including the time spent for the object (Δt) to decline its luminosity by a factor of two from maximum (top-left panel), the ^{56}Ni mass (top-right panel), the H_{α} FWHM velocity (bottom-left panel), and the H_{α} luminosity at maximum (bottom-right panel). The inferred values can be affected by incomplete information (e.g., some objects have poorly sampled light curve peaks, or lack of late-time observations, or have spectra with low resolution or modest SNR, or with incomplete wavelength sampling). Entering more in detail, there seems to be no correlation between L_{peak} and decline time scale Δt, which is in the range of 20-50 days[13] (see Figure 4.10, top-left panel). Within the framework of EC SN scenario, the lack of a correlation may be due to former progenitor mass-loss, CSM-ejecta interactions, or some dust extinction. A hint of correlation may exist from the peak luminosity and the ejected ^{56}Ni mass (Figure 4.10 top-right panel), although the ^{56}Ni mass has been accurately estimated for a limited number of objects, and the lower ^{56}Ni mass limit for UGC 8246 OT is somewhat discrepant from those of other ILRTs. Of course, we cannot rule out that ejecta-CSM interaction may significantly affect the late-time luminosity of the sampled objects. The modest range of ^{56}Ni masses (~ 1-5 $\times 10^{-3}$ $M_{\odot}$) may be attributed to their precursor masses lying within a narrow mass range (~ 8-10 $M_{\odot}$). In the bottom-left panel, the H_{α} FWHM velocity seems to be uncorrelated with L_{peak}. The fact that for v_{FWHM} (Hα) = 600 ± 200 km s^{-1} for all objects, suggests a common explosive/eruptive mechanism for all ILRTs, and a relatively small range of masses, while it makes a LBV giant eruption scenario less likely. The bolometric light curve peak vs. the Hα luminosity at peak diagram shows a possible trend, with ILRTs clustering two groups. In particular, we note ILRTs lying in the bottom part of the diagram (PTF10fqs, AT 2017be, and UGC 8246 OT) show a clear plateau in their light curves. A wider sample of well-monitored ILRTs is necessary to confirm or rule out the putative correlations mentioned above.

On the other hand, we also investigate the evolution of luminosity (L) against effective temperature (T) of ILRTs, along with LBVs, as shown in Figure 4.11. ILRTs show a homogeneous evolution, and lie in a narrow strip, in which the luminosity declines monotonically with the temperature. This physical homogeneity in L-T diagram is suggestive of a common mechanism triggering all ILRTs.

[13]NGC 5775 OT significantly deviates from other transients because it has a sharper peak profile, hence a lower Δt.

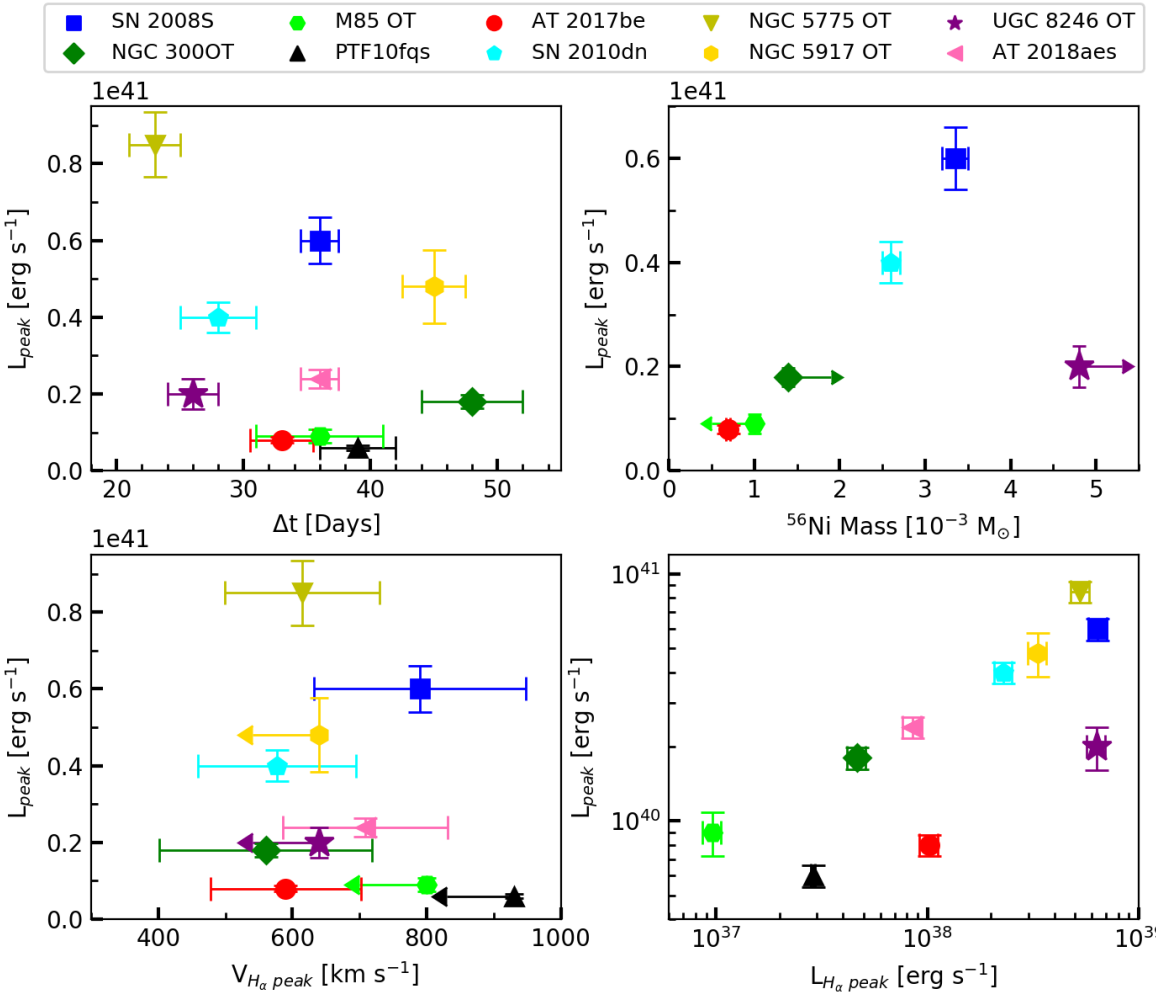

Figure 4.10: The peak luminosity (L_{peak}) vs. decline time (Δt) from L_{peak} to $0.5L_{peak}$ (top-left), L_{peak} vs. ^{56}Ni mass (top-right), L_{peak} vs. v_{FWHM} at peak (bottom-left), and L_{peak} vs. H_α peak luminosity (bottom-left). The errors are estimated as the standard deviations of repeated measurements.

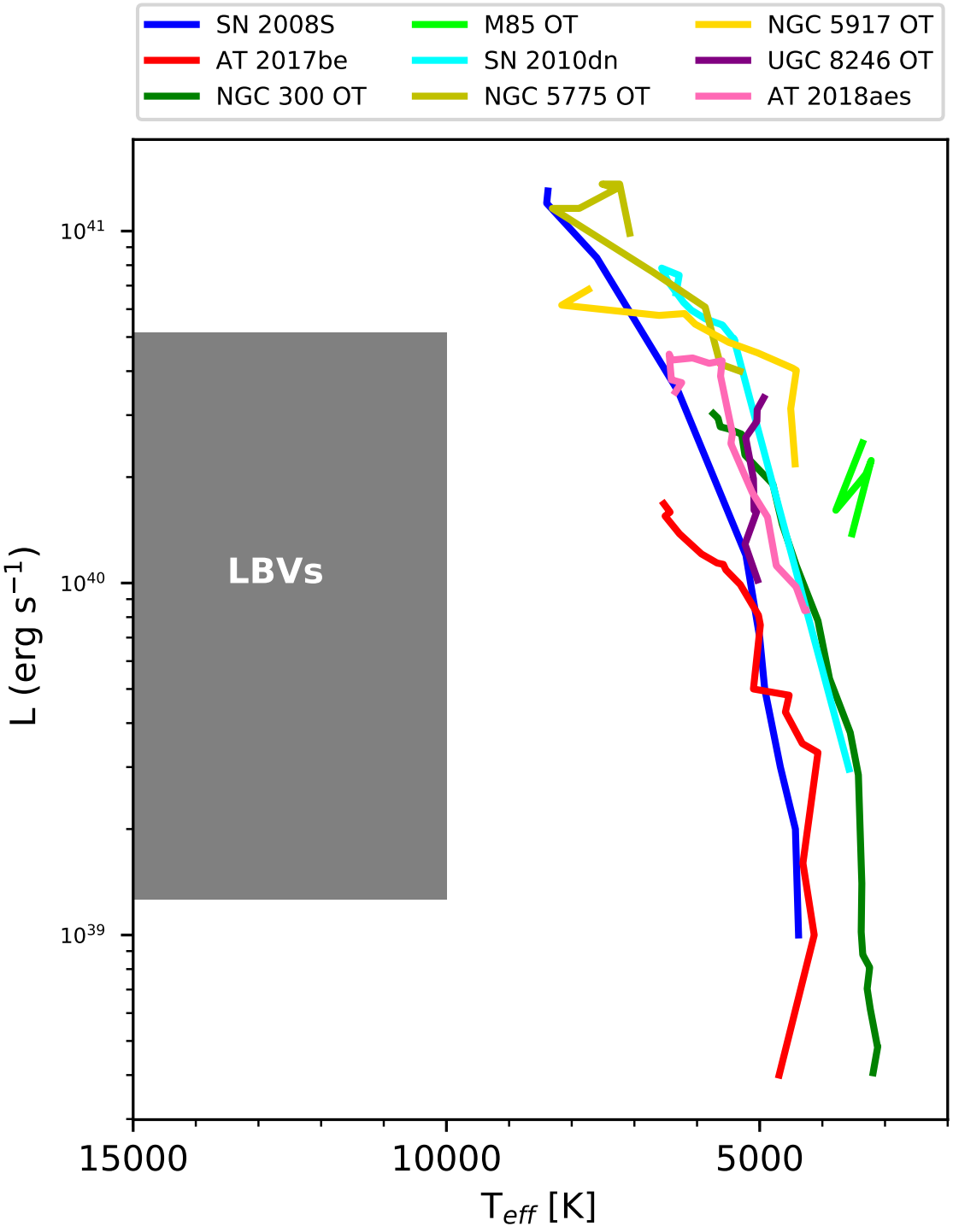

Figure 4.11: Luminosity (L) vs. effective temperature (T). ILRTs are marked as solid lines with different colours, while LBVs are marked with a shaded grey patch.

4.5.2 Rate estimates

In last 10 years (2008 - 2018), we have collected 9 ILRT events; the observed rate of discoveries is 0.9 events per year, and it does not account for the luminosity distribution of ILRTs and the efficiency or the observing strategies of the surveys. According to their distances, ILRTs are distributed in a volume of 113 097 Mpc^3 within the radius of 30 Mpc. Hence, we obtain a volumetric rate of ILRTs around 8×10^{-6} $Mpc^{-3}yr^{-1}$. Under this time coverage and volume range, we discovered 136 CC SNe [14] and thus its rate is 1.2×10^{-4} $Mpc^{-3}yr^{-1}$. Therefore, the rate of ILRTs is accounting for 7% of CC SNe. We note that Thompson et al. (2009) estimated an EC SN rate of 2%-10% of CC SNe in 10 years (before 2008), which is in agreement with our rough estimates. On the other hand, for a standard Salpeter Initial Mass Function (IMF; Salpeter 1955), and assuming that all stars from M_{max} 9.25 to 20 $M_\odot$ form CC SNe, the EC SN fraction is only about 6%. In this computation, the mass range of EC SNe (M_{min} = 9 $M_\odot$ to M_{max} = 9.25 $M_\odot$) is based on Poelarends et al. (2008)'s estimation. This theoretical prediction is roughly consistent with our rate estimate based on the observations.

4.5.3 Plausible scenarios for ILRTs and conclusions

Although several plausible scenarios have been proposed to explain ILRTs, their nature is still debated. As we discussed in Chapters 1.3.1 and 3, possible scenarios include LBV-like eruptions, LRN nature (stellar mergers), and EC induced SN explosions.

* As mentioned in Chapter 1.3.3, LBVs originate from massive star (> 20 $M_\odot$) eruptions, showing irregular light curves and SN IIn-like spectra [15]. A luminous progenitor is expected to be detected in pre-outburst optical/NIR images. No ^{56}Ni is expected to be produced. In addition, LBVs and ILRTs are distributed in two separate regions in the L-T diagram (see Figure 4.11). Our observables in (i), (iv), (v), (vii) disfavour a LBV-like eruption scenario for ILRTs.

* LRNe (see Chapter 1.3.2 and following Chapter 5) are another sub-class of gap transients, showing double-peaked (or triple-peaked) light curves and a remarkable spectral evolution. Specifically, the major decrease in the continuum temperature, the appearance of narrow metal lines in absorption, the dramatic change in the Hα strength and profile, and the emergence of molecular bands are typical spectral features of LRNe. In addition, the typical Hα FWHM velocities of LRNe are lower than 500 km s^{-1} (Pastorello et al. 2019b). The colours become progressively redder. For instance, $B - V$ can even reach about 1.8 mag at late phases (see Figure 4 of Pastorello et al. 2019b). They are likely produced by the coalescence of two stars. The observational features specified above for LRNe are different from ILRT ones (see (i), (ii), (v), (vi), (vii)). Hence, we disfavour a LRN nature for ILRTs.

* Stars with initial mass 8-10 $M_\odot$, previously experience a S-AGB phase with severe mass loss, and finally die as CC SNe induced by EC (see Chapters 1.3.1 and 3). Hence, EC SNe are expected to explode with low energy, low ejected ^{56}Ni mass, and a dense CSM. Our observational arguments (iii), (iv), (vi), and (vii) are in agreement with theoretical expectations. In addition, the Hα FWHM velocities (see (iii)) are lower than faint Type II SNe, and significantly lower

[14] Bright SNe archive `http://www.rochesterastronomy.org`;
Asiago SN group archive `http://graspa.oapd.inaf.it/asnc.html`.

[15] Although the [Ca II] doublet is sometimes visible in LBV spectra, LBVs have constant appearance of this signature in their spectra are never discovered so far.

than typical CC SNe, making ILRTs different from canonical CC SNe. Another argument in (viii) favours terminal SN explosions for ILRTs.

The observables of ILRTs disfavour LBV and LRN scenarios, and support EC SNe. In addition, the possibly trends existed in physical parameter correlations, along with homogenous observational properties and the L-T evolution, suggest all ILRTs are regulated by the same mechanism, very likely the EC SN scenario. And, the estimated ILRT event rate is roughly in agreement with theoretical prediction. Although we believe that M85 OT2006-1 and PTF10fqs are ILRTs on the basis of some observational arguments, a LRN scenario for them was previously proposed by Kulkarni et al. (2007); Kasliwal & Kulkarni (2010). We will discuss the nature of controversial objects, such as AT 2018hso and AT 2019abn, in Chapter 5.

Chapter 5

A transitional gap transient AT 2018hso in NGC 3729

As mentioned in previous chapters, many new types of Gap Transients are announced by modern all-sky surveys. This Gap Transient zoo is sparsely populated by giant eruptions of Luminous Blue Variables (LBVs) (e.g., Humphreys & Davidson 1994; Smith et al. 2011; Mehner et al. 2013), Intermediate Luminosity Red Transients (ILRTs; e.g., Botticella et al. 2009; Thompson et al. 2009; Cai et al. 2018), and Luminous Red Novae (LRNe; e.g., Williams et al. 2015; Goranskij et al. 2016; Lipunov et al. 2017; Pastorello et al. 2019b). However, with the emergence of some peculiar objects showing transitional observational properties, their classification is sometimes problematic. In particular, early time spectra of different types of Gap Transients are usually very similar, and their discrimination on the basis of a single classification spectrum may lead to errors. This problem is critical when we need to clarify ILRTs and LRNe.

ILRTs have single-peaked light curves, with shapes resembling those of faint SNe. Their spectra show prominent Balmer emission features, along with weak Fe II, Na I D and Ca II lines. In particular, the [Ca II] doublet feature, prominent at all phases, is a typical observational signature of ILRTs (e.g., Botticella et al. 2009; Berger et al. 2009b; Cai et al. 2018). ILRTs are observationally in agreement with low-energy explosion within a dusty CSM shell, and that they are physically consistent with be EC induced SN explosions from S-AGB stars (see, e.g., Botticella et al. 2009; Prieto et al. 2008; Pumo et al. 2009). Detailed discussions on ILRTs can be found in Chapters 1, 3 and 4.

LRNe make a distinct group of Gap Transients, which usually display double-peaked light curves (e.g., Kankare et al. 2015; Blagorodnova et al. 2017; Pastorello et al. 2019b) and a peculiar spectral evolution with time. In particular, a forest of narrow metal lines in absorption are detected in the spectra during the second light curve maximum, and broad molecular absorption bands (e.g., CaH, CN, TiO, and VO) are observed at very late epochs (Mason et al. 2010; Barsukova et al. 2014; Blagorodnova et al. 2017; Pastorello et al. 2019b). LRNe are very likely produced by extreme interaction in a close binary system leading to common-envelope (CE) ejection. The final outcome is likely a merger (e.g., Tylenda et al. 2011; Kochanek et al. 2014; Pejcha et al. 2016a, 2017; Metzger & Pejcha 2017; MacLeod et al. 2017; Pastorello et al. 2019b). More details on LRNe are presented in Section 1.3.2 of Chapter 1.

While most LRNe have a robust classification (see, e.g., AT 2017jfs; Pastorello et al. 2019b), oc-

casionally their discrimination from ILRTs is a difficult task (see, e.g., the previous confusing objects of PTF 10fqs, M85-2006OT1, and a recent transient AT 2019abn; Kulkarni et al. 2007; Pastorello et al. 2007a; Kasliwal et al. 2011; Burke et al. 2019; Jencson et al. 2019). In this chapter, we report the study of a transient, AT 2018hso, showing hybrid spectro-photometric properties that challenge the existing paradigm of LRNe. This suggests the need of monitoring the entire evolution of gap transients to avoid misclassifications. This work has been published in A&A Letter [1] (Cai et al. 2019).

5.1 Object information

AT 2018hso (also known with the survey name ZTF18acbwfza) was discovered on 2018 October 31.53 (UT) by the Zwicky Transient Facility (ZTF[2]) (De et al. 2018). Its coordinates are RA=$11^h33^m51.96^s$, Dec=+53°07′07.10″ [J2000], 24.9″ south, 23.7″ east of the core of the face-on, late-type galaxy NGC 3729.

The distances to NGC 3729 reported in the NASA/IPAC Extragalactic Database (NED[3]) are based on the Tully-Fisher method (e.g., Willick et al. 1997; Tully et al. 2009), and range from 21.10 to 21.88 Mpc. The kinematic distance corrected for Virgo Infall and obtained adopting a standard cosmology (H_0=73 km s^{-1}Mpc^{-1}, Ω_M=0.27, Ω_Λ=0.73) is $d_k = 20.80 \pm 1.5$ Mpc (Mould et al. 2000), and is in good agreement with Tully-Fisher estimates. Hence, hereafter, we will adopt as distance to NGC 3729 the weighted average of the above values, $d = 21.26 \pm 0.56$ Mpc, which provides a distance modulus $\mu = 31.64 \pm 0.06$ mag.

The Galactic reddening at the coordinates of AT 2018hso is very small, $E(B-V)_{\rm Gal} = 0.01$ mag (Schlafly & Finkbeiner 2011). Early spectra have modest resolution and limited signal-to-noise (SNR), while late-time spectra are affected by the presence of a forest of absorption metal lines. Yet, for an indicative estimate of the host galaxy reddening, we average the measured equivalent widths (EWs) of the Na I D absorption in two early spectra (at −3.8 and +11.3 days), obtaining $EW = 1.8 \pm 0.5$Å. Following the relation in Turatto et al. (2003), we obtain a host galaxy reddening $E(B-V)_{\rm Host} = 0.29 \pm 0.08$ mag. The total line-of-sight reddening is therefore $E(B-V)_{\rm Total} = 0.30 \pm 0.08$ mag.

5.2 Photometry

We started the monitoring of AT 2018hso soon after its discovery, with the follow-up campaign lasting ∼ 300 days. The photometric data were reduced using the *SNoOpy*[4] pipeline, following an ordinary PSF-fitting method as detailed in Section 2.1.1 of Chapter 2. The resulting optical and NIR apparent magnitudes are reported in the Appendix 7 (Tables 12 and 13). The multi-band light curves are shown in the top panel of Figure 5.1. The r-band light curve rises to the first maximum (on MJD=

[1] DOI: https://doi.org/10.1051/0004-6361/201936749

[2] ZTF: `https://www.ztf.caltech.edu/`

[3] NED: `http://nedwww.ipac.caltech.edu/`

[4] SNOoPy is a package developed by E. Cappellaro which performs photometry of point-like sources in complex environments using PSF-fitting and template subtraction methods. A package description can be found at `http://sngroup.oapd.inaf.it/snoopy.html`.

58431.0 ± 1.0) in ∼ 8 days. The peak magnitude is $r \sim 18.40$ mag (reddening-corrected $M_r \sim -13.93$ mag). After that, the r-band light curve first declines (∼ 5.3 mag/100d), then it slowly rises again to a second, fainter maximum at around 80 days (on MJD ≈ 58515). The magnitude of the second peak is $r \sim 19.57$ mag (reddening-corrected $M_r \sim -12.76$ mag). A monotonic decline follows, which is initially slow (∼ 1.7 mag/100d), but later it rapidly increases to about 3.8 mag/100d. While the i and z bands have a similar evolution as the r band, the bluer bands (B, g, and V) show a sort of plateau. The few u-band detections show a roughly linear decline of ∼ 15.7 mag/100d. The NIR light curves resemble those in the red bands, showing a more evident, long-duration (∼ 150 days) second maximum, followed by a moderate decline (∼ 1.3 mag/100d) starting from ∼ 190 days.

We compare the r-band absolute light curve of AT 2018hso with some well-followed Gap Transients, two ILRTs (SN 2008S and AT 2017be) and two LRNe (NGC4490-2011OT1 and AT 2017jfs, see bottom panel of Figure 5.1). Their absolute magnitudes range from -12 to -15.5 mag. ILRTs show a single-peaked, SN-like light curve, whilst LRNe have double-peaked light curves. We note that AT 2018hso reveals a transitional light curve, between ILRTs and LRNe, with a first sharp blue peak followed by a much shallower and broader red peak.

5.3 Spectroscopy

Our spectroscopic campaign spans a period of eight months, from ∼ −4 to +233 d, of the AT 2018hso evolution. We collected 10 epochs of spectroscopic observations with the 2.56-m Nordic Optical Telescope (NOT [5]) equipped with ALFOSC. In addition, through approved Director's Discretionary Time (DDT [6], PI: A. Morales-Garoffolo), a very late spectrum was obtained on 2019 June 29 with the 10.4-m Gran Telescopio Canarias (GTC [7]) plus OSIRIS (see details in Table 5.1). The spectra were processed following standard tasks in IRAF [8]. The spectral evolution of AT 2018hso is presented in Figure 5.2, while the comparison with ILRTs AT 2017be and SN 2008S, and LRN AT 2017jfs is shown in Figure 5.3. Prominent spectral lines are marked in Figure 5.3.

The spectral evolution of AT 2018hso is characterised by three distinct phases, in analogy with the behaviour of other LRNe (Pastorello et al. 2019b). At early epochs (until ∼30 d), the spectra show a blue continuum, with prominent Balmer lines, along with a number of Fe II features, Na I D (λ=5890, 5896 Å), and Ca II emission lines (see Figure 5.2 and Figure 5.3, top panel). The temperature inferred from the spectral continuum, assuming a black-body spectral energy distribution, decreases from around 8800 ± 800 K (at -3.8 d) to 6800 ± 600 K (at +11.3 d). We measured the full width at half-maximum (FWHM) velocity of Hα through a Lorentzian fit, and obtained $v_{\rm FWHM} \sim 500$ km s^{-1} (accounting for the instrumental resolution, see Table 5.1). This early-time velocity is similar to those measured for LRNe, but also some ILRTs, such as AT 2017be (also fitted by Lorentzian function, ∼ 500-800 km s^{-1}; Cai et al. 2018). A prominent Ca II NIR triplet (λ=8498, 8542, 8662 Å) is detected in emission in the AT 2018hso spectra, along with a very weak [Ca II] doublet (λ=7291, 7328 Å). We remark that a prominent [Ca II] is an ubiquitous feature in the spectra of ILRTs at all

[5] http://www.not.iac.es/

[6] http://vivaldi.ll.iac.es/OOCC/night-cat/ddt-at-gtc/

[7] http://www.gtc.iac.es/

[8] IRAF is written and supported by the National Optical Astronomy Observatories (NOAO) in Tucson, Arizona. NOAO is operated by the Association of Universities for Research in Astronomy (AURA), Inc. under cooperative agreement with the National Science Foundation.

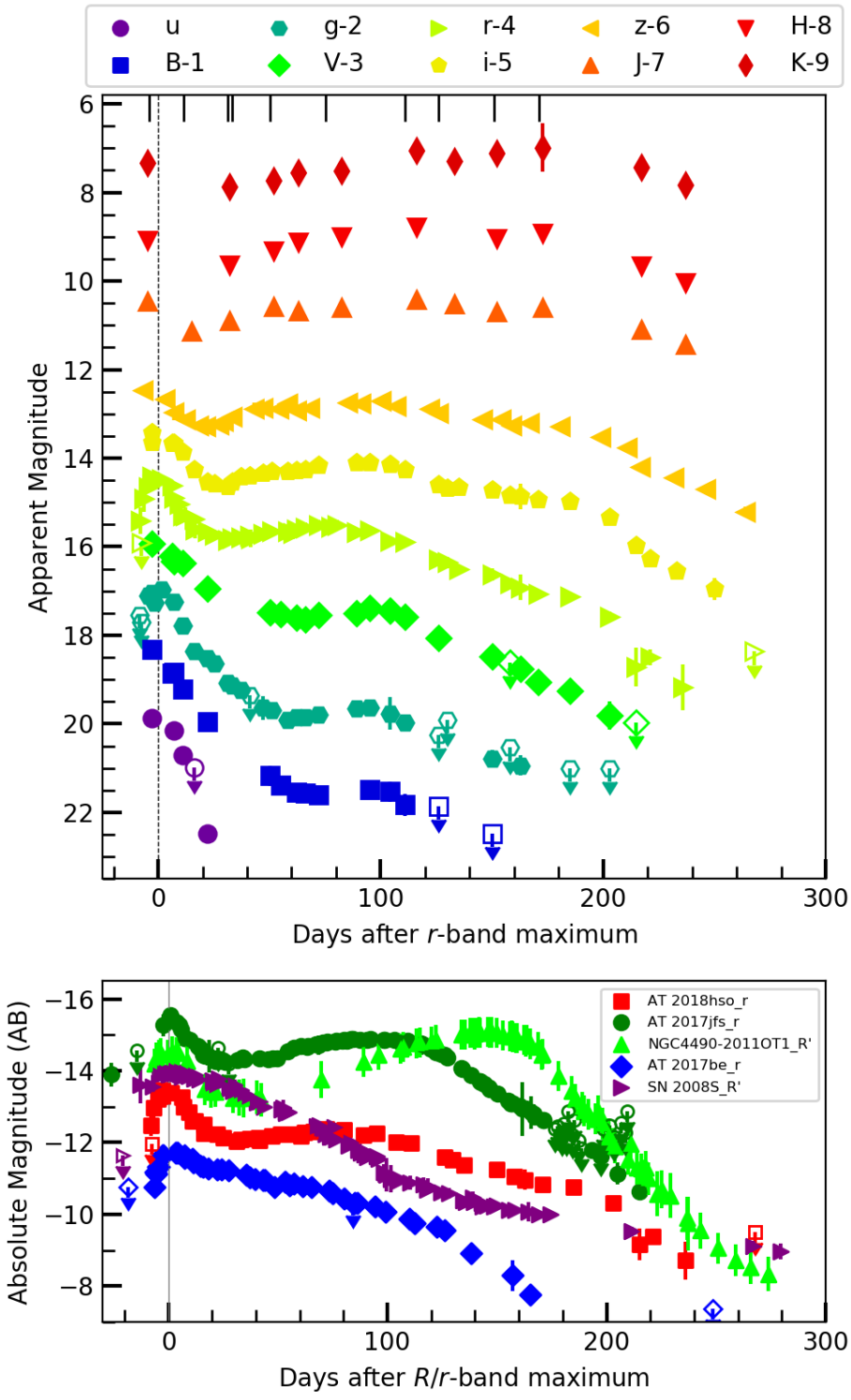

Figure 5.1: Top: Multi-band (*BVugrizJHK*) light curves of AT 2018hso. The epochs of optical spectra are also marked. Bottom: Sloan *r*-band absolute light curves of AT 2018hso, compared with those of two ILRTs, SN 2008S (Botticella et al. 2009) and AT 2017be (Cai et al. 2018), and two LRNe NGC4490-2011OT1 (Pastorello et al. 2019b) and AT 2017jfs (Pastorello et al. 2019a).

phases (Cai et al. 2018). In contrast, it has never been securely identified in LRN spectra so far. The Ca II H&K absorptions (λ=3934, 3968 Å) are not clearly detected, but the spectra are very noisy below 4000Å. All of this makes the early spectra of AT 2018hso similar to ILRTs (Figure 5.3, top panel).

During the rise to the second peak (from ∼30 d to 120 d), the spectra experience a dramatic evolution. The continuum becomes redder: the continuum temperature decreases from ∼ 4500 to 3000 K. Thus, the spectra resemble those of cool stars (K to early-M types). Hα is marginally detected at +31.2 d, and the emission component disappears until +111.0 d. In spectra with the highest S/N, we identify metal lines (Fe II, Ba II, and Sc II) in absorption. We note that these lines are also detected in ILRTs (Humphreys et al. 2011). These features, in particular the Ba II lines, are frequently detected in stellar outbursts or CC SN explosions, and originate in regions where the gas temperature is lower (Pastorello et al. 2004). As a remarkable note, the [Ca II] doublet is no longer detected. In contrast with early spectra, the NIR Ca II triplet is now seen in absorption. Ca II NIR triplet is formed by radiative de-excitation from $4p^2P_{1/2,3/2}$ to $3d^2D_{3/2,5/2}$ levels (Mallik 1997), while the [Ca II] doublet originates in low-density gas with a critical density of about 10^7 cm^{-3}, which is related to the metastable 3d^{2}D level (Ferland & Persson 1989). The strong change in these lines indicates that the gas densities evolve with time. At this phase, the spectra of AT 2018hso are reminiscent of LRNe and are clearly different from those observed in ILRTs (see Fig. 5.3, middle panel).

At very late times (over four months after peak), the spectra of AT 2018hso become slowly redder (T=2050 ± 200 K at +232.9 d)) and resemble those of a late M star. Hα becomes prominent again, with $v_{\rm FWHM}$ ∼ 370 km s^{-1} at +232.9 d as obtained by fitting a Gaussian function because the Lorentzian wings are no longer visible in the line profile. In addition, the Hα emission peak appears blue-shifted by about 300 to 400 km s^{-1} at ∼150 to 230 d respectively [9] (see right panel of Figure 5.2). This is reminiscent of the very late spectra of AT 2017jfs and NGC4490-2011OT1, supporting the LRN classification of AT 2018hso. The asymmetries in the Hα profile suggest aspherical geometry of the emitting region, or new dust formation obscuring the receding material, or both (Smith et al. 2016b; Pastorello et al. 2019b). In addition, very late spectra of AT 2018hso show broad molecular bands, such as TiO and possibly VO, CN (Figure 5.3, bottom panel). This is a key feature that allows us to distinguish LRNe from ILRTs (Pastorello et al. 2019b). Following the interpretation of Kamiński et al. (2009), we may speculate that the TiO molecular bands of AT 2018hso originate in the warm photosphere (T > 2000 K), but also in the cold outflowing material [10] (T ∼ 500 K) with a velocity about −3-400 km s^{-1}, where plausibly also VO features form.

5.4 Spectral Energy Distribution

We investigated the SED evolution of AT 2018hso using photometric data. The SEDs are selected at a few representative epochs along the whole monitoring period. The SEDs are fitted with a single Plankian function, assuming the photosphere radiates as a blackbody. At early phases, before the blue peak, the object was only occasionally observed. When individual broad-band data are not available, the missing point is estimated by interpolating the data at two consecutive epochs, or by extrapolating from the last available observation. All of this implies larger errors. At 30-110 d, the optical plus NIR SEDs are well reproduced with a single blackbody. Instead, although at later phases blue-band

[9] Narrow absorptions are found at +126.1 d and +171.0 d, are likely due to over-subtraction of contaminating background.
[10] Polar gas outflows are observed in the Galactic LRN V838 Mon (Kamiński et al. 2009).

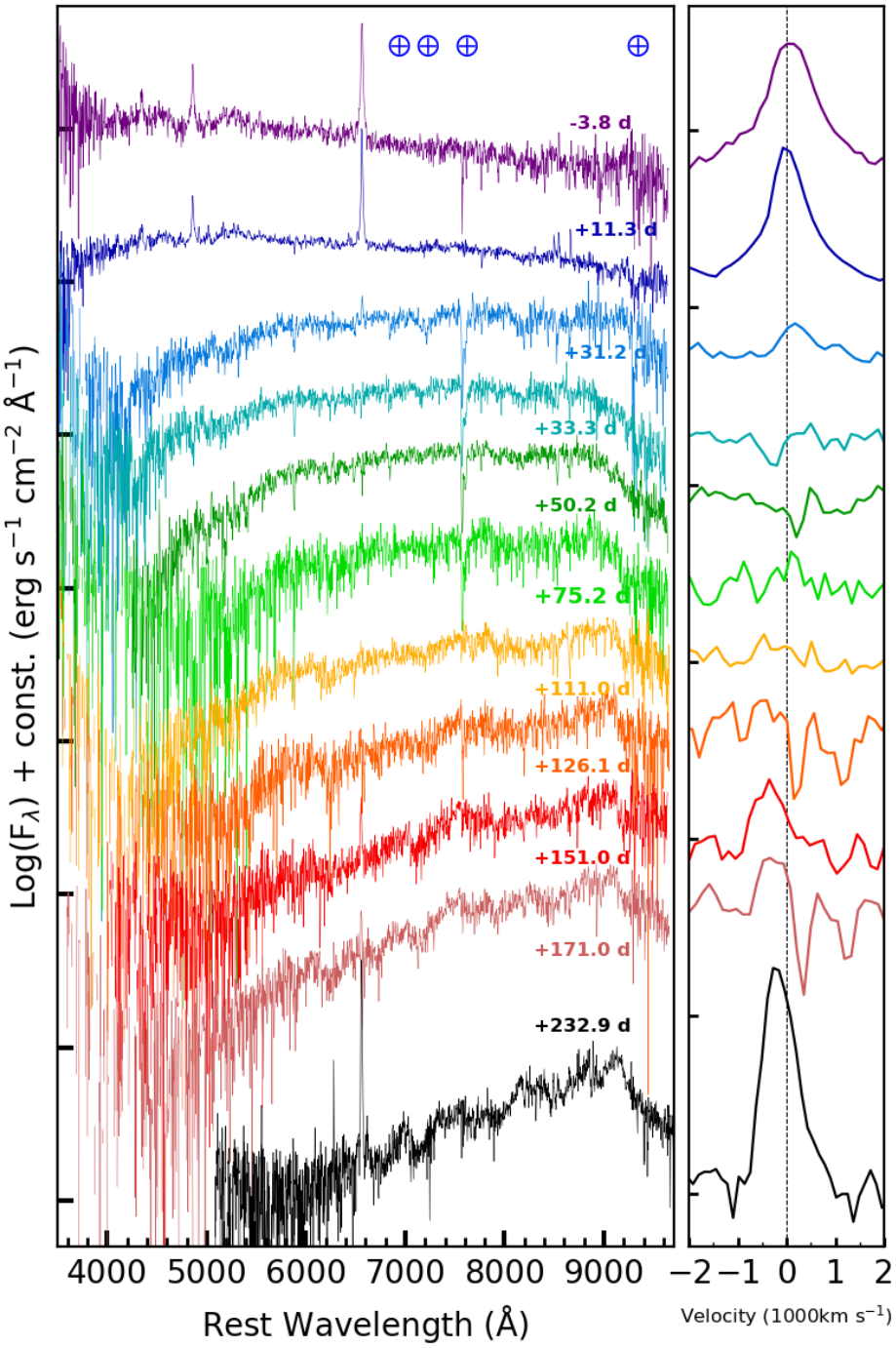

Figure 5.2: Left: Spectral evolution of AT 2018hso, from −3.8 to +232.9 days. Right: Temporal evolution of Hα profile in velocity space. The vertical dotted line marks the rest velocity. All spectra are redshift-corrected (z = 0.003536, see NED). The phases are from the r-band maximum (MJD = 58431.0 ± 1.0).

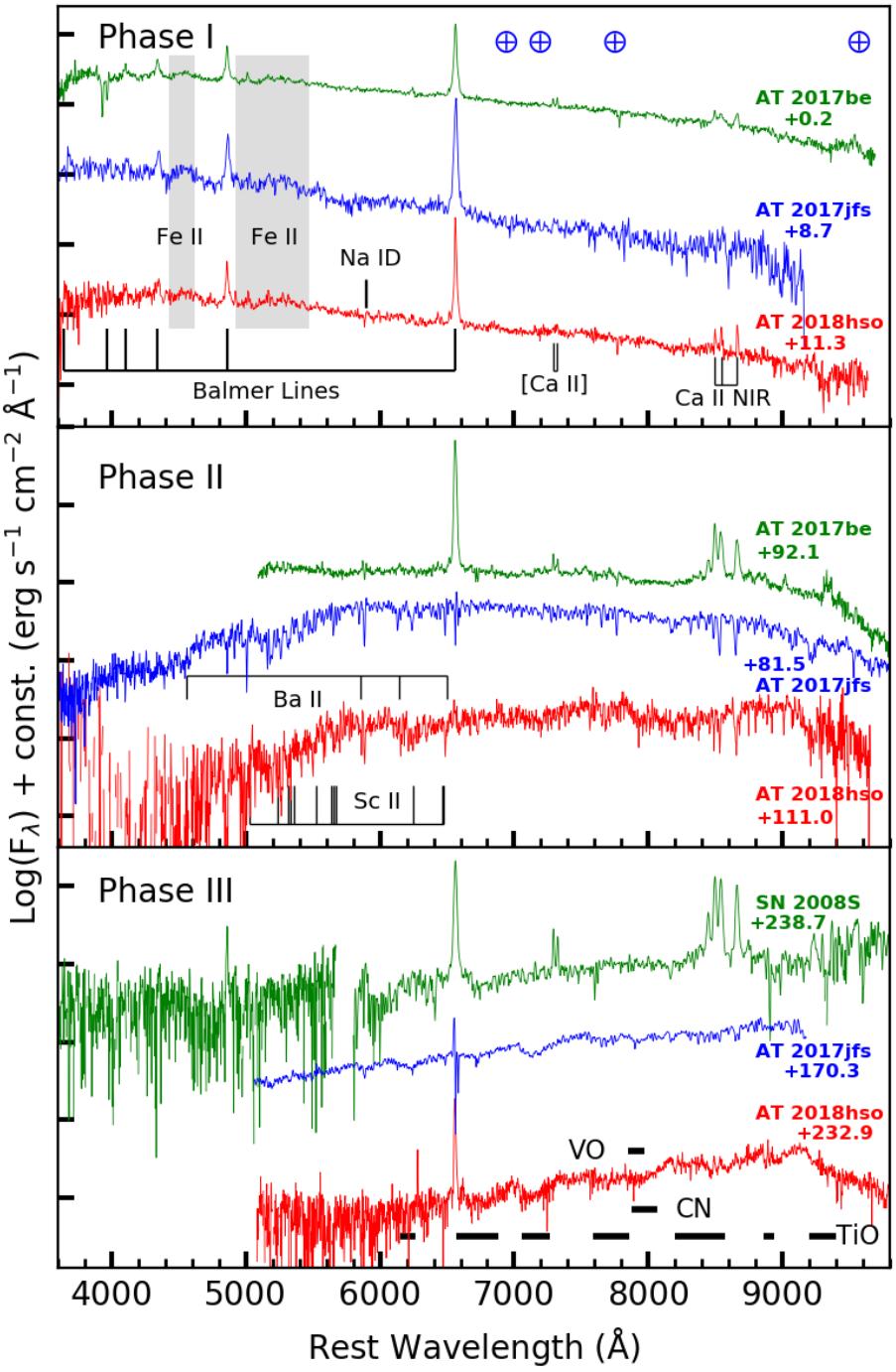

Figure 5.3: Spectral comparison of AT 2018hso with LRN AT 2017jfs, and ILRTs AT 2017be and SN 2008S, with line identification. The spectra are selected at three representative epochs: Phase I (0 to +10 d; top panel); Phase II (95 ± 15 d; middle panel); Phase III (>170 d; bottom panel). Phases are from the R/r-band maximum. All spectra are redshift and reddening corrected. The data of comparison objects are from Cai et al. (2018); Botticella et al. (2009); Pastorello et al. (2019a)

Table 5.1: General information of the spectroscopic observations of AT 2018hso.

Date		Phase [a] (days)	Telescope+Instrument	Grism+Slit	Spectral range (Å)	Resolution (Å)	Exp. time (s)
20181105	58427.2	−3.8	NOT+ALFOSC	gm4+1.0”	3400-9650	15	1670
20181120	58442.3	+11.3	NOT+ALFOSC	gm4+1.0”	3500-9630	15	3600
20181210	58462.2	+31.2	NOT+ALFOSC	gm4+1.0”	3400-9600	15	3600
20181212	58464.3	+33.3	NOT+ALFOSC	gm4+1.3”	3400-9600	18	3600
20181229	58481.2	+50.2	NOT+ALFOSC	gm4+1.0”	3400-9600	15	3600
20190123	58506.2	+75.2	NOT+ALFOSC	gm4+1.0”	3400-9650	15	3600
20190228	58542.0	+111.0	NOT+ALFOSC	gm4+1.0”	3400-9650	15	3600
20190315	58557.1	+126.1	NOT+ALFOSC	gm4+1.0”	3400-9650	15	3600
20190409	58582.0	+151.0	NOT+ALFOSC	gm4+1.0”	4000-9600	15	3600
20190428	58602.0	+171.0	NOT+ALFOSC	gm4+1.0”	3600-9600	15	3600
20190629	58663.9	+232.9	GTC+OSIRIS	R1000R+1.0”	5100-10350	8	3×1800

[a] Phases are relative to r-band maximum ($\mathrm{MJD_{AT2018hso}} = 58431.0 \pm 1.0$).

(u, B, g, V) data are not available, a single blackbody does not appear to accurately fit the observed SEDs. This is even more evident during the final steep lightcurve decline (at ∼210 d). This is suggestive of a second blackbody component peaking at much longer wavelengths (mid to far IR), although it cannot be confirmed due to the incomplete photometric coverage.

The temporal evolution of blackbody temperature is shown in Figure 5.4 (top panel). The temperature rapidly declines from ∼8000 K at maximum to ∼4000 K at about 30 d. Then, it declines more slowly to ∼3000 K until 180 d. A steeper temperature drop (to around 2500 K) follows at ∼210 d. The inferred bolometric luminosity, obtained integrating the SEDs along the full electromagnetic spectrum, is shown in the middle panel of Figure 5.4. The luminosity at peak is about 10^{41} erg s^{-1}, then it rapidly declines to a minimum ($L \sim 3.2 \times 10^{40}$ erg s^{-1}), rises again to the second, red maximum ($L \sim 4.4 \times 10^{40}$ erg s^{-1}), and finally rapidly drop to $L \sim 1.6 \times 10^{40}$ erg s^{-1}. The inferred radius, obtained through the Stefan-Boltzmann law ($L = 4\pi R^2 \sigma T^4$; where σ is the Stefan-Boltzmann constant), is shown in the bottom panel of Figure 5.4. The radius remains roughly constant at $\sim 2 \times 10^{14}$ cm (almost 2 900 $R_\odot$) during the first ∼30 d, then it rapidly increases to $\sim 5.3 \times 10^{14}$ cm (exceeding 7 600 $R_\odot$) at ∼80 d, to increase by a modest amount later. A significant increase in the radius is observed after ∼ 210 d (although affected by large uncertainties), and exceeds $\sim 7.2 \times 10^{14}$ cm ($R \sim 10\,350\ R_\odot$).

The above parameters of AT 2018hso are compared with those of a few ILRTs and LRNe in Figure 5.4. While the temperature evolution is not relevant to discriminate the two classes, the bolometric light curve and the radius evolution are markedly different in LRNe and ILRTs. Specifically, ILRT light curves decline monotonically after maximum, while LRN ones reveal a second bolometric peak. The difference between LRNe and ILRTs is even more evident in the radius evolution. While in ILRTs the radius at the photosphere of the hot blackbody component declines by a factor of two (see Botticella et al. 2009), it increases by one order of magnitude during the LRN evolution, with a major increase during the rise to the second photometric peak. A further increase in the value of the radius is observed at very late phases, during the final steep optical decline. This is observed also in AT 2017jfs, at the time of a NIR brightening. In this phase, the Hα profile is blue-shifted and the spectra show

molecular bands. The different light curves and radius evolution in ILRTs and LRNe suggest that the two classes of gap transients are regulated by different physical mechanisms. The contraction of ILRT radius after peak is likely a consequence of the outer layers becoming optically thin with the expansion, with the photosphere receding into deeper ejecta. The more complex evolution of the LRN radii, already noted by Blagorodnova et al. (2017) for M101-2015OT1, is more difficult to explain. In particular, while M31-2015LRN (MacLeod et al. 2017) showed a contraction of the radius at late phases consistent with the photosphere receding with expansion, brighter LRNe are characterised by at least two phases with an almost constant radius, occurring soon after the first and the second peaks. After the first peak, the expanding ejecta lower their opacity and thus the radius in mass coordinate decreases. When these ejecta reach the material expelled during the CE phase, this gas is initially heated, and a second photosphere forms far out leading the radius to increase. The ejecta plus CE shocked region expands remaining optically thick, hence the photospheric radius grows.

5.5 On the nature of AT 2018hso

AT 2018hso shows transitional light curves between ILRTs and LRNe, and early spectra similar to those of ILRTs. However, we favour a LRN classification for the following reasons:

- The spectra experience a major temporal evolution. Early-time spectra resemble those of ILRTs. Nonetheless, the [Ca II] doublet vanishing with time, the tremendous change of Hα profile, and the late appearance of molecular bands support the LRN scenario for AT 2018hso.

- In analogy to other LRNe, it peaks at an absolute magnitude of $M_{\rm r} \sim -13.93$ mag after a fast rise lasting about 8 d.

- The SED and the evolution of the photospheric radius are similar to those observed in other LRNe.

- The decay time from peak luminosity ($L_{\rm peak} \approx 10^{41}$ erg s^{-1}) to $0.5L_{\rm peak}$ is around 15 days, located near the LRN region in the luminosity vs. $\tau_{0.5\rm dex}$ diagram of Pastorello & Fraser (2019, see their figure 1).

- The outflow velocity of AT 2018hso is around 400 km s^{-1}, placing it slightly below NGC4490-2011OT1 in the $L_{\rm peak}$ vs. $v_{\rm out}$ diagram of Mauerhan et al. (2018), but still well aligned with other LRNe.

To add further support to the LRN classification, we inspected HST images obtained from the Hubble Legacy Archive. NGC3729 was observed on 2004 Nov. 17 with HST+ACS. Unfortunately, these observations were quite shallow, consisting of 2×350s in F658N, and 120s in F814W. In order to locate the position of the SN on these images, we aligned the drizzled F814W HST image to the NOT+AFOSC *i*-band image taken on 2019 Jan 14. Only five sources were used for the alignment, which has an RMS scatter of 0.12″. In light of the small number of fiducial sources for the alignment, we caution that there could be a larger systematic uncertainty in position. A bright source is detected with S/N ≈17, within 2σ of the transformed SN position (see Figure 5.5). From the density of sources close to the location of AT 2018hso in the HST images, we calculate that the probability

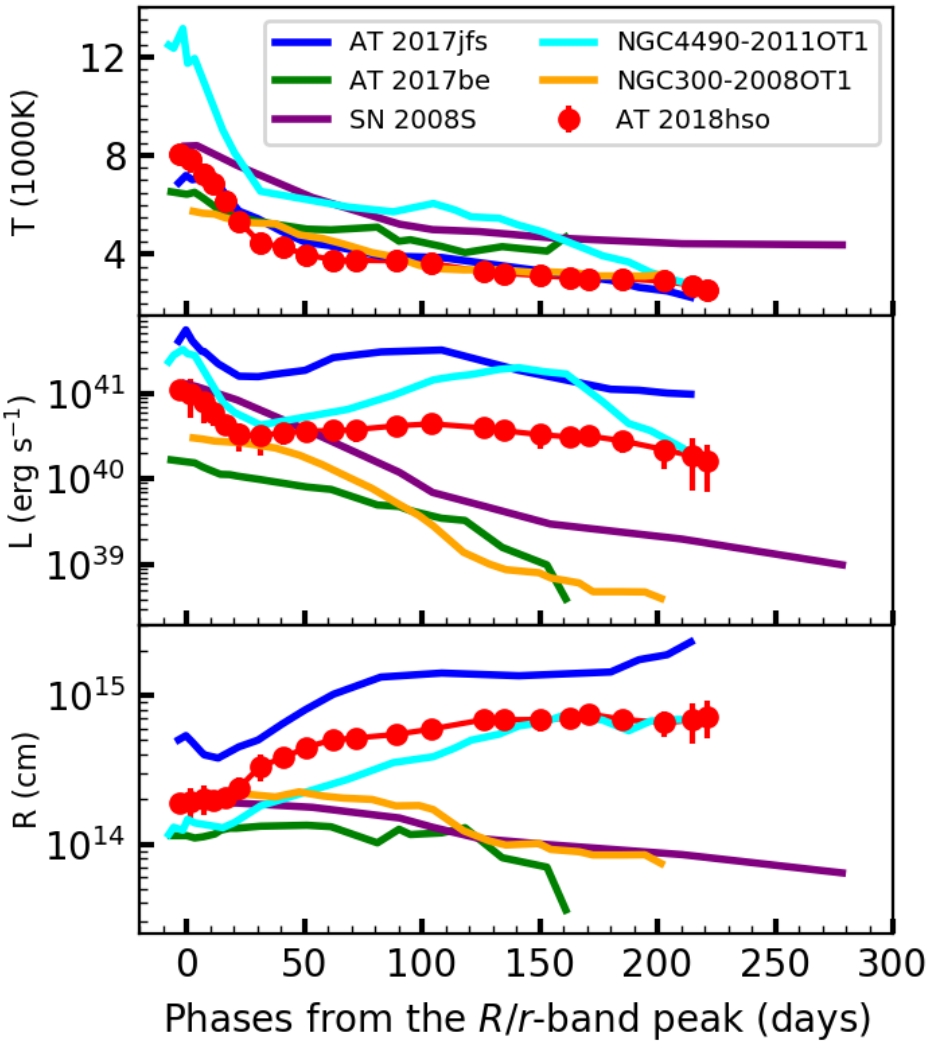

Figure 5.4: Comparison of AT 2018hso with three ILRTs (SN 2008S, NGC300-2008OT1 and AT 2017be; dashed lines), and two LRNe (AT 2017jfs, NGC4490-2011OT1; solid lines). Top: Evolution of Blackbody temperatures. Middle: Bolometric light curves. Bottom: Evolution of the photospheric radii. The data are from Botticella et al. (2009), Humphreys et al. (2011), Cai et al. (2018), and Pastorello et al. (2019a,b).

of a chance alignment with a source as bright as the progenitor candidate is 6%. Using DOLPHOT, we measure $F658N = 23.29 \pm 0.16$ mag and $F814W = 23.56 \pm 0.07$ mag (Vegamag, in the HST system), for the object. At the adopted distance, twe obtain an absolute magnitude of $M_I \sim -8$. This is at least plausibly consistent with a pre-merger system that has started to brighten around fifteen years before the coalescence, similar to what observed in the 2015 LRN in M101 (Blagorodnova et al. 2017). However, in the absence of more precise astrometry, and at the spatial resolution of our data at the distance of NGC 3729, we cannot exclude that this is a cluster, or an unrelated source. Late time observations after the merger has faded and cooled will reveal if this was the progenitor system, as we would expect this source to become dust-enshrouded, disappearing (or at least fading) in the optical. Pastorello et al. (2019b) studied a large sample of LRNe, supporting for them a stellar merger scenario in a binary system following the ejection of a CE (e.g. Tylenda et al. 2011; Kochanek et al. 2014; Pejcha et al. 2016a, 2017; MacLeod et al. 2017). Kochanek et al. (2014) and Smith et al. (2016b) suggested that energetic LRN events, such as NGC4490-2011OT1, are likely the outcome of massive ($10 \leq M \leq 50$ $M_\odot$) binary mergers. In this context, as AT 2018hso has a plausible luminous source detection and only marginally fainter than NGC4490-2011OT1, its progenitor system was very likely quite massive (Kochanek et al. 2014).

From the study of the spectro-photometric evolution of AT 2018hso and the possible detection of the progenitor system in archive HST images, we provided reasonable arguments for classifying AT 2018hso as a LRN, although with somewhat peculiar characteristics. So far, to our knowledge, only two other objects have controversial ILRT/LRN classifications. Although M85-2006OT1 was proposed to be a LRN (Kulkarni et al. 2007; Rau et al. 2007), Pastorello et al. (2007a) questioned this classification, and an ILRT scenario is still plausible from observational arguments (Kochanek et al. 2014; Pastorello et al. 2019b). Another gap transient, AT 2019abn, was classified as an ILRT by Jencson et al. (2019) on the basis of follow-up observations lasting $\sim$ 110 d and a detailed study of the progenitor in pre-outburst stage. However, the initial weakness of the [Ca II] doublet and its later disappearance (see Figure 5.6) are reminiscent of LRNe. Only the lack of strong TiO and VO bands in the optical spectra will provide further support to the ILRT classification. All of this suggests the existence of a grey zone in our ability to distinguish the different classes of gap transients.

We have limited knowledge on ILRTs and LRNe due to the still modest number of discoveries and incomplete data sets. Well-sampled light curves in a wide range of wavelengths, high-resolution spectroscopy, and detailed modelling are crucial to clarify the nature of both families of gap transients. The support of future generation instruments such as the Large Synoptic Survey Telescope (LSST; LSST Science Collaboration et al. 2009) and the Wide Field Infrared Survey Telescope (WFIRST; Spergel et al. 2015) is essential to largely increase the number of well-monitored gap transients, crucial to fine tune existing theoretical models.

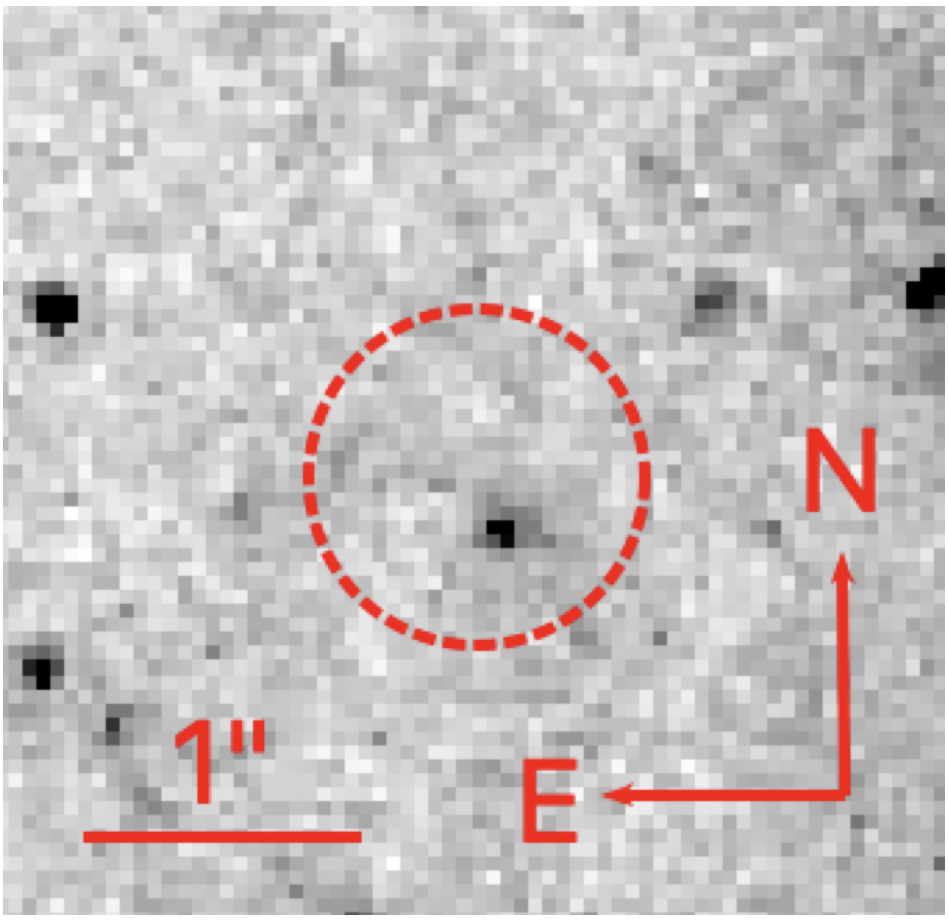

Figure 5.5: Pre-outburst archive image of AT 2018hso obtained with HST+F814W. The red dashed circle shows 5x RMS (0.6″) uncertainty in the position.

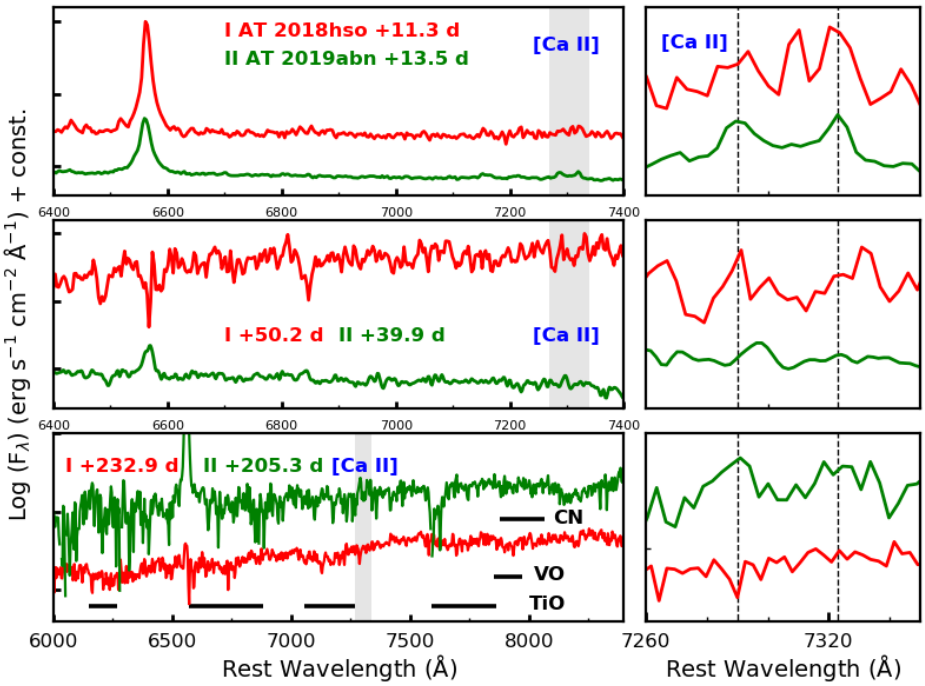

Figure 5.6: Spectral comparison of AT 2018hso and AT 2019abn. Left: spectral evolution at three representative phases: ∼12±1 d (top); ∼45±5 d (middle); ≥200 days (bottom). The molecular bands are identified in the left bottom panel. The [Ca II] doublet is marked with a shaded grey region in three left panels. Right: blow-up of the [Ca II] doublet profile at the the same phases. Phases are from their *r*-band maximum.

Chapter 6

Conclusions and future outlook

In this thesis, I studied ILRTs and LRNe, two subtypes of Intermediate Luminosity Optical Transients, following two different approaches: an individual investigation and a statistical study on a wide sample. Specifically, we performed detailed studies of the ILRT AT 2017be and the LRN AT 2018hso. Then, we focused on a systematically study of the spectro-photometric properties of a large sample of ILRTs (SN 2010dn, PSN J14535395+0334049, PSN J15213475-0722183, PSN J13100734+3410514 and AT 2018aes, plus other five published ILRTs). The data presented in this thesis are primarily collected through the *NUTS1/NUTS2* and *PESSTO* collaborations.

An extensive optical plus near-IR data set was obtained for AT 2107be (see Chapter 3). Pre-explosion images of HST and Spitzer allowed us to directly inspect the progenitor site, leading us to rule out a massive LBV progenitor for this transient. Post-explosion monitoring allowed us to constrain its observational features, and we inferred they are consistent with those of other ILRTs. We also performed a systematical study of a wider ILRT sample in Chapter 4, constraining their observational properties to be relatively homogenous and suggesting some possible parameter trends. All studies on ILRTs are suggestive of a common physical mechanism, which is very likely the EC SN scenario. On the other side, a new transient, AT 2018hso, showed transitional properties between those of ILRTs and LRNe. Through the detailed analysis of the observed parameters, our study supported that it actually was a LRN, likely produced by the coalescence of two massive stars. Although ILRTs and LRNe originate from different physical mechanisms, some observational overlap exists between them, as indicated by the discovery of AT 2018hso. The results, mentioned in Chapter 5, reveal more overlap in the observables of ILRTs/LRNe than thought in the past. These observations make the discrimination of the subtypes sometimes controversial, and only monitoring the entire evolution of gap transients may allow us to secure a solid classification.

The aim of my PhD projects is investigating the properties of ILRTs and LRNe in the context of gap transients. We populated existing ILRT/ LRN samples in the luminosity (L) vs. effective temperature (T), and peak luminosity (L_{peak}) vs. time scale ($\tau_{0.1dex}$) diagrams (see Figure 6.1). As shown in the left panel of Figure 6.1, although ILRTs and LRNe lie at a close region, they can be distinguished from their luminosity-temperature evolution. Specifically, ILRTs decline in a monotonic way, while LRNe show distinct double-peaked curves. This can be a physical indicator to classify them. Some typical transients are shown in the right panel of Figure 6.1, such as thermonuclear SNe, CC SNe, and SL SNe, along with kilonovae and classical novae. The regions, with peak luminosities between $\sim 5 \times 10^{39}$ erg s^{-1} and 1×10^{41} erg s^{-1} and time scale range of about 60 - 120 days, are mostly populated

by ILRTs. However, LRNe lie in the same peak luminosity range but usually have larger visibility time scales, around 150 days. The decay time ($\tau_{0.1dex}$) can discriminate the two sub-types, although some overlap still exists. The gap transient region is still under-populated and poorly studied. We have estimated a discovery event rate of about 0.9 yr^{-1} in last ten years (from 2008 to 2018) for ILRTs and they accounted for about 7% in CC SNe (see 4.5.2). On the other side, LRNe have observed Galactic rate of about 0.1 yr^{-1} for M_V brighter than −7 mag, while slightly lower rates (0.03 yr^{-1}) are expected for LRNe brighter than −10 mag (Kochanek et al. 2014). In addition, Kochanek et al. (2014) also estimate an integral Galactic rates of about 1-5 $\times$ 10^{-3} yr^{-1} for events having absolute magnitudes of −13 to −15 mag. Both ILRTs and LRNe have limited samples, hence the increasing number of events are crucial to improve our rate estimates, to define their classifications, and to understand their physical mechanisms.

Although some studies have increased our knowledge on the observational features and the physical mechanisms producing them, a lot of work still needs to be done. For instance, little pre-explosion/pre-outburst information exists for ILRTs/LRNe, and this prevent us to identify the progenitor in quiescence. The lack of entire electromagnetic coverage, particularly in the mid-IR domain, makes incomplete our knowledge on the integral SED evolution. High-cadence photometric follow up and high-resolution spectra are fundamental to clarify the reasons of their observational heterogeneity, as these observables are sometimes connected with stellar intrinsic parameters, such as mass, binarity, radius, spin, and chemical composition. The discovery of a large amount of gap transients is crucial, to increase the sample of well-followed events to fine-tune their observational features. Future work needs to be done in the following directions: a) to study progenitors of ILRTs/ LRNe and recover the source location several years after outbursts, through space facilities such as the Hubble Space Telescope and the Spitzer Space Telescope. b) to explore the dust properties (such as, dust species, size, and mass) of ILRTs/LRNe is a priority. The observations at longer wavelength (e.g., mid-IR, far-IR, and radio) will help us constrain it. c) to investigate the metallicity of host galaxies. In summary, well-sampled data, theoretical modelling, and increasing samples are key steps to improve our understanding of gap transients. Future facilities, such as the Large Synoptic Survey Telescope (LSST) and the Wide Field Infrared Survey Telescope (WFIRST), have a robust machinery to largely increase the numbers of gap transients, and in combination with high-resolution spectral analysis, they will reveal new perspectives on stellar evolution.

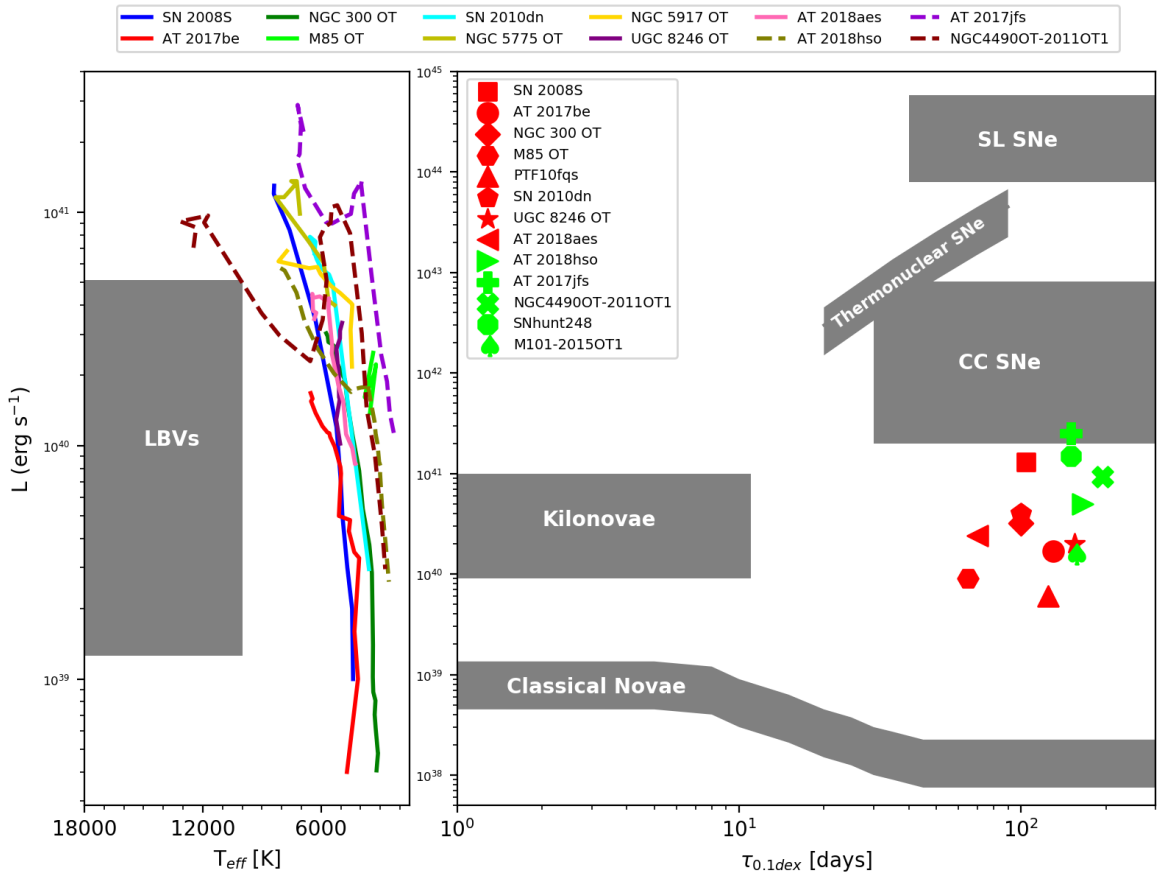

Figure 6.1: Left panel: luminosity (L) vs. effective temperature (T) for LBVs, ILRTs, and LRNe. Right panel: peak luminosity (L_{peak}) vs. time scale ($\tau_{0.1dex}$). $\tau_{0.1dex}$ is the decay time from $1L_{peak}$ to $0.1L_{peak}$. The markers with red colour are ILRTs and with green colour are LRNe.

Chapter 7

Appendix

Table 1: Optical (*BVgriz*) photometric data for AT 2017be. Early unfiltered observations are also reported.

Date	MJD	phase[a]	*B*(err)	*V*(err)	*g*(err)	*r*(err)	*i*(err)	*z*(err)	Instrument
20161229	57751.48	−18.34	···	···	···	>18.7[b]	···	···	LOSS[e]
20170106	57759.51	−10.31	···	···	···	18.71[b]	···	···	LOSS[e]
20170107	57760.12	−9.70	···	···	···	18.30	···	···	iPTF[f]
20170107	57760.16	−9.66	>17.8	···	···	···	···	···	fl05
20170107	57760.43	−9.39	···	···	···	18.347	···	···	iPTF[g]
20170108	57761.36	−8.47	18.982(0.234)	18.442(0.122)	18.645(0.216)	18.135(0.144)	18.010(0.065)	···	fl05
20170108	57761.42	−8.40	18.970(0.097)	18.454(0.061)	18.660(0.118)	18.140(0.060)	18.011(0.047)	···	fl05
20170110	57763.34	−6.48	18.286(0.278)	17.986(0.084)	18.171(0.200)	17.818(0.091)	17.742(0.083)	···	fl05
20170110	57763.42	−6.40	>17.8	>17.141	18.193(0.217)	17.821(0.199)	17.744(0.115)	···	fl05
20170116	57769.20	−0.63	18.449(0.088)	18.142(0.073)	18.276(0.123)	17.756(0.065)	17.748(0.088)	···	fl05
20170116	57769.98	+0.16	18.496(0.031)	18.167(0.034)	18.326(0.027)	17.743(0.026)	17.792(0.031)	17.783(0.068)	ALFOSC
20170120	57773.27	+3.45	18.518(0.075)	18.046(0.055)	18.209(0.059)	17.835(0.050)	17.777(0.048)	···	fl05
20170120	57773.31	+3.49	18.538(0.083)	18.067(0.046)	18.319(0.048)	17.908(0.040)	17.766(0.053)	···	fl05
20170123	57776.15	+6.33	18.733(0.023)	18.090(0.047)	···	···	17.905(0.139)	···	ALFOSC
20170123[c]	57776.95	+7.13	18.870(0.153)	18.112(0.090)	18.409(0.096)	17.914(0.083)	17.853(0.088)	17.967(0.075)	AFOSC
20170124	57777.28	+7.46	18.699(0.077)	18.160(0.057)	18.427(0.051)	18.028(0.042)	17.897(0.045)	···	fl05
20170127	57780.33	+10.51	18.852(0.087)	18.229(0.057)	18.634(0.061)	18.121(0.045)	18.037(0.052)	17.938(0.129)	fl05
20170128	57781.87	+12.05	18.989(0.074)	18.330(0.043)	18.665(0.045)	18.144(0.041)	18.028(0.051)	17.954(0.057)	ALFOSC
20170131	57784.27	+14.45	19.088(0.102)	18.358(0.065)	18.837(0.066)	18.207(0.056)	18.078(0.052)	17.927(0.106)	fl05
20170204	57788.25	+18.43	19.194(0.123)	18.427(0.066)	18.750(0.071)	18.208(0.058)	18.087(0.068)	17.996(0.122)	fl05
20170205[c,d]	57789.95	+20.13	19.297(0.043)	18.521(0.031)	18.809(0.043)	18.229(0.038)	18.058(0.031)	17.966(0.075)	ALFOSC
20170209	57793.37	+23.55	19.427(0.207)	18.435(0.089)	18.881(0.069)	18.243(0.067)	18.086(0.071)	17.974(0.150)	fl05
20170217	57801.22	+31.40	19.540(0.280)	18.668(0.106)	19.084(0.166)	18.368(0.058)	18.156(0.041)	17.988(0.084)	fl05
20170219	57803.07	+33.25	19.569(0.046)	18.627(0.099)	19.175(0.032)	18.451(0.021)	18.185(0.036)	18.058(0.040)	ALFOSC
20170221	57805.26	+35.44	19.598(0.369)	18.774(0.245)	19.214(0.399)	18.493(0.062)	18.194(0.038)	18.052(0.064)	fl05
20170225	57809.14	+39.32	19.772(0.202)	18.855(0.196)	19.275(0.192)	18.511(0.121)	18.263(0.064)	18.073(0.108)	fl05
20170225	57809.91	+40.09	19.750(0.047)	18.833(0.032)	19.288(0.031)	18.513(0.027)	18.269(0.016)	18.109(0.042)	ALFOSC
20170302	57814.28	+44.46	···	18.958(0.193)	19.364(0.107)	18.721(0.189)	18.389(0.133)	···	fl05
20170307	57819.20	+49.38	19.962(0.132)	18.946(0.060)	19.263(0.068)	18.570(0.045)	18.372(0.043)	18.112(0.085)	fl05
20170309	57821.02	+51.20	19.950(0.076)	18.923(0.047)	19.317(0.045)	18.653(0.028)	18.365(0.020)	18.153(0.040)	ALFOSC
20170311	57823.26	+53.44	20.019(0.222)	18.977(0.172)	19.359(0.132)	18.621(0.136)	18.431(0.134)	17.992(0.307)	fl05
20170315	57827.22	+57.40	20.024(0.190)	18.991(0.079)	19.387(0.058)	18.694(0.065)	18.450(0.053)	18.132(0.112)	fl05
20170319	57831.19	+61.37	20.052(0.180)	19.028(0.085)	19.406(0.084)	18.710(0.056)	18.488(0.071)	18.157(0.083)	fl05
20170327	57839.14	+69.32	20.085(0.092)	19.129(0.055)	19.595(0.055)	18.809(0.085)	18.551(0.104)	18.360(0.136)	fl05
20170328	57840.87	+71.05	20.119(0.093)	19.172(0.098)	19.604(0.176)	18.879(0.059)	18.623(0.046)	18.368(0.082)	AFOSC
20170403	57846.10	+76.28	20.122(0.191)	19.329(0.119)	19.816(0.077)	19.019(0.057)	18.785(0.051)	18.336(0.121)	fl05
20170407	57850.94	+81.12	20.216(0.079)	19.416(0.042)	19.993(0.084)	19.147(0.052)	18.831(0.040)	18.500(0.038)	ALFOSC
20170409	57852.22	+82.40	20.302(0.161)	19.414(0.127)	···	19.162(0.085)	18.817(0.072)	18.510(0.112)	fl05
20170411	57854.21	+84.39	>19.9	19.438(0.295)	19.918(0.312)	>19.2	···	···	fl05
20170414	57857.14	+87.32	20.349(0.112)	19.634(0.093)	···	···	···	···	fl05
20170417	57860.11	+90.29	20.432(0.548)	19.726(0.150)	20.259(0.065)	19.262(0.046)	18.979(0.043)	18.590(0.095)	fl05
20170421	57864.89	+95.07	20.860(0.118)	19.835(0.113)	20.287(0.051)	19.411(0.059)	19.131(0.078)	18.756(0.064)	ALFOSC
20170502	57875.87	+106.05	21.140(0.090)	20.235(0.056)	20.567(0.067)	19.599(0.045)	19.318(0.045)	18.886(0.054)	ALFOSC
20170505	57878.12	+108.30	>20.9	20.387(0.470)	20.704(0.202)	19.719(0.109)	19.344(0.105)	18.861(0.149)	fl05
20170515	57888.13	+118.31	21.303(0.469)	20.529(0.432)	¿20.8	19.824(0.106)	19.480(0.092)	18.923(0.154)	fl05
20170516	57889.89	+120.07	21.420(0.119)	20.606(0.087)	···	···	···	···	ALFOSC
20170518	57891.15	+121.33	···	···	>20.3	19.903(0.047)	19.589(0.063)	19.279(0.120)	ALFOSC
20170530	57903.89	+134.07	···	···	>21.2	20.544(0.093)	20.145(0.075)	19.767(0.204)	ALFOSC
20170618	57922.88	+153.06	···	···	···	21.172(0.427)	20.548(0.163)	20.356(0.137)	ALFOSC
20170619	57923.89	+154.07	···	21.395(0.167)	22.423(0.246)	···	···	···	ALFOSC
20170626	57930.89	+161.07	···	···	···	21.701(0.249)	21.409(0.201)	20.982(0.185)	ALFOSC
20170922	58018.19	+248.37	···	···	···	>22.1	···	···	ALFOSC
20170928	58024.18	+254.36	···	···	···	···	>22.4	···	ALFOSC
20171229	58116.17	+346.35	···	···	>22.6	>22.6	>22.5	>21.2	OSIRIS

[a] Phases are relative to *r*-band maximum light, MJD = 57769.8 ± 0.1.

[b] The original unfiltered magnitudes reported on the Vegamag system have been rescaled to ABmags.

[c] The *u*-band magnitudes for these two epochs are reported as 19.436 (0.098) and 21.160 (0.270) mag, respectively.

[d] The *R* and *I* band magnitudes for this epoch are reported as 18.037 (0.040) and 17.583 (0.035), respectively.

[e] Lick Observatory Supernova Search (LOSS) observation (using the Katzman Automatic Imaging Telescope (KAIT; http://w.astro.berkeley.edu/bait/kait.html), Lick Observatory, California, USA) obtained through the Transient Name Server (TNS; https://wis-tns.weizmann.ac.il/object/2017be).

[f] Intermediate Palomar Transient Factory (iPTF; https://www.ptf.caltech.edu/iptf) observation using Sloan-band filters, see Hosseinzadeh et al. 2017.

[g] iPTF observation (R-PTF filter, ABmag) obtained via the TNS.

Table 2: *JHK* photometric data for AT2017be.

Date	MJD	phase[a]	*J*(err)	*H*(err)	*K*(err)	Instrument
20170207	57791.09	+21.27	16.921(0.303)	16.102(0.269)	15.069(0.280)	NOTCam
20170307	57819.87	+50.05	17.078(0.258)	16.423(0.227)	15.501(0.253)	NOTCam
20170408	57851.95	+82.13	17.430(0.280)	16.508(0.376)	15.730(0.319)	NOTCam
20170524	57897.90	+128.08	18.049(0.140)	17.265(0.089)	16.224(0.294)	NOTCam
20170602	57906.91	+137.09	–	–	16.309(0.224)	NOTCam
20170620	57924.88	+155.06	–	–	16.498(0.211)	NOTCam
20170703	57937.89	+168.07	–	–	16.965(0.218)	NOTCam
20170930	58026.23	+256.41	19.926(0.261)	18.881(0.307)	17.524(0.228)	NOTCam
20171017	58043.14	+273.32	19.961(0.261)	19.346(0.395)	17.768(0.291)	NOTCam
20180104	58122.12	+352.30	>20.2	>19.5	18.525(0.215)	NOTCam

[a] Phases are relative to *r*-band maximum light, MJD = 57769.8 ± 0.1.
NOTCam: the 2.56-m Nordic Optical Telescope (NOT) with NOTCam.

Table 3: Information on the instrumental set-ups.

Code	Diameter m	Telescope	Instrument	Site
fl12	1.00	COJ Telescope	Sinistro	Siding Spring Observatory, New South Wales, Australia
ANDICAM-CCD	1.30	SMARTS Telescope	ANDICAM	Cerro Tololo Inter-American Observatory, Cerro Tololo, Chile
ANDICAM-IR	1.30	SMARTS Telescope	ANDICAM	Cerro Tololo Inter-American Observatory, Cerro Tololo, Chile
fl03	1.00	LSC Telescope	Sinistro	Cerro Tololo Inter-American Observatory, Cerro Tololo, Chile
PROMPT3/5	0.41	PROMPT Telescope	Apogee Alta	Cerro Tololo Inter-American Observatory, Cerro Tololo, Chile
EFOSC2	3.58	New Technology Telescope	EFOSC2	ESO La Silla Observatory, La Silla, Chile
SOFI	3.58	New Technology Telescope	SOFI	ESO La Silla Observatory, La Silla, Chile
TRAPPIST	0.60	TRAPPIST-S Telescope	FLI ProLine	ESO La Silla Observatory, La Silla, Chile
GMOS	8.10	Gemini South Telescope	GMOS-S	Gemini Observatory, Cerro Pachon, Chile
LDSS	6.50	Magellan II - Clay Telescope	LDSS-3	Las Campanas Observatory, Atacama Region, Chile
WFCCD	2.50	Irénée du Pont Telescope	WFCCD	Las Campanas Observatory, Atacama Region, Chile
QHY9	0.35	Celestron C14 35-cm reflector	QHY-9	Xingming Observatory, Xinjiang, China
AFOSC	1.82	Copernico Telescope	AFOSC	Osservatorio Astronomico di Asiago, Asiago, Italy
B&C	1.22	Galileo Telescope	B&C	Osservatorio Astronomico di Asiago, Asiago, Italy
Moravian	0.67/0.92	Schmidt Telescope	Moravian	Osservatorio Astronomico di Asiago, Asiago, Italy
SBIG	0.67/0.92	Schmidt Telescope	SBIG	Osservatorio Astronomico di Asiago, Asiago, Italy
fl06	1.00	CPT Telescope	Sinistro	South African Astronomical Observatory, Cape Town, South Africa
ALFOSC	2.56	Nordic Optical Telescope	ALFOSC	Observatorio Roque de Los Muchachos, La Palma, Spain
IO:O	2.00	Liverpool Telescope	IO:O	Observatorio Roque de Los Muchachos, La Palma, Spain
ISIS	4.20	William Hershel Telescope	ISIS	Observatorio Roque de Los Muchachos, La Palma, Spain
LRS	3.58	Telescopio Nazionale Galileo	LRS	Observatorio Roque de Los Muchachos, La Palma, Spain
NICS	3.58	Telescopio Nazionale Galileo	NICS	Observatorio Roque de Los Muchachos, La Palma, Spain
NOTCAM	2.56	Nordic Optical Telescope	NOTCAM	Observatorio Roque de Los Muchachos, La Palma, Spain
OSIRIS	10.40	Gran Telescopio CANARIAS	OSIRIS	Observatorio Roque de Los Muchachos, La Palma, Spain
RATCam	2.00	Liverpool Telescope	RATCam	Observatorio Roque de Los Muchachos, La Palma, Spain
SupIRCam	2.00	Liverpool Telescope	SupIRCam	Observatorio Roque de Los Muchachos, La Palma, Spain
EM01	0.40	FTN Telescope	EM01	Haleakala Observatory, Hawaii, USA
fl05	1.00	ELP Telescope	Sinistro	McDonald Observatory, Texas, USA

Table 4: Optical (*BVuriz*) light curves of SN 2010dn.

Date	MJD	Phase[a]	*B*(err)	*V*(err)	*u*(err)	*r*(err)[bc]	*i*(err)[b]	*z*(err)	Instrument
20010302	51970.50	-3384.4	–	>24.1	–	–	–	–	1
20090330	54921.11	-433.8	–	–	–	>19.0	–	–	2
20100521	55338.00	-16.9	–	–	–	>18.0	–	–	2
20100531	55348.04	-6.9	–	–	–	17.546(0.123)	–	–	2
20100601	55348.98	-5.9	–	–	–	17.407(0.211)	–	–	2
20100601	55349.45	-5.4	–	–	–	17.593(0.172)	–	–	ALFOSC
20100602	55350.36	-4.5	–	–	–	17.41	–	–	3
20100603	55350.65	-4.2	–	17.4	–	–	–	–	4
20100603	55350.99	-3.9	–	–	–	17.412(0.266)	–	–	2
20100603	55351.40	-3.5	18.036(0.028)	17.649(0.051)	18.780(0.105)	17.465(0.040)	17.379(0.043)	–	LRS
20100605	55352.85	-2.0	17.923(0.036)	17.411(0.044)	19.002(0.206)	17.346(0.040)	17.260(0.036)	17.252(0.065)	EM01
20100607	55355.42	+0.5	17.781(0.046)	17.298(0.047)	18.677(0.080)	17.215(0.060)	17.292(0.040)	–	LRS
20100609	55357.40	+2.5	–	–	–	17.264(0.167)	–	–	ALFOSC
20100611	55359.40	+4.5	18.102(0.034)	17.584(0.017)	–	17.477(0.037)	17.370(0.017)	–	RATCam
20100611	55359.43	+4.5	18.066(0.047)	17.481(0.092)	–	17.424(0.086)	17.347(0.052)	–	LRS
20100612	55360.41	+5.5	18.074(0.016)	17.607(0.029)	–	17.498(0.018)	17.386(0.038)	–	RATCam
20100613	55361.45	+6.6	18.177(0.021)	17.638(0.025)	18.990(0.207)	17.490(0.032)	17.430(0.039)	17.486(0.073)	RATCam
20100616	55363.84	+8.9	18.141(0.053)	17.663(0.031)	19.158(0.358)	17.552(0.034)	17.467(0.038)	17.366(0.048)	EM01
20100616	55364.39	+9.5	–	–	–	17.669(0.248)	–	–	LRS
20100617	55365.40	+10.5	18.139(0.028)	17.730(0.025)	19.237(0.114)	17.605(0.057)	17.495(0.040)	17.376(0.060)	RATCam
20100618	55366.38	+11.5	18.294(0.029)	17.790(0.028)	–	17.607(0.031)	17.486(0.039)	–	RATCam
20100620	55367.82	+12.9	18.261(0.041)	17.701(0.033)	19.233(0.148)	17.700(0.040)	17.442(0.037)	17.378(0.068)	EM01
20100621	55368.79	+13.9	18.325(0.051)	17.752(0.025)	19.186(0.109)	17.650(0.049)	17.550(0.046)	17.432(0.072)	EM01
20100623	55370.80	+15.9	18.367(0.096)	17.797(0.090)	–	17.665(0.048)	17.419(0.072)	17.313(0.088)	EM01
20100623	55371.41	+16.5	18.422(0.022)	17.850(0.033)	19.322(0.137)	17.687(0.049)	17.550(0.039)	17.428(0.056)	RATCam
20100625	55373.41	+18.5	18.449(0.039)	17.907(0.036)	19.405(0.160)	17.619(0.058)	17.504(0.039)	17.445(0.058)	RATCam
20100626	55373.80	+18.9	18.468(0.089)	17.810(0.049)	–	17.667(0.029)	17.574(0.046)	17.395(0.074)	EM01
20100627	55374.80	+19.9	18.489(0.054)	17.930(0.044)	–	17.854(0.047)	17.637(0.043)	17.374(0.073)	EM01
20100628	55375.79	+19.9	–	–	–	–	–	17.465(0.174)	EM01
20100628	55376.39	+21.5	18.699(0.052)	17.934(0.019)	19.612(0.123)	17.828(0.012)	17.558(0.044)	17.473(0.062)	RATCam
20100629	55377.42	+22.5	18.658(0.030)	17.922(0.027)	19.559(0.130)	17.799(0.010)	17.553(0.027)	17.466(0.115)	RATCam
20101117	55517.18	+162.3	22.555(0.101)	22.019(0.040)	–	21.461(0.066)	20.618(0.053)	–	LRS
20101213	55543.08	+188.2	–	22.057(0.116)	–	21.485(0.132)	20.679(0.075)	–	LRS
20101231	55561.20	+206.3	–	22.053(0.149)	–	21.494(0.101)	20.721(0.125)	–	LRS
20110105	55566.14	+211.3	–	–	–	21.542(0.036)	–	–	LRS
20111228	55923.11	+568.2	>23.0	>22.9	–	>22.8	–	–	AFOSC

[a] Phases are relative to the *r*-band maximum light: $MJD_{SN\ 2010dn}$=55354.9.

[b] Johnson-Cousins *R* and *I* filter data were converted to Sloan *r* and *i* band magnitudes respectively, following the relations of Jordi et al. (2006)

[c] Unfiltered data obtained by amateur astronomers, calibrated to Sloan *r*-band magnitudes.

1 Original data published by Berger (2010), and reported to Johnson-Cousins *V* and *I* (I >24.9 mag) magnitudes. This approximation is based on the similar throughputs between wide filters F555W/F814W and V/I .

2 Amateur data (K. Itagaki) scaled to *r* band .

3 Bright Supernova (see website: http://www.rochesterastronomy.org/sn2010/index.html#2010dn; Observation: J. Nicolas).

4 Bright Supernova (see website: http://www.rochesterastronomy.org/sn2010/index.html#2010dn; Observation: J. Brimacombe).

Table 5: NIR (JHK) light curves of SN 2010dn.

Date	MJD	Phase[a]	J(err)	H(err)	K(err)	Instrument
20100606	55353.89	-1.0	16.611(0.067)	15.690(0.065)	–	1 SupIRCam
20100607	55354.89	+0.0	16.412(0.133)	15.704(0.053)	15.278(0.068)	1 NICS
20100607	55354.96	+0.1	16.490(0.091)	15.703(0.119)	–	1 SupIRCam
20100611	55358.89	+4.0	16.491(0.064)	15.753(0.066)	–	1 SupIRCam
20100614	55361.90	+7.0	16.564(0.095)	15.830(0.091)	–	1 SupIRCam
20100627	55374.89	+20.0	16.744(0.340)	15.838(0.082)	–	1 SupIRCam
20100629	55376.90	+22.0	16.758(0.586)	15.875(0.594)	–	1 SupIRCam
20101201	55531.22	+176.3	18.974(0.167)	17.774(0.152)	16.868(0.128)	1 NICS
20101224	55554.14	+199.2	19.341(0.127)	18.053(0.141)	17.465(0.101)	1 NICS

[a] Phases are relative to the r-band maximum light: $\mathrm{MJD}_{SN\ 2010dn}$=55354.9.

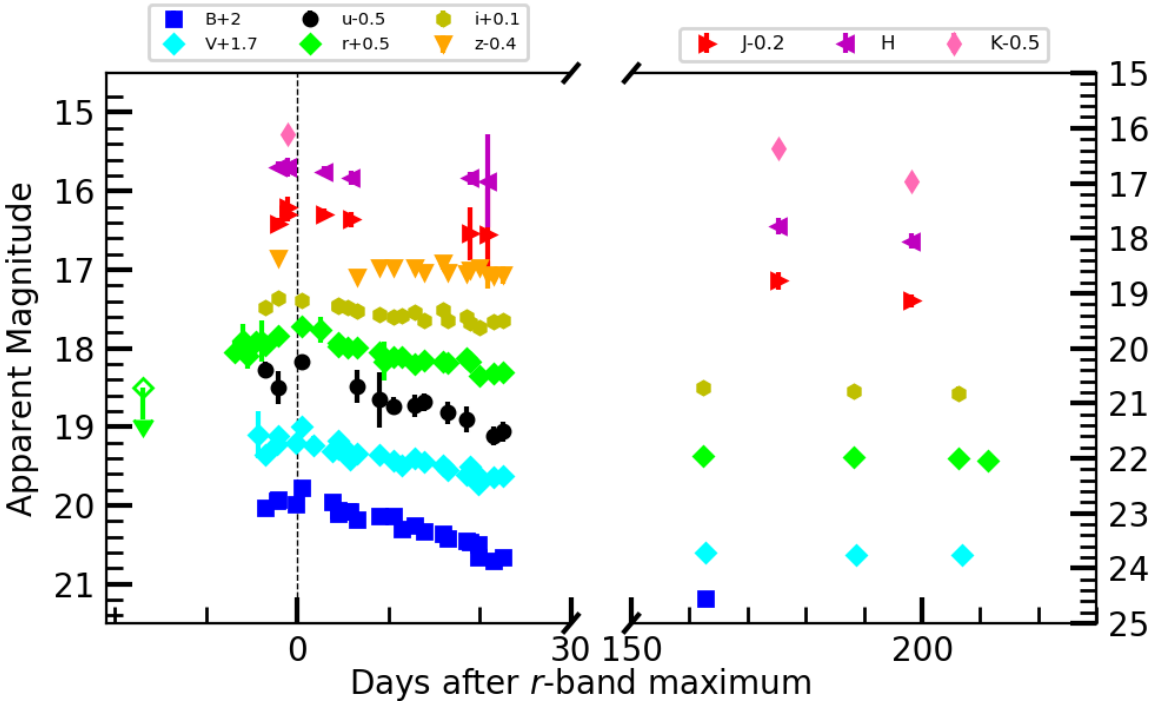

Figure 1: Optical and NIR light curves of SN 2010dn.

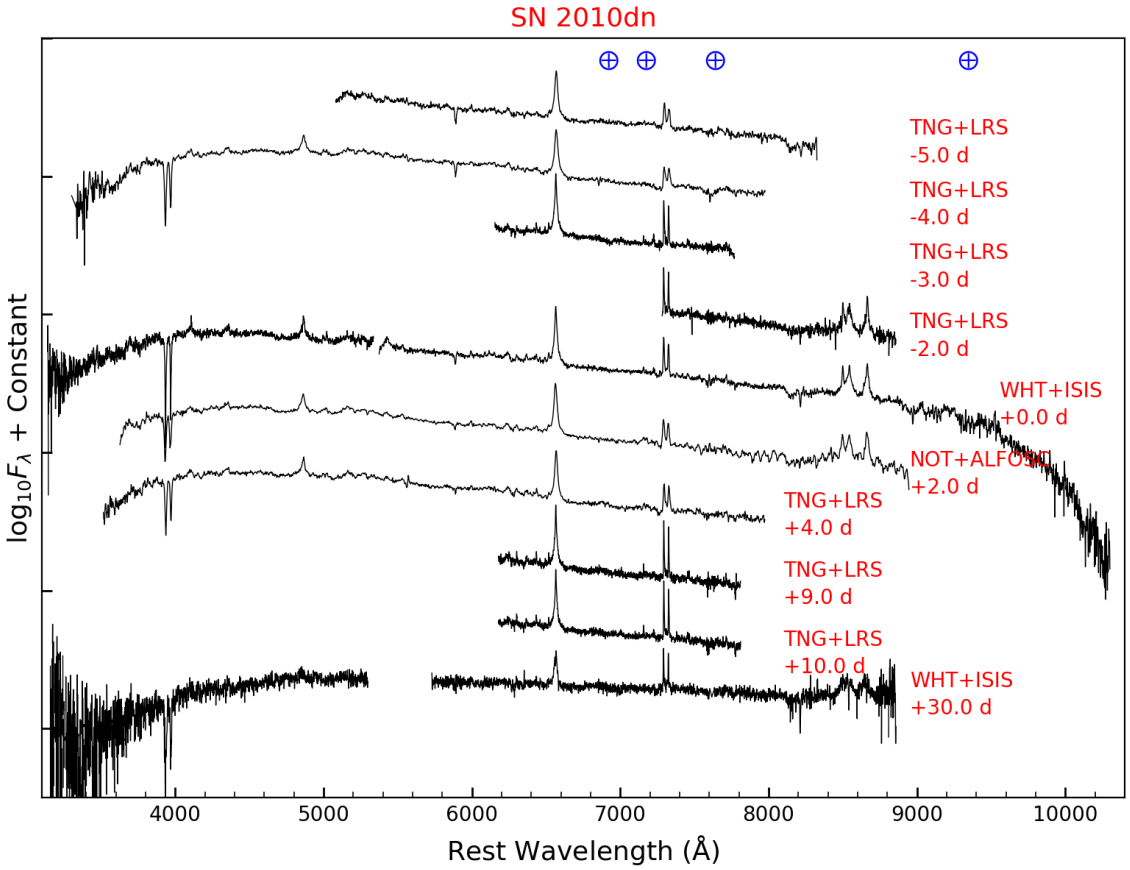

Figure 2: The spectral evolution of SN 2010dn. The epoch marked at the right of each spectrum are relative to the *R*-band maximum. The symbol ⊕ marks the positions of strongest telluric absorption bands. All spectra redshift corrected.

Table 6: Optical ($UBVRI$) light curves of NGC5775 OT.

Date	MJD	Phase[a]	U(err)	B(err)	V(err)	R(err)	I(err)	Instrument
20120313	55999.27	-24.2	–	–	–	>19.9	–	PROMPT35[b]
20120317	56003.39	-20.1	–	–	>19.5	–	–	1
20120327	56013.49	-10.0	–	–	18.7	–	–	1
20120328	56014.07	-9.4	–	–	18.5	–	–	1
20120329	56015.06	-8.4	20.308(0.114)	18.823(0.022)	18.206 (0.027)	17.855 (0.031)	17.460 (0.058)	RATCam
20120329	56015.14	-8.4	–	18.744(0.053)	18.259 (0.044)	17.924 (0.034)	17.521 (0.129)	AFOSC
20120329	56015.35	-8.2	–	–	18.0 (0.1)	–	–	2
20120331	56017.26	-6.2	–	18.390(0.113)	17.888 (0.051)	17.503 (0.064)	17.129 (0.056)	PROMPT3
20120412	56029.24	+5.7	–	–	17.776 (0.069)	17.403 (0.057)	17.102 (0.045)	PROMPT35
20120414	56031.37	+7.9	–	18.422(0.020)	17.901 (0.020)	17.564 (0.013)	17.164 (0.029)	EFOSC
20120415	56032.41	+8.9	–	–	–	17.614 (0.062)	–	PROMPT35
20120416	56033.24	+9.7	–	–	17.904 (0.055)	17.561 (0.059)	17.239 (0.049)	PROMPT35
20120416	56033.97	+10.5	19.391(0.093)	18.494(0.028)	17.902 (0.029)	17.552 (0.032)	17.285 (0.112)	RATCam
20120417	56034.05	+10.6	–	18.443(0.034)	17.947 (0.030)	17.591 (0.017)	17.287 (0.055)	AFOSC
20120417	56034.19	+10.7	–	–	17.900 (0.069)	17.634 (0.056)	17.201 (0.067)	PROMPT35
20120421	56038.25	+14.8	–	18.694(0.062)	18.064 (0.049)	17.825 (0.084)	17.445 (0.057)	PROMPT35
20120422	56039.01	+15.5	19.917(0.109)	18.598(0.024)	18.117 (0.025)	17.856 (0.031)	17.511 (0.053)	RATCam
20120425	56042.11	+18.6	–	–	18.478 (0.109)	18.094 (0.168)	17.710 (0.126)	SBIG
20120501	56048.17	+24.7	–	19.011(0.084)	18.436 (0.080)	18.083 (0.055)	17.649 (0.071)	PROMPT35
20120501	56048.20	+24.7	–	19.155(0.013)	18.479 (0.018)	–	–	ALFOSC
20120501	56048.38	+24.9	–	19.064(0.031)	18.487 (0.032)	18.112 (0.029)	17.696 (0.074)	EFOSC
20120502	56049.21	+25.7	–	19.134(0.113)	18.485 (0.088)	18.073 (0.058)	17.647 (0.094)	PROMPT35
20120509	56056.10	+32.6	–	19.386(0.033)	18.595 (0.035)	18.154 (0.076)	17.700 (0.088)	LRS
20120515	56062.11	+38.6	21.101(0.212)	19.560(0.039)	18.743 (0.044)	18.292 (0.050)	17.701 (0.226)	RATCam
20120515	56062.24	+38.7	–	–	18.707 (0.068)	18.226 (0.072)	17.647 (0.042)	PROMPT35
20120520	56067.18	+43.7	–	–	–	–	17.788 (0.052)	PROMPT35
20120521	56068.17	+44.7	–	19.710(0.132)	18.807 (0.068)	18.325 (0.078)	17.819 (0.035)	PROMPT35
20120601	56079.97	+56.5	>21.3	20.142(0.111)	19.217 (0.051)	18.699 (0.058)	18.089 (0.057)	RATCam
20120603	56081.11	+57.6	–	–	–	18.804 (0.154)	–	PROMPT35[b]
20120603	56081.96	+58.5	>21.3	20.196(0.148)	19.263 (0.093)	18.741 (0.040)	18.115 (0.079)	RATCam
20120620	56098.24	+74.7	–	20.501(0.148)	19.512 (0.101)	>19.7	–	TRAPPIST

[a] Phases are relative to R-band maximum light: $\mathrm{MJD}_{NGC5775\ OT}$=56023.5.

[b] These unfiltered data were reported to Johnson-Cousins R magnitudes, as suggested by the quantum efficiency of the CCD.

1 Observations from The Astronomer's Telegram (ATel, No. 4004; see Howerton et al. 2012).

2 Bright Supernova (see website: http://www.rochesterastronomy.org/sn2012/index.html#PSNJ14535395+0334049; Observation: J. Brimacombe)

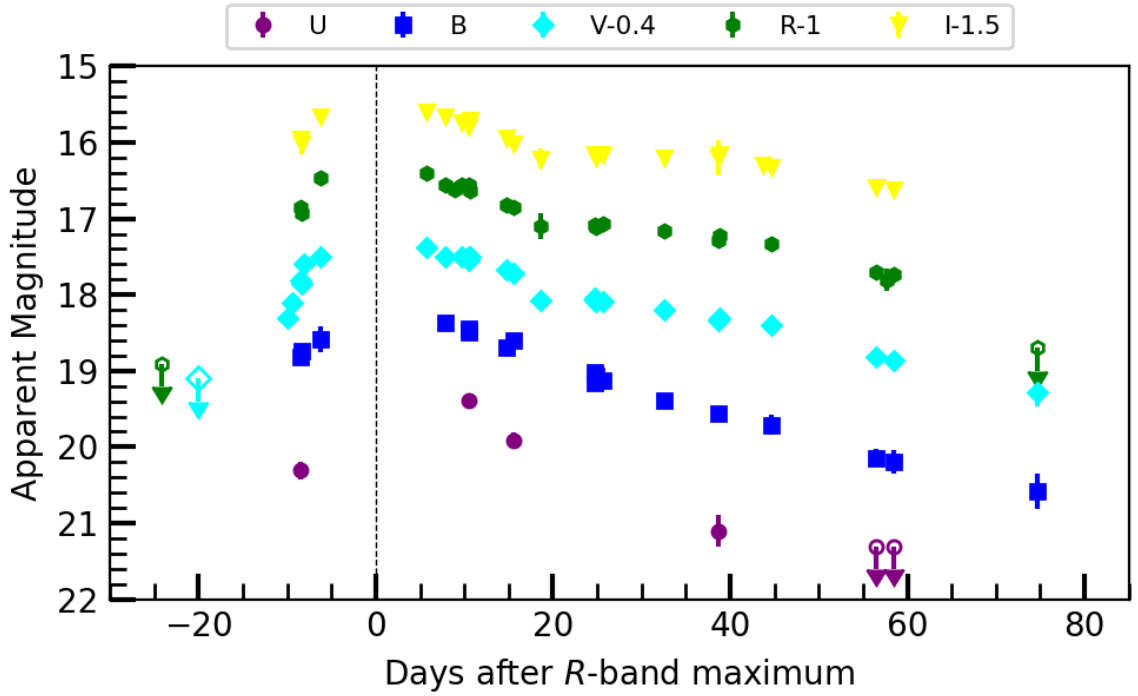

Figure 3: The light curve of NGC 5775 OT.

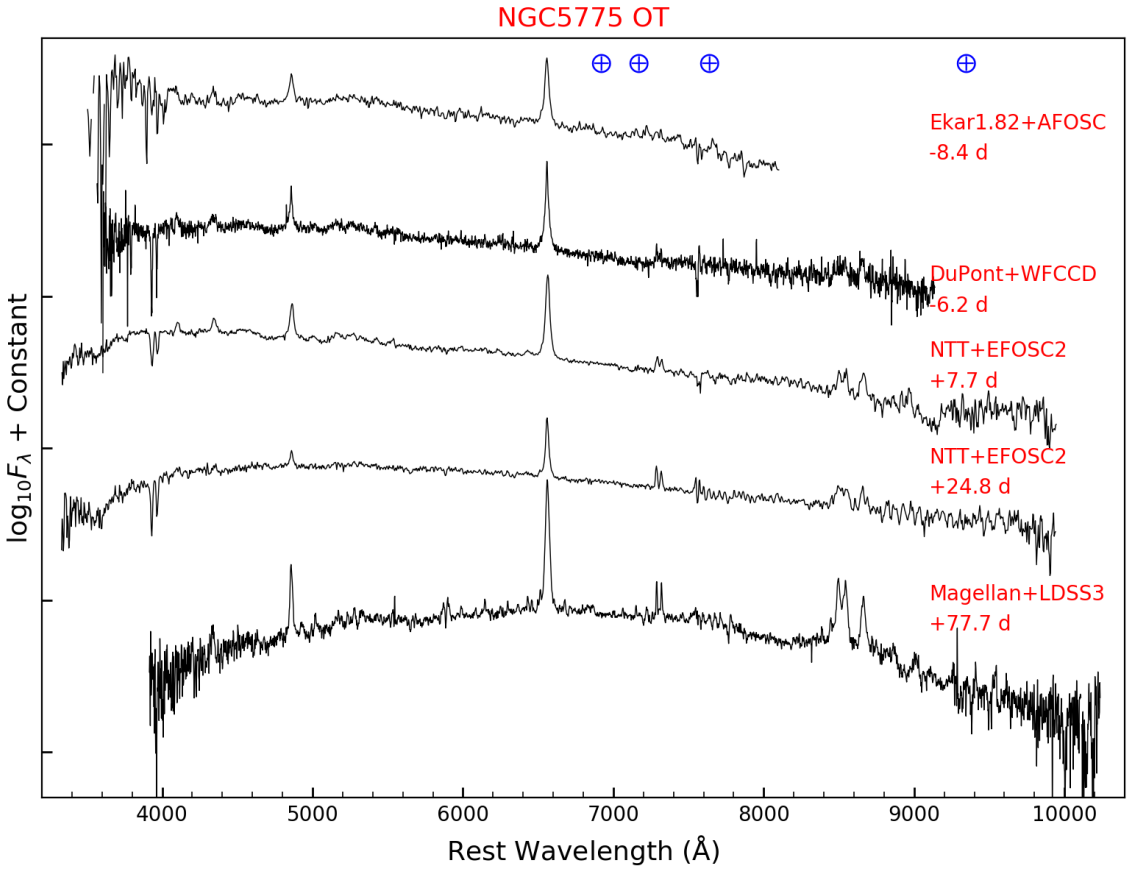

Figure 4: Spectral evolution of NGC 5775 OT. The epochs marked at the right of each spectrum are relative to the *R*-band maximum. The symbol ⊕ marks the positions of strongest telluric absorption bands. All spectra were redshift .

Table 7: Optical ($UBVRI$) light curves of NGC 5917 OT.

Date	MJD	Phase[a]	U(err)	B(err)	V(err)	R(err)	I(err)	Instrument
20120624	56102.05	-222.4	–	–	–	>19.2	–	PROMPT35[b]
20130127	56319.34	-5.2	–	–	–	18.897(0.138)	–	PROMPT35[b]
20130131	56323.34	-1.2	–	–	–	18.728(0.099)	–	PROMPT35[b]
20130204	56327.36	+2.9	–	–	–	18.601(0.143)	–	PROMPT35[b]
20130204	56327.41	+2.9	–	–	–	>18.3	–	1
20130207	56330.20	+5.7	–	–	19.132(0.144)	18.833(0.078)	18.422(0.090)	AFOSC
20130207	56330.39	+5.9	–	–	19.143(0.035)	–	–	EFOSC2
20130208	56331.23	+6.7	–	–	–	18.859(0.029)	18.450(0.038)	RATCam
20130209	56332.28	+7.8	–	–	19.237(0.035)	–	–	EFOSC2
20130211	56334.23	+9.7	–	–	–	18.998(0.030)	18.466(0.035)	RATCam
20130215	56338.28	+13.8	–	19.878(0.046)	19.368(0.029)	18.882(0.043)	18.455(0.064)	ANDICAM-CCD
20130218	56341.23	+16.7	19.541(0.160)	19.997(0.060)	–	19.005(0.037)	18.415(0.038)	RATCam
20130218	56341.32	+16.8	–	19.963(0.047)	19.444(0.034)	18.888(0.062)	18.346(0.068)	ANDICAM-CCD
20130220	56343.30	+18.8	–	19.937(0.042)	19.350(0.031)	19.050(0.031)	18.474(0.042)	ANDICAM-CCD
20130221	56344.22	+19.7	>19.9	19.998(0.046)	19.307(0.034)	18.987(0.050)	18.455(0.040)	RATCam
20130223	56346.20	+21.7	>19.9	20.084(0.110)	19.413(0.046)	18.937(0.078)	18.458(0.064)	RATCam
20130225	56348.14	+23.6	>19.9	20.188(0.178)	19.385(0.082)	19.001(0.088)	18.550(0.075)	RATCam
20130227	56350.30	+25.8	–	20.226(0.124)	19.510(0.093)	–	–	ANDICAM-CCD
20130301	56352.32	+27.8	–	–	–	19.111(0.071)	18.695(0.087)	ANDICAM-CCD
20130305	56356.25	+31.8	–	–	–	19.113(0.054)	–	EFOSC2[b]
20130305	56356.26	+31.8	–	20.367(0.077)	19.616(0.056)	19.167(0.045)	18.558(0.065)	ANDICAM-CCD
20130310	56361.22	+36.7	–	>20.4	>19.6	19.115(0.226)	18.496(0.293)	RATCam
20130311	56362.26	+37.8	–	20.509(0.052)	19.618(0.052)	19.076(0.050)	18.594(0.063)	ANDICAM-CCD
20130312	56363.09	+38.6	>19.9	20.590(0.080)	19.688(0.051)	19.143(0.054)	18.625(0.051)	RATCam
20130315	56366.28	+41.8	–	20.689(0.051)	19.857(0.057)	19.082(0.038)	18.755(0.043)	ANDICAM-CCD
20130318	56369.07	+44.6	>20.0	20.850(0.138)	19.802(0.071)	19.284(0.075)	18.675(0.090)	RATCam
20130320	56371.33	+46.8	–	20.949(0.060)	19.984(0.063)	19.257(0.030)	18.735(0.084)	ANDICAM-CCD
20130321	56372.11	+47.6	>20.1	20.921(0.088)	19.991(0.049)	19.295(0.067)	18.721(0.057)	RATCam
20130324	56375.29	+50.8	–	21.018(0.120)	20.111(0.094)	19.484(0.056)	18.634(0.071)	ANDICAM-CCD
20130328	56379.26	+54.8	–	21.277(0.358)	19.913(0.131)	19.469(0.159)	18.610(0.125)	ANDICAM-CCD
20130401	56383.12	+58.6	–	>21.2	20.089(0.195)	19.386(0.202)	18.656(0.130)	RATCam
20130407	56389.07	+64.6	–	21.584(0.195)	20.280(0.083)	19.682(0.085)	19.049(0.059)	RATCam
20130409	56392.00	+67.5	–	21.746(0.225)	20.476(0.097)	19.863(0.104)	18.963(0.102)	RATCam
20130414	56396.30	+71.8	–	21.839(0.028)	20.794(0.046)	20.054(0.037)	19.391(0.063)	EFOSC2
20150214	57067.31	+742.8	–	–	–	>19.8	–	PROMPT35[b]

[a] Phases are relative to R-band maximum light: $\mathrm{MJD}_{NGC5917\ OT}$=56324.5.

[b] Unfiltered data reported to broad-band Johnson-Cousins R magnitudes.

1 This limit was obtained by L. Elenin (Lyubertsy, Russia) and I. Molotov (Moscow, Russia) through a 0.45-m f/2.8 telescope plus KAF09000 CCD, which is also reported in the Central Bureau for Astronomical Telegrams (CBAT, see http://www.cbat.eps.harvard.edu/unconf/followups/J15213475-0722183.html).

Table 8: NIR (JHK) light curves of NGC 5917 OT.

Date	MJD	Phase[a]	J(err)	H(err)	K(err)	Instrument
20130208	56331.29	+6.8	17.700(0.038)	17.239(0.039)	16.761(0.047)	SOFI
20130218	56341.30	+16.8	17.967(0.165)	–	–	ANDICAM-IR
20130220	56343.29	+18.8	17.988(0.184)	–	–	ANDICAM-IR
20130222	56345.36	+20.9	17.977(0.096)	17.339(0.039)	16.975(0.052)	SOFI
20130227	56350.29	+25.8	17.947(0.161)	–	–	ANDICAM-IR
20130301	56352.30	+27.8	17.936(0.179)	–	–	ANDICAM-IR
20130305	56356.25	+31.8	18.036(0.145)	–	–	ANDICAM-IR
20130306	56357.31	+32.8	18.002(0.096)	17.505(0.101)	16.981(0.060)	SOFI
20130311	56362.25	+37.8	18.137(0.205)	–	–	ANDICAM-IR
20130315	56366.27	+41.8	18.070(0.135)	–	–	ANDICAM-IR
20130320	56371.32	+46.8	18.004(0.153)	–	–	ANDICAM-IR
20130324	56375.27	+50.8	18.068(0.136)	–	–	ANDICAM-IR
20130328	56379.25	+54.8	18.182(0.215)	–	–	ANDICAM-IR
20130412	56394.33	+ 69.8	18.292(0.081)	17.705(0.067)	17.362(0.065)	SOFI

[a] Phases are relative to the R-band maximum light: $\mathrm{MJD}_{NGC5917\ OT}$=56324.5.

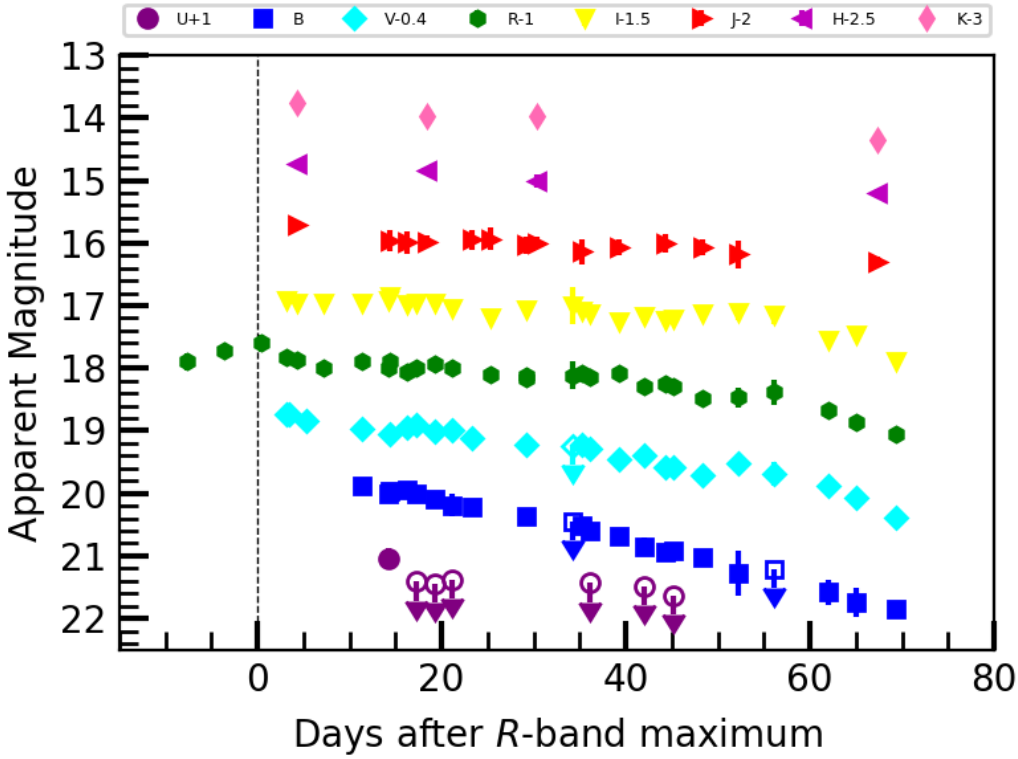

Figure 5: The light curve of NGC 5917OT.

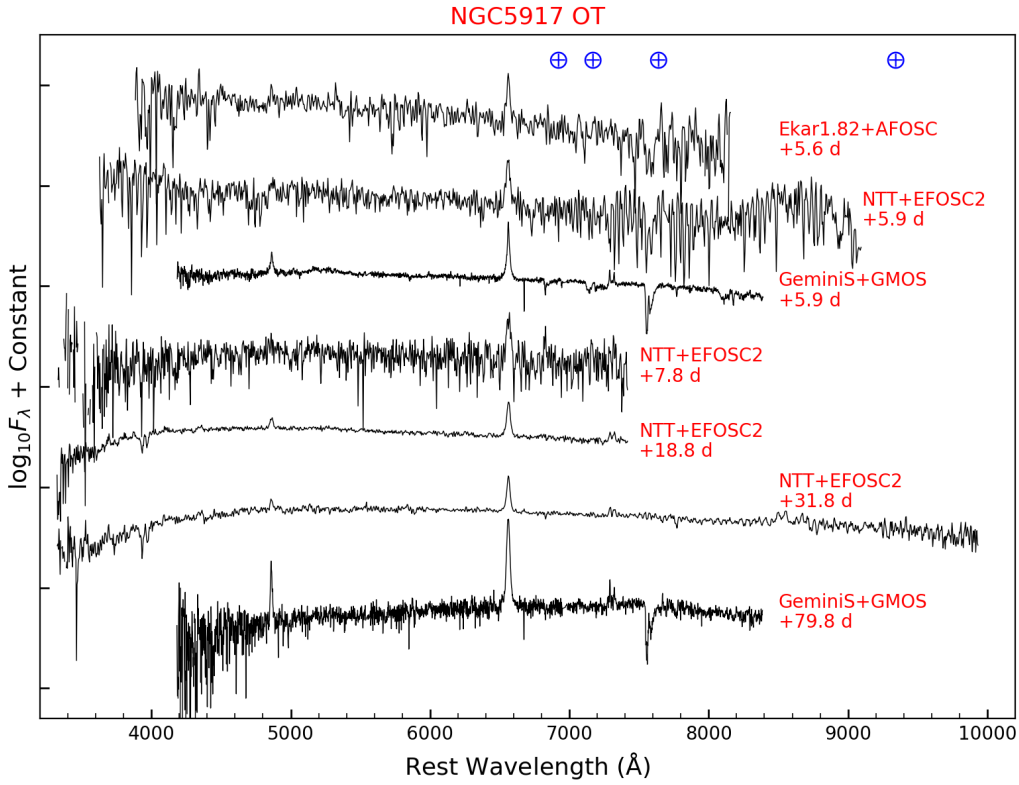

Figure 6: Spectral evolution of NGC 5917OT. The epoch marked at the right of each spectrum are relative to the *R*-band maximum. The symbol ⊕ marks the positions of strongest telluric absorption bands. All spectra were redshift corrected.

Table 9: Optical (*BVugriz*) light curves of UGC 8246 OT.

Date	MJD	Phase[a]	*B*(err)	*V*(err)	*u*(err)	*g*(err)	*r*(err)[b]	*i*(err)[b]	Instrument
20130331	56382.71	-269.3	–	–	–	–	>18.8	–	QHY9[c]
20131220	56646.93	-5.4	–	–	–	–	18.246(0.251)	–	QHY9[c]
20131226	56652.96	+1.0	–	–	–	–	17.992(0.230)	–	QHY9[c]
20131227	56653.93	+1.9	–	–	–	–	17.964(0.180)	–	QHY9[c]
20131229	56655.87	+3.9	–	–	–	–	18.062(0.165)	–	QHY9[c]
20131230	56656.87	+4.9	–	–	–	–	>17.8	–	QHY9[c]
20140101	56658.21	+6.2	19.393(0.035)	18.634(0.013)	20.840(0.186)	–	18.314(0.011)	18.101(0.010)	IO:O
20140102	56659.16	+7.2	19.386(0.045)	18.691(0.030)	20.519(0.218)	–	18.351(0.015)	18.133(0.016)	IO:O
20140104	56661.26	+9.3	19.373(0.045)	18.702(0.014)	20.227(0.136)	–	18.360(0.013)	18.202(0.012)	IO:O
20140107	56664.26	+12.3	19.522(0.034)	18.763(0.051)	20.160(0.108)	–	18.490(0.039)	18.293(0.121)	IO:O
20140107	56664.84	+12.8	–	–	–	–	18.467(0.396)	–	QHY9[c]
20140108	56665.16	+13.2	19.432(0.112)	18.774(0.055)	>19.6	–	18.511(0.069)	18.208(0.044)	IO:O
20140108	56665.23	+13.2	–	18.811(0.180)	–	–	18.417(0.218)	–	AFOSC
20140109	56666.96	+15.0	–	–	–	–	18.501(0.224)	–	QHY9[c]
20140111	56668.88	+16.9	–	–	–	–	18.529(0.213)	–	QHY9[c]
20140115	56672.15	+21.1	19.559(0.066)	18.888(0.073)	20.093(0.211)	–	18.555(0.028)	18.404(0.022)	IO:O
20140122	56679.14	+27.1	19.650(0.085)	19.083(0.058)	–	–	18.636(0.256)	18.672(0.058)	SBIG
20140127	56684.27	+32.3	19.957(0.042)	19.154(0.026)	–	–	18.803(0.022)	18.751(0.028)	IO:O
20140204	56692.23	+40.2	–	–	–	–	19.111(0.008)	–	LRS
20140207	56695.24	+43.2	20.223(0.037)	19.357(0.022)	20.386(0.186)	–	19.030(0.019)	18.985(0.023)	IO:O
20140209	56697.61	+45.6	–	–	–	20.06	–	–	2
20140209	56697.61	+45.6	–	–	–	20.063(0.17)	–	–	1
20140209	56697.62	+45.6	–	–	–	20.13	–	–	2[d]
20140209	56697.62	+45.6	–	–	–	20.133(0.2)	–	–	1[d]
20140210	56698.24	+46.2	20.187(0.038)	19.480(0.032)	20.485(0.150)	–	19.037(0.018)	19.002(0.027)	IO:O
20140213	56701.10	+49.1	20.213(0.093)	19.556(0.050)	–	–	19.054(0.037)	19.086(0.033)	IO:O
20140221	56709.60	+57.6	–	–	–	–	19.144(0.08)	–	1
20140221	56709.60	+57.6	–	–	–	–	19.14	–	2
20140221	56709.61	+57.6	–	–	–	–	19.219(0.13)	–	1
20140221	56709.61	+57.6	–	–	–	–	19.22	–	2
20140223	56711.22	+59.2	20.350(0.051)	19.607(0.029)	–	–	19.205(0.022)	19.244(0.027)	IO:O
20140226	56714.28	+62.3	–	–	–	–	19.263(0.017)	19.258(0.038)	OSIRIS
20140228	56716.19	+64.2	20.550(0.054)	19.653(0.033)	>20.6	–	19.277(0.022)	19.306(0.039)	IO:O
20140309	56725.17	+73.2	20.603(0.238)	19.923(0.104)	–	–	19.535(0.104)	19.389(0.049)	AFOSC
20140323	56739.10	+87.1	21.051(0.038)	20.250(0.061)	–	–	19.644(0.008)	19.781(0.010)	LRS
20140401	56748.08	+96.1	21.267(0.158)	20.291(0.219)	–	–	–	19.934(0.032)	AFOSC
20140425	56772.99	+121.0	–	20.697(0.023)	–	–	19.838(0.012)	20.107(0.019.)	ALFOSC
20140428	56775.94	+123.9	–	–	–	–	19.849(0.080)	20.173(0.085)	OSIRIS
20140514	56791.93	+139.9	–	20.985(0.086)	–	–	19.927(0.039)	20.357(0.064)	LRS
20140615	56823.94	+171.9	21.713(0.048)	21.340(0.033)	–	–	20.151(0.015)	20.545(0.017)	LRS
20140723	56861.92	+209.9	21.949(0.054)	21.454(0.035)	–	–	20.310(0.013)	20.619(0.023)	LRS
20140808	56877.88	+225.9	22.257(0.070)	21.693(0.047)	–	–	20.447(0.020)	20.816(0.025)	LRS
20140814	56883.88	+231.9	–	–	–	–	20.540(0.165)	20.925(0.046)	OSIRIS
20141217	57008.20	+356.2	–	–	–	–	21.531(0.106)	–	ALFOSC
20141220	57011.19	+359.2	–	22.302(0.539)	–	–	21.406(0.106)	21.540(0.196)	AFOSC
20141223	57014.25	+362.2	–	–	–	–	21.450(0.168)	21.612(0.124)	OSIRIS
20150125	57047.27	+395.3	–	>22.5	–	–	21.815(0.034)	21.967(0.041)	ALFOSC
20150311	57092.27	+440.3	–	>22.6	–	–	22.436(0.070)	–	ALFOSC
20150428	57140.77	+488.8	–	–	–	–	>23.0	–	ALFOSC

[a] Phases are relative to *r*-band maximum light: $\mathrm{MJD}_{UGC8246\ OT}$=56652.0.

[b] Johnson-Cousins *R* and *I* filter data were transformed to Sloan *r* and *i* band magnitudes respectively, following the relations of Jordi et al. (2006)

[c] Measurements on unfiltered images, calibrated to the Sloan *r*-band magnitudes.

[d] These two epochs have also *z*-band detections at 18.69 mag and 18.686 (0.21) mag, respectively. In addition, there is a very early (2013-03-07; MJD=56476.29) *z*-band limit of > 20.8 m*ag*.

1 These data were taken from the OSC.

2 These data were taken from the Pan-STARRS Survey for Transients (see website: https://star.pst.qub.ac.uk/ps1threepi/psdb/candidate/113100735134105100 0/).

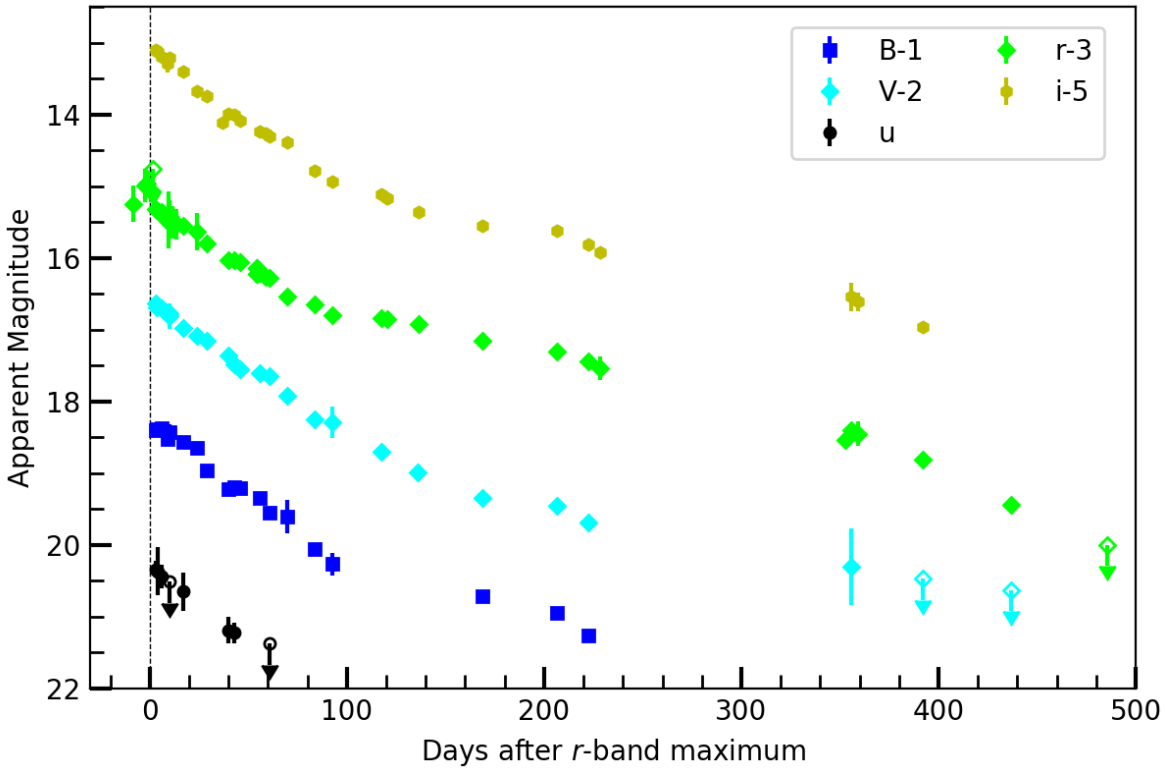

Figure 7: The light curve of UGC8246 OT.

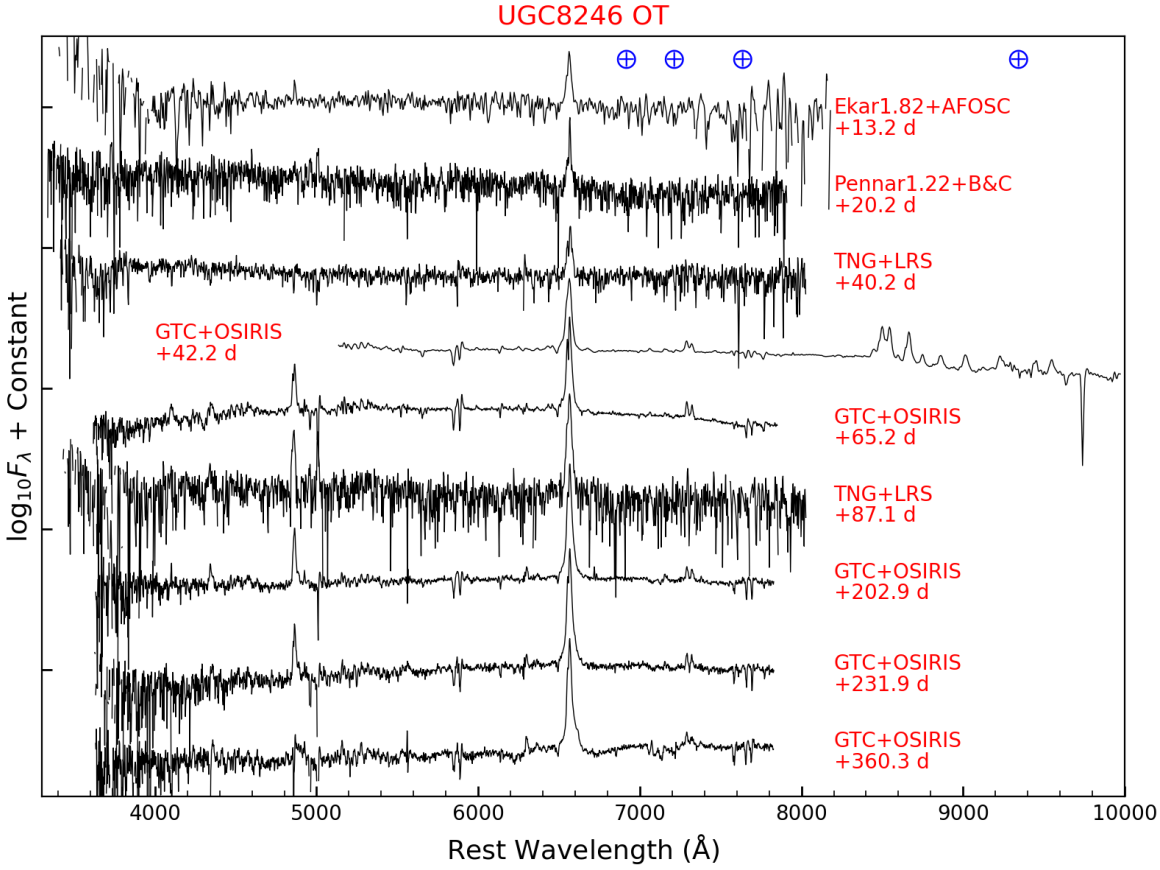

Figure 8: The spectral temporal evolution of UGC8246 OT. The epoch marked at the right of each spectrum are relative to the *R*-band maximum. The symbol ⊕ marks the positions of strongest telluric absorption bands. All spectra were redshift corrected.

Table 10: Optical (*BVgriz*) light curves of AT 2018aes.

Date	MJD	Phase[a]	*B*(err)	*V*(err)	*g*(err)	*r*(err)	*i*(err)	*z*(err)	Instrument
20180218	58167.57	-43.5	–	–	–	>18.7	–	–	1
20180311	58188.54	-22.6	–	–	–	18.51(0.3)	–	–	1
20180311	58188.55	-22.6	–	–	–	–	19.103(0.029)	–	2
20180314	58191.73	-19.4	20.004(0.089)	19.321(0.084)	19.613(0.054)	19.051(0.061)	18.881(0.103)	–	fl12
20180318	58195.09	-16.0	19.794(0.074)	19.185(0.084)	19.558(0.021)	18.997(0.052)	18.727(0.080)	–	fl06
20180322	58199.12	-12.0	19.841(0.027)	19.140(0.020)	19.509(0.011)	18.949(0.023)	18.896(0.023)	–	ALFOSC
20180322	58199.38	-11.7	19.868(0.131)	19.082(0.078)	19.402(0.047)	18.919(0.061)	18.775(0.080)	–	fl05
20180326	58203.23	-7.9	>19.6 –	18.904(0.064)	19.314(0.045)	18.830(0.048)	18.663(0.072)	–	fl03
20180330	58207.11	-4.0	19.714(0.068)	19.089(0.065)	19.383(0.064)	18.827(0.045)	18.716(0.041)	18.634(0.075)	ALFOSC
20180405	58213.09	+2.0	19.830(0.020)	19.019(0.010)	19.386(0.010)	18.858(0.010)	18.546(0.049)	18.569(0.027)	ALFOSC
20180407	58215.19	+4.1	–	19.069(0.026)	19.465(0.031)	18.750(0.050)	18.575(0.027)	18.479(0.045)	ALFOSC
20180408	58216.16	+5.1	19.923(0.029)	19.068(0.019)	19.486(0.010)	18.871(0.015)	18.652(0.025)	18.605(0.041)	ALFOSC
20180411	58219.14	+8.0	19.934(0.025)	19.011(0.011)	19.559(0.010)	18.876(0.019)	18.632(0.030)	18.596(0.035)	ALFOSC
20180417	58225.03	+13.9	20.104(0.042)	19.220(0.024)	19.590(0.025)	18.952(0.024)	18.725(0.018)	18.574(0.037)	ALFOSC
20180418	58226.10	+15.0	20.184(0.075)	19.224(0.029)	19.653(0.018)	19.021(0.022)	18.773(0.040)	18.758(0.051)	IO:O
20180418	58226.98	+15.9	–	19.138(0.104)	19.648(0.094)	19.039(0.078)	19.005(0.135)	–	Moravian
20180419	58227.98	+16.9	20.121(0.175)	19.205(0.088)	19.736(0.090)	18.969(0.099)	18.811(0.219)	–	Moravian
20180426	58234.13	+23.0	20.389(0.033)	19.563(0.017)	19.885(0.025)	19.172(0.021)	18.899(0.038)	18.785(0.043)	ALFOSC
20180501	58239.04	+27.9	20.584(0.049)	19.570(0.022)	20.099(0.019)	19.390(0.043)	19.089(0.032)	19.033(0.046)	ALFOSC
20180504	58242.98	+31.9	20.771(0.134)	19.654(0.050)	20.124(0.054)	19.476(0.031)	19.200(0.050)	18.999(0.078)	IO:O
20180507	58245.98	+34.9	20.820(0.104)	19.781(0.028)	20.478(0.033)	19.538(0.013)	19.313(0.061)	19.021(0.090)	IO:O
20180513	58251.02	+39.9	21.111(0.146)	20.175(0.043)	20.566(0.065)	19.798(0.041)	19.568(0.082)	19.145(0.068)	IO:O
20180515	58254.00	+42.9	21.182(0.086)	20.189(0.041)	20.693(0.041)	19.938(0.036)	19.473(0.037)	19.181(0.044)	ALFOSC
20180517	58255.95	+44.8	21.239(0.210)	20.276(0.080)	20.972(0.051)	20.008(0.039)	19.651(0.121)	19.313(0.070)	IO:O
20180522	58260.92	+49.8	>21.2	20.468(0.120)	21.261(0.373)	20.140(0.087)	19.985(0.116)	19.498(0.118)	IO:O
20180525	58263.05	+52.0	21.714(0.111)	20.559(0.105)	21.343(0.046)	20.356(0.071)	20.092(0.082)	19.728(0.071)	ALFOSC
20180531	58269.02	+57.9	22.048(0.164)	20.986(0.060)	21.813(0.062)	20.608(0.024)	20.257(0.121)	19.910(0.093)	ALFOSC
20180531	58269.94	+58.8	>21.8	20.9	>21.6	>20.7	20.332(0.275)	19.900(0.267)	IO:O
20180605	58274.05	+62.9	22.189(0.128)	21.106(0.070)	21.898(0.073)	20.907(0.032)	20.567(0.114)	19.917(0.060)	ALFOSC
20180605	58274.91	+63.8	>21.8	21.280(0.075)	21.956(0.120)	20.831(0.044)	20.708(0.435)	19.911(0.161)	IO:O
20180610	58279.99	+68.9	>21.8	21.454(0.193)	22.124(0.147)	21.304(0.123)	20.712(0.258)	20.258(0.235)	IO:O
20180626	58295.97	+84.9	–	–	>22.5	22.335(0.104)	>21.8	20.996(0.226)	ALFOSC
20180704	58303.97	+92.9	–	–	–	22.865(0.221)	21.866(0.379)	21.414(0.211)	ALFOSC

[a] Phases are relative to *r*-band maximum light: $\mathrm{MJD}_{AT\ 2018aes}$= 58211.1.

1 Unfiltered KAIT data reported to the sloan *r* magnitudes (AB system). Data from the Transient Name Server (TNS; https://wis-tns.weizmann.ac.il/object/2018aes).

2 Thie *i*-band magnitude is the weighted mean value obtained from the Pan-STARRS Survey for Transients (see website: https://star.pst.qub.ac.uk/sne/ps13pi/psdb/lightcurve/1134817771035644300/.

Table 11: NIR (*JHK*) light curves of AT 2018aes.

Date	MJD	Phase[a]	*J*(err)	*H*(err)	*K*(err)	Instrument
20180331	58209.00	-2.1	17.781(0.040)	17.387(0.075)	16.235(0.088)	NOTCam
20180511	58249.92	+38.8	18.257(0.065)	17.994(0.063)	17.148(0.076)	NOTCam
20180627	58296.95	+85.9	19.752(0.209)	19.363(0.299)	17.957(0.160)	NOTCam
20180731	58330.88	+119.8	> 20.5	19.662(0.392)	–	NOTCam
20180819	58349.86	+138.8	–	–	18.442(0.186)	NOTCam

[a] Phases are relative to *r*-band maximum light: $\mathrm{MJD}_{AT\ 2018aes}$= 58211.1.

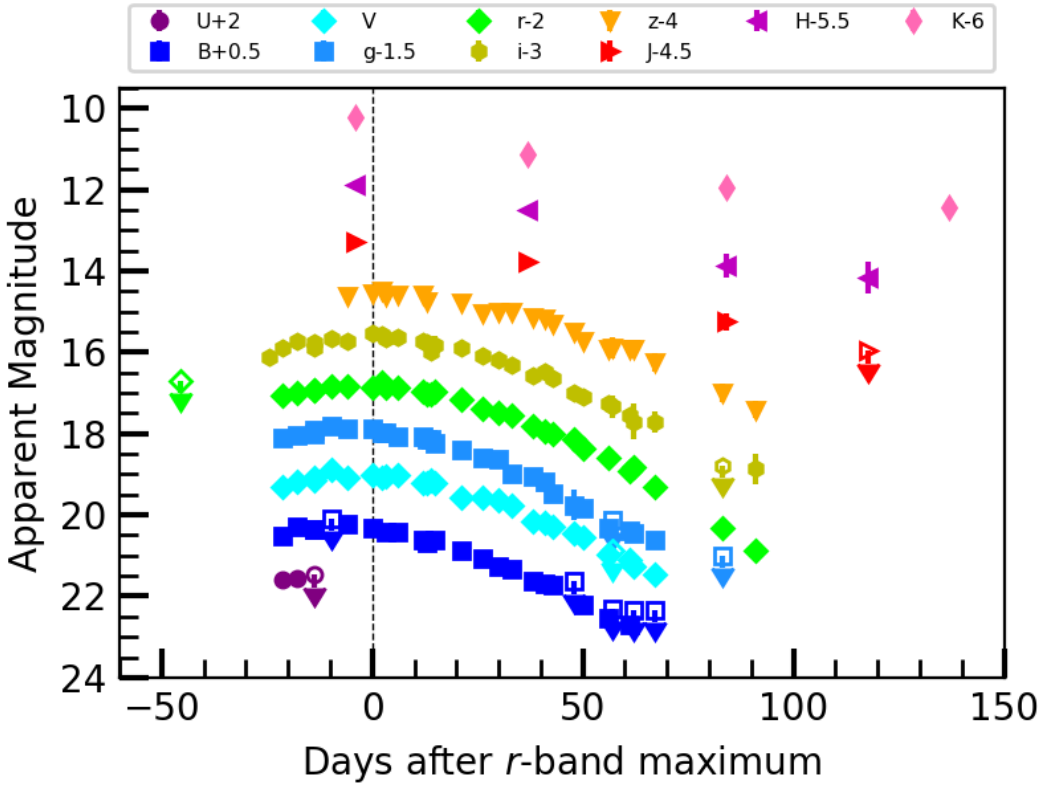

Figure 9: The light curves of AT 2018aes.

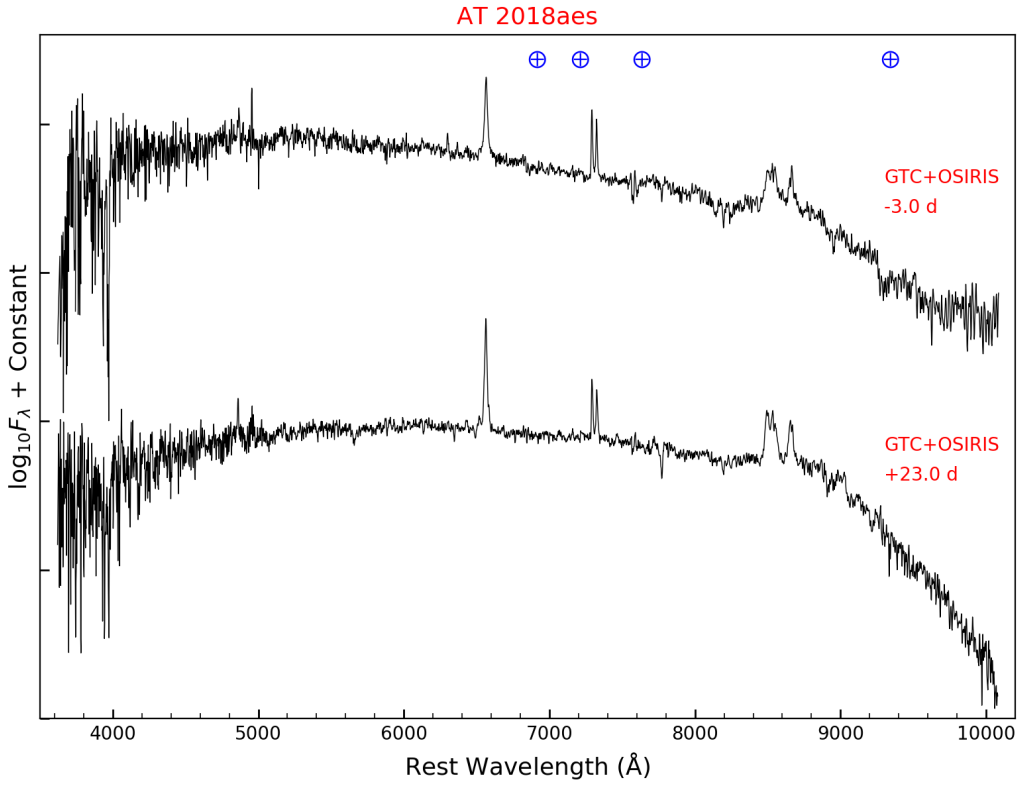

Figure 10: Spectral evolution of AT 2018aes. The epoch marked at the right of each spectrum are relative to the *r*-band maximum. The symbol ⊕ marks the positions of strongest telluric band bands. All spectra were rdshift corrected.

Table 12: Optical (*BVugriz*) light curves of AT 2018hso.

Date	MJD	*B*(err)	*V*(err)	*u*(err)	*g*(err)	*r*(err)	*i*(err)	*z*(err)	Instrument
20181031	58422.487	–	–	–	>19.5	–	–	–	1
20181031	58423.036	–	–	–	–	19.410 (0.3)	–	–	1
20181101	58423.466	–	–	–	>19.7	–	–	–	1
20181101	58423.534	–	–	–	–	>19.9	–	–	1
20181102	58424.529	–	–	–	–	18.920 (0.3)	–	–	1
20181104	58426.487	–	–	–	19.103 (0.096)	–	–	–	1
20181104	58426.530	–	–	–	–	18.656 (0.081)	–	–	1
20181106	58428.270	19.310 (0.047)	18.926 (0.040)	19.876 (0.119)	19.088 (0.042)	18.627 (0.035)	18.638 (0.044)	18.508 (0.053)	2
20181107	58429.469	–	–	–	19.259 (0.115)	–	–	–	1
20181110	58432.456	–	–	–	18.960 (0.088)	–	–	–	1
20181110	58432.547	–	–	–	–	18.483 (0.066)	–	–	1
20181115	58437.210	19.864 (0.030)	19.206 (0.039)	–	–	18.612 (0.114)	18.666 (0.054)	–	3
20181116	58438.210	19.838 (0.154)	19.321 (0.070)	20.147 (0.157)	19.236 (0.050)	18.895 (0.037)	18.665 (0.039)	18.671 (0.056)	2
20181118	58440.530	–	–	–	–	19.025 (0.078)	–	–	1
20181120	58442.215	20.212 (0.088)	19.378 (0.081)	20.709 (0.089)	19.777 (0.031)	19.285 (0.040)	18.870 (0.059)	18.971 (0.171)	3
20181121	58443.431	–	–	–	–	19.291 (0.168)	–	–	1
20181125	58447.270	–	–	>21.0	20.352 (0.120)	19.378 (0.058)	19.262 (0.091)	19.130 (0.116)	2
20181125	58447.470	–	–	–	–	19.620 (0.186)	–	–	1
20181201	58453.240	20.947(0.105)	19.955 (0.109)	22.482 (0.148)	20.509 (0.069)	19.659 (0.077)	19.529 (0.057)	19.254 (0.042)	3
20181204	58456.175	–	–	–	20.638 (0.101)	19.735 (0.059)	19.582 (0.113)	19.276 (0.058)	2
20181210	58462.190	–	–	–	21.082 (0.089)	19.844 (0.043)	19.627 (0.026)	19.248 (0.032)	3
20181212	58464.180	–	–	–	21.126 (0.132)	19.807 (0.062)	19.546 (0.071)	19.164 (0.093)	2
20181216	58468.175	–	–	–	21.233 (0.111)	19.783 (0.057)	19.423 (0.054)	19.068 (0.079)	2
20181220	58472.110	–	–	–	>21.3	19.746 (0.062)	19.407 (0.044)	–	2
20181220	58472.550	–	–	–	–	19.811 (0.194)	–	–	1
20181226	58478.135	–	–	–	21.637 (0.267)	19.702 (0.073)	19.337 (0.053)	18.883 (0.131)	2
20181229	58481.135	22.168 (0.229)	20.475 (0.099)	–	–	–	–	–	3
20181230	58482.115	–	–	–	21.690 (0.120)	19.649 (0.075)	19.307 (0.032)	18.861 (0.086)	2
20190103	58486.225	22.381 (0.171)	20.528 (0.048)	–	–	–	–	–	3
20190106	58489.085	–	–	–	21.908 (0.180)	19.644 (0.107)	19.308 (0.042)	18.878 (0.070)	2
20190108	58491.557	–	–	–	–	19.698 (0.130)	–	–	1
20190110	58493.235	22.544 (0.142)	20.608 (0.045)	–	21.861 (0.100)	19.607 (0.079)	19.284 (0.063)	18.772 (0.048)	3
20190114	58497.175	22.559 (0.134)	20.644 (0.085)	–	21.843 (0.084)	19.567 (0.113)	19.268 (0.113)	18.926 (0.067)	3
20190120	58503.175	22.594 (0.195)	20.543 (0.040)	–	21.788 (0.154)	19.510 (0.110)	19.156 (0.054)	18.875 (0.034)	3
20190125	58508.484	–	–	–	–	19.543 (0.178)	–	–	1
20190128	58511.386	–	–	–	–	19.516 (0.122)	–	–	1
20190206	58520.145	–	20.494 (0.043)	–	21.657 (0.074)	19.672 (0.026)	19.091 (0.020)	18.737 (0.040)	3
20190212	58526.175	22.479 (0.197)	20.392 (0.059)	–	21.637 (0.068)	19.632 (0.041)	19.093 (0.013)	18.773 (0.014)	3
20190221	58535.095	22.529 (0.223)	20.452 (0.051)	–	21.767 (0.366)	19.869 (0.051)	19.146 (0.040)	18.715 (0.040)	3
20190227	58541.995	22.824 (0.249)	20.580 (0.049)	–	21.968 (0.115)	19.900 (0.032)	19.258 (0.020)	18.832 (0.038)	3
20190315	58557.085	>22.9	21.064 (0.124)	–	>22.2	20.288 (0.051)	19.591 (0.037)	18.887 (0.048)	3
20190318	58560.875	–	–	–	>21.9	20.358 (0.139)	19.675 (0.079)	18.983 (0.073)	2
20190323	58565.950	–	–	–	–	20.512 (0.095)	19.659 (0.051)	–	2
20190407	58580.995	–	–	–	22.790 (0.200)	20.631 (0.138)	19.712 (0.045)	19.120 (0.073)	3
20190408	58581.005	>23.5	21.469 (0.075)	–	–	–	–	–	3
20190416	58589.080	–	>21.6	–	>22.5	20.835 (0.131)	19.835 (0.043)	19.133 (0.057)	3
20190420	58593.930	–	21.755 (0.204)	–	22.936 (0.221)	20.918 (0.284)	19.863 (0.290)	19.267 (0.059)	3
20190428	58601.950	–	22.061 (0.211)	–	–	21.060 (0.086)	19.932 (0.033)	19.202 (0.036)	3
20190512	58615.890	–	22.249 (0.176)	–	>23.0	21.126 (0.090)	19.982 (0.036)	19.279 (0.032)	3
20190530	58633.885	–	22.819 (0.319)	–	>23.1	21.577 (0.119)	20.326 (0.044)	19.528 (0.043)	3
20190611	58645.925	–	>23.0	–	–	22.007 (0.073)	21.001 (0.054)	19.750 (0.054)	3
20190617	58651.945	–	–	–	–	22.497 (0.183)	21.269 (0.051)	20.203 (0.052)	3
20190629	58663.880	–	–	–	–	–	21.544 (0.118)	–	4
20190702	58666.895	–	–	–	–	23.172 (0.521)	–	20.433 (0.058)	3
20190716	58680.915	–	–	–	–	–	21.952 (0.243)	20.705 (0.091)	3
20190803	58698.875	–	–	–	–	–	>22.4	21.216 (0.127)	3

1 ZTF data from the Palomar 1.2-m Oschin Telescope equipped with ZTF-Cam, taken from LASAIR [a] (Smith et al. 2019) and Transient Name Server (TNS [b]).

2 The 2-m fully automatic Liverpool Telescope (LT) equipped with IO:O, located at Roque de los Muchachos Observatory (La Palma, Canary Islands, Spain).

3 The 2.56-m Nordic Optical Telescope (NOT) equipped with ALFOSC, located at Roque de los Muchachos Observatory (La Palma, Canary Islands, Spain).

4 The 10.4-m Gran Telescopio Canarias (GTC) with OSIRIS, located at Roque de los Muchachos Observatory (La Palma, Canary Islands, Spain).

[a] LASAIR: https://lasair.roe.ac.uk/object/ZTF18acbwfza/

[b] TNS: https://wis-tns.weizmann.ac.il/object/2018hso

Table 13: NIR (JHK) light curves of AT 2018hso.

Date	MJD	J(err)	H(err)	K(err)	Instrument
20181104	58426.217	17.462 (0.034)	17.074 (0.024)	16.332 (0.026)	NOTCAM
20181124	58446.150	18.143 (0.091)	–	–	NOTCAM
20181211	58463.153	17.890 (0.104)	17.641 (0.119)	16.877 (0.126)	NOTCAM
20181231	58483.070	17.585 (0.117)	17.329 (0.115)	16.725 (0.111)	NOTCAM
20190111	58494.160	17.673 (0.098)	17.131 (0.098)	16.560 (0.163)	NOTCAM
20190130	58513.213	17.598 (0.097)	17.014 (0.102)	16.506 (0.125)	NOTCAM
20190305	58547.080	17.424 (0.092)	16.782 (0.093)	16.060 (0.119)	NOTCAM
20190322	58564.045	17.518 (0.122)	–	16.301 (0.106)	NOTCAM
20190410	58583.053	17.693 (0.035)	17.053 (0.124)	16.106 (0.114)	NOTCAM
20190430	58603.950	17.599 (0.074)	16.933 (0.096)	15.991 (0.547)	NOTCAM
20190613	58647.970	18.091 (0.122)	17.666 (0.119)	16.437 (0.121)	NOTCAM
20190703	58667.933	18.430 (0.098)	18.030 (0.064)	16.833 (0.155)	NOTCAM

NOTCAM: The 2.56-m Nordic Optical Telescope (NOT) equipped with NOTCAM, located at Roque de los Muchachos Observatory (La Palma, Canary Islands, Spain).

Acknowledgements

Yongzhi Cai is very grateful for the scientific training by his supervisor Andrea Pastorello during 3-year PhD career.
Yongzhi Cai thanks for the Padova-Asiago Supernova Group (Enrico Cappellaro, Stefano Benetti, Massimo Turatto, Nancy Elias-Rosa, Lina Tomasella, Giacomo Terreran, Leonardo Tartaglia, Andrea Reguitti, Giorgio Valerin, etc), who gave generous help during these research activities.
Yongzhi Cai also thanks the help of external collaborators, such as Morgan Fraser (University College Dublin, Ireland), Maria Teresa Botticella (INAF-OAC, Italy), Christa Gall (Niels Bohr Institute, University of Copenhagen, Denmark), Antonia Morales Garoffolo (Universidad de Cadiz, Spain), Simon Prentice (The University of Dublin, Ireland), and Tom Reynolds (University of Turku, Finland).
Yongzhi Cai appreciates his family members, in particular his fiancee Qiusheng Zhang who gave great encouragements during the 3-year abroad life.
Yongzhi Cai thanks for the recommendations from Prof. Zong-Hong Zhu, Prof. Jiang-Hua Wu, Dr. Zheng-Xiang Li, Dr. Fang Huang and Dr. Shuo Cao.
Yongzhi Cai acknowledges the support of the China Scholarship Council (No. 201606040170).

Observations from the NOT were obtained through the NUTS/NUTS2 collaboration which is supported in part by the Instrument Centre for Danish Astrophysics (IDA). This work makes use of data from Las Cumbres Observatory and these data were taken as part of the LCO Supernova Key Project. Based on observations collected at the European Organisation for Astronomical Research in the Southern Hemisphere under ESO programme 199.D—0143. The Liverpool Telescope (LT), operated by the Liverpool John Moores University at the Spanish Spanish Observatorio del Roque de los Muchachos of the Instituto de Astrofisica de Canarias. Observations based on LT are financed by the UK Science and Technology Facilities Council. Some data are based on observations collected at Copernico (or/and Schmidt) telescope(s) (Asiago, Italy) of the INAF - Osservatorio Astronomico di Padova. Funding for SDSS-III has been provided by the Alfred P. Sloan Foundation, the Participating Institutions, the National Science Foundation, and the U.S. Department of Energy Office of Science. The SDSS-III web site is http://www.sdss3.org/. Based on observations made with the GTC telescope, in the Spanish Observatorio del Roque de los Muchachos of the Instituto de Astrofisica de Canarias, under Director's Discretionary Time (GTC2019-127). This theisis makes use of data products from the Two Micron All Sky Survey, which is a joint project of the University of Massachusetts and the Infrared Processing and Analysis Center/California Institute of Technology, funded by the National Aeronautics and Space Administration and the National Science Foundation. IRAF is distributed by the National Optical Astronomy Observatories, which are operated by the Association of Universities for Research in Astronomy, Inc., under cooperative agreement with the National Science Foundation. This research has made use of the NASA/IPAC Extragalactic Database (NED), which is operated by the Jet Propulsion Laboratory, California Institute of Technology, under contract with the National Aeronautics and Space Administration. We acknowledge the usage of the HyperLeda database (http://leda.univ-lyon1.fr). This research makes use of Lasair data (https://lasair.roe.ac.uk/), which is supported by the UKRI Science and Technology Facilities Council and is a collaboration between the University of Edinburgh (grant ST/N002512/1) and Queen's University Belfast (grant ST/N002520/1) within the LSST:UK Science Consortium.

Bibliography

Abbott, B., Abbott, R., Adhikari, R., et al. 2008, Phys. Rev. D, 77, 062004

Adams, S. M., Blagorodnova, N., Kasliwal, M. M., et al. 2018, PASP, 130, 034202

Adams, S. M., Kochanek, C. S., Prieto, J. L., et al. 2016, MNRAS, 460, 1645

Aldering, G., Antilogus, P., Bailey, S., et al. 2006, ApJ, 650, 510

Althaus, L. G., Córsico, A. H., Isern, J., & García-Berro, E. 2010, A&ARv, 18, 471

Andretta, V., Busà, I., Gomez, M. T., & Terranegra, L. 2005, A&A, 430, 669

Arcavi, I. 2017, Hydrogen-Rich Core-Collapse Supernovae, 239

Athem Alsabti, A. 2015, IAU General Assembly, 22, 2253696

Atwood, W. B., Abdo, A. A., Ackermann, M., et al. 2009, ApJ, 697, 1071

Aufderheide, M. B., Baron, E., & Thielemann, F. K. 1991, ApJ, 370, 630

Axelrod, T. S. 1980, PhD thesis, California Univ., Santa Cruz.

Baade, W. & Zwicky, F. 1934, Proceedings of the National Academy of Science, 20, 254

Banerjee, D. P. K., Nuth, Joseph A., I., Misselt, K. A., et al. 2015, ApJ, 814, 109

Barbon, R., Benetti, S., Cappellaro, E., Rosino, L., & Turatto, M. 1990, A&A, 237, 79

Barbon, R., Buondí, V., Cappellaro, E., & Turatto, M. 1999, A&AS, 139, 531

Barbon, R., Ciatti, F., & Rosino, L. 1979, A&A, 72, 287

Baron, E. & Cooperstein, J. 1990, ApJ, 353, 597

Barsukova, E. A., Goranskij, V. P., Valeev, A. F., & Zharova, A. V. 2014, Astrophysical Bulletin, 69, 67

Becker, A. 2015, HOTPANTS: High Order Transform of PSF ANd Template Subtraction, Astrophysics Source Code Library

Berger, E. 2010, The Astronomer's Telegram, 2655

Berger, E., Marion, G. H., Hsiao, E., Foley, R., & Chornock, R. 2012, The Astronomer's Telegram, 4009

Berger, E., Roth, K., Stubbs, C., et al. 2009a, Exotic Explosions and Eruptions: Exploring a New Transient Phase-Space with Pan-STARRS, NOAO Proposal

Berger, E., Soderberg, A. M., Chevalier, R. A., et al. 2009b, ApJ, 699, 1850

Bertin, E. & Arnouts, S. 1996, A&AS, 117, 393

Bertola, F. 1964, AJ, 69, 236

Bertola, F. 1965, Mem. Soc. Astron. Italiana, 36, 299

Bessell, M. S. 2005, ARA&A, 43, 293

Bessell, M. S. & Brett, J. M. 1988, PASP, 100, 1134

Bhandari, S., Bannister, K. W., Murphy, T., et al. 2018a, MNRAS, 478, 1784

Bhandari, S., Keane, E. F., Barr, E. D., et al. 2018b, MNRAS, 475, 1427

Bhardwaj, A., Kanbur, S. M., Macri, L. M., et al. 2016, AJ, 151, 88

Blagorodnova, N., Kotak, R., Polshaw, J., et al. 2017, ApJ, 834, 107

Blinnikov, S. I. 2010, Physics of Atomic Nuclei, 73, 604

Blondin, S. & Tonry, J. L. 2007, ApJ, 666, 1024

Bohannan, B. & Walborn, N. R. 1989, PASP, 101, 520

Bond, H. E., Bedin, L. R., Bonanos, A. Z., et al. 2009, ApJ, 695, L154

Bono, G., Caputo, F., Marconi, M., & Musella, I. 2010, ApJ, 715, 277

Bose, S., Dong, S., Pastorello, A., et al. 2018, ApJ, 853, 57

Botticella, M. T., Pastorello, A., Smartt, S. J., et al. 2009, MNRAS, 398, 1041

Bottinelli, L., Gouguenheim, L., Paturel, G., & de Vaucouleurs, G. 1984, A&AS, 56, 381

Branch, D., Baron, E., Thomas, R. C., et al. 2004a, PASP, 116, 903

Branch, D., Thomas, R. C., Baron, E., et al. 2004b, ApJ, 606, 413

Branch, D. & Wheeler, J. C. 2017, Supernova Explosions

Burke, J., Howell, D. A., Arcavi, I., et al. 2019, Transient Name Server Classification Report, 2019-328, 1

Busà, I., Aznar Cuadrado, R., Terranegra, L., Andretta, V., & Gomez, M. T. 2007, A&A, 466, 1089

Bychkov, V. V. & Liberman, M. A. 1995, A&A, 304, 440

Cai, Y.-Z., Pastorello, A., Fraser, M., et al. 2018, MNRAS, 480, 3424

Cai, Y.-Z., Pastorello, A., Fraser, M., et al. 2019, arXiv e-prints, arXiv:1909.13147

Caleb, M., Keane, E. F., van Straten, W., et al. 2018, MNRAS, 478, 2046

Canal, R., Ruiz-Lapuente, P., & Burkert, A. 1996, ApJ, 456, L101

Candia, P., Krisciunas, K., Suntzeff, N. B., et al. 2003, PASP, 115, 277

Cao, Y., Kasliwal, M. M., Arcavi, I., et al. 2013, ApJ, 775, L7

Cappellaro, E., Mazzali, P. A., Benetti, S., et al. 1997, A&A, 328, 203

Cappellaro, E., Patat, F., Mazzali, P. A., et al. 2001, ApJ, 549, L215

Cardelli, J. A., Clayton, G. C., & Mathis, J. S. 1989, ApJ, 345, 245

Catchpole, R. M., Whitelock, P. A., Feast, M. W., et al. 1988, MNRAS, 231, 75p

Catchpole, R. M., Whitelock, P. A., Menzies, J. W., et al. 1989, MNRAS, 237, 55P

Chen, J., Wang, X., Ganeshalingam, M., et al. 2014, ApJ, 790, 120

Chen, T.-W., Smartt, S. J., Yates, R. M., et al. 2017, MNRAS, 470, 3566

Chevalier, R. A. & Fransson, C. 1994, ApJ, 420, 268

Chonis, T. S. & Gaskell, C. M. 2008, AJ, 135, 264

Chugai, N. N. & Danziger, I. J. 1994, MNRAS, 268, 173

Clocchiatti, A., Wheeler, J. C., Benetti, S., & Frueh, M. 1996, ApJ, 459, 547

Conti, P. S. & Frost, S. A. 1977, ApJ, 212, 728

Couch, S. M. 2017, Philosophical Transactions of the Royal Society of London Series A, 375, 20160271

Couch, S. M. & Ott, C. D. 2015, ApJ, 799, 5

Courant, R. & Friedrichs, K. O. 1948, Supersonic flow and shock waves

Cousins, A. W. J. 1976, Monthly Notes of the Astronomical Society of South Africa, 35, 70

Crowther, P. A. 2007, ARA&A, 45, 177

De, K., Fremling, C., Miller, A. A., et al. 2018, The Astronomer's Telegram, 12162

de, S., Baron, E., & Hauschildt, P. H. 2010, MNRAS, 401, 2081

De Cia, A., Gal-Yam, A., Rubin, A., et al. 2018, ApJ, 860, 100

de Groot, M. 1969a, Bull. Astron. Inst. Netherlands, 20, 225

de Groot, M. 1969b, Commmunications of the Konkoly Observatory Hungary, 65, 203

de Groot, M. 1988, Irish Astronomical Journal, 18, 163

de Vaucouleurs, G. 1959, Handbuch der Physik, 53, 275

de Vaucouleurs, G., de Vaucouleurs, A., Buta, R., Ables, H. D., & Hewitt, A. V. 1981, PASP, 93, 36

Delgado, A., Harrison, D., Hodgkin, S., et al. 2017, Transient Name Server Discovery Report, 2017-1485, 1

Dessart, L., Hillier, D. J., Woosley, S., et al. 2016, MNRAS, 458, 1618

Dhawan, S., Jha, S. W., & Leibundgut, B. 2018, A&A, 609, A72

Dhawan, S., Leibundgut, B., Spyromilio, J., & Maguire, K. 2015, MNRAS, 448, 1345

Dilday, B., Howell, D. A., Cenko, S. B., et al. 2012, Science, 337, 942

Djorgovski, S. G., Mahabal, A., Drake, A., Graham, M., & Donalek, C. 2013, Sky Surveys, ed. T. D. Oswalt & H. E. Bond, 223

Doherty, C. L., Gil-Pons, P., Siess, L., & Lattanzio, J. C. 2017, Publ. Astron. Soc. Australia, 34, e056

Doherty, C. L., Gil-Pons, P., Siess, L., Lattanzio, J. C., & Lau, H. H. B. 2015, MNRAS, 446, 2599

Doi, M., Tanaka, M., Fukugita, M., et al. 2010, AJ, 139, 1628

Drake, A. J., Djorgovski, S. G., Mahabal, A., et al. 2009, in Bulletin of the American Astronomical Society, Vol. 41, American Astronomical Society Meeting Abstracts #213, 421

Drout, M. R., Piro, A. L., Shappee, B. J., et al. 2017, Science, 358, 1570

Eastman, R. G., Woosley, S. E., Weaver, T. A., & Pinto, P. A. 1994, ApJ, 430, 300

Eldridge, J. J., Fraser, M., Smartt, S. J., Maund, J. R., & Crockett, R. M. 2013, MNRAS, 436, 774

Elias, J. H., Matthews, K., Neugebauer, G., & Persson, S. E. 1985, ApJ, 296, 379

Elias-Rosa, N., Pastorello, A., Maund, J. R., et al. 2013, MNRAS, 436, L109

Elias-Rosa, N., Van Dyk, S. D., Li, W., et al. 2010, ApJ, 714, L254

Elias-Rosa, N., Van Dyk, S. D., Li, W., et al. 2011, ApJ, 742, 6

Ensman, L. M. & Woosley, S. E. 1988, ApJ, 333, 754

Exter, K. M., Cox, N. L. J., Swinyard, B. M., et al. 2016, A&A, 596, A96

Ferland, G. J. & Persson, S. E. 1989, ApJ, 347, 656

Ferrarese, L., Mould, J. R., Kennicutt, Jr., R. C., et al. 2000, ApJ, 529, 745

Filippenko, A. V. 1988, AJ, 96, 1941

Filippenko, A. V. 1997, ARA&A, 35, 309

Filippenko, A. V., Li, W. D., Treffers, R. R., & Modjaz, M. 2001, in Astronomical Society of the Pacific Conference Series, Vol. 246, IAU Colloq. 183: Small Telescope Astronomy on Global Scales, ed. B. Paczynski, W.-P. Chen, & C. Lemme, 121

Filippenko, A. V., Matheson, T., & Ho, L. C. 1993, ApJ, 415, L103

Filippenko, A. V., Porter, A. C., & Sargent, W. L. W. 1990, AJ, 100, 1575

Filippenko, A. V., Richmond, M. W., Branch, D., et al. 1992a, AJ, 104, 1543

Filippenko, A. V., Richmond, M. W., Matheson, T., et al. 1992b, ApJ, 384, L15

Foley, R. J. 2015, MNRAS, 452, 2463

Foley, R. J., Berger, E., Fox, O., et al. 2011, ApJ, 732, 32

Foley, R. J., Koekemoer, A. M., Spergel, D. N., et al. 2018, arXiv e-prints, arXiv:1812.00514

Foley, R. J., McCully, C., Jha, S. W., et al. 2014, ApJ, 792, 29

Foley, R. J., Van Dyk, S. D., Jha, S. W., et al. 2015, ApJ, 798, L37

Fox, O. D., Silverman, J. M., Filippenko, A. V., et al. 2015, MNRAS, 447, 772

Fraser, M., Inserra, C., Jerkstrand, A., et al. 2013, MNRAS, 433, 1312

Fraser, M., Kotak, R., Pastorello, A., et al. 2015, MNRAS, 453, 3886

Gal-Yam, A. 2012, Science, 337, 927

Gal-Yam, A., Fox, D. B., Kulkarni, S. R., et al. 2005, ApJ, 630, L29

Gal-Yam, A. & Leonard, D. C. 2009, Nature, 458, 865

Gal-Yam, A., Leonard, D. C., Fox, D. B., et al. 2007, ApJ, 656, 372

Gal-Yam, A., Mazzali, P., Ofek, E. O., et al. 2009, Nature, 462, 624

Gall, C., Hjorth, J., Rosswog, S., Tanvir, N. R., & Levan, A. J. 2017, ApJ, 849, L19

Ganeshalingam, M. 2012, PhD thesis, University of California, Berkeley

Ganeshalingam, M., Li, W., Filippenko, A. V., et al. 2012, ApJ, 751, 142

Georgy, C., Ekström, S., Meynet, G., et al. 2012, A&A, 542, A29

Georgy, C., Meynet, G., Walder, R., Folini, D., & Maeder, A. 2009, A&A, 502, 611

Gibson, B. K., Stetson, P. B., Freedman, W. L., et al. 2000, ApJ, 529, 723

González-Gaitán, S., Perrett, K., Sullivan, M., et al. 2011, ApJ, 727, 107

Goranskij, V. P., Barsukova, E. A., Spiridonova, O. I., et al. 2016, Astrophysical Bulletin, 71, 82

Graham, M. L., Harris, C. E., Fox, O. D., et al. 2017, ApJ, 843, 102

Granot, J., Guetta, D., & Gill, R. 2017, ApJ, 850, L24

Grassberg, E. K., Imshennik, V. S., & Nadyozhin, D. K. 1971, Ap&SS, 10, 28

Greenstein, J. L. & Minkowski, R. 1973, ApJ, 182, 225

Gutiérrez, C. P., Anderson, J. P., Hamuy, M., et al. 2014a, ApJ, 786, L15

Gutiérrez, C. P., Anderson, J. P., Hamuy, M., et al. 2014b, ApJ, 786, L15

Gutiérrez, C. P., Anderson, J. P., Hamuy, M., et al. 2017, ApJ, 850, 89

Habergham, S. M., Anderson, J. P., James, P. A., & Lyman, J. D. 2014, MNRAS, 441, 2230

Hamuy, M., Maza, J., Pinto, P. A., et al. 2002, AJ, 124, 417

Hamuy, M. A. 2001, PhD thesis, The University of Arizona

Han, Z. & Podsiadlowski, P. 2004, MNRAS, 350, 1301

Hanke, F., Marek, A., Müller, B., & Janka, H.-T. 2012, ApJ, 755, 138

Harkness, R. P., Wheeler, J. C., Margon, B., et al. 1987, ApJ, 317, 355

Hashimoto, M., Iwamoto, K., & Nomoto, K. 1993, ApJ, 414, L105

Heger, A., Fryer, C. L., Woosley, S. E., Langer, N., & Hartmann, D. H. 2003, ApJ, 591, 288

Herwig, F. 2005, ARA&A, 43, 435

Hildebrand, R. H. 1983, QJRAS, 24, 267

Hoeflich, P. & Khokhlov, A. 1996, ApJ, 457, 500

Hoeflich, P., Khokhlov, A., Wheeler, J. C., et al. 1996, ApJ, 472, L81

Höflich, P. 1995, ApJ, 443, 89

Höfner, S. & Olofsson, H. 2018, A&ARv, 26, 1

Hosseinzadeh, G., Mccully, C., Arcavi, I., Howell, D. A., & Valenti, S. 2017, Transient Name Server Classification Report, 43

Howell, D. A. 2001, ApJ, 554, L193

Howerton, S., Prieto, J., Drake, A. J., et al. 2012, The Astronomer's Telegram, 4004

Huang, C. & Chevalier, R. A. 2018, MNRAS, 475, 1261

Huang, F., Wang, X., Zampieri, L., et al. 2016, ApJ, 832, 139

Huang, F., Wang, X., Zhang, J., et al. 2015, ApJ, 807, 59

Hubble, E. 1926, Contributions from the Mount Wilson Observatory / Carnegie Institution of Washington, 324, 1

Humphreys, R. M., Bond, H. E., Bedin, L. R., et al. 2011, ApJ, 743, 118

Humphreys, R. M. & Davidson, K. 1994, PASP, 106, 1025

Humphreys, R. M., Davidson, K., & Smith, N. 1999, PASP, 111, 1124

Humphreys, R. M., Weis, K., Davidson, K., & Gordon, M. S. 2016, ApJ, 825, 64

Iben, Icko, J. & Tutukov, A. V. 1992, ApJ, 389, 369

Inserra, C. 2019, arXiv e-prints, arXiv:1908.02314

Inserra, C., Baron, E., & Turatto, M. 2012a, MNRAS, 422, 1178

Inserra, C., Fraser, M., Smartt, S. J., et al. 2016, MNRAS, 459, 2721

Inserra, C., Nichol, R. C., Scovacricchi, D., et al. 2018a, A&A, 609, A83

Inserra, C., Nicholl, M., Chen, T. W., et al. 2017, MNRAS, 468, 4642

Inserra, C., Pastorello, A., Turatto, M., et al. 2013a, A&A, 555, A142

Inserra, C., Prajs, S., Gutierrez, C. P., et al. 2018b, ApJ, 854, 175

Inserra, C. & Smartt, S. J. 2014, ApJ, 796, 87

Inserra, C., Smartt, S. J., Gall, E. E. E., et al. 2018c, MNRAS, 475, 1046

Inserra, C., Smartt, S. J., Jerkstrand, A., et al. 2013b, ApJ, 770, 128

Inserra, C., Smartt, S. J., Scalzo, R., et al. 2014, MNRAS, 437, L51

Inserra, C., Turatto, M., Pastorello, A., et al. 2011, MNRAS, 417, 261

Inserra, C., Turatto, M., Pastorello, A., et al. 2012b, MNRAS, 422, 1122

Jack, D., Hauschildt, P. H., & Baron, E. 2012, A&A, 538, A132

Janka, H.-T. 2017a, Neutrino-Driven Explosions, 1095

Janka, H.-T. 2017b, Neutrino Emission from Supernovae, 1575

Janka, H.-T., Hanke, F., Hüdepohl, L., et al. 2012, Progress of Theoretical and Experimental Physics, 2012, 01A309

Janka, H.-T., Melson, T., & Summa, A. 2016, Annual Review of Nuclear and Particle Science, 66, 341

Jencson, J. E., Adams, S. M., Bond, H. E., et al. 2019, The Astrophysical Journal, 880, L20

Jha, S., Branch, D., Chornock, R., et al. 2006, AJ, 132, 189

Jha, S. W. 2017, Type Iax Supernovae, 375

Johnson, H. L. & Morgan, W. W. 1953, ApJ, 117, 313

Johnson, S. A., Kochanek, C. S., & Adams, S. M. 2017, MNRAS, 472, 3115

Jones, M. I., Hamuy, M., Lira, P., et al. 2009, ApJ, 696, 1176

Jordi, K., Grebel, E. K., & Ammon, K. 2006, A&A, 460, 339

Justham, S. 2011, ApJ, 730, L34

Kaiser, N., Burgett, W., Chambers, K., et al. 2010, in Proc. SPIE, Vol. 7733, Ground-based and Airborne Telescopes III, 77330E

Kamiński, T., Schmidt, M., Tylenda, R., Konacki, M., & Gromadzki, M. 2009, ApJS, 182, 33

Kankare, E., Ergon, M., Bufano, F., et al. 2012, MNRAS, 424, 855

Kankare, E., Kotak, R., Pastorello, A., et al. 2015, A&A, 581, L4

Kasen, D. 2006, ApJ, 649, 939

Kasen, D. & Bildsten, L. 2010, ApJ, 717, 245

Kasliwal, M. M. 2012, Publ. Astron. Soc. Australia, 29, 482

Kasliwal, M. M., Bally, J., Masci, F., et al. 2017, ApJ, 839, 88

Kasliwal, M. M. & Kulkarni, S. R. 2010, The Astronomer's Telegram, 2590

Kasliwal, M. M., Kulkarni, S. R., Arcavi, I., et al. 2011, ApJ, 730, 134

Kasliwal, M. M., Kulkarni, S. R., Gal-Yam, A., et al. 2012, ApJ, 755, 161

Kawabata, K. S., Maeda, K., Nomoto, K., et al. 2010, Nature, 465, 326

Keane, E. F., Barr, E. D., Jameson, A., et al. 2018, MNRAS, 473, 116

Keane, E. F., Ludovici, D. A., Eatough, R. P., et al. 2010, MNRAS, 401, 1057

Keller, S. C., Schmidt, B. P., Bessell, M. S., et al. 2007, Publ. Astron. Soc. Australia, 24, 1

Kelly, P. L., Filippenko, A. V., Modjaz, M., & Kocevski, D. 2014, ApJ, 789, 23

Kelly, P. L., Kirshner, R. P., & Pahre, M. 2008, ApJ, 687, 1201

Khokhlov, A. M. 1991, A&A, 245, 114

Kilpatrick, C. D., Foley, R. J., Abramson, L. E., et al. 2017, MNRAS, 465, 4650

Kim, H.-J., Yoon, S.-C., & Koo, B.-C. 2015, ApJ, 809, 131

Kimeswenger, S., Lederle, C., Schmeja, S., & Armsdorfer, B. 2002, MNRAS, 336, L43

Kirshner, R. P., Jeffery, D. J., Leibundgut, B., et al. 1993, ApJ, 415, 589

Kirshner, R. P. & Oke, J. B. 1975, ApJ, 200, 574

Kirshner, R. P., Oke, J. B., Penston, M. V., & Searle, L. 1973, ApJ, 185, 303

Kitaura, F. S., Janka, H. T., & Hillebrandt, W. 2006, A&A, 450, 345

Kochanek, C. S. 2011, ApJ, 741, 37

Kochanek, C. S., Adams, S. M., & Belczynski, K. 2014, MNRAS, 443, 1319

Kochanek, C. S., Szczygieł, D. M., & Stanek, K. Z. 2012, ApJ, 758, 142

Koester, D. & Chanmugam, G. 1990, Reports on Progress in Physics, 53, 837

Krisciunas, K., Suntzeff, N. B., & Candia, P. 2004, in Bulletin of the American Astronomical Society, Vol. 36, American Astronomical Society Meeting Abstracts, 1617

Kromer, M., Fremling, C., Pakmor, R., et al. 2016, MNRAS, 459, 4428

Kromer, M., Pakmor, R., Taubenberger, S., et al. 2013, ApJ, 778, L18

Kuchner, M. J., Kirshner, R. P., Pinto, P. A., & Leibundgut, B. 1994, ApJ, 426, 89

Kulkarni, S. R., Ofek, E. O., Rau, A., et al. 2007, Nature, 447, 458

Lambert, D. L., Mallia, E. A., & Warner, B. 1969, Sol. Phys., 7, 11

Lamers, H. J. G. L. M. 1986, A&A, 159, 90

Landau, L. D. & Lifshitz, E. M. 1975, The classical theory of fields

Landolt, A. U. 1992, AJ, 104, 340

Law, N. M., Kulkarni, S. R., Dekany, R. G., et al. 2009, PASP, 121, 1395

Leibundgut, B., Kirshner, R. P., Phillips, M. M., et al. 1993, AJ, 105, 301

Leitherer, C., Appenzeller, I., Klare, G., et al. 1985, A&A, 153, 168

Leloudas, G., Schulze, S., Krühler, T., et al. 2015, MNRAS, 449, 917

Leung, S. C. & Nomoto, K. 2017, Mem. Soc. Astron. Italiana, 88, 266

Leung, S.-C. & Nomoto, K. 2019, Publ. Astron. Soc. Australia, 36, e006

Levan, A., Crowther, P., de Grijs, R., et al. 2016, Space Sci. Rev., 202, 33

Levesque, E. M. 2014, PASP, 126, 1

Li, L., Wang, X., Zhang, J., et al. 2018, MNRAS, 478, 4575

Li, W., Filippenko, A. V., Chornock, R., et al. 2003, PASP, 115, 453

Li, W., Filippenko, A. V., Gates, E., et al. 2001, PASP, 113, 1178

Li, W., Leaman, J., Chornock, R., et al. 2011, MNRAS, 412, 1441

Li, W., Wang, X., Van Dyk, S. D., et al. 2007, ApJ, 661, 1013

Li, W. D., Filippenko, A. V., Treffers, R. R., et al. 2000, in American Institute of Physics Conference Series, Vol. 522, American Institute of Physics Conference Series, ed. S. S. Holt & W. W. Zhang, 103–106

Lipunov, V. M., Blinnikov, S., Gorbovskoy, E., et al. 2017, MNRAS, 470, 2339

Lisewski, A. M., Hillebrandt, W., Woosley, S. E., Niemeyer, J. C., & Kerstein, A. R. 2000, ApJ, 537, 405

Liu, Z.-W., Moriya, T. J., Stancliffe, R. J., & Wang, B. 2015a, A&A, 574, A12

Liu, Z.-W., Zhang, J.-J., Ciabattari, F., et al. 2015b, MNRAS, 452, 838

Loebman, S. R., Wisniewski, J. P., Schmidt, S. J., et al. 2015, AJ, 149, 17

LSST Science Collaboration, Abell, P. A., Allison, J., et al. 2009, arXiv e-prints, arXiv:0912.0201

Lunnan, R., Chornock, R., Berger, E., et al. 2014, ApJ, 787, 138

Lunnan, R., Chornock, R., Berger, E., et al. 2016, ApJ, 831, 144

Lyman, J. D., Levan, A. J., Church, R. P., Davies, M. B., & Tanvir, N. R. 2014, MNRAS, 444, 2157

Lyman, J. D., Taddia, F., Stritzinger, M. D., et al. 2018, MNRAS, 473, 1359

MacLeod, M., Macias, P., Ramirez-Ruiz, E., et al. 2017, ApJ, 835, 282

Makarov, D., Prugniel, P., Terekhova, N., Courtois, H., & Vauglin, I. 2014, A&A, 570, A13

Mallik, S. V. 1997, A&AS, 124, 359

Mallik, S. V. 1998, Bulletin of the Astronomical Society of India, 26, 479

Margheim, S. J., Rest, A., & Smartt, S. J. 2013, The Astronomer's Telegram, 4798

Marshall, S., Akerlof, C., Kehoe, R., et al. 1997, in Bulletin of the American Astronomical Society, Vol. 29, American Astronomical Society Meeting Abstracts, 1290

Martin, J., Fuhrmeister, B., Mittag, M., et al. 2017, A&A, 605, A113

Martin, R. G., Tout, C. A., & Lesaffre, P. 2006, MNRAS, 373, 263

Mason, E., Diaz, M., Williams, R. E., Preston, G., & Bensby, T. 2010, A&A, 516, A108

Matheson, T. 2001, PASP, 113, 1155

Mauerhan, J. C., Smith, N., Filippenko, A. V., et al. 2013a, MNRAS, 430, 1801

Mauerhan, J. C., Smith, N., Silverman, J. M., et al. 2013b, MNRAS, 431, 2599

Mauerhan, J. C., Van Dyk, S. D., Johansson, J., et al. 2018, MNRAS, 473, 3765

Maund, J. R., Mattila, S., Ramirez-Ruiz, E., & Eldridge, J. J. 2014a, MNRAS, 438, 1577

Maund, J. R., Reilly, E., & Mattila, S. 2014b, MNRAS, 438, 938

Maund, J. R. & Smartt, S. J. 2009, Science, 324, 486

Maund, J. R., Smartt, S. J., Kudritzki, R.-P., et al. 2006, MNRAS, 369, 390

Maund, J. R., Smartt, S. J., & Schweizer, F. 2005, ApJ, 630, L33

Mazurek, T. J., Truran, J. W., & Cameron, A. G. W. 1974, Ap&SS, 27, 261

Mazzali, P. A., Chugai, N., Turatto, M., et al. 1997, MNRAS, 284, 151

Mazzali, P. A., Kawabata, K. S., Maeda, K., et al. 2005, Science, 308, 1284

Mazzali, P. A., Lucy, L. B., Danziger, I. J., et al. 1993, A&A, 269, 423

McCollum, B., Laine, S., Väisänen, P., et al. 2014, AJ, 147, 11

McGregor, P. J., Hyland, A. R., & McGinn, M. T. 1989, A&A, 223, 237

Mehner, A., Baade, D., Rivinius, T., et al. 2013, A&A, 555, A116

Meikle, W. P. S., Cumming, R. J., Geballe, T. R., et al. 1996, MNRAS, 281, 263

Mesler, Robert A., I. 2013, PhD thesis, The University of New Mexico

Metzger, B. D. & Pejcha, O. 2017, MNRAS, 471, 3200

Minkowski, R. 1939, ApJ, 89, 156

Minkowski, R. 1941, PASP, 53, 224

Miyaji, S. & Nomoto, K. 1987, ApJ, 318, 307

Miyaji, S., Nomoto, K., Yokoi, K., & Sugimoto, D. 1980, Publications of the Astronomical Society of Japan, 32, 303

Mo, H., van den Bosch, F. C., & White, S. 2010, Galaxy Formation and Evolution

Monard, L. A. G. 2008, IAU Circ., 8946

Moriya, T. J. & Eldridge, J. J. 2016, MNRAS, 461, 2155

Moriya, T. J., Tominaga, N., Langer, N., et al. 2014, A&A, 569, A57

Mould, J. R., Huchra, J. P., Freedman, W. L., et al. 2000, ApJ, 545, 547

Mukherjee, S., Feigelson, E. D., Jogesh Babu, G., et al. 1998, ApJ, 508, 314

Mulchaey, J. S., Kasliwal, M. M., & Kollmeier, J. A. 2014, ApJ, 780, L34

Müller, B., Wanajo, S., Janka, H. T., et al. 2017, Memorie della Societa Astronomica Italiana, 88, 288

Munari, U., Henden, A., Kiyota, S., et al. 2002, A&A, 389, L51

Murphy, J. W. & Burrows, A. 2008, ApJS, 179, 209

Murphy, J. W., Dolence, J. C., & Burrows, A. 2013, ApJ, 771, 52

Neill, J. D., Sullivan, M., Howell, D. A., et al. 2009, ApJ, 707, 1449

Niemeyer, J. C. 1999, ApJ, 523, L57

Nomoto, K. 1984, ApJ, 277, 791

Nomoto, K. 1987, ApJ, 322, 206

Nomoto, K., Thielemann, F.-K., Yokoi, K., & Branch, D. 1986, Ap&SS, 118, 305

Nomoto, K., Tominaga, N., & Blinnikov, S. I. 2014, in American Institute of Physics Conference Series, Vol. 1594, American Institute of Physics Conference Series, ed. S. Jeong, N. Imai, H. Miyatake, & T. Kajino, 258–265

Norris, R. P., Afonso, J., Bacon, D., et al. 2013, Publ. Astron. Soc. Australia, 30, e020

Nota, A., Livio, M., Clampin, M., & Schulte-Ladbeck, R. 1995, ApJ, 448, 788

Nyholm, A., Sollerman, J., Taddia, F., et al. 2017, A&A, 605, A6

O'Connor, E. & Ott, C. D. 2010, Classical and Quantum Gravity, 27, 114103

Ofek, E. O., Kulkarni, S. R., Rau, A., et al. 2008, ApJ, 674, 447

Oke, J. B. & Gunn, J. E. 1983, ApJ, 266, 713

Osterbrock, D. E. 1951, ApJ, 114, 469

Osterbrock, D. E. & Bochkarev, N. G. 1989, Soviet Ast., 33, 694

Ott, C. D., Roberts, L. F., da Silva Schneider, A., et al. 2018, ApJ, 855, L3

Papadopoulos, A., D'Andrea, C. B., Sullivan, M., et al. 2015, MNRAS, 449, 1215

Pastorello, A. 2012, Memorie della Societa Astronomica Italiana Supplementi, 19, 24

Pastorello, A., Cappellaro, E., Inserra, C., et al. 2013, ApJ, 767, 1

Pastorello, A., Chen, T. W., Cai, Y. Z., et al. 2019a, A&A, 625, L8

Pastorello, A., Della Valle, M., Smartt, S. J., et al. 2007a, Nature, 449, 1

Pastorello, A. & Fraser, M. 2019, Nature Astronomy, 3, 676

Pastorello, A., Mason, E., Taubenberger, S., et al. 2019b, A&A, 630, A75

Pastorello, A., Mattila, S., Zampieri, L., et al. 2008, MNRAS, 389, 113

Pastorello, A., Sauer, D., Taubenberger, S., et al. 2006, MNRAS, 370, 1752

Pastorello, A., Smartt, S. J., Botticella, M. T., et al. 2010, ApJ, 724, L16

Pastorello, A., Taubenberger, S., Elias-Rosa, N., et al. 2007b, MNRAS, 376, 1301

Pastorello, A., Zampieri, L., Turatto, M., et al. 2004, MNRAS, 347, 74

Patat, F., Barbon, R., Cappellaro, E., & Turatto, M. 1994, A&A, 282, 731

Patat, F., Benetti, S., Cappellaro, E., et al. 1996, MNRAS, 278, 111

Patat, F., Benetti, S., Cappellaro, E., & Turatto, M. 2006, MNRAS, 369, 1949

Pejcha, O. 2014, ApJ, 788, 22

Pejcha, O., Metzger, B. D., & Tomida, K. 2016a, MNRAS, 461, 2527

Pejcha, O., Metzger, B. D., & Tomida, K. 2016b, MNRAS, 455, 4351

Pejcha, O., Metzger, B. D., Tyles, J. G., & Tomida, K. 2017, ApJ, 850, 59

Pejcha, O. & Thompson, T. A. 2012, ApJ, 746, 106

Perets, H. B., Gal-Yam, A., Mazzali, P. A., et al. 2010, Nature, 465, 322

Perlmutter, S., Aldering, G., Goldhaber, G., et al. 1999, ApJ, 517, 565

Phillips, M. M. 1993, ApJ, 413, L105

Phillips, M. M. 2003, in Lecture Notes in Physics, Berlin Springer Verlag, Vol. 635, Stellar Candles for the Extragalactic Distance Scale, ed. D. Alloin & W. Gieren, 175–185

Phillips, M. M., Wells, L. A., Suntzeff, N. B., et al. 1992, AJ, 103, 1632

Pilyugin, L. S., Vílchez, J. M., & Contini, T. 2004, A&A, 425, 849

Podsiadlowski, P., Hsu, J. J. L., Joss, P. C., & Ross, R. R. 1993, Nature, 364, 509

Podsiadlowski, P., Mazzali, P. A., Nomoto, K., Lazzati, D., & Cappellaro, E. 2004, ApJ, 607, L17

Poelarends, A. J. T., Herwig, F., Langer, N., & Heger, A. 2008, ApJ, 675, 614

Poznanski, D., Ganeshalingam, M., Silverman, J. M., & Filippenko, A. V. 2011, MNRAS, 415, L81

Pozzo, M., Meikle, W. P. S., Rayner, J. T., et al. 2006, MNRAS, 368, 1169

Prajs, S., Sullivan, M., Smith, M., et al. 2017, MNRAS, 464, 3568

Prieto, J. L., Kistler, M. D., Thompson, T. A., et al. 2008, ApJ, 681, L9

Prieto, J. L., Sellgren, K., Thompson, T. A., & Kochanek, C. S. 2009, ApJ, 705, 1425

Pumo, M. L., Turatto, M., Botticella, M. T., et al. 2009, ApJ, 705, L138

Quimby, R. M. 2006, PhD thesis, The University of Texas at Austin

Quimby, R. M., Aldering, G., Wheeler, J. C., et al. 2007, ApJ, 668, L99

Quimby, R. M., Kulkarni, S. R., Kasliwal, M. M., et al. 2011, Nature, 474, 487

Rane, A., Lorimer, D. R., Bates, S. D., et al. 2016, MNRAS, 455, 2207

Rau, A., Kulkarni, S. R., Ofek, E. O., & Yan, L. 2007, ApJ, 659, 1536

Rebassa-Mansergas, A., Toonen, S., Korol, V., & Torres, S. 2019, MNRAS, 482, 3656

Richardson, D., Jenkins, Robert L., I., Wright, J., & Maddox, L. 2014, AJ, 147, 118

Richtler, T. & Sadler, E. M. 1983, A&A, 128, L3

Riess, A. G., Filippenko, A. V., Challis, P., et al. 1998, AJ, 116, 1009

Rodríguez, Ó., Pignata, G., Hamuy, M., et al. 2019, MNRAS, 483, 5459

Rosswog, S. & Liebendörfer, M. 2003, MNRAS, 342, 673

Rouleau, F. & Martin, P. G. 1991, ApJ, 377, 526

Rui, L., Wang, X., Mo, J., et al. 2019, MNRAS, 485, 1990

Ruiz-Lapuente, P., Cappellaro, E., Turatto, M., et al. 1992, ApJ, 387, L33

Sahu, D. K., Anupama, G. C., Srividya, S., & Muneer, S. 2006, MNRAS, 372, 1315

Salpeter, E. E. 1955, ApJ, 121, 161

Sandage, A. & Tammann, G. A. 1990, ApJ, 365, 1

Schilizzi, R. T., Dewdney, P. E. F., & Lazio, T. J. W. 2010, in Proc. SPIE, Vol. 7733, Ground-based and Airborne Telescopes III, 773318

Schlafly, E. F. & Finkbeiner, D. P. 2011, ApJ, 737, 103

Schlegel, E. M. 1990, MNRAS, 244, 269

Schlegel, E. M. 1996, AJ, 111, 1660

Schmidt, B. P., Kirshner, R. P., Leibundgut, B., et al. 1994, ApJ, 434, L19

Schulze, S., Krühler, T., Leloudas, G., et al. 2018, MNRAS, 473, 1258

Schurmann, S. R., Arnett, W. D., & Falk, S. W. 1979, ApJ, 230, 11

Sharina, M. E., Karachentsev, I. D., & Tikhonov, N. A. 1999, Astronomy Letters, 25, 322

Siess, L. 2007, A&A, 476, 893

Silverman, J. M., Ganeshalingam, M., Li, W., & Filippenko, A. V. 2012, MNRAS, 425, 1889

Silverman, J. M., Ganeshalingam, M., Li, W., et al. 2011, MNRAS, 410, 585

Silverman, J. M., Nugent, P. E., Gal-Yam, A., et al. 2013a, ApJS, 207, 3

Silverman, J. M., Nugent, P. E., Gal-Yam, A., et al. 2013b, ApJ, 772, 125

Smartt, S. J. 2009, ARA&A, 47, 63

Smartt, S. J., Chen, T. W., Jerkstrand, A., et al. 2017, Nature, 551, 75

Smartt, S. J., Maund, J. R., Hendry, M. A., et al. 2004, Science, 303, 499

Smartt, S. J., Valenti, S., Fraser, M., et al. 2015, A&A, 579, A40

Smith, K. W., Williams, R. D., Young, D. R., et al. 2019, Research Notes of the American Astronomical Society, 3, 26

Smith, N. 2013, MNRAS, 434, 102

Smith, N. 2017, Interacting Supernovae: Types IIn and Ibn, 403

Smith, N., Andrews, J. E., Mauerhan, J. C., et al. 2016a, MNRAS, 455, 3546

Smith, N., Andrews, J. E., Van Dyk, S. D., et al. 2016b, MNRAS, 458, 950

Smith, N., Ganeshalingam, M., Chornock, R., et al. 2009, ApJ, 697, L49

Smith, N., Götberg, Y., & de Mink, S. E. 2018, MNRAS, 475, 772

Smith, N. & Hartigan, P. 2006, ApJ, 638, 1045

Smith, N., Li, W., Silverman, J. M., Ganeshalingam, M., & Filippenko, A. V. 2011, MNRAS, 415, 773

Smith, N., Miller, A., Li, W., et al. 2010, AJ, 139, 1451

Smith, N. & Stassun, K. G. 2017, AJ, 153, 125

Smith, N., Vink, J. S., & de Koter, A. 2004, ApJ, 615, 475

Sobacchi, E., Granot, J., Bromberg, O., & Sormani, M. C. 2017, MNRAS, 472, 616

Sollerman, J., Lindahl, J., Kozma, C., et al. 2004, A&A, 428, 555

Sorce, J. G., Tully, R. B., Courtois, H. M., et al. 2014, MNRAS, 444, 527

Spergel, D., Gehrels, N., Baltay, C., et al. 2015, arXiv e-prints, arXiv:1503.03757

Spiro, S., Pastorello, A., Pumo, M. L., et al. 2014, MNRAS, 439, 2873

Stancliffe, R. J. & Eldridge, J. J. 2009, MNRAS, 396, 1699

Stephens, H. F., Zheng, W., & Filippenko, A. V. 2017, Transient Name Server Discovery Report, 33

Stetson, P. B. 1987, PASP, 99, 191

Szczygieł, D. M., Prieto, J. L., Kochanek, C. S., et al. 2012, ApJ, 750, 77

Taddia, F., Sollerman, J., Fremling, C., et al. 2015, A&A, 580, A131

Taddia, F., Stritzinger, M. D., Bersten, M., et al. 2018, A&A, 609, A136

Taddia, F., Stritzinger, M. D., Phillips, M. M., et al. 2012, A&A, 545, L7

Taddia, F., Stritzinger, M. D., Sollerman, J., et al. 2013, A&A, 555, A10

Takahashi, K., Sumiyoshi, K., Yamada, S., Umeda, H., & Yoshida, T. 2019, ApJ, 871, 153

Takáts, K. & Vinkó, J. 2012, MNRAS, 419, 2783

Tanikawa, A., Nomoto, K., & Nakasato, N. 2018, ApJ, 868, 90

Tartaglia, L., Elias-Rosa, N., Pastorello, A., et al. 2016, ApJ, 823, L23

Taubenberger, S. 2017, The Extremes of Thermonuclear Supernovae, 317

Taubenberger, S., Benetti, S., Childress, M., et al. 2011, MNRAS, 412, 2735

Taubenberger, S., Floers, A., Vogl, C., et al. 2019, arXiv e-prints, arXiv:1907.06753

Terreran, G., Jerkstrand, A., Benetti, S., et al. 2016, MNRAS, 462, 137

Terreran, G., Margutti, R., Bersier, D., et al. 2019, arXiv e-prints, arXiv:1905.02226

Terry, J. N., Paturel, G., & Ekholm, T. 2002, A&A, 393, 57

Theureau, G., Rauzy, S., Bottinelli, L., & Gouguenheim, L. 1998, A&A, 340, 21

Thomas, R. C., Branch, D., Baron, E., et al. 2004, ApJ, 601, 1019

Thompson, T. A., Prieto, J. L., Stanek, K. Z., et al. 2009, ApJ, 705, 1364

Thuan, T. X. & Gunn, J. E. 1976, PASP, 88, 543

Tody, D. 1986, in Proc. SPIE, Vol. 627, Instrumentation in astronomy VI, ed. D. L. Crawford, 733

Tody, D. 1993, in Astronomical Society of the Pacific Conference Series, Vol. 52, Astronomical Data Analysis Software and Systems II, ed. R. J. Hanisch, R. J. V. Brissenden, & J. Barnes, 173

Tominaga, N., Blinnikov, S. I., & Nomoto, K. 2013, ApJ, 771, L12

Truran, J. W., Arnett, W. D., & Cameron, A. G. W. 1967, Canadian Journal of Physics, 45, 2315

Tully, R. B., Courtois, H. M., Dolphin, A. E., et al. 2013, AJ, 146, 86

Tully, R. B., Courtois, H. M., & Sorce, J. G. 2016, AJ, 152, 50

Tully, R. B., Rizzi, L., Shaya, E. J., et al. 2009, AJ, 138, 323

Turatto, M. 2003, in Lecture Notes in Physics, Berlin Springer Verlag, Vol. 598, Supernovae and Gamma-Ray Bursters, ed. K. Weiler, 21–36

Turatto, M., Benetti, S., & Cappellaro, E. 2003, in From Twilight to Highlight: The Physics of Supernovae, ed. W. Hillebrandt & B. Leibundgut, 200

Turatto, M., Benetti, S., Cappellaro, E., et al. 1996, MNRAS, 283, 1

Turatto, M., Cappellaro, E., Danziger, I. J., et al. 1993, MNRAS, 262, 128

Tylenda, R. 2004, A&A, 414, 223

Tylenda, R., Hajduk, M., Kamiński, T., et al. 2011, A&A, 528, A114

Tylenda, R. & Kamiński, T. 2012, A&A, 548, A23

Valenti, S., Howell, D. A., Stritzinger, M. D., et al. 2016, MNRAS, 459, 3939

Valenti, S., Pastorello, A., Cappellaro, E., et al. 2009, Nature, 459, 674

Valenti, S., Yuan, F., Taubenberger, S., et al. 2014, MNRAS, 437, 1519

Van Dyk, S. D. 2007, Highlights of Astronomy, 14, 205

Van Dyk, S. D. 2017, Philosophical Transactions of the Royal Society of London Series A, 375, 20160277

Van Dyk, S. D., Li, W., & Filippenko, A. V. 2003a, PASP, 115, 1

Van Dyk, S. D., Li, W., & Filippenko, A. V. 2003b, PASP, 115, 1289

Van Dyk, S. D., Peng, C. Y., Barth, A. J., & Filippenko, A. V. 1999, AJ, 118, 2331

Van Dyk, S. D., Peng, C. Y., King, J. Y., et al. 2000, PASP, 112, 1532

Van Dyk, S. D., Zheng, W., Brink, T. G., et al. 2018, ApJ, 860, 90

van Horn, H. M. 1979, Physics Today, 32, 23

Varani, G. F., Meikle, W. P. S., Spyromilio, J., & Allen, D. A. 1990, MNRAS, 245, 570

Wainscoat, R. J. & Cowie, L. L. 1992, AJ, 103, 332

Wanajo, S., Janka, H.-T., & Müller, B. 2011, ApJ, 726, L15

Wang, L., Cui, X., Zhu, H., & Tian, W. 2015, in Advancing Astrophysics with the Square Kilometre Array (AASKA14), 64

Wang, X., Chen, J., Wang, L., et al. 2018, arXiv e-prints, arXiv:1810.11936

Wang, X., Li, W., Filippenko, A. V., et al. 2009, ApJ, 697, 380

Wang, X., Wang, L., Filippenko, A. V., Zhang, T., & Zhao, X. 2013, Science, 340, 170

Wang, X., Wang, L., Pain, R., Zhou, X., & Li, Z. 2006, ApJ, 645, 488

Wang, X., Yang, Y., Zhang, T., et al. 2005a, ApJ, 626, L89

Wang, X. F., Zhou, X., Zhang, T. M., & Li, Z. W. 2005b, in Astronomical Society of the Pacific Conference Series, Vol. 342, 1604-2004: Supernovae as Cosmological Lighthouses, ed. M. Turatto, S. Benetti, L. Zampieri, & W. Shea, 272

Weaver, T. A. & Woosley, S. E. 1979, in BAAS, Vol. 11, Bulletin of the American Astronomical Society, 724

Wells, L. A., Phillips, M. M., Suntzeff, B., et al. 1994, AJ, 108, 2233

Wheeler, J. C., Harkness, R. P., Clocchiatti, A., et al. 1994, ApJ, 436, L.135

Wheeler, J. C. & Levreault, R. 1985, ApJ, 294, L17

Whitelock, P. A., Catchpole, R. M., Menzies, J. W., et al. 1988, MNRAS, 234, 5P

Williams, B. F., Hillis, T. J., Murphy, J. W., et al. 2018, ApJ, 860, 39

Williams, S. C., Darnley, M. J., Bode, M. F., & Steele, I. A. 2015, ApJ, 805, L18

Willick, J. A., Courteau, S., Faber, S. M., et al. 1997, ApJS, 109, 333

Wilson, J. R. & Mayle, R. W. 1988, Phys. Rep., 163, 63

Winters, J. M., Le Bertre, T., Jeong, K. S., Nyman, L. Å., & Epchtein, N. 2003, A&A, 409, 715

Winters, J. M., Le Bertre, T., Pety, J., & Neri, R. 2007, A&A, 475, 559

Wolf, B. 1989a, A&A, 217, 87

Wolf, B. 1989b, in Astrophysics and Space Science Library, Vol. 157, IAU Colloq. 113: Physics of Luminous Blue Variables, ed. K. Davidson, A. F. J. Moffat, & H. J. G. L. M. Lamers, 91–98

Wolf, B. & Zickgraf, F. J. 1986, A&A, 164, 435

Wood-Vasey, W. M., Wang, L., & Aldering, G. 2004, ApJ, 616, 339

Woosley, S. E., Blinnikov, S., & Heger, A. 2007, Nature, 450, 390

Woosley, S. E. & Bloom, J. S. 2006, ARA&A, 44, 507

Woosley, S. E., Heger, A., & Weaver, T. A. 2002, Reviews of Modern Physics, 74, 1015

Woosley, S. E., Langer, N., & Weaver, T. A. 1993, ApJ, 411, 823

Woosley, S. E., Taam, R. E., & Weaver, T. A. 1986, ApJ, 301, 601

Woosley, S. E. & Weaver, T. A. 1986, ARA&A, 24, 205

Wright, E. L. 2006, PASP, 118, 1711

Xiang, D., Wang, X., Mo, J., et al. 2019, ApJ, 871, 176

Yamanaka, M., Kawabata, K. S., Kinugasa, K., et al. 2009, ApJ, 707, L118

Yasuda, Y., Suzuki, T. K., & Kozasa, T. 2019, ApJ, 879, 77

Yoon, S.-C., Dessart, L., & Clocchiatti, A. 2017, ApJ, 840, 10

Yuan, F., Akerlof, C., Quimby, R., et al. 2007, in Bulletin of the American Astronomical Society, Vol. 39, American Astronomical Society Meeting Abstracts, 929

Yunus, S., Zheng, W., & Filippenko, A. V. 2018, Transient Name Server Discovery Report, 338

Yusof, N., Hirschi, R., Meynet, G., et al. 2013, MNRAS, 433, 1114

Zampieri, L., Colpi, M., Shapiro, S. L., & Wasserman, I. 1998, ApJ, 505, 876

Zeldovich, Y. B. & Spalding, D. B. 1985, Nature, 316, 586

Zhang, J., Wang, X., Mazzali, P. A., et al. 2014, ApJ, 797, 5

Zhang, J.-J., Wang, X.-F., Sasdelli, M., et al. 2016, ApJ, 817, 114

Zhang, T., Wang, X., Wu, C., et al. 2012, AJ, 144, 131

Zhao, X., Maeda, K., Wang, X., et al. 2016, ApJ, 826, 211

Zwicky, F. 1938, Physical Review, 53, 1019

Zwicky, F. 1940, Reviews of Modern Physics, 12, 66